High-temperature dielectric ceramics of the tetragonal tungsten-bronze structure and the role of aerosol deposition in modulating permittivity-temperature relationships

Harry John Peirson

Submitted in accordance with the requirements for the degree of Doctor of Philosophy

The University of Leeds

School of environmental and physical sciences (EPS)

February 2024

Intellectual Property and Publication Statements

The candidate confirms that the work submitted is their own, except where work which has formed part of jointly authored publications has been included. The contribution of the candidate and the other authors to this work has been explicitly indicated below. The candidate confirms that appropriate credit has been given within the thesis where reference has been made to the work of others.

The work presented in Section 5.3, Results chapter 1, is based on work from a jointly authored publication:

Structure and dielectric properties of yttrium-doped $Ca_{0.28}Ba_{0.72}Nb_2O_6$ ceramics. *J. Alloy Compd*. **950 (2023)**. 169891

Contributing authors: Peirson, H. Pan, J. Li, Y. Hooper, T. E. Hall, D. A. Brown, A. P. Drummond-Brydson, R. M. Milne, S. J.

For this publication the author was responsible for the manuscript, synthesis of the samples, and experimentation including; X-ray diffraction, scanning electron microscopy and dielectric spectrometry.

Dr. Jungcheng Pan and Dr. Yizhe Li were responsible for ferroelectric (polarisation-electric field response) experimentation on the Yttria doped calcium barium niobate samples. Dr. David A. Hall and the author performed Rayleigh analysis on this data. Dr. Yizhe Li performed Rietveld analysis on the X-ray diffraction data.

Acknowledgements

I would like to acknowledge the contributions of the technical staff and research group at the University of Leeds, as well as those from collaborating institutions at Manchester, Sheffield, Warwick, Durham, and Erlangen. With thanks to my primary supervisors Prof. Steve J. Milne and Prof. Andy P. Brown for their extensive support, for which I am most grateful. A special thanks to my family, friends, and Elizabeth for all their encouragement and support over the past four and a half years.

Abstract

This work explores the development of high temperature dielectrics based on an unfilled tungsten bronze-structured ceramic, $Ca_{0.28}Ba_{0.72}Nb_2O_6$ (CBN28), for potential power electronics applications. CBN28 exhibited ferroelectric P-E loops, a slightly diffuse permittivity peak around T_C at 231 °C, and high losses above 250 °C due to ionic conductivity (tan δ > 0.2). Subsequent A site substitution of Y^{3+} for Ca^{2+}/Ba^{2+} with assumed vacancy addition, in the nominal composition $(Ca_{0.28}Ba_{0.72})_{1-3w/2}Y_wNb_2O_6$ [0 ≤ w ≤ 0.20], increased permittivity-temperature stability at the single-phase limit, w = 0.04 (ε_r = 1143 ±15 % from 71 to 210 °C), and narrowed P-E loops (P_r at 40 kV cm^{-1} = 1.5 µC cm^{-2}, whereas in CBN28 P_r = 2.4 µC cm^{-2}). Doping with Y^{3+} and Ta^{5+}, in the nominal composition $(Ca_{0.28}Ba_{0.72})_{0.94}Y_{0.04}Nb_{1.8}Ta_{0.2}O_6$, induced permittivity-frequency dependence, lowered the temperature of ε_r-Max (T_M) to 13 °C at 1 kHz and 46 °C at 1000 kHz, further improved temperature stability of permittivity (ε_r = 954 ±15 % from -58 to 110 °C) and substantially narrowed P-E loops (P_r at 40 kV cm^{-1} = ~0.5 µC cm^{-2}). Decreasing Ca content, in the formulation $(Ca_{0.22}Ba_{0.78})_{0.94}Y_{0.04}Nb_{1.8}Ta_{0.2}O_6$, produced ε_r = 972 ±15 % from -9 to 166 °C and removed a secondary phase.

To develop low-temperature deposition of strained ceramic films, a particle aerosol deposition (PAD) system was commissioned at Leeds. This produced submicron Al_2O_3 and CBN28 anchor layer films with evidence of severe ceramic deformation in the layers by electron microscopy. Subsequent PAD (on a system in Manchester) of a calcined, high-energy milled and granulated CBN28 powder produced a thick film (10+ µm) with highly supressed polarisation responses (P_{Max} at 40 kV cm^{-1} = ~0.3 µC cm^{-2}, ε_r = ~85). Annealing, up to 750 °C, partially recovered permittivity, retained improved temperature stability, and induced relaxor-like frequency dependence (ε_r = ~225 ±15 % from ~20 to ~240 °C). XRD peak broadening analysis of the CBN film pre- and post- annealing at 750 °C suggested microstrain reduction from 0.14 to 0.11 % strain in combination with crystallite size increases from ~125 to ~270 nm.

Table of Contents

List of Tables

List of Figures

Abbreviations

$a^{/}$	Rayleigh coefficient for the real part of permittivity
$a^{//}$	Rayleigh coefficient for the imaginary part of permittivity
AC	Alternating current
AGC	Aerosol generation chamber
AS	A Site occupying ion
at.%	Atomic percentage
avg.	Average
B_L	Peak broadening due to mean crystallite size
BNN	Barium sodium niobate
BNT	Barium sodium titanate
BZT	Barium zirconate titanate
CN	Coordination number
CBN	Calcium barium niobate
CBN22	Calcium barium niobate, $Ca_{0.22}Ba_{0.78}Nb_2O_6$
CBN28	Calcium barium niobate, $Ca_{0.28}Ba_{0.72}Nb_2O_6$
CBNNS	Calcium barium sodium niobate antimonate
CBNNT	Calcium barium sodium niobate tantalate
CSBN	Calcium strontium barium niobate
d	Lattice spacing
DC	Direct current
DTA	Differential thermal analysis
d(50)	50 percent of particles at or below (the stated size)
d(90)	90 percent of particles at or below (the stated size)
δ	Phase difference
ΔT	Difference in temperature
E_0	Electric field
E_C	Coercive field
E_{Max}	Maximum applied field
ED	Electron diffraction
EELS	Electron energy loss spectroscopy
EIA	Electronic industries alliance
ER	Ergodic relaxor
ε	Permittivity
ε_o	Permittivity of the vacuum
ε_r	Relative permittivity
ε_r'	Real component of permittivity
ε_r''	Imaginary component of permittivity
ε_r-Max	Permittivity maxima
FE	Ferroelectric
FHE	Fume hood exhaust
FIB	Focussed ion beam
Fil_1	Filter (number 1)
Fil_2	Filter (number 2)
FM	Flow meter
HAADF	High angle annular darkfield
I	Current (in a real capacitor)
I_c	Current in an ideal capacitor

$K_{\alpha1}$	$K_{\alpha1}$ X-ray radiation
$K_{\alpha2}$	$K_{\alpha2}$ X-ray radiation
K_{β}	K_{β} X-ray radiation
KNN	Potassium sodium niobate
λ	Wavelength
Max.	Maximum
Min.	Minimum
MG	Manual gauge
MLCCs	Multi-layer ceramic capacitors
NA	Numerical aperture
NC	Nitrogen cannister
NR	Nonergodic relaxor
η	Energy recovery efficiency
PAD	Particle aerosol deposition
Pe	Pressure at end
PG_1	Pirani gauge (number 1)
PG_2	Pirani gauge (number 2)
P_{Max}	Maximum polarisation
PMN	Lead magnesium niobate
PNRs	Polar nano regions
P_r	Residual polarisation
PR	Pressure relief valve
P_S	Saturation polarisation
P_{Sp}	Spontaneous polarisation
Pst	Pressure at start
P-E	Polarisation-electric field (response)
P	Polarisation
R_a	Radius of the A site ion
R_o	Radius of the oxygen ion
R_b	Radius of the B site ion
RF	Relaxor (ferroelectric)
rpm	Revolutions per minute
RSS	Removable sample stage
R_{wp}	Goodness of fit parameter
S_{BET}	Specific surface area
SBN	Strontium barium niobate
SBN30	Strontium barium niobate, $Sr_{0.3}Ba_{0.7}Nb_2O_6$
SBN61	Strontium barium niobate, $Sr_{0.61}Ba_{0.39}Nb_2O_6$
SBT	Strontium barium titanate
SNN	Strontium sodium niobate
STEM	Scanning transmission electron microscopy
SUS304	Stainless steel
σ	Incommensurability factor
T	Temperature
t	Tolerance factor (perovskite)
tan δ	Dielectric loss factor
t_{A1}	Tungsten bronze A1 site tolerance factor
t_{A2}	Tungsten bronze A2 site tolerance factor
TB	Tungsten bronze
T_C	Curie temperature

TEM	Transmission electron microscopy
T_f	Freezing temperature (of dipole)
$T_{C/M}$	Either the Curie temperature or the temperature of permittivity maxima
T_M	Temperature of permittivity maxima
TTB	Tetragonal tungsten bronze
t_{TB}	Tungsten bronze tolerance factor
Ti-4V-6Al	Ti-alloy
T_0	Temperature analogous to T_C, for relaxors
T*	Critical temperature
VC	Vacuum chamber
W_{re}	Total recoverable energy
wt.%	Weight percentage
XPS	X-ray photoelectron spectroscopy
XRD	X-ray diffraction
X7R	Electronic industries alliance specification, see Table 1
X9R	Electronic industries alliance specification from -55 to 200 °C, see Table 1
χ	Dielectric susceptibility
YZT	Yttria stabilised zirconia
Υ	Modified curie Weiss law coefficient
z	Nozzle stand-off distance
2-D	2 dimensional
3-D	3 dimensional

1. Introduction

1.1 Capacitors and high temperature dielectric material

Capacitors are passive electronic components that store charge (Q) in proportion to an applied field (voltage, V). They have a variety of applications including power electronics, energy storage, remote sensing, signal filtering and electrical decoupling. A parallel plate capacitor consists of 2 conducting plates separated by a dielectric medium. The magnitude of its capacitance (C) is dependent on the permittivity (ε) of the dielectric medium, the area of the plates (A) and the distance between them (d), as shown in Equation 1.

$$C = \frac{Q}{V} = \frac{A\varepsilon}{d} \qquad \text{Equation 1}$$

High volumetric efficiency is achieved in multi-layer ceramic capacitors (MLCCs) by stacking thin layers of high permittivity ceramic material between parallel plate electrodes. Traditionally precious metal electrodes have been employed, these have been replaced by cheaper and more readily sourced base metals such as Ni.

The Electronic Industries Alliance (EIA) classifies capacitors according to their volumetric efficiency, temperature stability and dielectric loss. Class I capacitors offer high temperature stability and low losses. Class II capacitors have high volumetric efficiencies of capacitance but typically have higher losses and poorer temperature stability. Ceramic dielectric materials often have high permittivity due to their polar crystal structure. However, this structure, and so the materials permittivity, is temperature dependant. Table 1 shows the nomenclature used to detail capacitor operating specifications, for example the X7R series has a ±15 % stability in permittivity (denoted by R) from -55 °C (X) to 125 °C (7).

Table 1. Select EIA nomenclature for the specification of capacitor performance [EIA. 2002].

Lower temperature bound (°C)	Higher temperature bound (°C)	Permissible change in permittivity over the temperature range (%)
X (= -55 °C)	5 (= +85 °C)	P (= ±10 %)
Y (= -30 °C)	6 (= +105 °C)	R (= ±15 %)
Z (= +10 °C)	7 (= +125 °C)	S (= ±22 %)

An industry push for new high temperature dielectrics that can operate from -55 to 300 °C is being driven by the automotive, aerospace and power electronic industries. Such high temperature dielectrics, operating alongside existing high temperature cladding, would reduce the need for temperature control by cooling systems (or distancing of the component from the engine) in automotive and aerospace applications, thus reducing weight and increasing efficiency. Increased efficiency could likewise be unlocked in the power electronics industry by the employment of novel high temperature dielectrics alongside existing high temperature semiconductors and transistors. Here, the control of voltage and frequency during renewable energy generation results in heat generation and increased operating temperatures. High breakdown strengths and low dielectric losses are also ideal for these industry applications.

The perovskite structured barium titanate ($BaTiO_3$), with sufficient chemical modification, can exhibit R-type stable permittivity up 200 ^{o}C, which is insufficient for emerging applications [Jiang, X. 2021]. A number of Bi or Pb containing materials have achieved near temperature stable permittivity up to and above 300 ^{o}C [Zeb, A. 2014], however Bi-oxide based dielectrics are incompatible with modern base metal electrode manufacturing techniques. Bi containing dielectrics are prone to oxidation of the Ni electrodes due to the comparable Gibbs free energies of Bi and Ni (and their oxides). Such oxidation would reduce the conductivity of the electrode and induce conductive defects in the dielectric, necessitating the employment of reducing (low oxygen) firing conditions and thus limiting industry uptake. Additionally, Pb content in electronic components has been subject to environmental litigation, due to its toxicity. More recently, a strontium sodium niobate (SNN) based composition has leveraged the structural complexities of the tungsten bronzes to achieve near temperature stable permittivity from -65 to 325 ^{o}C [Brown, T. 2021]. However, the phase-stability of SNN is problematic [Tang, D-S. 1979]. Another tungsten bronze, calcium barium niobate (CBN), has been selected here for chemical modification and processing-induced structural modification with the aim of producing industry applicable material with near temperature stable permittivity to high temperatures, beyond that of existing $BaTiO_3$-based dielectrics.

Conventional MLCC manufacturing, via tape casting, involves the sintering of a ceramic slurry at high temperatures to produce thin layers of dielectric. An alternative technique, particle aerosol deposition (PAD), operates at room temperature and reduced pressures to consolidate micron scale ceramic particles into a film via mechanical impact forces [Akedo, J. 2008]. Such films exhibit high levels of microstrain, which have been shown in ferroelectric thin films to induce structural disorder and inhibit ferroelectric character, potentially improving temperature stability of permittivity. If required, a combination of CBN chemical modification and PAD processing will be employed.

1.2 Research problem

There is an industry push for high temperature, high voltage dielectrics to accompany pre-existing high temperature circuit technology (wide band gap semiconductors, interconnects and packaging). This dielectric should be temperature stable from -55 to +300 °C with electrical breakdown strengths of > 100 kV mm^{-1}. High energy density (> 10 kJ cm^{-3}) and low dielectric loss (tan δ < 0.02) are also essential. Such a material would find application in sectors of the multi-billion dollar capacitor industry that include; automotive, aerospace and power electronics.

Here, an investigation into optimising the dielectric properties of the promising and structurally complex tungsten bronze (TB) calcium barium niobate shall be achieved by chemical modification and a mix of bulk ceramic sintering and particle aerosol deposition film manufacture.

1.3 Aims and Objectives

Understand how particle aerosol deposition can be used to fabricate high quality tungsten bronze niobate dielectric films that exhibit stable performance over very wide temperature ranges (-55 to 300 °C) as required for next generation high temperature Class II capacitors.

1.3.1 Objectives

- Manufacture calcium barium niobate (CBN) powders of controlled composition and physical properties using conventional techniques, such as mixed oxide sintering.
- Understand the role of chemical modification on the microstructure and dielectric properties of the bulk ceramic.
- Commission a particle aerosol deposition (PAD) system in Leeds.
- Understand how particle aerosol deposition process variables can be controlled to deposit high quality CBN dielectric films.
- Investigate structure-property relations in the films.
- Manufacture films exhibiting stable relative permittivity (ε_r > 500 ±15 %) from -55 to 300 °C.

1.4 References

Akedo, J. 2008. Room Temperature Impact Consolidation (RTIC) of Fine Ceramic Powder by Aerosol Deposition Method and Applications to Microdevices. *J. Therm. Spray Technol*. **17**. 181-198

DOI: https://doi.org/10.1007/s11666-008-9163-7

Brown, T. Brown, A. P. Hall, D. A. Hooper, T. E. Li, Y. Micklethwaite, S. Aslam, Z. Milne, S. J. 2021. New high temperature dielectrics: Bi-free tungsten bronze ceramics with stable permittivity over a very wide temperature range. *J. Eu. Ceram. Soc*. **41**. 3416-3424

DOI: https://doi.org/10.1016/j.jeurceramsoc.2020.10.034

EIA. 2002. EIA-198-1-F. Ceramic Dielectric Capacitors Classes I, II, III and IV – Part I: Characteristics and Requirements. Technology Strategy & Standards Department (U.S.A and Canada). Vancouver

Jiang, X. Hao, H. Yang, Y. Zhou, E. Zhang, S. Wei, P. Cao, M. Yao, Z. Liu, H. 2021. Structure and enhanced dielectric temperature stability of $BaTiO_3$-based ceramics by Ca ion B site-doping. *J. Mater*. **7**. 295-301

DOI: https://doi.org/10.1016/j.jmat.2020.09.001

Tang, D-S. Liang, J-K. Shi, T-J. Zhang, Y-L. Tian, J-H. Li, W-X. 1979. INVESTIGATION OF THE PSEUDO-TERNARY SYSTEM $SrNb_2O_6$-$NaNbO_3$-$LiNbO_3$. *Acta Phys. Sin*. **28**. 62-77

DOI: https://doi.org/10.7498/aps.28.62

Zeb, A. Bai, Y. Button, T. Milne, S. J. 2014. Temperature-Stable Relative Permittivity from −70°C to 500°C in $(Ba_{0.8}Ca_{0.2})TiO_3$–$Bi(Mg_{0.5}Ti_{0.5})O_3$–$NaNbO_3$ Ceramics. *J. Am. Ceram. Soc*. **97**. 2479-2483

DOI: https://doi.org/10.1111/jace.12949

2. Background science

2.1 Chapter overview

This chapter introduces the background science of the materials relevant to this research, in relation to their crystal structure and functional properties. Processing techniques are also covered. The phenomenon of ferroelectricity is illustrated using the perovskite crystal structure of barium titanate ($BaTiO_3$). The materials researched in this thesis have the tungsten bronze structure, alternatively referred to as the tetragonal tungsten bronze structure (TTB). The key features of this structure-type are detailed. The influence of chemical modification and processing conditions on the phase transitions and permittivity responses of ferroelectrics is also described.

2.2 Crystal structure

Crystals are solids whose properties depend on internal atomic order [Brown, P. J. 1973]. The unit cell is the smallest repeatable unit in a crystal structure which reflects the structures overall symmetry, its periodic arrangement produces an atomic or molecular lattice of long-range order. The shape of the unit cell can be defined by a geometric reference frame using the vectors a, b and c and the angles α, β and γ, as shown in Figure 1. The variation of these parameters, shown in Table 2, allows for the generation of 7 unique shapes, or 3-D crystal systems, namely; cubic, tetragonal, orthorhombic, rhombohedral, hexagonal, monoclinic, and triclinic.

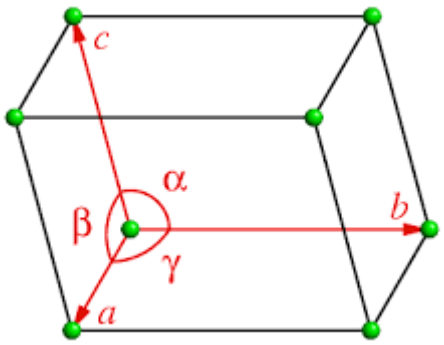

Figure 1. The 3-D reference frame used to describe crystal systems [Cockcroft, J. K. 2006].

Table 2. The parameters for efficiently describing the 7 crystal systems [West, A. R. 2014].

3-D crystal system	Vectors	Angles
Cubic	a = b = c	α = β = γ = 90°
Tetragonal	a = b ≠ c	α = β = γ = 90°
Orthorhombic	a ≠ b ≠ c	α = β = γ = 90°
Rhombohedral	a ≠ b ≠ c	α = β = γ ≠ 90°
Hexagonal	a = b ≠ c	α = β = 90°, γ = 120°
Monoclinic	a ≠ b ≠ c	α = γ = 90°, β ≠ 90°
Triclinic	a ≠ b ≠ c	α ≠ β ≠ γ

When describing the unit cell a cartesian vector notation is used, with the axis notation x, y and z used interchangeably with a, b, c -axis notation. Take the example of cube, with vertices at the origin (0, 0, 0) as well as 1 unit along the x-axis (1, 0, 0), y-axis (0, 1, 0), z-axis (0, 0, 1) and also (1, 1, 1), (1, 1, 0), (0, 1, 1) and (1, 0, 1). Here, a line vector (noted by square brackets), [1 1 1], begins at the origin and ends at the vertex (1, 1, 1), commonly this vector is called the body diagonal as it passes through the centre of the cubic unit cell. Pointed brackets denote symmetrically equivalent directions, for example an atoms displacement along the z-axis, in either direction, would be noted as <0 0 1>.

When describing (atomic) planes, values are given in round brackets, (hkl), as shown in Figure 2. The magnitude of these hkl values, or Miller indices, is the reciprocal of where the plane intersects the respective axis. A value of zero indicates no interception of the plane with the respective axes, i.e. the plane is parallel to the axis. Take the plane (110) in Figure 2. If the plane was modified to intersect the y-axis at the point y = 0.5, rather than y = 1, then the new Miller indices would be (120). Curly brackets denote a set of symmetrically equivalent planes, i.e. {1 0 0} refers the set of planes containing (100), (010) and (001).

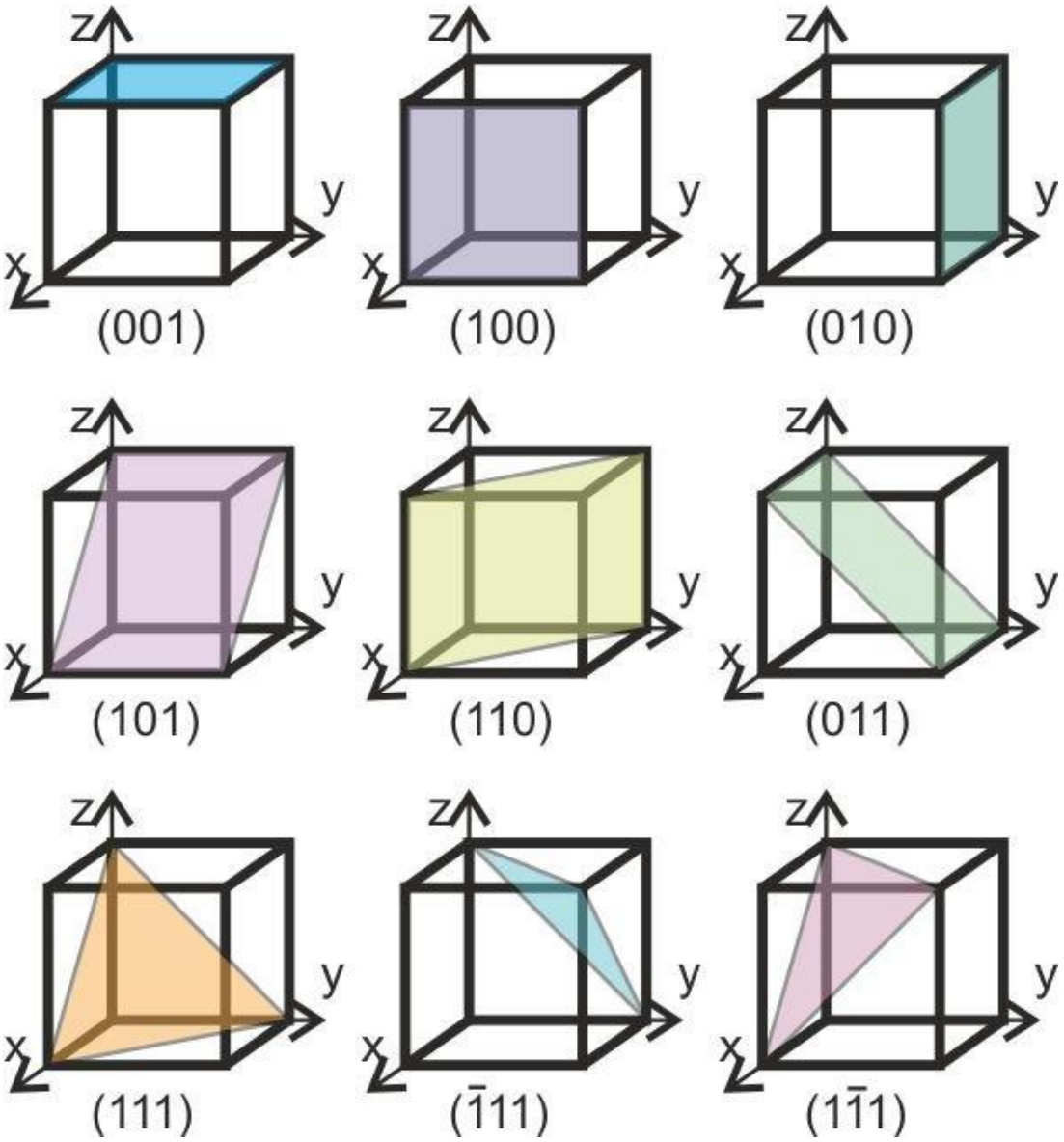

Figure 2. Plane notation for unit cells. The symbol $\bar{1}$ indicates the value -1 in conventional Miller indices notation [Waeselmann, N. 2012].

In addition to its crystal system, a material may have a specific 3-D lattice type. There are 14 Bravais lattices which can be generated by combining a crystal system and a lattice type, see Figure 3. Lattice points are locations in the lattice where an atom may be situated. A cubic 3-D system possessing lattice points located solely at its vertices is defined as possessing the primitive (or simple) cubic Bravais lattice, see Figure 3. If, in addition to the lattice points at the vertices, there is also a lattice point at the centre of the cube, then the lattice type is defined as body-centred cubic. If, in addition to the lattice points at the vertices, there are also lattice points at the centre of each face, then the lattice type is defined as face-centred cubic. Base-centred rhombohedral and monoclinic Bravais lattices exist, in which, in addition to the lattice points at the vertices, there are also 2 additional lattice points present at opposite faces.

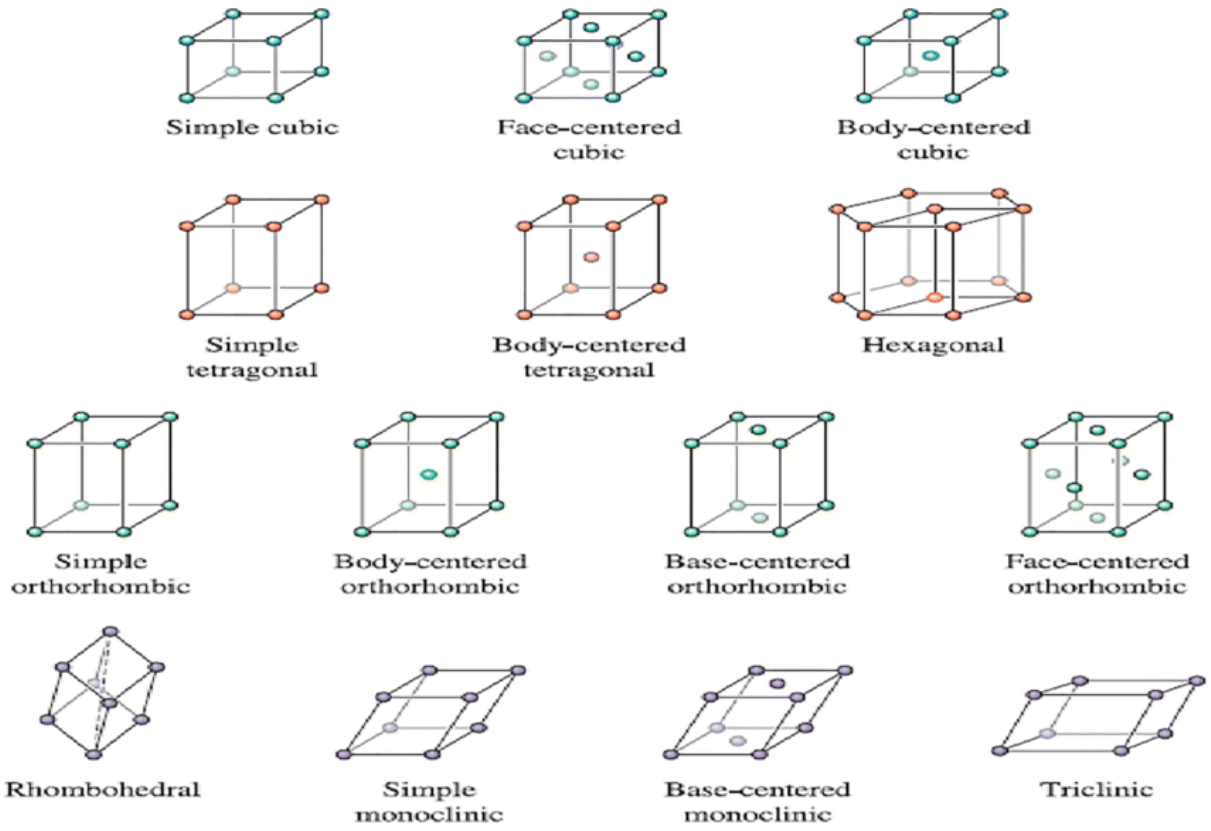

Figure 3. The 14 Bravais lattices [Ameh, E. S. 2019].

The symmetry possessed by a structure can also be used to define it. A symmetry operation is a geometric transformation which leaves the structure indistinguishable from its starting state. Crystals, which must possess a continuous lattice, are restricted to 2-, 3-, 4- or 6-fold rotational symmetry. Shapes with, for example, 5- or 7- rotational symmetry, i.e. in the case of 5-fold symmetry a (2-D) pentagon, do not tesselate and so cannot form a continuous lattice. Crystal systems may be symmetrical in up to 3 distinct mirror planes, one for each special dimension. A total of 32 symmetrically distinct crystal classes exist. Combining the 32 crystal classes with the 14 Bravais lattices gives 230 distinct ways to repeat a pattern in 3-D space, these are known as the 230 space groups [Hammond, C. 2015]. Hermann-Mauguin notation is used to distinguish these space groups.

Of the 32 crystal classes, 20 non-centrosymmetric classes allow for the asymmetric distribution of atomic, ionic, or molecular charge which gives rise to electroceramic functional properties such as piezo-, pyro- and ferroelectricity, with ferroelectricity being of particular relevance to this project.

In reality, deviations from ideal crystal symmetry and order are common and varied, often they influence a materials functional properties. Of particular interest to this project are point defects, in which a particular atomic site is subject to substitution or left vacant. A material may be polymorphic, transitioning between structures as external conditions such as temperature vary. Different materials with a shared structure are called isomorphs.

2.3 Dielectrics properties

Dielectrics are electrical insulators which polarise in proportion to an applied electric field. The short-range movement of bound charge carriers relative to an applied field produces this polarisation, or dielectric, response. These polarisation properties allow dielectric materials to inhibit direct current (DC) whilst conveying alternating currents (AC). Dielectric materials are utilised in capacitors in proximity to conducting plates, the polarisation of the dielectric induces greater charge storage on the plate. This charge can be rapidly released upon removal or reversal of the applied field.

Permittivity (ε) is the capacity of a material to store electrical energy when an electric field is applied, the relative permittivity of a material (ε_r) is measured relative to the permittivity of free space (ε_o). Equation 2 shows the relationship between polarisation (P), the permittivity of free space (ε_0), dielectric susceptibility (χ) and the applied electric field (E).

$$P = \varepsilon_o XE \qquad \text{Equation 2}$$

Where dielectric susceptibility (χ) is the rate of polarisation in response to an applied field.

Whilst ideal insulators allow no long-range movement of charge carriers, real dielectric materials allow some degree of conduction and can be modelled as wide band-gap semi-conductors. This conduction, or dielectric loss, can be represented in circuit theory as a capacitor and resistor in parallel. When a (sinusoidal) alternating current is applied to an ideal dielectric the voltage leads the current by 90°. In a real dielectric there exists a phase difference, δ, between the ideal (90°) voltage lead and the actual voltage lead. This is often referred to as lag, see Figure 4.

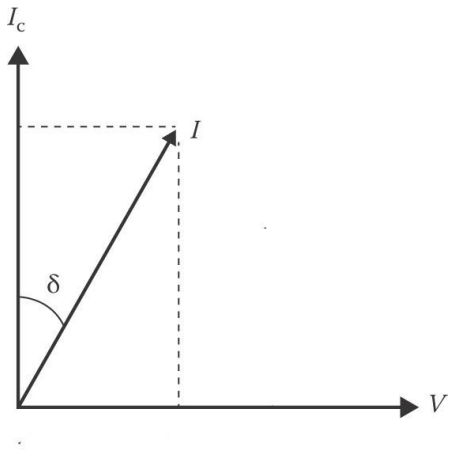

Figure 4. Phasor diagram for a dielectric material under an applied field. The applied voltage, V, is at 90° to the current (I_C) in an ideal dielectric and at 90-δ° in a real, lossy dielectric (I) [Raju, G. G. 2017].

The dielectric loss factor, tan δ, is related to the phase difference, or lag, such that tan δ is equal to the ratio of the imaginary (or lost) component of permittivity (ε_r'') to real component permittivity (ε_r').

Given a large enough electric field, charge carriers will break free of their structural bonds and conduction, or dielectric breakdown, will occur. This results in failure of the dielectric component. A materials dielectric strength is the maximum electric field it can withstand prior to dielectric breakdown.

2.4 Polarisation

There are four main polarisation mechanisms that can occur within a polycrystalline dielectric material. They can be readily distinguished by their relaxation time, which is determined by the highest frequency of alternating current (AC) that their respective charge carriers can follow [Kao, K. 2004]. The mechanisms of polarisation, and the frequencies at which they depolarise are shown in Table 3, their relaxation is visualised in Figure 5. Dielectric loss increases around relaxation as the charge carrier lags behind (is partially out of phase with respect to) the applied field.

Polarisation may also occur independent of an external electric field, the origin of such spontaneous polarisation can be explained in terms of the minimisation of free energy of a particular structure [Zheludev, I. S. 1971]. Equation 3 shows the relationship and inequality required for spontaneous polarisation. E_t is total energy, E_d is the energy of the dipole, E_s is the electrostatic energy due to the charge carrier's distortion of the unit cell.

$$Et = Ed + Es \qquad \text{Equation 3}$$

$$if\ Ed < Es, then\ spontaneous\ polarisation\ occurs$$

All dielectrics can exhibit electrical (atomic) polarisation, whilst dielectrics containing ions and spontaneous dipoles may exhibit ionic and dipolar (orientational) polarisation respectively. Spontaneous polarisation, and the ability to undergo the reorientation of dipoles, can contribute significantly to a materials permittivity. Space charge polarisation refers to the entrapment of mobile charge carriers by structural boundaries and is often associated with structural defects in dielectrics.

Table 3. The 4 main polarisation mechanisms for a dielectric and their typical depolarisation frequencies [Moulson, A. J. 2002].

Mechanism	Description	Depolarisation Frequency (Hz)
Space charge	Charge carriers move within grains, and along but not across grain boundaries.	10^2 <
dipolar	Distortion and reorientation of dipoles.	10^2 - 10^{10}
Ionic	Modulation of the distance between charge carriers.	10^9 - 10^{13}
atomic	Distortion of the electron cloud around nuclei.	10^{13} - 10^{15}

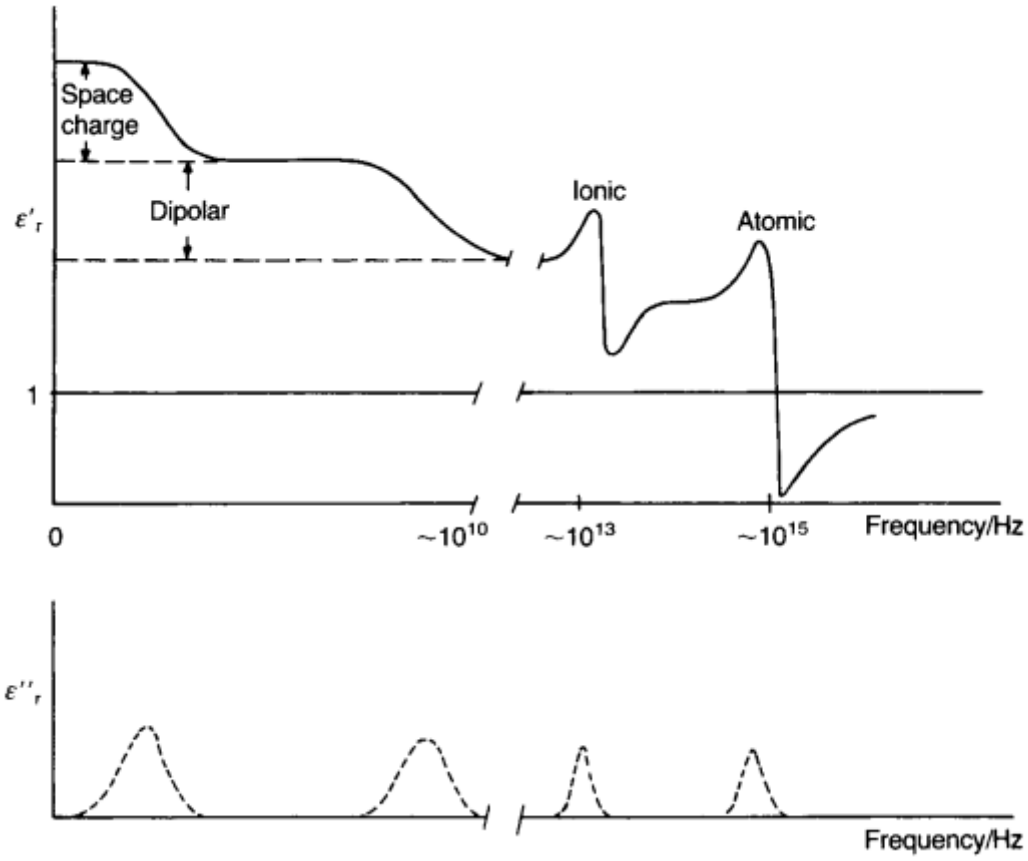

Figure 5. The variation in the real (ε_r') and imaginary (ε_r'') parts of permittivity with frequency and the origin of this variation in the 4 main polarisation mechanisms [Moulson, A. J. 2002].

2.5 Ferroelectricity

Ferroelectrics can be defined as dielectrics which display spontaneous polarisation (in the absence of an applied electric field), the direction of this polarisation can be reversed between 2 or more stable states by application of an electric field [Lines, M. 1979]. The ability to reorder polarisation by application of a field gives ferroelectrics increased dielectric susceptibility. The state of polar ordering within a ferroelectric, and so its dielectric properties, depends on past exposure to external fields. Such "hysteresis properties" are often used to identify ferroelectrics.

2.5.1 Barium titanate ($BaTiO_3$) and the perovskite structure

The perovskite structure, first noted in calcium titanate ($CaTiO_3$), is possessed by many compounds due to its tolerance of ions of different radii. Whilst the true perovskite structure exemplified by $CaTiO_3$ is cubic and non-polar, the structure distorts to lower symmetry over specific temperature ranges as a consequence of chemical substitutions, for example when substituting Ba for Ca.

The features of the perovskite structure, generic formula ABO_3, can be illustrated by $BaTiO_3$. In the structure 6 O^{2-} ions form an octahedron with a B site cation (Ti^{4+}) at is core, in plane with 4 of the O^{2-} ions which form a square/diamond around it. The TiO_6 octahedra is shown in Figure 6(a), the octahedral framework and the situation of A site Ba ions in the interstitial sites between the octahedra is depicted in Figure 6(b).

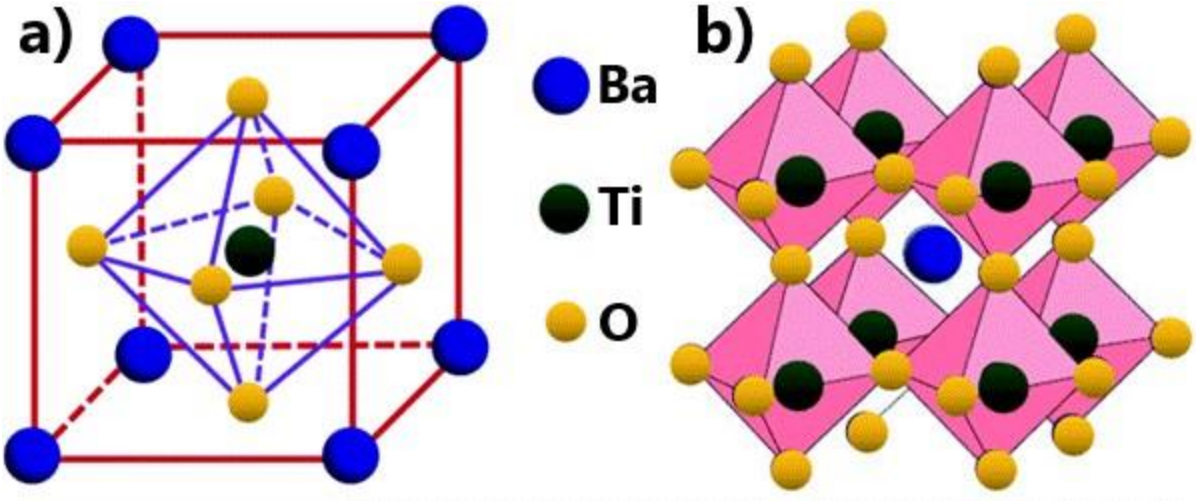

Figure 6. Two representations of the perovskite structured $BaTiO_3$, showing, in a), the TiO_6 octahedra within a framework of interstitially situated (A site) Ba ions and, shown in b), the framework formed by multiple oxygen-octahedra, with Ti locate within the octahedra (at the B site). Adapted from [Yi, Z. 2019].

2.5.2 The Goldschmidt tolerance factor

In perovskites the distortion of the ostensibly cubic unit cell is influenced by the radii of the ions in the potential structure, particularly the A site cations. The Goldschmidt tolerance factor is used to calculate the stability and distortion of crystal structures with reference to ionic radii [Goldschmidt, V. M. 1926]. The tolerance factor is derived from geometric considerations using a hard-sphere ion model, as shown in Figure 7. A tolerance factor, t, of 1 indicates an ideal (cubic) perovskite. Strontium titanate ($SrTiO_3$) and $BaTiO_3$ have tolerance factors between 0.9 and 1.0. Higher tolerance factors (t > 1) tend to result in tetragonal, or hexagonal structures whilst lower tolerance factors (t < 0.9) tend to result in orthorhombic or rhombohedral structures [Kour, R. 2019].

For the (cubic) perovskite ABO_3 structure the parameters are found by passing along the *c*-axis, through the center ion, $(2R_a + 2R_o)$, and by using Pythagoras's theorem on the side diagonal, $2\sqrt{2}(R_b + R_o)$, see Figure 7. The ratio of these distances gives the tolerance factor, as shown in Equation 4.

$$t = \frac{R_a + R_o}{\sqrt{2}(R_b + R_o)} \qquad \text{Equation 4}$$

Where t is the tolerance factor, R_a is the radius of the A cation, R_b the radius of the B cation and R_o the radius of the anion.

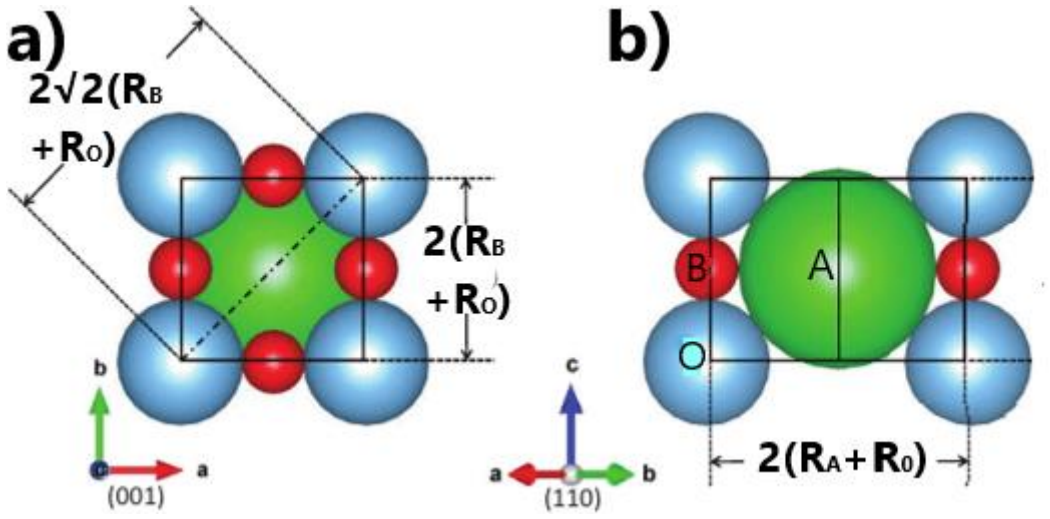

Figure 7. Derivation of the denominator, in (a), and numerator, in (b), of the Goldschmidt tolerance factor, using a hard-sphere representation of the ions in a cubic perovskite (ABO_3). Adapted from [George, G. 2020].

2.5.3 Polymorphism and polarisation in $BaTiO_3$

When cooling at ~130 ^{o}C, $BaTiO_3$ undergoes a phase transition from a cubic to a less symmetrical tetragonal structure. A dipole moment is formed as the Ti ion moves along the <0 0 1> direction, out of the equatorial plane with the 4 oxygen ions, see Figure 8. This separation of the high valency Ti^{4+} ion from the equatorial-plane oxygen ions results in a large polarisation that contributes to the high permittivity present in $BaTiO_3$.

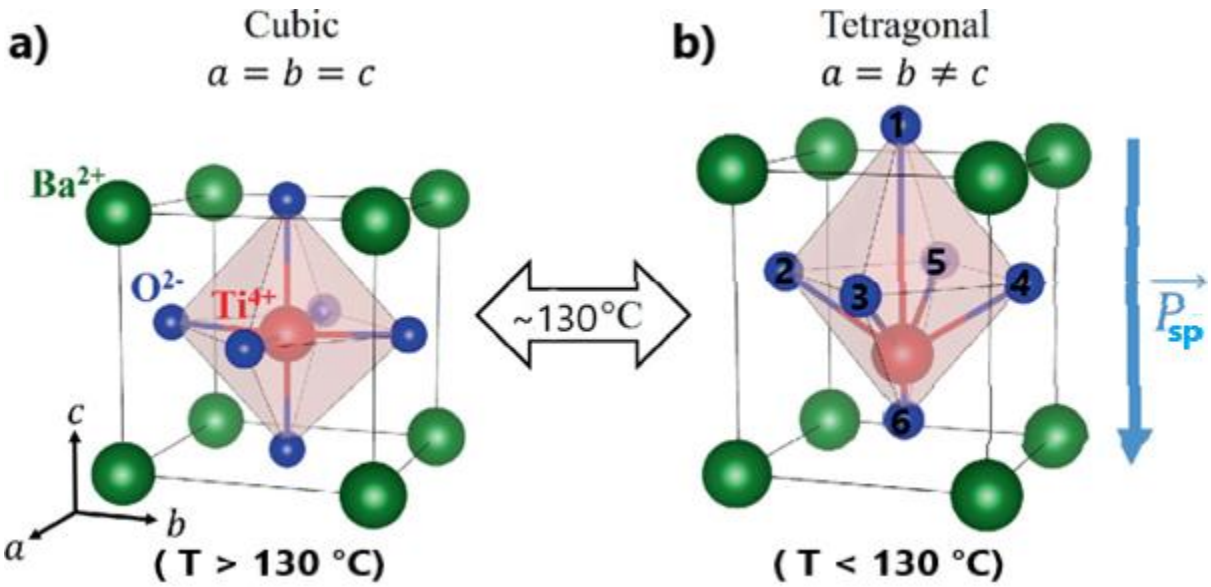

Figure 8. The structural transformation of $BaTiO_3$ at around 130 ^{o}C. At higher temperatures a cubic crystal system is present with the Ti ion situated within the equatorial plane of the O_6 octahedra, shown in (a). Upon cooling, a tetragonal crystal system is formed with the Ti ion displaced from the equatorial plane, shown in (b). The spontaneous polarisation (P_{Sp}) caused by the <0 0 1> directional displacement of the Ti^{4+} ion is indicated. The magnitude of the resulting dipole is slightly reduced by the compensatory displacement of the O1 and O6 ions, which result in a shorter Ti-O6 bond length and an elongated Ti-O1 bond length. The "in plane" O2, O3, O4 and O5 ions also displace slightly away from the Ti^{4+} ion. Adapted from [da Silva, L. L. 2021].

$BaTiO_3$ transitions through a series of structural polymorphs upon further cooling, from tetragonal to orthorhombic (with Ti ion displacements along <1 1 0>) and orthorhombic to rhombohedral (with Ti ion displacements along <1 1 1>).

2.5.4 Domain structure

In a ferroelectric, neighbouring unit cells tend to align their dipoles so as to minimise the electric field between one another. Regions of uniformly orientated spontaneous polarisation are called domains. Within the confines of a typically micron-scale grain, the concerted alignment of polarisation within a domain is inhibited by the electrostatic and mechanical strain that these polar distortions induce. Such inhibitory forces are often called depolarisation fields, they promote a polydomain structure in which the differing polar alignments of the neighbouring domains reduces the depolarisation field. Domain walls separate the individual regions of uniformly orientated polarisation. Domains typically have nano/micron scale dimensions in contrast to the Angstrom scaled dimensions of the unit cell and P_{Sp}.

The possible orientational relationships that neighbouring domains can possess is dependent upon unit cell shape (crystal/3-D system), as shown in Figure 9. For a ferroelectric tetragonal system, which polarises along the <0 0 1> direction, neighbouring domains can be orientated antiparallel (180^o) or perpendicular (90^o) to each other [Damjanovic, D. 1998]. Electrostatic stress is relieved by the presence of 180^o domains, whilst 90^o domains can also alleviate mechanical stresses [Damjanovic, D. 1998].

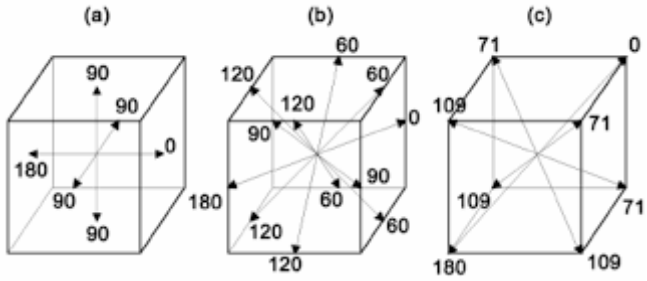

Figure 9. The number of polarisation directions and domain angles for polar crystal systems. The unit cell in (a) is tetragonal (with polarisation along <0 0 1>), (b) is orthogonal (with polarisation along <0 1 1>) and (c) is rhombohedral (with polarisation along <1 1 1>) [Martin, P. 2010].

The properties of domain walls may vary significantly from that of the bulk material, they often have a higher dielectric susceptibility [Xu, R. 2014]. Within a domain the coercive electrical field generated by neighbouring unit cells, with aligned polarisation, inhibits reorientation. Hence, unit cells at domain walls, which experience lesser coercive fields, are more prone to reorientation due to an applied field, when compared to a unit cell within the centre of a domain. When the average domain size is small the domain wall density (volume fraction) increases. Domains are often anisotropic, being larger and more variable in length (in the direction of polarisation) and narrower in width (perpendicular to polarisation), with domain width sometimes being related to the square root of

grain size [Kittel, C. 1946]. Hence, limiting the grain size, by control of processing conditions, can decrease domain size, increasing domain wall density and measured permittivity [Scott, J. 2012]. Very small (sub-micron) grains may, however, inhibit polarisation entirely and reduce permittivity.

Figure 10 shows the grain size effect of fine grains on the dielectric constant and T_C of $BaTiO_3$. A core-shell phase structure has been proposed for the grains in $BaTiO_3$, in which a cubic structured shell surrounds a tetragonal core [Jiang, B. 2019]. The intermediate or gradated region between these two dissimilar lattice structures is dynamic and has high dielectric susceptibility, similarly to how the domain walls between regions of differently orientated polarisation have high dielectric susceptibility [Hoshina, T. 2008]. As grain size decreases in $BaTiO_3$, towards ~1 µm, the proportion of the intermediate region increases and so permittivity increases. Below 1 µm, the grain boundaries exert a sufficiently large depolarisation field to reduce the presence of the (polar and high permittivity) tetragonal core and also the intermediate region. This suppression of polar distortions can be seen in Figure 10(b) as a reduction in T_C [Curecheriu, L. 2012]. Here, a greater driving force for phase change is required to overcome the depolarisation fields in nm-scaled $BaTiO_3$ grains and establish the tetragonal/ferroelectric phase.

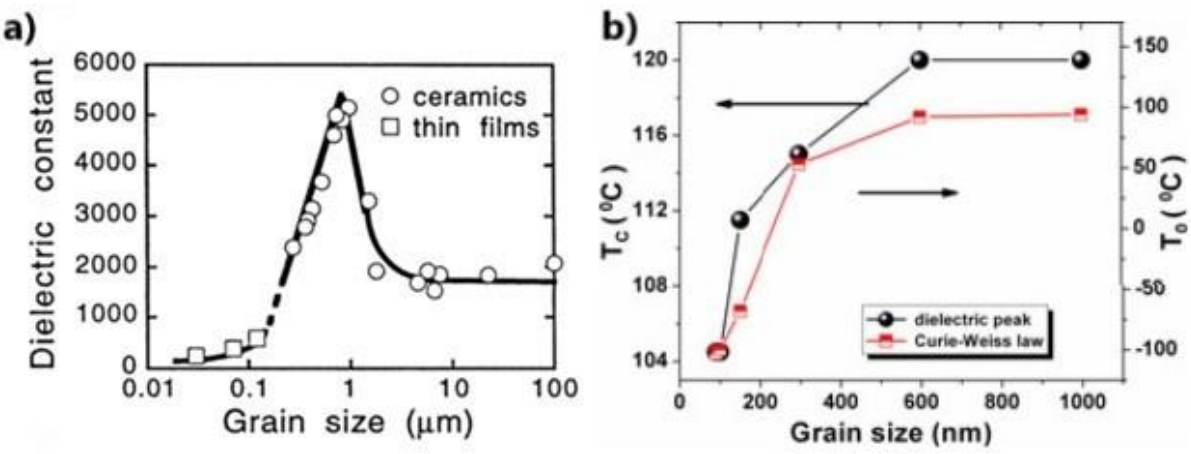

Figure 10. The effect of grain size on the permittivity and T_C of $BaTiO_3$ is shown in (a) and (b), respectively. Compiled from [Jiang, B. 2019] and [Curecheriu, L. 2012].

2.5.5 Polarisation-electric field (P-E) response

In a ferroelectric material with a polydomain microstructure that has not recently been subject to a significant applied field, the net polarisation of the domains may be near zero. Upon application of an electric field, polarisation is reorientated such that domain walls migrate and domains with polarisation in line with the applied field grow at the expense of domains with polarisation that is orientated against the field. The effect of an applied field on the polarisation within a ferroelectric is

detailed in Figure 11. After overcoming initial energy barriers to repolarisation, a linear response of increasing polarisation with increasing applied field is established. The polarisation response tails off as polarisation reorientation reaches a saturation point, P_S. At this point the material still retains some domains that are aligned against the applied field, but the polarisation in line with the field is at its maximum (P_{Max}). As the electric field is then reduced to zero some of the domains revert to their previous/disordered state and polarisation decreases. However, energy barriers exist between different polarisation states. This causes some domains to retain their applied polarisation in the subsequent absence of the field. The remnant polarisation (P_r) is defined as the polarisation present upon the removal of field ($E_0 = 0$). Reversing the field causes the domains to begin to grow in the opposite direction. At the coercive field (E_C) the (+)P_r is overcome and no net polarisation exists. Increasing this negative field further results in polarisation saturation in the negative direction. This non-linear polarisation response, or hysteresis loop, is characteristic of ferroelectrics and infers significant energy losses upon the cycling of a field [Uchino, K. 2017]. Lower coercive field strengths and reduced residual polarisations (narrower loops) result in reduced energy losses and greater potential energy storage (judged by P_{Max} - P_r). See Figure 11 for the P-E response hysteresis loop.

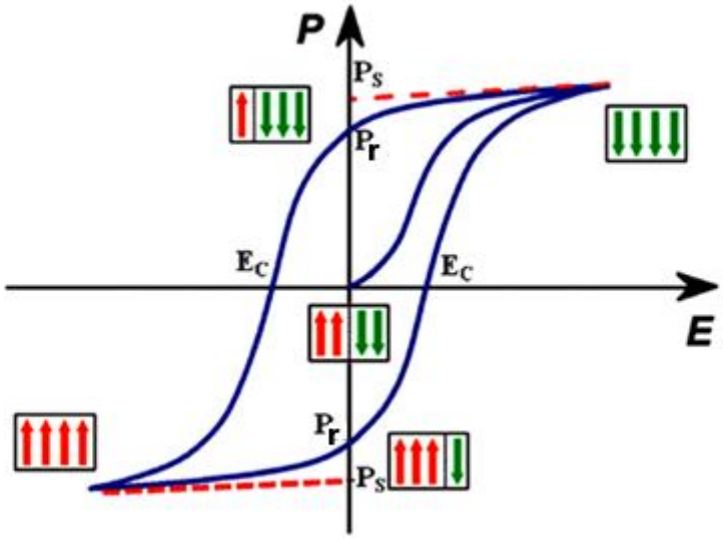

Figure 11. The polarisation-electric field response (hysteresis loop) of a ferroelectric and its origins in domain structure. The P_{Max} is the maximum polarisation at a given electric field, P_S is the saturation polarisation, P_r is the residual polarisation and E_C is the coercive field. Arrows indicate the presence and alignment of domains [Lone, I. H. 2019].

2.5.6 Paraelectric-ferroelectric phase transition and the Curie-Weiss law

As mentioned, ferroelectrics may possess multiple polymorphs which they transition between as external conditions, such as temperature, vary. Typically, at high temperatures a cubic perovskite phase exists which lacks the asymmetry required for macroscopic net-polarisation. This is called the paraelectric phase. Upon decreasing temperature, to the Curie point (T_C), there is a phase transition from the non-polar (i.e. cubic) phase to a polar/ferroelectric (typically tetragonal) phase. As detailed in Figure 12, this transition occurs at around 130 ^{o}C for $BaTiO_3$ and is accompanied by a large increase in permittivity and the materials permittivity maxima (ε_r-Max). Multiple ferroelectric-ferroelectric, or inter-ferroelectric, transitions may also occur at lower temperatures, with each phase transition being accompanied by a peak in permittivity. Permittivity peaks appear around the temperatures of phase transition as the structure softens, polarisation increases, and the energy required to generate or reorientate dipoles decreases [Guo, H. 2023] and [Polinger, V. 2015].

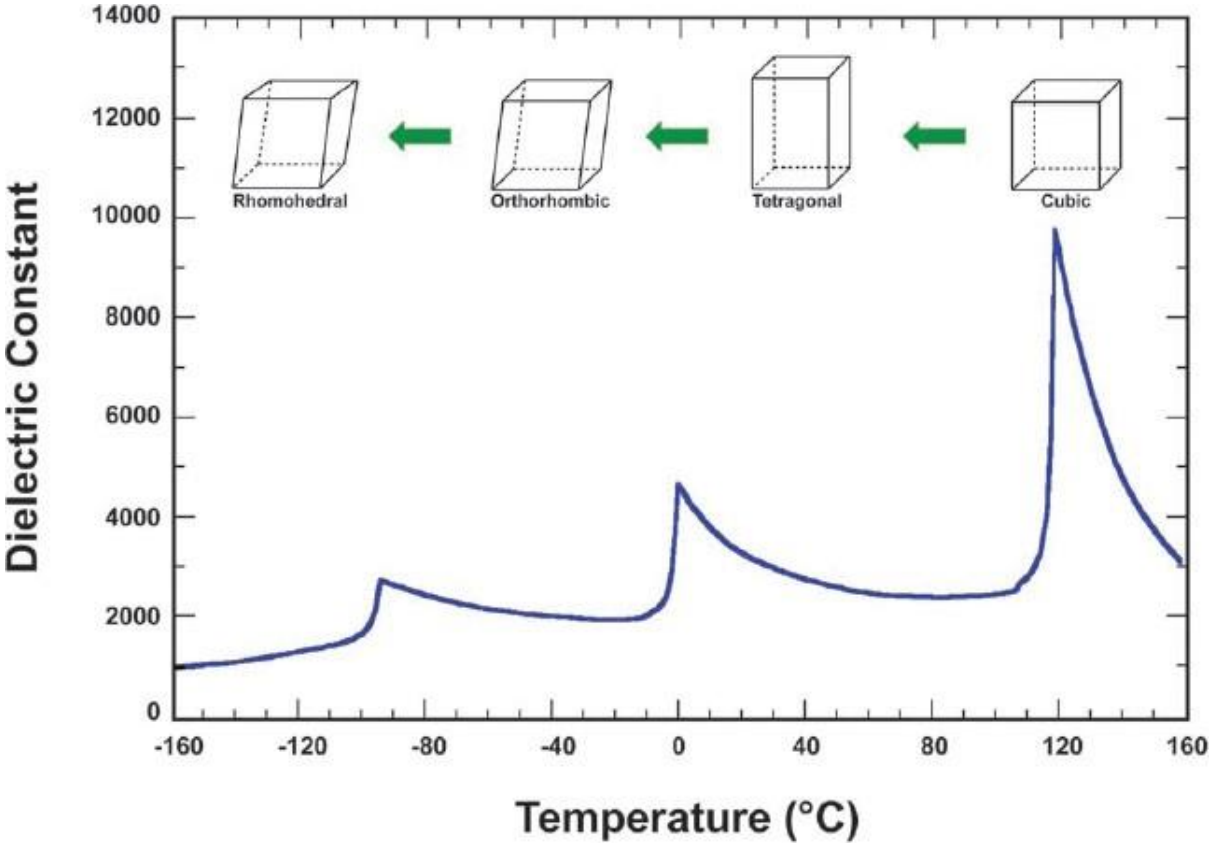

Figure 12. The temperature dependence of phase transition and permittivity in $BaTiO_3$, with T_C (and ε_r-Max) occurring around 120 to 130 °C. Illustrated unit cell distortions not to scale [Pan, M. J. 2010].

The profile of the permittivity peak in normal ferroelectrics around T_C is described by the Curie-Wiess law. The Curie-Weiss law dictates that on approach to T_C the permittivity tends to infinity and above T_C it decreases linearly with temperature [Trainer, M. 2000]. Equation 5 describes the law which applies above T_C.

$$\frac{1}{\varepsilon} = \frac{T - T_C}{C} \qquad \text{Equation 5}$$

Where ε is the permittivity, T is the temperature, T_C is the Curie temperature and C is the capacitance constant.

The permittivity temperature profile of $BaTiO_3$ can be seen, in Figure 12, to adhere quite well to the Curie-Weiss law, exhibiting an anomaly in permittivity around T_C. However, some ferroelectrics undergo more diffuse transitions. Relaxor ferroelectrics (RFs) often show highly diffuse permittivity-temperature profiles in which the temperature at ε_r-Max (T_M) is frequency dependant. When describing the origins of permittivity-peaks in RFs the use of T_C is inappropriate, as a corresponding macroscopic phase transition cannot be associated with ε_r-Max. Hence, the term T_M and a modified Curie-Weiss law are used. Usually the modified Curie-Wiess law is arranged into a form which allows graphical interpretation of the ϒ coefficient. The ϒ coefficient indicates the diffusivity of the transition, it typically varies from 1 to 2, with a value of 1 indicating an ideal ferroelectric transition and 2 (or sometimes > 2) indicating a highly diffuse transition. See Equation 6, which is in the form y = mx + c.

$$\log\left(\frac{1}{\epsilon} - \frac{1}{\epsilon r - Max}\right) = \gamma log(T - Tm) + logG \qquad \text{Equation 6}$$

Where ε is the permittivity, ε_r-Max its maximum, T the temperature, T_M the temperature at ε_r-Max, G and ϒ are fitting coefficients. i.e. the gradient of the plot in the case of ϒ.

2.6 Relaxor ferroelectrics

Relaxor ferroelectrics are often characterised as having large and diffuse permittivity-temperature peaks and frequency dependence of permittivity, with a temperature of ε_r-Max, T_M, that increases with increasing frequency [Cross, L. E. 1987]. The polar ordering in RFs has been shown to differ from that observed in normal ferroelectrics (FEs) [Yoshida, M. 1998]. The polar structuring in RFs is complex and evolves with temperature, though some debate exists as to the influence of these unique polar features on dielectric properties [Bokov, A. A. 2012].

2.6.1 The properties of, and polar ordering in, relaxors

The permittivity-temperature profile of lead magnesium niobate (PMN), $Pb(Mg_{1/3}Nb_{2/3})O_3$, is shown in Figure 13. The strong frequency dependence, or dispersion, of permittivity and high values of relative (and real, ε',) permittivity are typical for RFs. The properties of RFs make them desirable candidates for capacitor applications, they are also often excellent piezoelectrics [Cross, L. E. 2008]. Whilst lead containing RFs tend to have superior dielectric properties, research into lead-free RFs has been spurred by the environmental and legal concerns surrounding lead content in electronic devices [Wei, H. 2018]. Examples of lead-free RFs include $BaTiO_3$-based compositions, potassium sodium niobate (KNN), $K_{0.5}Na_{0.5}NbO_3$, Bismuth sodium titanate (BNT), $Bi_{0.5}Na_{0.5}TiO_3$, and bismuth-layer structured ferroelectrics [Wei, H. 2018].

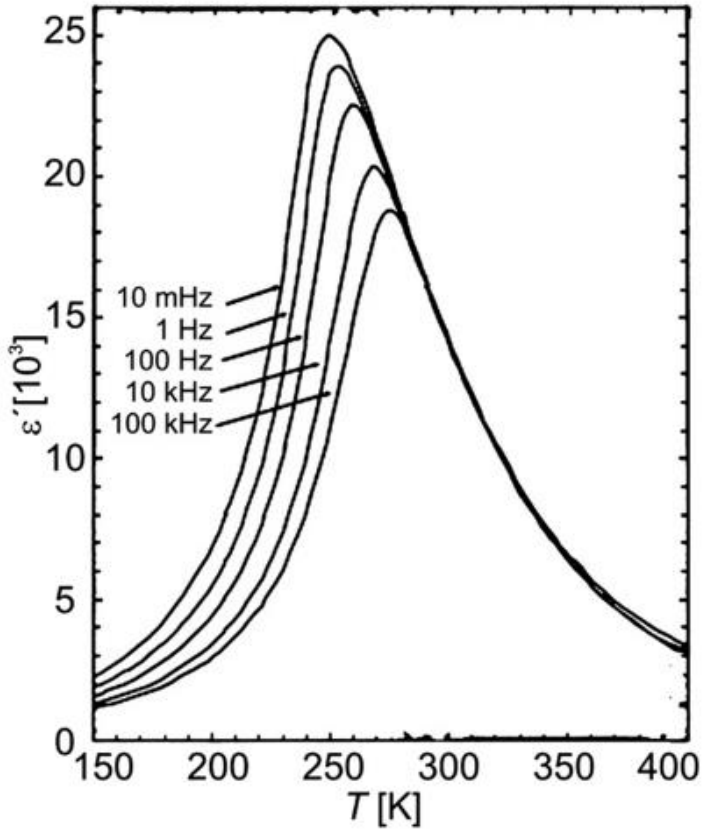

Figure 13. The permittivity temperature profile of a lead magnesium niobate, $Pb(Mg_{1/3}Nb_{2/3})O_3$, single crystal, which shows strong frequency dependence of permittivity (ε') and T_M. As frequency increases from 10 mHz to 100 kHz T_M increases and ε_r-Max decreases [Rojac, T. 2023].

In a FE a distinct change in symmetry (phase transition) occurs at T_C. Upon heating to just below T_C the micron-scaled domains give way to smaller polar clusters, or domain precursors. These polar clusters may exist permanently at this temperature. Increasing the temperature to above T_C causes the depolarisation to complete, resulting in the paraelectric phase. Contrastingly, the polar ordering in RFs has been directly imaged and shown to be of much smaller correlation lengths, when

compared to FE domains [Yoshida, M. 1998]. The long-range polar ordering observed in FEs is said to be disrupted in RFs, due to the presence of fluctuating electrostatic and strain fields which arise from chemical heterogeneities at the nm-scale or unit cell level [Qian, H. 1996]. The term polar nano-regions (PNRs) is sometimes used to describe these fine polar structures, though there exists some debate as to the nature of the polar structuring in RFs. Unlike the polar clusters/domain precursors found in FEs near T_C the PNRs in RFs are dynamic, readily reorientating their net dipole, and transient, disappearing and reappearing in a particular volume of the material at isothermal conditions. No significant change in structural symmetry is observed in RFs near T_M. The permittivity peak around T_M, and its frequency dependence, is often said to depend on a complex relationship between the size and dynamism of the PNRs [Qian, H. 1996].

The coercive fields in PNRs are much reduced, when compared to those of FE domains. As such, the coherence of the alignment of unit cell dipoles is less strong in PNRs, with some unit cell dipoles orientated against the net dipole of the PNR [Bokov, A. A. 2012]. In RFs the PNRs are typically randomly orientated, with no net dipole over the bulk, and are dynamic in response to external stimuli. Due to the lesser coercive fields and random orientation of PNRs, the P_r of RFs is often much smaller than that of FEs, this contributes to a greater polarizability (P_{Max} - P_r) and improved energy storage potential.

2.6.2 The temperature evolution of polar nanoregions

In RFs, PNRs exist at temperatures often hundreds of degrees above T_M, up to a temperature known as the Burns temperature, T_B. Above T_B any temporary dipoles present will be uncorrelated and so randomly orientated with respect to their neighbours, resulting in no net dipole moments at the nm-scale as well as at macroscales, see Figure 14(a). Below T_B, PNRs can form, See Figure 14(b). These PNRs are dynamic, changing the orientation of their dipoles with fluctuating electrostatic and strain fields. They are also transient, the polarised unit cells in a particular area may depolarise and repolarise as a PNR/electrostatic fluctuation passes through the material. The correlation lengths (at which the “primary” dipoles of the unit cells can interact) of these high-temperature PNRs are very short, extending into the nm-scale at maximum. Outside of the PNRs any dipoles are temporary and uncorrelated, the PNRs are said to exist within a non-polar framework. This is known as the ergodic relaxor (ER) state, where ergodic refers to the PNRs ability to occupy, given sufficient time, any and all locations in the material [Bokov, A. A. 2012].

Flipping, or dipole reorientation, in PNRs contributes significantly to dielectric susceptibility. In contrast, for more-static (and often larger) polar units the direction of the net dipole is fixed and only the domain walls fluctuate, this is sometimes referred to as a breather-mode response, in contrast to the flipper-mode response. As temperature decreases below T_B to T* some of the

dynamic PNRs may become static and incapable of reorientating their dipoles. As temperature continues to decrease the correlation lengths of the PNRs continue to increase and a growing proportion of the PNRs become static, see Figure 14(c). At a much lower temperature, T_f (where $T_f < T_M$), all PNRs become static, see Figure 14(h). Below T_f there is a non-ergodic relaxor (NR) state [Hong, C-H. 2019]. Dielectric susceptibility below T_f is reduced as the (breather-mode) motion of PNR walls becomes the primary contribution to permittivity, similarly to domain wall contributions to permittivity in FEs.

The application of a sufficiently large electric field to a non-ergodic relaxor produces long-ranged ferroelectric order, See Figure 14(g). This results in a permanent normal ferroelectric state with textured, i.e. 180^o, domain structures and more significant coercive fields and polarity-correlation lengths.

At T_M, see Figure 14(d), PNRs exist with a distribution of sizes/correlation lengths. This distribution results in the frequency dispersed dielectric properties observed in RFs. Smaller PNRs are more mobile and relax at higher frequencies. Larger PNRs have greater net dipole moments but relax at lower frequencies. The ε_r-Max in a RF at any given frequency is a play-off between the magnitude of the dipoles that can be reorientated and the relaxation of larger PNRs that cannot reorientate their dipoles at high frequencies.

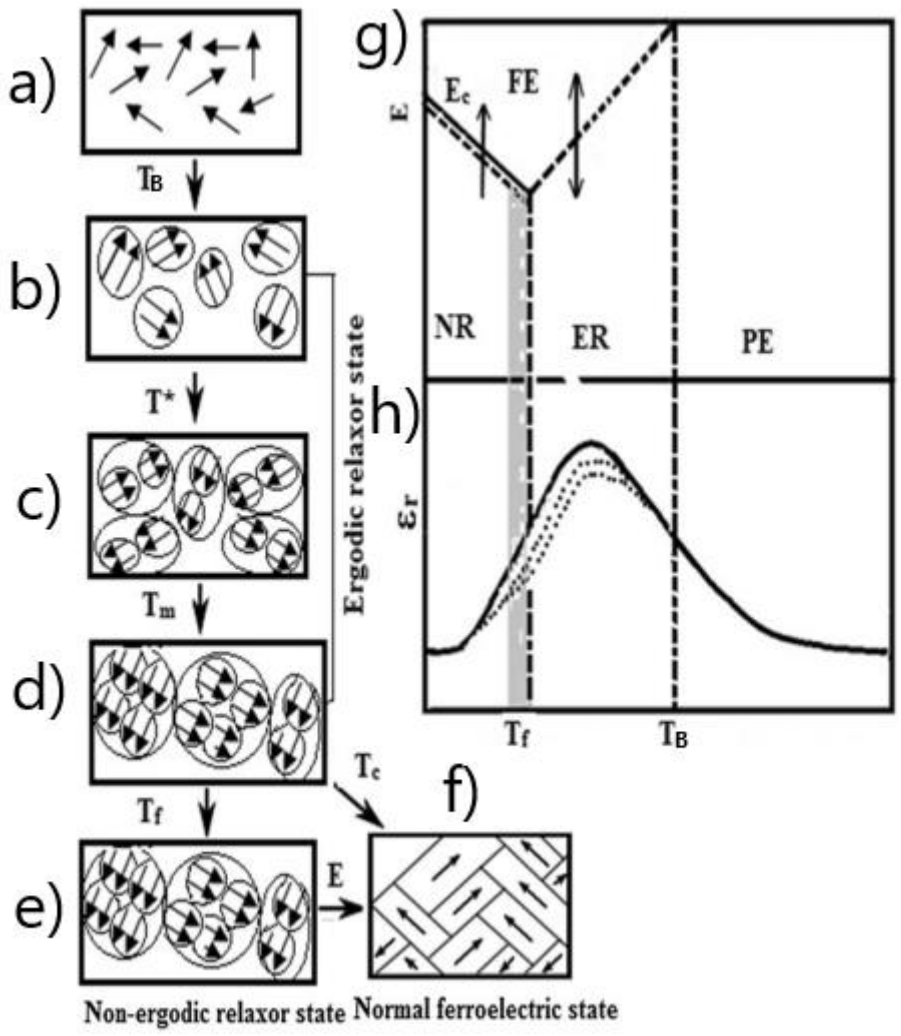

Figure 14. A representation of the thermal evolution of polar structures in a (relaxor) ferroelectric, (a) to (f). The role of electric fields in the transition of nonergodic relaxors to normal ferroelectrics, shown in (e), (f) and (g). In (h) a permittivity temperature plot for a typical relaxor is shown with a frequency dependant ε_r-Max situated between the Burns temperature, T_B, and the freezing temperature, T_f [Zaman, A. 2014].

The inverse permittivity-temperature plot of a RF is shown in Figure 15. The permittivity variation just below T_B conforms to Curie-Wiess law. Deviation from Curie-Wiess law increases as T decreases towards T_M. The extrapolation of the gradient just below T_B to the y-intercept gives the temperature T_0, which is analogous to T_C in a FE. The permittivity peak associated with ε_r-Max is better modelled by a modified Curie-Wiess law.

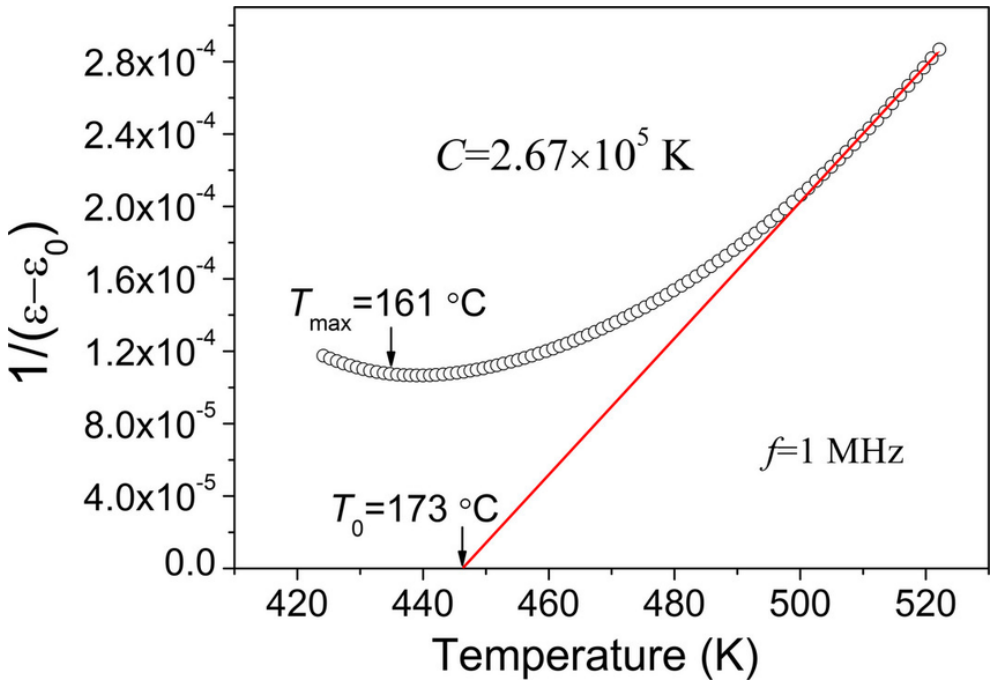

Figure 15. The inverse permittivity-temperature plot of a relaxor ferroelectric, showing deviation from Curie-Wiess law, measured at 1 MHz. Extrapolation of Curie-Wiess law to the x-axis gives the value T_0, which is analogous to T_C in a normal ferroelectric [Nie, R. 2016].

2.7 Chemical modification of barium titanate

High permittivity in ferroelectrics like $BaTiO_3$ is desirable for volumetrically efficient capacitors. However, industry often requires the performance of these passive components to vary within set limits across the wide temperature ranges of their operation. For example, the EIA specifications for a X7R capacitor assert a maximum variation in permittivity of ±15 % from -55 to 125 ^{o}C. As such the structurally and compositionally dependant phase transitions and permittivity-temperature responses of ferroelectrics must be engineered.

Chemical modification, or doping, is a common approach to engineering a ferroelectrics permittivity-temperature response. Here, an incumbent ion may be substituted for one of differing valency, size and electron structure. The resulting variation in local structure and disordering of site occupation can have profound effects on the diffusivity and temperature of the phase transitions and the size and size distributions of polar units, even at low dopant inclusion levels (< 1 - 5 at.%).

When selecting a dopant ion there are two key properties to consider; ionic radius and valency. The site an ion occupies is typically determined by its ionic radius. An ion in a site which is too large will be highly unstable, whereas as a structure may be strained by the inclusion of a large ion on a small site. Using a hard-sphere model of the ions in a structure, a site which is too large would allow the “small” ion to move freely and vacate its site, whereas one that was too small would result in the ion

displacing neighbouring ions. The retention of charge parity in a composition is of high importance to the chemical stability of ionic compounds and must be considered when performing chemical substitutions. This is most simply achieved by isovalent doping where the included and substituted cations possesses the same valency. Ions of different valence can induce site vacancies to attain crystal neutrality.

An indication of the varied effects of doping on phase transition and permittivity may be illustrated by the modification of the well-studied $BaTiO_3$. The isovalent A site inclusion of Sr^{2+} for Ba^{2+}, in $(Ba_{1-x}Sr_x)TiO_3$, significantly reduces T_C (see Figure 16(a)), whereas Ca^{2+} inclusion has a complex effect on T_C and significantly reduces the temperature of the tetragonal-orthorhombic transition [Yu, Y. 2013] and [Tian, Y. 2013]. Here, the separation of the two permittivity peaks, that are associated with the phase transitions, improves the temperature stability of permittivity. A small increase in T_C, from 130 ^oC to 136 ^oC, is reported when Ca content is increased to x = 0.08 in the solid solution formula $Ba_{1-x}Ca_xTiO_3$ [Jaffe, B. 1971]. Above x = 0.08, T_C begins to decrease to ~105 ^oC for x = 0.30 [Zhang, L. 2007]. Figure 16(b) depicts the separation of the paraelectric-ferroelectric phase transition from the inter-ferroelectric transitions with Ca modification of $BaTiO_3$, the depicted variation in T_C is a simplified (linear) trend. Both the A (Ba^{2+}) and B (Ti^{4+}) sites can be occupied by Ca^{2+}, with Ca occupation of the B site being associated with a reduction in T_C [Zhang, L. 2007]. Isovalent B site doping, in the form of Zr^{4+} inclusion in the formulation $BaTi_{1-x}Zr_xO_3$ (BZT), causes the temperatures of the cubic to tetragonal and the tetragonal to orthorhombic phase transitions to approach and eventually merge [Kuang, S. J. 2009], see Figure 16(c).

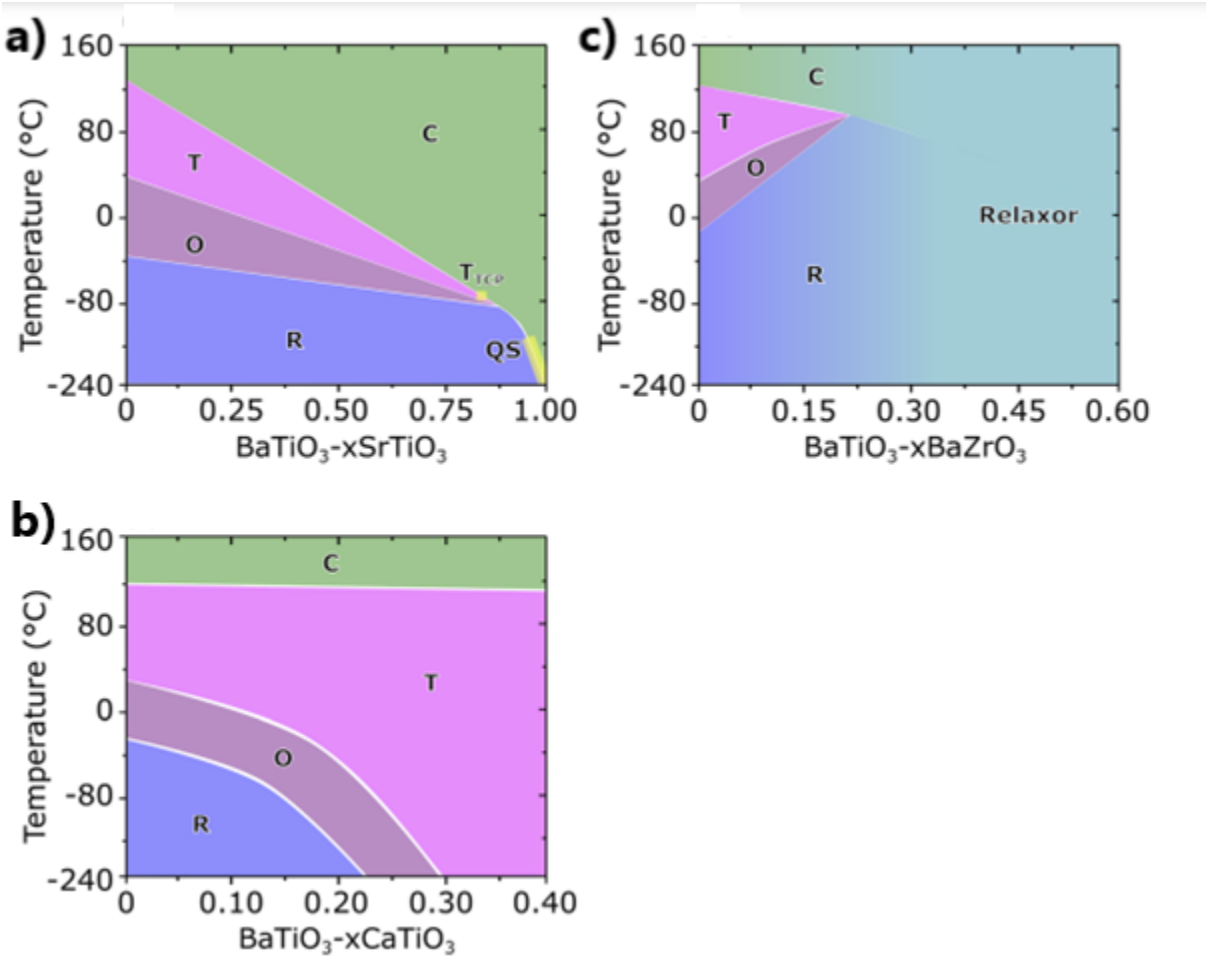

Figure 16. the phase diagrams of select pseudo binary-$BaTiO_3$ solid solutions, with simplified phase boundaries. The symbols C, T, O and R represent Cubic, tetragonal, orthorhombic and rhombohedral phases. Edited from [Acosta, M. 2017].

In addition to modulating the temperature at which phase transitions occur, chemical modifications generally increase the diffusivity of phase transitions and permittivity peaks due to structural-disordering effects. The precise implications of chemical substitution on a structure and its electrical properties often requires empirical investigation. Such research into the tailoring of dielectric properties has resulted in many complex perovskite solid-solutions. The barium calcium titanate - barium zirconate titanate solid solution, $0.85(Ba_{0.96}Ca_{0.04}TiO_3)$-$0.15(BaZr_{0.5}Ti_{0.5}O_3)$, shows a < ±15 % variation in permittivity from -55 to 200 ^{o}C, meeting the EIA X9R capacitor specifications [Jiang, X. 2021], see Figure 17. See Table 1 from the Introduction section for details of the EIA specifications. Maintaining temperature stable permittivity above 200 ^{o}C is challenging when using $BaTiO_3$-based systems [Acosta, M. 2017]. This fact largely prohibits $BaTiO_3$-based devices from high temperature (250+ ^{o}C) applications.

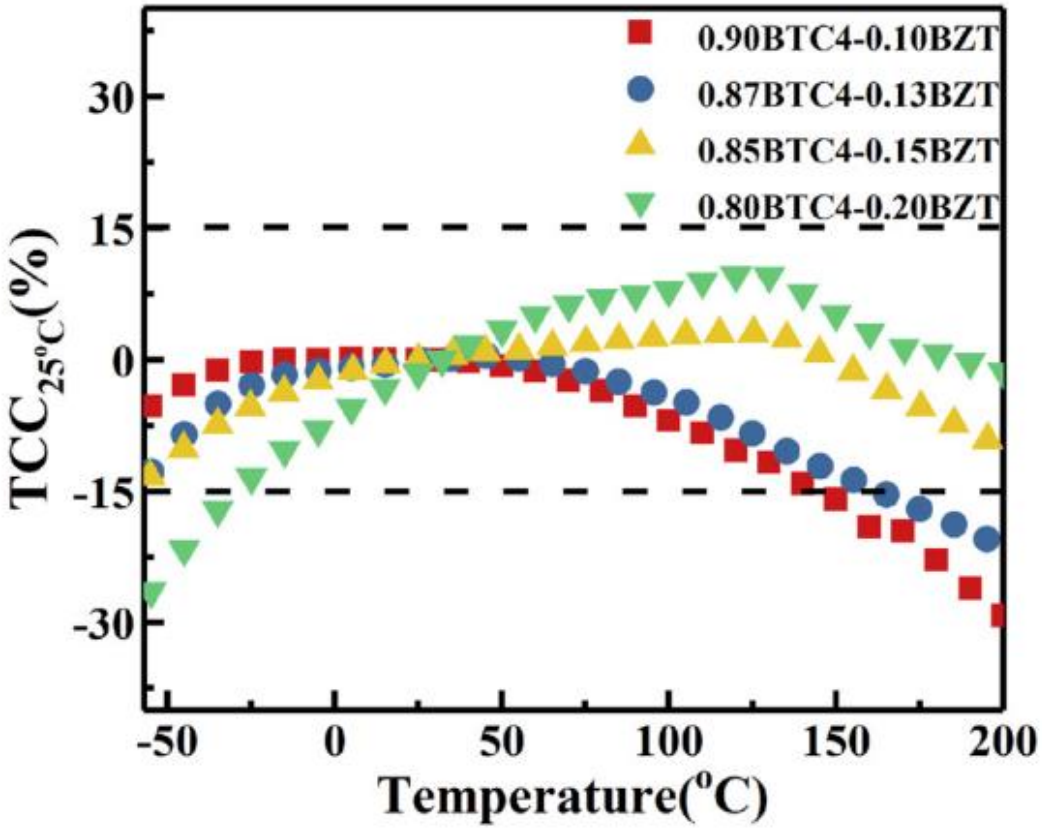

Figure 17. Temperature stable permittivity in barium calcium titanate – barium zirconate titanate solid solutions, 1-y($Ba_{0.96}Ca_{0.04}TiO_3$)-y($BaZr_{0.5}Ti_{0.5}O_3$). where $TCC_{25°C}$(%) refers to the percentage variation in capacitance with respect to capacitance measured at 25 ^{o}C [Jiang, X. 2021].

Additional to the effects of isovalent doping, the inclusion of off-valent ions results in variations in cation and oxygen site occupancy so as to ensure charge parity in the structure. This type of doping is termed aliovalent doping. The inclusion of a higher valency cations, termed donor doping, requires the addition of cation site vacancies and can repress the presence of oxygen vacancies. The inclusion of lower valency cations, termed acceptor doping, promotes the presence of oxygen vacancies in the perovskite structure. In other structures, which possess some vacant cation sites, acceptor doping may promote greater cation site occupation.

2.8 Tungsten-bronze structure

Tungsten bronzes (TBs) are one of the four main groups of ferroelectric materials, they have also been employed as superconductors and pigments. Their structures are similar to that of the perovskite structure, though more complex [Magnéli, A. 1949]. Tungsten bronzes (TBs) possess non-linear optical properties, for which they are often studied.

2.8.1 The tungsten bronze unit cell and superstructures

Structurally, TBs consist of a matrix of corner sharing (BO_6) oxygen octahedra, each surrounding a high valency cation, similarly to perovskites. Unlike the perovskite structure, the <0 0 1> interstitial channels in TBs are of variable shape, size and coordination number. Visually, the TB structure can be generated by appropriately rotating several neighbouring octahedra in the perovskite structure.

In TBs, the BO_6 octahedra have 2 distinct orientations ($B1O_6$ and $B2O_6$) which are tilted differently to generate interstitial A1, A2 sites and C sites which cations may occupy, according to the formula $(A2)_4(A1)_2(C)(B1)_2(B2)_8O_{30}$. The coordination numbers (CN-) of the three sites (A2, A1 and C) are 15, 12 and 9 respectively. They can be identified as pentagonal, square and triangular columns when viewed along the <0 0 1> direction, see Figure 18.

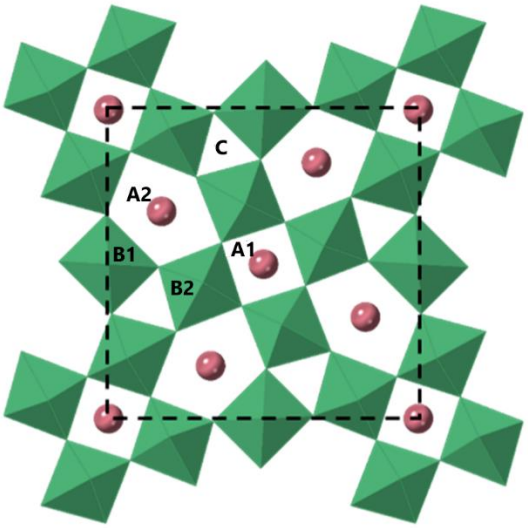

Figure 18. A representation of the tungsten bronze structure, $(A2)_4(A1)_2(C)\ (B1)_2(B2)_8O_{30}$, viewed along the [001]. Tetragonal unit cell projections are indicated by the dotted line. Figure produced by Dr. Yizhe Li, of the University of Manchester, for the publication [Peirson, H. 2023].

At higher temperatures, i.e. above T_C, the TB structure may be non-polar, adopting a tetragonal symmetry at lower temperatures. However, lower symmetry orthorhombic structures are identifiable in many TBs. Subtle orthogonal distortions, resulting from octahedral (and polarisation) tilts into the *ab* plane, are common though often difficult to determine by average structure, or bulk, techniques such as XRD (i.e. by XRD peak splitting). Commensurate modulations of the modified TB structure are ones in which the modifications repeat periodically and can be described by a (larger) superstructure. Incommensurate modulations do not repeat periodically and are associated with a perturbation of long-range periodic order.

The dimensions of a superstructure are related to the unit cell parameters by some integer or geometric factor (e.g. √2). A commonly observed TB superstructure involves the "antiphase" tilting of the octahedra, which results in a doubling of the *c* parameter [Gardner, J. 2014]. Figure 19 depicts two orthorhombic structures, space groups Ama2 and Ima2, in relation to the primary TB unit cell.

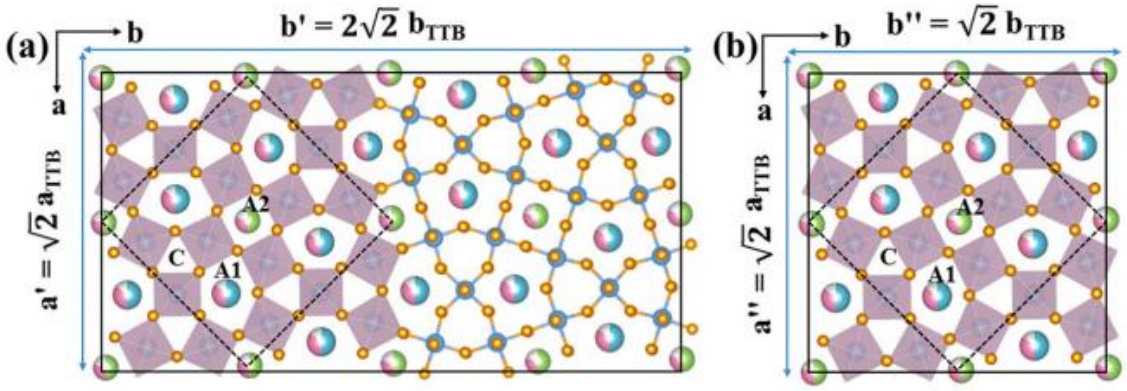

Figure 19. A [001] projection of the tetragonal TB primary cell (space group Pb4/mbm) in relation to two orthorhombic structures with lattice parameters of $\sqrt{2}a$ x $2\sqrt{2}b$ (shown in Figure (a)) and $\sqrt{2}a$ x $\sqrt{2}b$ (shown in Figure (b)), with respect to the lattice parameters (*a* and *b*) of the primary TB unit cell. Space group Ama2 is incommensurate and shown in (a), and Ima2 is commensurate and shown in (b) [Hou, S. 2023].

2.8.2 Polarisation, conduction, and site occupancy in tungsten bronzes

In tungsten bronzes the displacement of the high valency B site cation occurs primarily along the <0 0 1> direction. Similarly to perovskites, this out of plane displacement of the cation in the BO6 octahedra results in a large polarisation and high permittivity. In plane polarisation (tilt and rotation) of the $B2O_6$ octahedra may also occur, disrupting ordered chains of <0 0 1> unit cell polarisation [Gardner, J. 2014]. The differing Nb-O bond lengths of the two BO_6 octahedra of strontium sodium niobate (SNN) are illustrated in Figure 20.

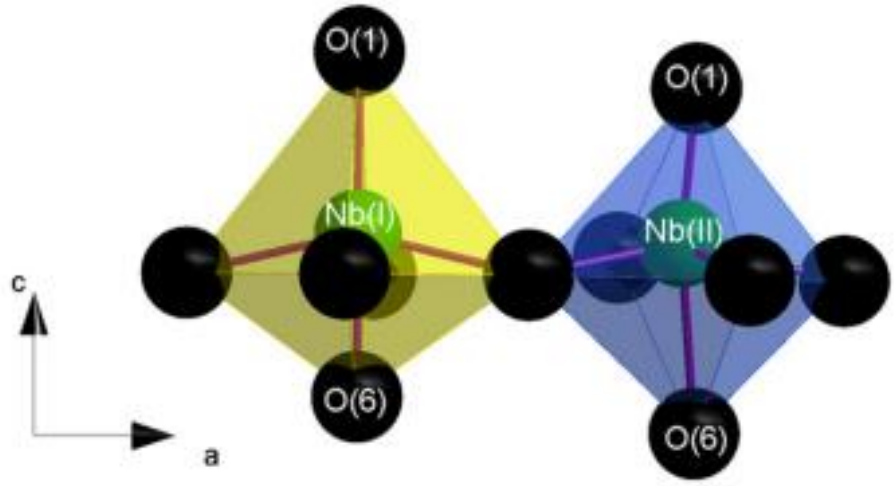

Figure 20. Nb(I) and Nb(II) ions, also referred to as Nb1 and Nb2 ions, are positioned out of the equatorial plane of oxygen ions, with differing octahedra distortions (i.e. differing 01 and 06 bond lengths) [Lanfredi, S. 2011].

Site occupancy and Ionic radii

The site that an ion occupies in the TB structure is largely determined by its ionic radii. The ionic radii of an element varies with the valence state of the element and the coordination number (CN-) of the site it occupies. When comparing ionic radii it is important to use a value associated with the same coordination number, ideally a CN matching that of the proposed site. Although, experimental data for high coordination numbers (i.e. CN15, for the A2 site) is sparse. Often the ionic radii data is incomplete and extrapolation of trends is required.

Smaller high valency ions such as Nb^{5+} occupy the B site (CN6) and are coordinated by the 6 oxygen ions of the octahedra. Lower valency and so larger ions may occupy the A sites, their size dependant distribution can be illustrated by the alkaline-earth metals, see Table 4. Relatively small Ca^{2+} is almost exclusively confined to the A1 site (CN12) in the TB $Ca_{0.28}Ba_{0.72}Nb_2O_6$, whereas Ba^{2+} is almost exclusively confined to the A2 (CN15) site, the intermediate sized Sr^{2+} can occupy both A sites [Graetsch. G. A. 2012] and [Paściak, M. 2019]. Small low valency ions such as Li^{+} may occupy the C sites in the TB structure.

Table 4. The radii, at different coordination numbers, and typical site occupancies of select cations in the TB structure. The coordination numbers of the TB sites; B, C, A1 and A2 are 6, 9, 12 and 15, respectively [Shannon, R. D. 1976].

Ion	Valency	Typical site occupation	Ionic radii (Å)			
			CN6	CN9	CN12	CN15
Nb	5+	B	0.64			
Sb	5+	B	0.60			
Li	1+	C	0.76			
Ca	2+	A1	1.00	1.18	1.34	
Sr	2+	A1/A2	1.18	1.31	1.44	
Ba	2+	A2	1.35	1.47	1.61	1.65*

*Value taken from [Zhu, X. 2015].

A site occupancy and structure

Depending on full or partial occupancy of the A2 and A1 sites, tungsten bronzes may be classed as 'filled' or 'partially filled/unfilled'. An example of a "filled" TB is barium sodium niobate ($Ba_4Na_2Nb_{10}O_{30}$, often abbreviated to $Ba_2NaNb_5O_{15}$). In TBs, the C sites are usually empty, but are capable of occupation by small ions, such as Li^+. The term 'stuffed' is used should the C sites be occupied, as is the case in potassium lithium niobate ($K_6Li_4Nb_{10}O_{30}$). The formula of unfilled TBs, such as lead niobate ($Pb_5Nb_{10}O_{30}$), is usually abbreviated to the empirical formula (i.e. $PbNb_2O_6$).

In the unfilled TB strontium barium niobate (SBN), $Sr_xBa_{1-x}Nb_2O_6$, vacancies on the A1 site can be promoted by reducing the Sr:Ba ratio, with the larger Ba^{2+} favourably occupying the larger A2 site. The $B2O_6$ octahedra around a vacant SBN A1 site show increased tilt, as depicted in Figure 21.

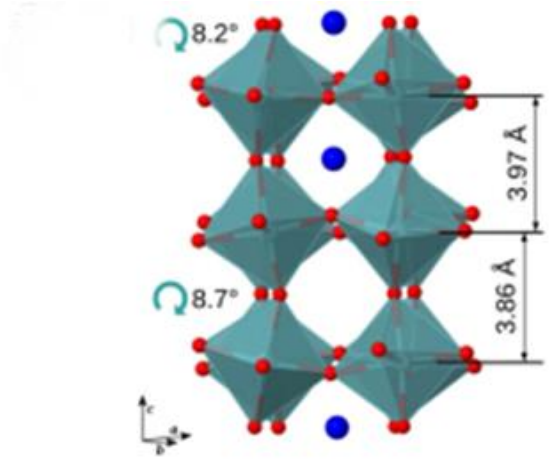

Figure 21. A1 site vacancies result in greater distortion and tilt angle of the B2 octahedra and reduced Nb-Nb distances in SBN [Paściak, M. 2019].

Where the A1 site is occupied, $B2O_6$ octahedral tilt has been linked to the size of the occupying cation. The presence of the large Ba^{2+} on the A1 site is less favourable than on the larger A2 site, however its presence has been noted in materials like barium sodium niobate (BNN) and cited as a cause of greater octahedral tilting [Lin, P. J. 1987].

In structures with mixed site occupancy, this site occupancy may be generally disordered with some local ordering features, such as an alternating arrangement of a larger and a smaller cation (i.e. Ba and Sr) along the sites of the A1 channel (accompanied by cooperative tilting) [Paściak, M. 2019].

Oxygen vacancies and conduction

Oxygen vacancies in perovskites and TBs are associated with conductivity, wherein conduction occurs predominantly by the long-range motion of ions, rather than electrons. For solid electrolyte applications (i.e. solid oxygen fuel cells) oxygen vacancies are desirable and may be induced by sintering in oxygen deficient (reducing) atmospheres [Molak, A. 1987].

In ferroelectrics, oxygen vacancies are often associated with high-temperature, low-frequency dielectric losses and are undesired. These losses particularly afflict volatile containing compositions. The loss of volatiles, such as K- or Na- oxide, during sintering leads to cation and (oxygen) anion deficiencies in the structure [Lee, J-H. 2022]. Proximate pairs of vacant cation and anion sites allows for local charge compensation and are termed Schottky defects. At higher temperatures, typically above 250 ^{o}C, oxygen vacancies or Schottky pairs becomes mobile and contributes to bulk conductivity/dielectric loss.

Oxygen vacancies can also occur due to reduction on the cation site, rather than site vacancy. Many TBs contain niobium which occupies the B site at the centre of the oxygen octahedra. The valency of the Nb ion is typically 5+, but reduction to Nb^{4+} is possible and can be promoted by sintering and annealing in reducing atmospheric conditions [Ketchum, J. L. 1983]. The presence of Nb^{4+} has been linked to oxygen vacancies in perovskites and TBs [Ofoegbuna, T. 2019].

2.8.3 Structure-property relationships in tungsten bronzes

The multiplicity of interstitial sites, the potential for their mixed or partial occupation, and the more complex origins of their spontaneous polarisation make TBs promising candidates for permittivity-temperature response engineering. The complexity and structural flexibility of the TBs does however complicate attempts to develop structure-property relationships.

A number of relationships between structure and ferroelectric nature have been established in perovskites and these are often translatable to TBs. In perovskites the displacement of the B site ion from the oxygen centre plane correlates with polarisation, *c* lattice parameter and T_C [Abrahams, S.

C. 1968]. A comparable relationship between T_C and the tetragonality of a TB (the ratio of *c*:*a* lattice parameter) has been shown [Scott, B. A. 1968]. The Goldschmidt tolerance factor, that is applied to perovskites, can likewise be modified and applied to TBs. The differing geometries and average ion size occupancies of the A1 and A2 sites requires different tolerance factors (t_{A1} and t_{A2}) to be calculated. In TBs there is a 1:2 ratio of A1 to A2 sites and a weighted average of the tolerance factor is taken. This value (t_{TB}) does not correspond to a preferred crystal system, as is seen in perovskites. However, the size of the A site ions and t_{A1} has been correlated with measured structural modulation and ferroelectric nature in TBs, as is shown in Figure 22.

The TB A1 site is coordinated by $B2O_6$ octahedra and its occupation, or lack thereof (see Figure 21), may influence the tilting arrangement in these octahedra. Larger A site ions tend to result in incommensurate modulation of the substructure and normal ferroelectric behaviour [Zhu, X. 2015]. This normal ferroelectric behaviour has been explained by increased out of plane distortion of the octahedra and elongated bonds which result in larger polarisations and more stable dipoles which are prone to long-range order, often despite the presence of incommensurate modulation [Zhu, X. 2015]. Smaller A site ions also tend to result in normal ferroelectric behaviour, though with typically commensurate structural modulation. A region of intermediate average A site size, and t_{A1} around ~0.96, typically results in incommensurate structural modulation with disrupted long-range polar order and relaxor ferroelectric properties.

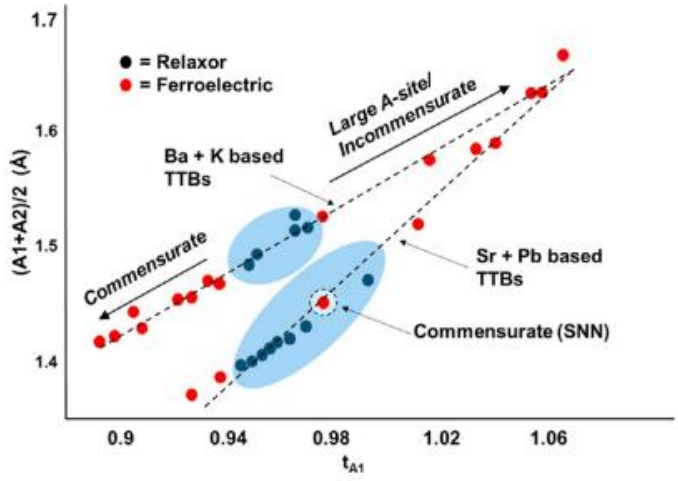

Figure 22. A crystal-chemical framework for relaxor versus normal ferroelectric behaviour in tetragonal tungsten bronzes [Zhu, X. 2015].

2.9 Outlook

Low Sr-content SBN (i.e. SBN30, $Sr_{0.30}Ba_{0.70}Nb_2O_6$) is an unfilled TB that shows potential for temperature-stable permittivity applications [Zhang, J. 2013]. Chemical modification of SBN can also improve permittivity-temperature stability [Wang, L. 2012] and [Volk, T. 2004]. However, the T_M of SBN61 ($Sr_{0.61}Ba_{0.61}Nb_2O_6$) is below the T_C of $BaTiO_3$. Decreasing Sr content in the SBN solid solution only somewhat increases T_M, to ~170 °C in the case of SBN30. To achieve permittivity-temperature stability to higher temperatures a material with higher $T_{C/M}$ may be required. Calcium barium niobate, isostructural to SBN, has a high T_C of ~250 °C for the composition CBN28 ($Ca_{0.28}Ba_{0.72}Nb_2O_6$), which (like SBN61) solidifies congruently from the melt. CBN28 does not exhibit significant frequency dispersion of permittivity [Han, X. 2013]. However, a TB t_{A1} tolerance factor of 0.95 situates it within the region of likely-relaxors in Figure 22 ((A1+A2)/2 = 1.5). This suggests that CBN28, with sufficient permittivity-temperature-stability inducing chemical modification, could also exhibit relaxor properties which would benefit potential energy storage applications.

2.10 References

Abrahams, S. C. Kurtz, S. K. Jamieson, P. B. 1968. Atomic Displacement Relationship to Curie Temperature and Spontaneous Polarization in Displacive Ferroelectrics. *Phys. Rev*. **172**. 551

DOI: https://doi.org/10.1103/PhysRev.172.551

Acosta, M. Novak, N. Rojas, V. Patel, S. Vaish, R. Koruza, J. Rossetti, G. A. Rödel, J. 2017. BaTiO3-based piezoelectrics: Fundamentals, current status, and perspectives. *Appl. Phys. Rev*. **4**. 041305

DOI: https://doi.org/10.1063/1.4990046

Ameh, E. S. 2019. A review of basic crystallography and x-ray diffraction applications. *Int. J. Adv. Manuf. Technol.* **105**. 3289-3302

DOI: http://doi.org.10.1007/s00170-019-04508-1

Bokov, A. A. Ye, Z-G. 2012. DIELECTRIC RELAXATION IN RELAXOR FERROELECTRICS. *J. Adv. Dielectr*. **2**. 1241010

DOI: https://doi.org/10.1142/S2010135X1241010X

Brown, P. J. Forsyth, J. B. 1973. The crystal structure of solids. New York: *Edward Arnold*.

ISBN: 978-0-7131-2388-3

Cockcroft, J. K. 2006. Lattices and unit cells. University of London. [Accessed online 17th April 2020]. [Available from]: http://pd.chem.ucl.ac.uk/pdnn/symm1/trans1.htm

Cross, L. E. 1987. Relaxor ferroelectrics. *Ferroelectrics*. **76**. 241-267

DOI: https://doi.org/10.1080/00150198708016945

Cross, L. E. 2008. Relaxor Ferroelectrics. Piezoelectricity: Evolution and Future of a Technology. Springer

ISBN: 978-3540686804

Curecheriu, L. Balmus, S-B. Buscaglia, T. M. Buscaglia, V. Ianculescu, A. Mitoseriu, L. 2012. Grain Size-Dependent Properties of Dense Nanocrystalline Barium Titanate Ceramics. *J. Am. Ceram. Soc.* **95**. 3912-3921

DOI: https://doi.org/10.1111/j.1551-2916.2012.05409.x

da Silva, L. L. Hinterstien, M. 2021. Technological application of nanomaterials. Size Effect on Ferroelectricity in Nanoscaled $BaTiO_3$. 123-133

ISBN: 978-3-030-86900-7

DOI: https://doi.org/10.1007/978-3-030-86901-4_7

Damjanovic, D. 1998. Ferroelectric, dielectric and piezoelectric properties of ferroelectric thin films and ceramics. *Rep. Prog. Phys.* **61.** 1267

DOI: https://doi.org/10.1088/0034-4885/61/9/002

Gardner, J. Morrison, F. D. 2014. A-site size effect in a family of unfilled ferroelectric tetragonal tungsten bronzes: $Ba_4R_{0.67}Nb_{10}O_{30}$ (R = La, Nd, Sm, Gd, Dy and Y). *Dalton Trans*. **43**. 11687

DOI: **https://doi.org/10.1039/C4DT00126E**

George, G. Ede, S. R. Luo, Z. 2020. Fundamentals of Perovskite Oxides. Crystal Structure of Simple Perovskites. CRC press: Boca Raton

ISBN: 9780429351419

DOI: https://doi.org/10.1201/9780429351419

Goldschmidt, V. M. 1926. Die Gesetze der Krystallochemie. *Die Naturwissenschaften*. **14**. 477-485

DOI: https://doi.org/10.1007/BF01507527

Graetsch, H. A. Schreuer, J. Burianek, M. Mühlberg, M. 2012. Thermally induced structural changes in incommensurate calcium barium niobate $Ca_{0.28}Ba_{0.72}Nb_2O_6$ (CBN28). *J. Solid State Chem*. **196**. 255-266

DOI: https://doi.org/10.1016/j.jssc.2012.06.028

Guo, H. Baker, J. S. Wu, W. Choy, K. L. 2023. High Dielectric Constants in $BaTiO_3$ Due to Phonon Mode Softening Induced by Lattice Strains: First Principles Calculations. *Adv. Phys*. 2300001

DOI: **https://doi.org/10.1002/apxr.202300001**

Han, X. Wei, L. Yang, Z. Zhang, T. 2013. Phase formation, dielectric and ferroelectric properties of $Ca_xBa_{1-x}Nb_2O_6$ ceramics. *Ceram. Int*. **39**. 4853-4860

DOI: https://doi.org/10.1016/j.ceramint.2012.11.078

Hammond, C. 2015. The Basics of Crystallography and Diffraction. 4th ed. Oxford university press

ISBN: 9780198738688

Hong, C-H. Guo, H. Tan, X. Daniels, J. E. Jo, W. 2019. Polarization reversal *via* a transient relaxor state in nonergodic relaxors near freezing temperature. *J. Mater*. **5**. 634-640

DOI: https://doi.org/10.1016/j.jmat.2019.06.004

Hou, S. Wang, X. Liu, X(in). Liu, X(iaoyu). Lu, J. Liang, P. Wu, D. Chao, X. Yang, Z. Wei, L. 2023. Significant increase in comprehensive energy storage performances of $Ca_{0.5}(Sr_{0.5}Ba_{0.5})_2Nb_5O_{15}$-based tungsten bronze relaxor ceramics. *J. Eur. Ceram*. [Currently in press, 15th August 2023]

DOI: https://doi.org/10.1016/j.jeurceramsoc.2023.07.039

Hoshina, T. Wada, S. Kuroiwa, Y, Tsurumi, T. 2008. Composite structure and size effect of barium titanate nanoparticles. *Appl. Phys. Lett.* **93**. 192914

DOI: https://doi.org/10.1063/1.3027067

Jaffe, B. Cook, W. R .(Jr.) Jaffe, H. 1971. Piezoelectric ceramics. London and New York: *Academic press*.

ISBN: 978-0-32-315568-7

Jiang, B. Locozzia, J. Zhao, L. Zhang, H. Harn, Y-W. Chena, Y. Lin, Z. 2019. Barium titanate at the nanoscale: controlled synthesis and dielectric and ferroelectric properties.
Chem. Soc. Rev. **48**. 1194-1228

DOI: **https://doi.org/10.1039/C8CS00583D**

Jiang, X. Hao, H. Yang, Y. Zhou, E. Zhang, S. Wei, P. Cao, M. Yao, Z. Liu, H. 2021. Structure and enhanced dielectric temperature stability of $BaTiO_3$-based ceramics by Ca ion B site-doping. *J. Mater*. **7**. 295-301

DOI: https://doi.org/10.1016/j.jmat.2020.09.001

Kao, K. 2004. Dielectric Phenomena in Solids with Emphasis on Physical Concepts of Electronic Processes. Elsevier

ISBN: 978-0-12-396561-5

Ketchum, J. L. Sweeney, K. L. Halliburton, L. E. Armington, A. F. 1983. Vacuum annealing effects in lithium niobate. *Phys. Lett. A.* 1983. **94**. 450-453

DOI: https://doi.org/10.1016/0375-9601(83)90852-6

Kittel, C. 1946. Theory of the structure of ferromagnetic domains in films and small particles. *Phys. Rev*. **70**. 965-971

DOI: https://doi.org/10.1103/PhysRev.70.965

Kour, R. Arya, S. Verma, S. Gupta, J. Bandhoria, P. Bharti, V. Datt, R. Gupta, V. 2019. Potential Substitutes for Replacement of Lead in Perovskite Solar Cells: A Review. *Global chall.* **3**. 1900050F

DOI: **https://doi.org/10.1002/gch2.201900050**

Kuang, S. J. Tang, X. G. Li, L Y. Jiang, Y. P. Liu, Q. X. 2009. Influence of Zr dopant on the dielectric properties and Curie temperatures of $Ba(Zr_xTi_{1-x})O_3$ ($0 \leq x \leq 0.12$) ceramics. *Scr. Mater.* **61**. 68-71

DOI: https://doi.org/10.1016/j.scriptamat.2009.03.016

Lanfredi, S. Gênova, D. H. M. Brito, L. A. O. Lima, A. R. F. Nobre, M. A. L. 2011. Structural characterization and Curie temperature. determination of a sodium strontium niobate ferroelectric nanostructured powder. *J. Solid State Chem*. **184**. 990-1000

DOI: https://doi.org/10.1016/j.jssc.2011.03.001

Lee, J-H. Lee, G. J. Hoang, A-N. Frömling, T. Pham, T-L. Lee, J-S. Jo, W. 2022. Suppression of high-temperature dielectric loss by designed thermal annealing treatment in $(Bi_{1/2}Na_{1/2})TiO_3$ ceramics. *J. Eur. Ceram*. **42**. 1388-1395

DOI: https://doi.org/10.1016/j.jeurceramsoc.2021.12.029

Lin, P. J. Bursill, L. A. 1987. Superlattice structure of ferroelectric barium sodium niobate (BNN). *Acta Cryst*. B**43**. 504-512

DOI: https://doi.org/10.1107/S0108768187097416

Lines, M. Glass, A. 1979. Principles and applications of ferroelectrics and related materials. Oxford: *Clarendon Press*.

ISBN: 978-0-19-851286-8

Lone, I. H. Aslam, J. Radwan, N. R. E. Bashal, A. H. Ajlouni, A. F. A. Akhter, A. 2019. Multiferroic ABO_3 Transition Metal Oxides: a Rare Interaction of Ferroelectricity and Magnetism. *Nanoscale Res. Lett*. **14**. 142

DOI: https://doi.org/10.1186/s11671-019-2961-7

Magnéli, A., 1949. The crystal structure of tetragonal potassium tungsten bronze. *Arkiv Kemi*. **1**. 213-221

DOI: *Missing*

Martin, P. Rychetsky, I. Hlinka, J. 2010. Domain walls of ferroelectric BaTiO3 within the Ginzburg-Landau-Devonshire phenomenological model. *Phys. Rev*. B **81**. 144125

DOI: https://doi.org/10.1103/PhysRevB.81.144125

Molak, A. 1987. The Influence of Reduction in Valency of Nb Ions on the Antiferroelectric Phase Transition in $NaNbO_3$. *Solid State Commun*. 62. 413-417

DOI: https://doi.org/10.1016/0038-1098(87)91045-3

Moulson, A. J. Herbert, J. R. 2002. Electroceramics: materials, properties, applications. 2nd ed. Wiley: Chinchester

ISBN: 0471497479

Nie, R. Zhang, Q. Yue, Y. Hong, L. Chen, Q. Zhu, J. Yu, P. Xiao, D. 2016. Properties of Low-Temperature Sintering PNN–PMW–PSN–PZT Piezoelectric Ceramics with $Ba(Cu_{1/2}W_{1/2})O_3$ Sintering Aids. *Int. J. Appl. Ceram*. **13**. 1119-1124

DOI: **https://doi.org/10.1111/ijac.12581**

Ofoegbuna, T. Darapaneni, P. Sahu, S. Plaisance, C. Dorman, J. A. 2019. Stabilizing the B-site oxidation state in ABO_3 perovskite nanoparticles. *Nanoscale*. **30**. 14303-14312

DOI: https://doi.org/10.1039/C9NR04155A

Pan, M. J. Randall, C. A. 2010. A brief introduction to ceramic capacitors. *IEEE Electr. Insul*. Mag. **26**. 44-50

DOI: https://doi.org/10.1109/MEI.2010.5482787

Paściak, M. Ondrejkovic, P. Kulda, J. Vaněk, P. Drahokoupil, J. Steciuk, G. Palatinus, Welberry, L. Fischer, H. Hlinka, J. Buixaderas, E. 2019. Local structure of relaxor ferroelectric $Sr_xBa_{1-x}Nb_2O_6$ from a pair distribution function analysis. *Phys. Rev*. B **99**. 104102

DOI: https://doi.org/10.1103/PhysRevB.99.104102

Peirson, H. Pan, J. Li, Y. Hooper, T. E. Hall, D. A. Brown, A. P. Drummond-Brydson, R. M. Milne, S. J. 2023. Structure and dielectric properties of yttrium-doped $Ca_{0.28}Ba_{0.72}Nb_2O_6$ ceramics. *J. Alloy Compd*. **950**. 169891

DOI: https://doi.org/10.1016/j.jallcom.2023.169891

Polinger, V. Garcia-Fernandez, P. Bersuker, I. B. 2015. Pseudo Jahn–Teller origin of ferroelectric instability in $BaTiO_3$ type perovskites: The Green's function approach and beyond. *Phys. B: Condens*. **457**. 296- 309

DOI: https://doi.org/10.1016/j.physb.2014.09.048

Qian, H. Bursill, L. A. 1996. PHENOMENOLOGICAL THEORY OF THE DIELECTRIC RESPONSE OF LEAD MAGNESIUM NIOBATE AND LEAD SCANDIUM TANTALATE. *Int. J. Mod. Phys. B*. **10**. 2007-2025

DOI: https://doi.org/10.1142/S021797929600091X

Raju, G. G. 2017. Dielectric in Electric Fields. Dielectric loss and relaxation. 2nd ed. Routledge

ISBN: 9781498765213

Rojac, T. 2023. Piezoelectric response of disordered lead-based relaxor ferroelectrics. *Commun. Mater*. **4**. 12

DOI: https://doi.org/10.1038/s43246-023-00336-9

Scott, B. A. Giess, E. A. Burns, G. O'Kane, D. F. 1968. Alkali-rare earth niobates with the tungsten bronze-type structure. *Mat. Res. Bull*. **3**. 831-842

DOI: https://doi.org/10.1016/0025-5408(68)90100-1

Scott, J. et al. 2012. Domain wall nanoelectronics. *Rev. Mod. Phys*. **84**. 119-156

DOI: https://doi.org/10.1103/RevModPhys.84.119

Shannon, R. D. 1976. Revised effective ionic radii and systematic studies of interatomic distances in halides and chalcogenides. *Acta Cryst*. A**32**. 751-767

DOI: https://doi.org/10.1107/S0567739476001551

Tian, Y. Chao, X. Wei, L. Liang, P. Yang, Z. 2013. Phase transition behavior and electrical properties of lead-free $(Ba_{1-x}Ca_x)(Zr_{0.1}Ti_{0.9})O_3$ piezoelectric ceramics. *J. App. Phys*. **113**. 1 84107

DOI: https://doi.org/10.1063/1.4804173

Trainer, M. 2000. Ferroelectrics and the Curie-Weiss law. *Eur. J. Phys.* **21**. 459

DOI: https://doi.org/10.1088/0143-0807/21/5/312

Uchino, K. 2017. Advanced Piezoelectric Materials - Science and Technology. 2nd Ed. Elsevier.

ISBN: 978-0-08-102135-4

Volk, T. Isakov, D. Salobutin, V. Ivleva, L. Lykov, P. Ramzaev, V. Wöhlecke, M. 2004. Effects of Ni doping on properties of strontium–barium–niobate crystals. *Solid State Commun*. ***130***. 223-226

DOI: https://doi.org/10.1016/j.ssc.2004.01.039

Waeselmann, N. 2012. Structural transformations in complex perovskite-type relaxor and relaxor-based ferroelectrics at high pressures and temperatures. P.h.D thesis, Hamburg University. [Accessed Online: 7th August 2023].

[Available from]: https://www.researchgate.net/publication/302838100

Wang, L. Sui, W. Luan, S. Song, R. Tan, J. 2012. Sintering behavior and dielectric properties of Ce doped strontium barium niobate ceramics with silica sintering additive. *Mater. Chem. Phys.* **134**. 531-535

DOI: https://doi.org/10.1016/j.matchemphys.2012.03.028

Wei, H. Xia, Y. Cui, D. Shi, Y. Dong, M. Liu, C. Ding, T. Zhang, J. Ma, Y. Wang, N. Wang, Z. Sun, Y. Wei, R. Guo, Z. 2018. An overview of lead-free piezoelectric materials and devices**.** *J. Mater. Chem.* **6.** 12446-12467

DOI: **https://doi.org/10.1039/C8TC04515A**

West, A. R. Solid State Chemistry and its Applications. 2nd ed (Student Edition). Wiley: Chinchester

ISBN: 978-1-119-94294-8

Xu, R. Karthik, J. Damodaran, A. R. Martin, L. W. 2014. Stationary domain wall contribution to enhanced ferroelectric susceptibility. *Nat. Commun.* **5**. 3120

https://doi.org/10.1038/ncomms4120

Yi, Z. Ladi, N. H. Shai, X. Li, H. Shen, Y. Wang, M. 2019. Will organic–inorganic hybrid halide lead perovskites be eliminated from optoelectronic applications?. *Nanoscale adv*. **4**. 1276-1289

DOI: https://doi.org/10.1039/C8NA00416A

Yoshida, M. Mori, S. Yamamoto, N. Uesu, Y. Kiat, J. M. 1998. Tem observation of polar domains in relaxor ferroelectric $Pb(Mg_{1/3}Nb_{2/3})O_3$. *Ferroelectrics*. **217**. 327-333

DOI: https://doi.org/10.1080/00150199808015053

Yu, Y. Wang, X. Yao, X. 2013. Dielectric properties of $Ba_{1-x}Sr_xTiO_3$ ceramics prepared by microwave sintering. *Ceram. Int*. **39**. 5335-5339

DOI: https://doi.org/10.1016/j.ceramint.2012.10.089

Zaman, A. Iqbal, Y. Hussain, A. Kim, H. A. Malik, R. A. 2014. Dielectric, ferroelectric, and field-induced strain properties of Ta-doped $_{0.99}Bi_{0.5}(Na_{0.82}K_{0.18})_{0.5}TiO_3$–$_{0.01}LiSbO_3$ ceramics. *J. Mater. Sci*. **49**. 3205-3214

DOI: https://doi.org/10.1007/s10853-014-8024-7

Zhang, J. Wang, G. Gao, F. Mao, C. Cao, F. Dong, X. 2013. Influence of Sr/Ba ratio on the dielectric, ferroelectric and pyroelectric properties of strontium barium niobate ceramics. *Ceram. Int*. **39**. 1971-1976

DOI: https://doi.org/10.1016/j.ceramint.2012.08.048

Zhang, L. Thakur, O. M. Feteira, A. Keith, G. M. Mould, A. G. Sinclair, D. C. West, A. R. 2007. Comment on the use of calcium as a dopant in X8R $BaTiO_3$-based ceramics. *Appl. Phys. Lett.* **90**. 142914

DOI: https://doi.org/10.1063/1.2720305

Zheludev, I. S. 1971. Physics of crystalline dielectrics. New York: *Plenum press*.

ISBN: 978-1-4684-8076-4

Zhu, X. Fu, M. Stennett, C. Vilarinho, P. M. Levin, I. Randall, C. A. Gardner, J. Morrison, F. D. Reaney, I M. 2015. A Crystal-Chemical Framework for Relaxor versus Normal Ferroelectric Behavior in Tetragonal Tungsten Bronzes. *Chem. Mater.* **27**. 3250-3261

DOI: https://doi.org/10.1021/acs.chemmater.5b00072

3. Experimental techniques, principles, and methods

This section concerns the relevant experimental techniques, their principles of operation and the employed methods of sample production and preparation. X-ray diffraction, optical and electron microscopy are detailed as well as the electrical measurement techniques of dielectric spectrometry and polarisation-electric (P-E) field response. The synthesis of calcined ceramic powders is covered as well as the further processing of these powders into bulk ceramics and particle aerosol deposition films.

3.1 X-ray diffraction (XRD)

X-ray diffraction is a non-destructive technique widely employed to determine the structure of materials. The phase, or phases, present in a sample can be determined from the diffraction pattern that results from the interaction of a monochrome X-ray beam with the sample. In situ heating of a sample during (hot stage) XRD allows for the monitoring of temperature dependant phase transitions. Sample specific details, such as grain size and strain, can be calculated by comparison of a sample's diffraction pattern to a known standard reference file for that material.

3.1.1 X-ray generation

The generation of an intense and near-monochrome X-ray beam is essential for the production of interpretable diffraction patterns. To achieve this, primary electrons from a cathode are made to interact with an anode (usually copper) leading to the emittance of inner shell electrons from the anode. As outer shell electrons drop into the vacant inner electron shell a characteristic X-ray is emitted whose wavelength is dependant on the difference between the electron shell energy levels, see Figure 23. When a Cu K-shell electron is emitted an M shell electron may take its place and an X-ray, known as K_β is emitted, this X-ray is of higher energy and shorter wavelength, when compared with characteristic X-rays generated from the transition from L to K energy shells. Two comparable X-rays of wavelength 1.5406 Å ($K_{\alpha1}$) and 1.5443 Å ($K_{\alpha2}$) are emitted when electrons from the L shell drop into the K shell [Fellin, M. 2014]. The dissimilarity of the K_β X-ray allows for its removal by a monochronometer in the diffractor. The presence of $K_{\alpha2}$ in the diffraction pattern can be detected and removed by computational methods. This stripping of $K_{\alpha2}$ allows for a clearer interpretation of wavelength dependant diffraction pattern properties.

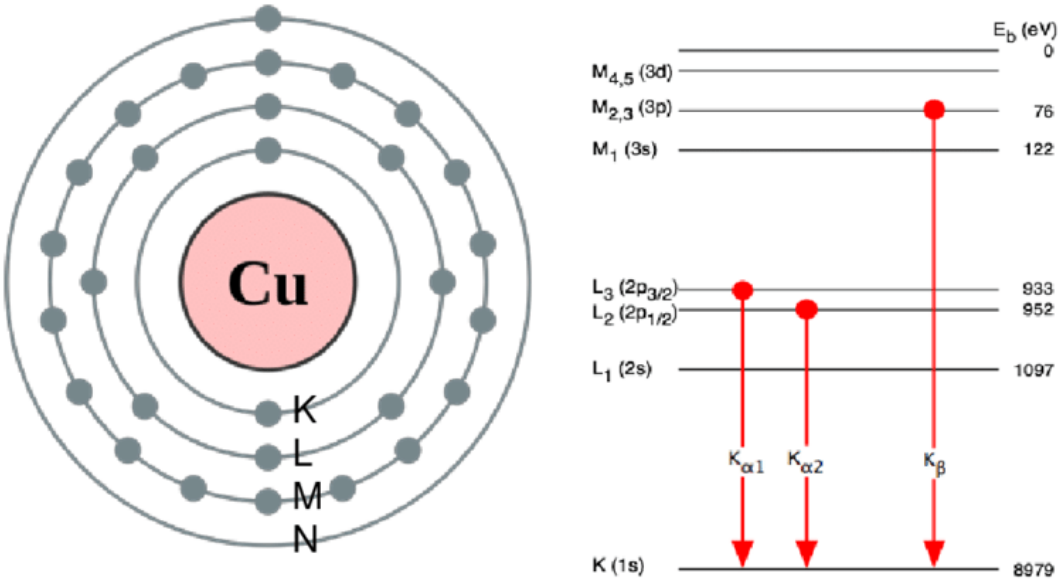

Figure 23. The electron energy shells of Cu and the changes in energy associated with the characteristic X-rays emitted during a transition from outer (L and M) shells to the K shell [Fellin, M. 2014].

3.1.2 X-ray diffraction and Braggs law

X-rays diffract upon interaction with charged species such as electrons. Where the atomic structure of a material is ordered, such as in the atomic layers, or planes, of crystals, a corresponding ordering of diffraction will occur. Figure 24 shows the diffraction of X-rays from different lattice planes and equation 7, the Bragg equation, relates X-ray wavelength (λ), angle of incidence and diffraction (θ) and lattice spacing (d). The destructive interference of diffracted X-rays results from their peaks and troughs becoming out of phase. At a particular interplanar spaces, an angle of incidence, the Bragg angle, produces X-rays that interfere constructively, see Figure 24. The peaks (increased intensity of X-rays detected) produced by this constructive interference produces a diffraction pattern. When interpreting these patterns, knowledge of the X-ray wavelength and angle of incidence allows inference of the lattice spacing, and so structure, of the material.

$$n\lambda = 2dsin\theta \qquad \text{Equation 1}$$

Where n is and integer, usually 1. Wavelength (λ) and lattice spacing (d) are measured in Angstroms. Angle of incidence (θ) is measured in radians.

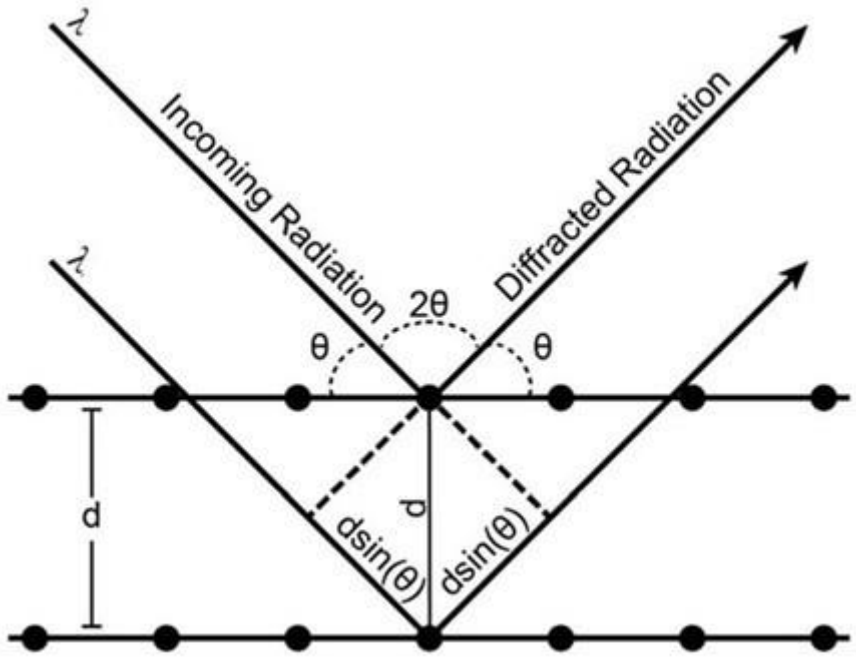

Figure 24. The origin of Braggs law in the constructive interference of X-rays of the same wavelength that travel different distances due to diffraction from different lattice planes, with lattice planes separated by a distance, or interplanar space, d. For constructive interference the two X-rays must travel distances that differ by whole integers of the X-ray wavelength (i.e. $\lambda = 2d\sin\theta$) [Stan, C. V. 2018].

Elements with a high atomic number possess more electrons and so have a higher X-ray scattering factor, producing more intense diffraction peaks [Hammond, C. 2015]. As well as this atomic factor a structural factor also determines the likelihood of diffraction. The structural diffraction factor of a material is dependent on the relative arrangements of the lattice planes in a crystal (given by the Miller indices) and so the frequency of atomic interaction when passing through the material in any given direction.

3.1.3 Crystallite strain and size effects

XRD is typically performed on ceramic powders as the random arrangement of fine grains, or crystallites, allows for diffraction without the bias or textural disposition of incidence angle that might occur when using larger ceramic pellets or single crystals.

Structural strains may exist within crystallites, effecting interplanar distances. Figure 25 shows how an ordered strain may modify the interplanar spacing and so measured peak position. Disordered microstrains result in a distribution of interplanar spacing and a broader diffraction peak.

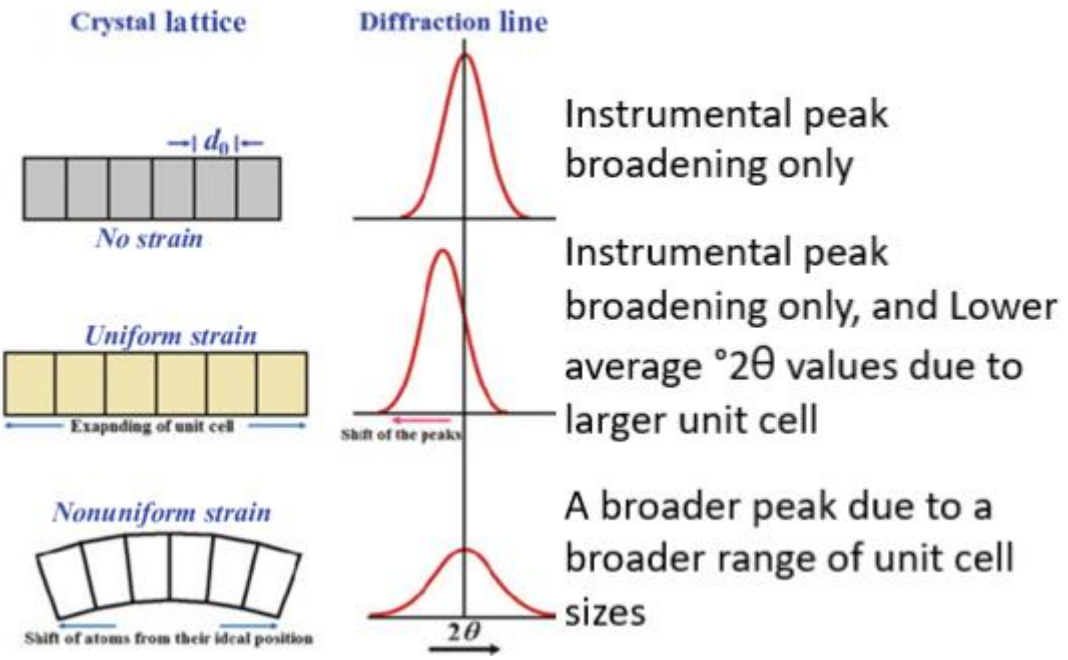

Figure 25. The effect of ordered and disordered strain on XRD peak position. Some instrumental peak broadening is inherent. This instrumental broadening can be found by measuring a sample known to have marginal strain (and large crystallite sizes), and can be subtracted when assessing peak broadening due to microstrain or fine crystallite size (see below) [Nasiri-Tabrizi, B. 2014].

The pattern produced by diffracted X-rays depends on the constructive interference of X-rays that have interfered with different lattice planes. In very small crystallites a lesser number of lattice planes are present to induce this constructive interference. Consequently, a less sharply defined, broader peak in detected X-rays is produced from very fine crystallites. Scherrer's equation, Equation 8, shows the inverse relationship between peak broadening, B_L, and average crystallite size, L.

$$B_L = \frac{K\lambda}{Lcos\theta} \qquad \text{Equation 8}$$

Scherrer's equation relates the mean crystallite size, L, to peak broadening, B_L. A constant, K, is typically 0.9 for isotropic crystals, λ is the wavelength and θ is the Bragg angle.

X-ray powder diffraction was typically performed on crushed sintered pellets by rotating the samples in a Bruker D8 powder diffractometer (Bruker, Germany), using Cu Kα X-ray radiation. Typical 12 h scans measured from 10 to 90 °2θ, with a step size of 0.008 °2θ and a time per step of 4.2 s.

3.2 Optical microscopy

In optical microscopy the refractive properties of light are used to produce a magnified image of the sample. The ability to resolve between two neighbouring features of a sample depends on the overlapping diffraction patterns produced by (incoherently scattered) light from the illuminated features, according to the Rayleigh criterion. Equation 9 shows the relationship between the smallest observable distance (δ), the wavelength of the diffracted species (λ), which for visible light is 400 – 700 nm, and numerical aperture (NA). Where numerical aperture denotes the range of angles over which the device can accept light.

$$\frac{0.61\lambda}{NA} = \delta \qquad \text{Equation 9}$$

A higher numerical aperture increases the amount of light that can be captured, producing brighter images from the same exposure time. Resolution also increases with numerical aperture. According to the Abbe limit two distinct objects cannot be resolved if their separation distance, d, is not greater than λ/2. The Abbe limit is described in Equation 10, as two neighbouring objects diffract light an interference pattern is produced. The angle at which the first order of interference is produced increases as d decreases. A wider numerical aperture can therefore capture the first order interference produced by closer objects, and so resolve them.

$$d = \frac{\lambda}{2sin\theta}\ , \quad d > \frac{\lambda}{2} \qquad \text{Equation 10}$$

Figure 26 shows the layout of a compound microscope which uses lenses to produce a focused beam to illuminate the sample and produce a magnified image. Brightfield images can be produced when diffracted or scattered light is blocked and unscattered incident light is used to construct the image. Whilst darkfield images are constructed from diffracted or scattered light. Widefield microscopes illuminate the whole sample whilst confocal microscopes illuminate only the observed section and produce images of a large area by sequential capture.

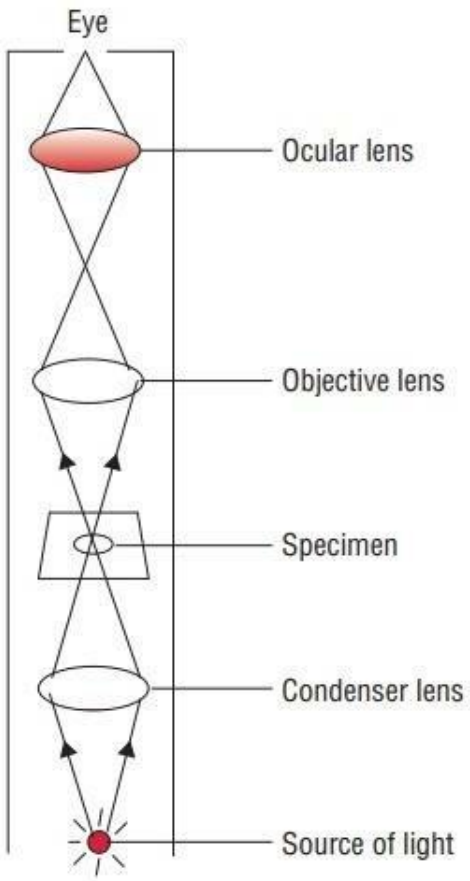

Figure 26. A diagram of a compound microscope [Suryandari, R. 2020].

3.3 Electron microscopy

3.3.1 Scanning electron microscopy

Scanning electron microscopy uses the wavelike properties of the electron to produce high resolution images. The de Broglie wavelength of an electron accelerated at 10 - 100 keV is ~0.001 - 0.01 nm, much less than the wavelength of light, allowing for the high magnification observation of microstructure.

In the microscope electrons may be produced by thermionic emission from a tungsten filament and then an accelerating voltage is applied. Electromagnetics focus these electrons into a high energy beam. Upon the beams impact with the sample various species are produced and detected, these include secondary electrons, backscatter electrons and X-rays. Figure 27 shows a diagram of a scanning electron microscope.

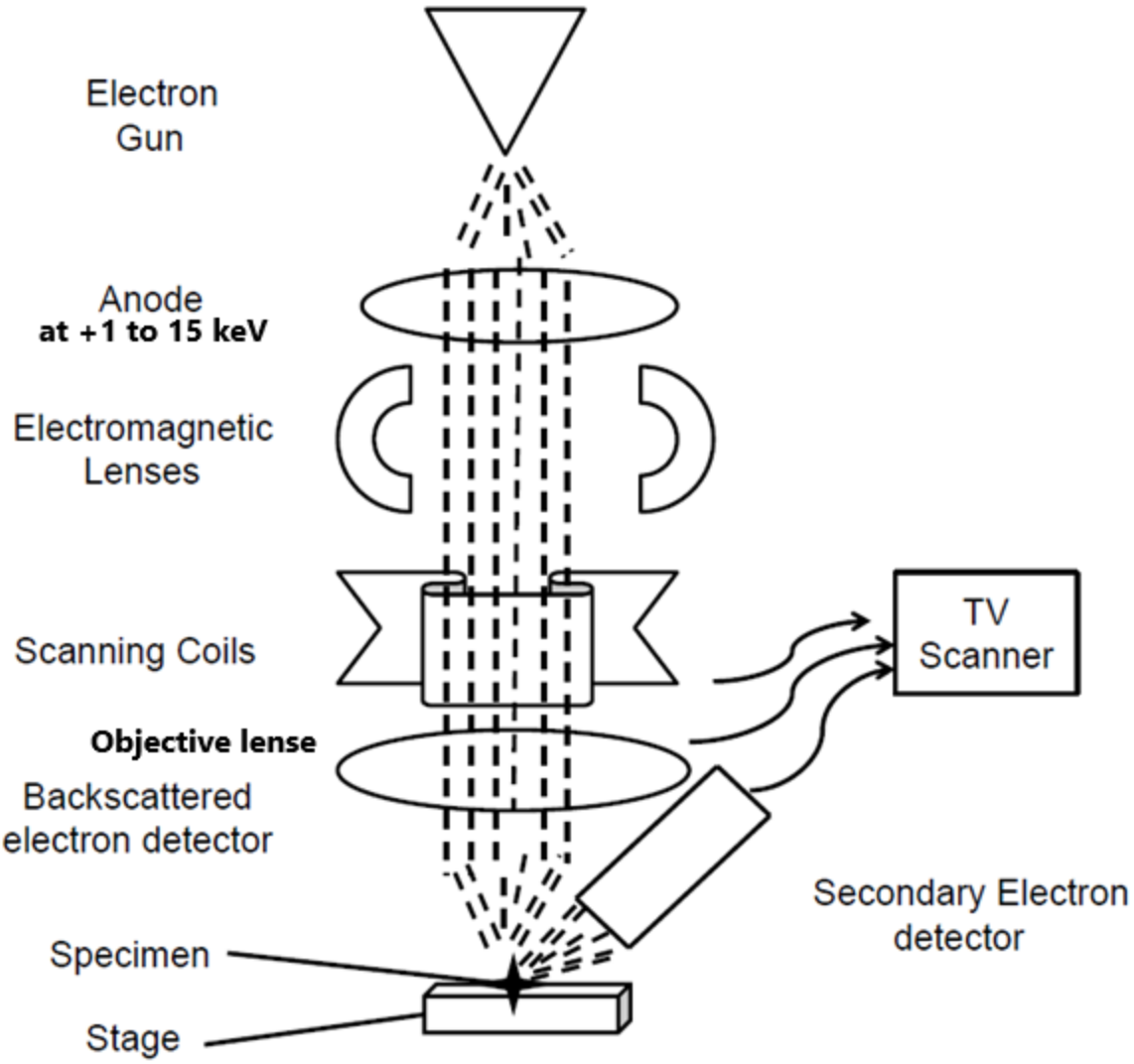

Figure 27. A diagram of a scanning electron microscope. Adapted from [Tare, M. 2009].

Secondary electrons are relatively low energy (< 50 eV), they originate from near the surface of the sample. They result from a primary (beam) electrons inelastic collision with the sample. Backscattered electrons penetrate deeper within the sample and elastically collide with nuclei, they have higher energies (>> 50 eV), close, or equal, to that of the incident electrons. A sample containing larger nuclei (higher atomic Z number) produces a greater intensity of scattered electrons.

The electrons in a sample may be excited, as well as emitted, due to interactions with primary electrons. Upon the transition of excited electrons back to lower energy states characteristic X-rays are produced. The detection of these X-rays provides compositional information, by a technique known as energy dispersive X-ray spectroscopy.

In preparation for microstructural examination sintered ceramic pellets were mounted in epoxy resin (Epothin, Buehler). These samples were ground with silicon carbide abrasive paper (P800 and P2500) and polished to a scratch-free surface using Texmet P microcloths then MetaDi 2 diamond suspensions with sequentially decreasing particle sizes of 9, 3 and 1 µm (Buehler, Germany). To elucidate grain structure, chemical etching was carried out at room temperature with a 2:1 ratio of hydrofluoric acid and concentrated nitric acid for 60 - 180 s. Scanning electron microscopy was undertaken on sample pellets sputter coated with 20 nm amorphous carbon, in a Hitachi SU8230 high performance, cold field emission instrument which typically operated at 2 kV and 5000x magnification. In a field emission instrument, the electron beam is generated by an applied field, as opposed to by heating in the case of thermionic emission. Powder samples were also sputter coated prior to microscopy.

3.3.2 Focused Ion beam (FIB-SEM)

In a focused ion beam (FIB) instrument samples are illuminated by an ion beam, as opposed to an electron beam. Often a FIB instrument will also have electron beam capacity.

To produce the ion beam, a metal, such as Ga, is allowed to wet a tungsten needle and is then ionised by an applied electric field (of 1 - 50 keV). When the primary Ga-ion beam impacts on the specimen surface it sputters surface material but also produces secondary electrons and a backscatter electron component.

The ion beam is destructive, milling the surface, resulting in the emission of ions and atoms from the sample surface and some implantation of Ga ions into the sample. Operating at higher beam currents allows for precision cutting or milling, for example in the production of a submicron lamella from a sample cross-section, for transmission electron microscopy (TEM). Gas assisted deposition of conductive material on the top surface of a specimen, such as Pt, prior to milling, prevents charging of the specimen area and shields the surface from damage or implantation during the production of a cross-section, prior to secondary or backscattered electron imaging.

Samples (ceramics or films) required no prior preparation for FIB-SEM in a Helios G4 CX DualBeam (Thermofisher, UK), with the application of a Pt coating and the production of a cross section, by milling, occurring prior to cross-sectional imaging with either electron or ion beam illumination.

3.3.3 Transmission electron microscopy (TEM)

High energy electrons can transmit through ultrathin (< 500 nm) samples, allowing for very high magnification and resolution in transmission electron microscopes. Transmission electron microscopes operate at higher keV's and vacuums than scanning electron microscopes. To image an area scanning transmission electron microscopy (STEM) is used. Darkfield images are produced from diffracted electrons whilst brightfield images are produced from the undiffracted beam. To produce a dark field image the transmitted electrons are blocked and a ring, or annulus, of diffracted electrons are captured (annular dark field). High-angle annular dark field (HAADF) images have high resolution.

Electron diffraction (ED) patterns of a selected area of crystalline material can be interpreted, with individual diffraction points corresponding to a lattice plane. Polycrystallinity, over the 100's of nm range of detection, can be inferred from a multiplicity of points, termed a polycrystalline diffraction band.

In preparation for transmission electron microscopy, within a Titan Themis Cubed 300 TEM (Thermofisher, UK), samples were coated in Pt, milled and sample mounted within a Helios G4 CX DualBeam (Thermofisher, UK), focused ion beam SEM to produce a thin lamella.

3.4 Electrical characterisation

3.4.1 Dielectric spectrometry

The relative permittivity and dielectric loss of a sample can be determined by dielectric spectroscopy, by situating it between parallel plate electrodes and applying an alternating current. A frequency generator can vary the current, typically between 0.1 kHz and 1 MHz, whilst a furnace or environment chamber allows for the variance of temperature. The capacitance of the material can then be measured and compared to the capacitance of a material with known permittivity.

For electrical measurements, silver electrodes (Gwent Electronic Materials) were deposited on ceramic pellets at a firing temperature of 550 ^{o}C for 5 h. Relative permittivity and dielectric loss were measured as a function of temperature by using a HP4284a LCR analyser (Hewlett Packard, USA). The oscillator was set at 2 V, whilst frequencies ranged from 10^{3}-10^{6} Hz and temperatures from 20 to 350 ^{o}C. A controlled environment chamber was used for lower temperatures down to -70 ^{o}C (Tenney Environmental-SPX, White Deer).

3.4.2 Polarisation-electric field response

A modified sawyer-tower circuit can be used to measure the induction of current by application of an electric field. For ferroelectrics, upon cycling of the field, a characteristic hysteresis response is produced.

Ferroelectric hysteresis measurements were performed by applying four sinusoidal cycles of an AC electric field waveform with a frequency of 2 Hz, using a function generator (HP33120A, Keysight Technologies, Berkshire, UK) and a high voltage (5 kV) amplifier (HVA1B, Chevin Research, Otley, UK). Ceramic samples of ~1 mm thickness experienced maximum field strengths of 50 kV cm^{-1}.

3.5 Bulk ceramic synthesis

A conventional solid-state method was used to produce calcined powder. Reagent grade carbonates and oxides, listed in Table 5, were dried at 200 ^{o}C for 24+ h, to remove moisture, and were stored in an evacuated desiccator. Composition dependent stoichiometric mass measurements were made to a precision of ±0.001 g, using an electric balance (Sartorius UK LTD, UK), producing standard 50 g batches. The batches were ball milled in cylindrical plastic bottles 10 cm in diameter and 15 cm height, with cylindrical (~1 cm^3) yttria stabilised zirconia (YZT) milling media (Tosoh, Japan) and 80 mL of Iso-2-propanol (Fisher chemicals, UK), for 12 h. The obtained slurry was dried in a Kenwood mixer with inbuilt heating element, to retain the mix whilst drying. The dried powder was sieved through a 300 µm gauze and stored in a plastic container. Sieved powder was calcined in a covered zirconia crucible typically at 1200 ^{o}C for 12 h with a ramp rate of 300 ^{o}C h^{-1}, to reduce the carbonates to oxides and facilitate the formation of a single-phase solid solution. Calcined powder was sieved ready for either finishing route.

Table 5. The purity and sources of precursor powders.

Precursor	Purity (%)	Source	CAS code
$CaCO_3$	99.95	Alfa Aesar	207-439-9
$BaCO_3$	99.95	Alfa Aesar	208-167-3
Y_2O_3	99.9	Alfa Aesar	1314-36-9
Nb_2O_5	99.9	Alfa Aesar	215-213-6
Ta_2O_5	99.85	Alfa Aesar	1314-61-0

Sieved calcined powder was ball milled with 2 wt.% Optapix ceramic binder (Zschimmer & Schwarz, Germany) and distilled water (80 mL) and milled for 12 h. The obtained slurry was dried, sieved and formed into 10 mm diameter green pellets via uniaxial pressing at a pressure of 1.5 tons for 30 s. Pellets were sintered in a bed of same-composition sacrificial powder inside a covered zirconia or alumina crucible.

Typically, a 2-stage sinter regime was used for densification with a ramp rate of 300 ^{o}C h^{-1}. The pellets were heated at 550 ^{o}C for 5 h to promote binder burnout, then heated to 1350 ^{o}C for 4 h before cooling to room temperature. Sintered pellets were cleaned of sacrificial powder aggregates via light abrasion and their densities were calculated via the geometric method. The polycrystalline sintered samples (pellets) were then ready for analysis-technique specific processing.

3.6 Particle aerosol deposition (PAD) film fabrication

More detail on the Leeds PAD system, and the standard operating conditions employed, can be found in Section 7.2.1 (Results chapter 2). Substrates with ~8 x 8 mm dimensions, typically made from SUS304 stainless steel, were attached to the Leeds PAD system's removable sample (X-Y) stage within the vacuum chamber (Diener electronic, Ebhausen, Germany). The chamber was then sealed, the Edwards direct-drive rotary vane vacuum pump (Edwards vacuum, London, UK) turned on, and internal pressure reduced until stable at 5 - 10 mbar.

Typically, 12- or 20- h calcined powder was further processed prior to PAD. Further (low-energy) ball milling, for 24 h at the conditions described above, typically preceded high-energy attrition milling.

Attrition milling was undertaken to produce powders with a submicron primary particle sizes. The high-energy attrition mill reduced particle size via mechanical impact with yttria-stabilised zirconia beads of variable size (650 µm and 1000 µm). Typically, 150 g of calcined powder was mixed with 800 mL of iso-propanol and passed through the attrition mill for 1 h, which operated with 1 kg of 650 µm yttria stabilised zirconia beads. The powder was then dried in a in a Kenwood mixer with inbuilt heating element and sieved with 300 µm nylon mesh.

Thermal pretreatment, of milled powders, was ostensibly undertaken to promote the formulation of aggregates formed from submicron primary particles, with necked bonds between them, and regrow fine particle fragments (< 250 nm). Powders were heated to 1000 °C for 4 h at a ramp rate of 300 °C h^{-1}.

Calcined, or further processed, powder was dried for 24+ h at 200 ^{o}C prior to sieving, with 200 µm mesh, and poured into the aerosol generation chamber (AGC). The borosilicate AGC was of custom design (Asynt Ltd., Cambridgeshire, UK). A filter paper, Durapore^{TM} (Merk Millipore**,** Darmstadt, Germany), served as bed for the powder and allowed for through-flow of the aerosol.

The X-Y stage was set into motion by programmed actuators. These actuator programs were produced using G code and a Duet 3D control board (Duet3D Ltd, UK). Typically, the X-Y stage travelled from the origin to X = +40 mm (over multiple substrates) and back to the origin at a rate of 20 mm s^{-1}, for multiple cycles or passes.

The flow of nitrogen gas, limited to an absolute pressure of 1.5 bar, was initiated and controlled by a manual flowmeter. The flowmeter was calibrated to atmospheric conditions, which likely resulted in an underestimation of flowrates. Typically, measured flowrate varied between 2-8 L min^{-1}. Deposition typically occurred for ~30 s. During deposition, chamber pressure often exceeded 20 mbar and the deposition was paused and chamber pressure was allowed to return to < 10 mbar. Often, a 3-stage deposition protocol was employed to extend the total deposition time at low pressures (< 20 mbar). After deposition the vacuum chamber was repressurised and the produced films were retrieved.

3.6.1 Mechanical sectioning

To produce mechanical cross sections for cross-sectional SEM, PAD films were mounted in epoxy resin (Epothin, Buehler). These samples were ground with silicon carbide abrasive paper (P800 and P2500) to expose the cross-section, and polished to a scratch-free surface using Texmet P microcloths then MetaDi 2 diamond suspensions with sequentially decreasing particle sizes of 9, 3 and 1 µm (Buehler, Germany).

3.6.2 Electroding

Electrodes were applied to the PAD films by use of a dual target sequential sputterer (Qorum Q300T D). To control the area of the electrodes, pattern masks were designed in Solidworks and laser cut onto either plastic or metal. The pattern masks and electroded films can be seen in Appendices 13 and 14. Typically, 5 electrodes, of radius = 1 mm, were deposited onto a film. A 10 nm thick Cr layer was deposited prior to a 30 nm thick Au electron, with the Cr aiding the adhesion of the Au.

3.7 References

Fellin, M. 2014. Monitoring wooden materials for recycling. Ph.D. thesis. University of Turin

DOI: https://doi.org/10.13140/2.1.1460.5128

Hammond, C. 2015. The Basics of Crystallography and Diffraction. 4th ed. Oxford university press

ISBN: 9780198738688

Stan, C. V. Beavers, C. M. Kuntz, M. Tamura, N. X-Ray Diffraction under Extreme Conditions at the Advanced Light Source. *Quantum Beam Sci.* **2**. 4

DOI: https://doi.org/10.3390/qubs2010004

Tare, M. Puli, O. Oros, S. Singh, A. 2009. Drosophila adult eye model to teach Scanning Electron Microscopy in an undergraduate cell biology laboratory. Population Data Information Service. 92. 174-180. [Accessed online 18th February 2024] [Accessed from]: https://www.researchgate.net/publication/263910532_Drosophila_adult_eye_model_to_teach_Scanning_Electron_Microscopy_in_an_undergraduate_cell_biology_laboratory

Nasiri-Tabrizi, B. 2014. Thermal treatment effect on structural features of mechano-synthesized fluorapatite-titania nanocomposite: A comparative study. *J. Adv. Ceram*. **3**. 31-42

DOI: https://doi.org/10.1007/s40145-014-0090-4

Suryandari, R. 2020. Addition of Illuminator Fiber Optic to Produce 3 Dimension Effects in Micrographic Observation Using Upright Microscope. International Conference on Science and Engineering III. Yogyakarta [Accessed online 18th February 2024] [Accessed from]: https://www.researchgate.net/publication/354948266_Addition_of_Illuminator_Fiber_Optic_to_Produce_3_Dimension_Effects_in_Micrographic_Observation_Using_Upright_Microscope

4. Material of study

4.1 Calcium barium niobate

The functional properties of CBN, as with other TB's, give rise to distinct fields of interest, namely non-linear electro-optics and ceramic capacitor applications [Eßer, M. 2003]. These dielectric and non-linear optical properties are highly dependent on material structure. Many characterisation techniques have been employed to examine different aspects of the CBN structure and its crystal structure transitions; notably they include XRD (lattice and crystal structure), SEM/TEM (micro/nano structure, domain structure and chemical composition), X-ray photoelectron spectroscopy (surface chemistry and bonding), Raman spectroscopy (bonding), second harmonic generation/k-space spectroscopy (domain structure) and differential scanning calorimetry (phase transition). Characterisation of the dielectric and ferroelectric properties of CBN has included the temperature and electric field dependence of permittivity and dielectric loss tangent (ε_r-T, tan δ-T and ε_r-E, tan δ-E) and polarisation-electric field response (P-E).

Below, the published research most relevant to the work presented in this thesis is summarised, with emphasis on the reporting of chemical modification of CBN and its effect on structural, dielectric and ferroelectric properties.

4.2 Single-phase region

The partially filled TB $Ca_xBa_{1-x}Nb_2O_6$ was identified as a ferroelectric in 1959 [Ismailzade, I. G. 1960]. More recent powder XRD on sintered and annealed samples has identified a single-phase solid solution whose existence region was between compositions $0.15 \leq x \leq 0.40$, after annealing at 1400 °C. The solutions solubility limits narrowed after annealing at 1200 °C and the room temperature single-phase region was extrapolated and found to exist between compositions $0.17 \leq x \leq 0.33$ [Muehlberg, M. 2008]. The $BaNb_2O_6$-$CaNb_2O_6$ binary phase diagram is shown in Figure 28. Single crystal XRD of CBN28 showed that that 62 % of A1 (CN12) and 94 % of A2 (CN15) sites were occupied. The Ba^{2+} ions (1.61 Å, CN12) are reported to occupy 88 % of the larger A2 sites and Ca^{2+} ions (1.34 Å, CN12) to occupy 59 % of the smaller A1 sites [Graetsch, H. A. 2012]. This near complete segregation of the dissimilarly sized A site cations results in a narrow single-phase region, when compared to the isostructural strontium barium niobate ($0.20 \leq x \leq 0.80$), which shows a greater degree of mixed site occupancy [Muehlberg. M. 2008] and [Trubelja, M. P. 1996].

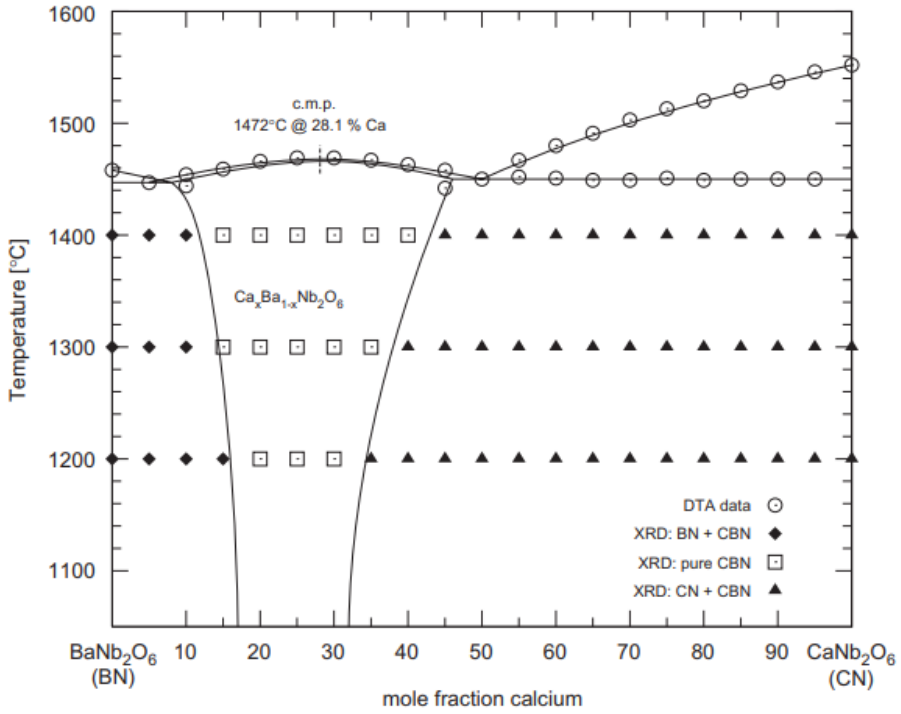

Figure 28. The $BaNb_2O_6$-$CaNb_2O_6$ binary phase diagram derived from XRD measurements and, for the determination of melting point, differential thermal analysis (DTA). Taken from [Muehlberg, M. 2008].

4.3 Structural identification and transformation

Whilst often described as a tetragonal TB, the structure of CBN is only pseudo-tetragonal. High resolution TEM has identified an incommensurate superlattice structure arising from the "uniform mixture of 2 orthorhombic cells" with respective lattice parameters of $4{\cdot}a$ x $2{\cdot}c$ and $2{\cdot}a$ x $2{\cdot}c$ (where a and c refer to the tetragonal cell parameters, a = 12.49 Å, c = 3.95 Å) [Lu, C. J. 2006]. The origin of similar supercell structures in strontium barium niobate (SBN) and barium sodium niobate (BNN) have been ascribed to the "concerted rotary" displacement of the B site octahedra [Lin, P. J. 1987]. Here, the unfavourable occupation of A1 sites by the (large) Ba ion causes the displacement of oxygen ions and a tilting of the oxygen octahedra.

The room temperature ferroelectric phase of CBN28 ($Ca_{0.28}Ba_{0.72}Nb_2O_6$) has been characterised by XRD as best fitting the space group P4bm (No. 100) [Graetsch, H. A. 2012]. No change in symmetry was observed when increasing temperature, above the temperature of permittivity maxima, up to 330 ^{o}C. Rather a diffuse, with respect to temperature, transition occurred with the Nb ions approaching and some of the Nb ion crossing the equatorial plane of the oxygen octahedra. Observation of the domain structure, by TEM with *in situ* heating, revealed macro- to micro-domain switching around these temperatures [Lu, C. J. 2006]. A relationship between polar structures and

incommensurate modulation was identified by TEM with in situ heating [Beanland, R. 2023]. There, two orthorhombic structures were identified and shown by dark field TEM to be intimately mixed at length scales of 10-50 nm. This structuring is similar to that identified in SBN [Krayzman, V. 2022].

4.4 Microstructure

The microstructure of CBN, as with many TBs, is typically non-equiaxed. A [0 0 1] growth habit often results in grains of a pillar type morphology. This propensity for pillar-type grains and exaggerated grain growth increases with increasing Ca:Ba ratio, see Figure 29 [Han, X. 2013]. SEM of the (0 0 1) facet showed the occurrence of stepwise growth [Ke, S. 2008]. Due to the high rates of atomic diffusion required, this growth mechanism is strongly suggestive of partial liquid phase sintering. Although the sintering temperature employed (1340 ^{o}C) was ~100 ^{o}C below that of the melting temperature indicated in the phase diagram for high Ca content CBN, see Figure 28. Micro-cracking in Sr doped CBN grains has been observed [Abdelli, F. 2016].

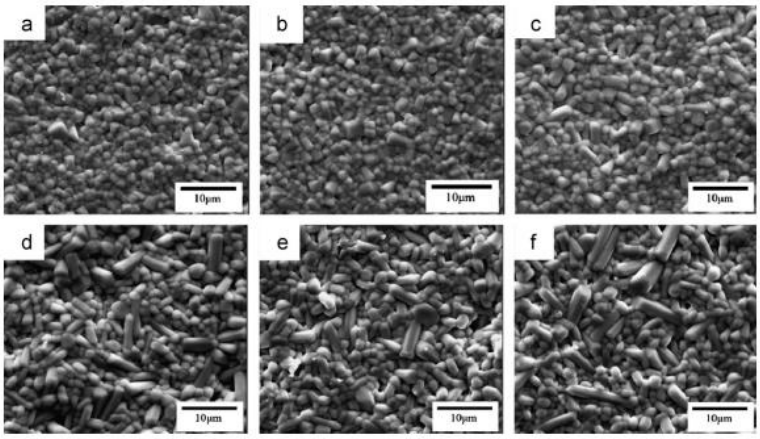

Figure 29. Scanning electron micrographs of $Ca_xBa_{1-x}Nb_2O_6$ ($0.20 \leq x \leq 0.35$) ceramics sintered at 1340 ^{o}C, highlighting the anisotropic growth habit of CBN grains with increasing Ca content. (a) x = 0.20, (b) x = 0.22, (c) x = 0.25, (d) x = 0.28, (e) x = 0.30, (f) x = 0.35. Taken from [Han, X. 2013].

4.5 Dielectric and ferroelectric properties

The permittivity-temperature profile of CBN28 exhibits a slightly diffuse peak around 235-270 ^{o}C, the diffusivity of this peak reflects the displacive structural transformation that was observed to occur, by XRD, above 200 ^{o}C [Graetsch, H. A. 2012]. Despite the absence of a well-defined symmetry change/phase transformation in CBN, the term T_C is often used to define the temperature around permittivity (ε_r-)maximum, in contrast to materials with a more frequency dependant ε_r-Max, for which T_M is often preferred.

The T_C of CBN decreases with increasing Ca content. CBN28 solidifies congruently from the melt, See Figure 28, its permittivity-peak is the least diffuse of all the single phase CBNs and shows the highest value of ε_r-Max (typically 2000-3000), see Figure 30.

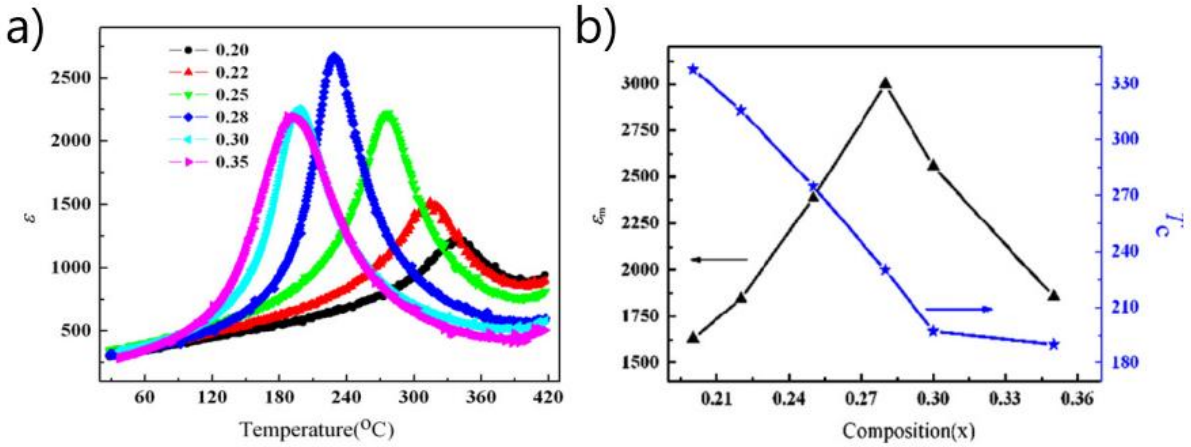

Figure 30. The permittivity-temperature responses, in (a), and variation in ε_r-Max and T_C, in (b), for $Ca_xBa_{1-x}Nb_2O_6$ ($0.20 \leq x \leq 0.35$) ceramics, measured at 1 kHz. Taken from [Han, X. 2013].

In higher Ca content CBN, tan δ peaks are present below T_C. These peaks are frequency dispersed, increasing in magnitude with increasing frequency. Such $T < T_{C/M}$ dielectric loss profiles are commonly observed in relaxor ferroelectrics. The temperature dependence of dielectric loss factor for CBN30 ($Ca_{0.30}Ba_{0.70}Nb_2O_6$) is shown in Figure 31, along with that of CBN22 ($Ca_{0.22}Ba_{0.78}Nb_2O_6$), which also shows increased low frequency dielectric losses at temperatures above T_C [Ke, S. 2008]. The P-E response of $Ca_xBa_{1-x}Nb_2O_6$ (for $0.20 \leq x \leq 0.35$) is that of a normal ferroelectric with a lossy hysteresis loop whose residual polarisation (P_r) decreases slightly at lower Ca:Ba levels below (Ca) x = 0.28 [Han, X. 2013].

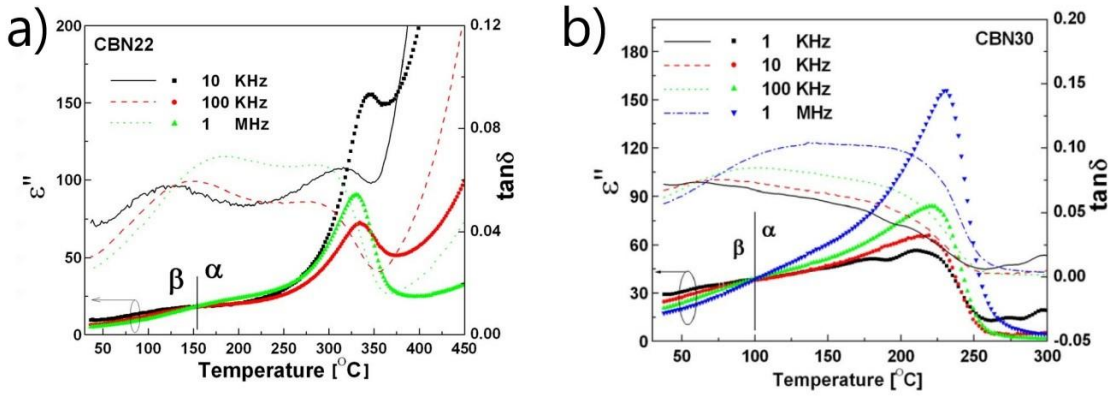

Figure 31. Dielectric loss- (ε'') and tan δ-temperature response for (a) $Ca_{0.22}Ba_{0.78}Nb_2O_6$ and (b) $Ca_{0.30}Ba_{0.70}Nb_2O_6$ ceramics sintered at 1350 °C. Taken from [Ke, S. 2008].

4.6 Dielectric and ferroelectric properties of chemically modified CBN

Though less well studied than the isostructural SBN, CBN has been chemically modified with a variety of dopants.

After the first single crystal synthesis [Eßer, M. 2002], modification of single crystal structure and electro-optical properties by doping with Ce^{4+}, *Na^{+}, Nd^{3+} and **Yb^{3+} has been reported [*Zhao, J-H. 2018] and [**Di, J. 2014]. Though often not included, some dielectric data are available from the optical papers. In Ce doped CBN ("1% cerium content") [Niemer, A. 2012], the permittivity peak became more diffuse and T_M decreased to 189 °C whilst becoming slightly frequency dependent. Low level Nd^{3+} doped CBN ($Nd_{0.016}Ca_{0.264}Ba_{0.712}Nb_2O_6$) showed a decrease in T_C to 223 °C with no broadening of the permittivity peak [Gao, W. L. 2010].

4.6.1 Calcium strontium barium niobate

The ternary system calcium-strontium-barium-niobate (CSBN) has been well studied, often by varying the composition $Ca_xSr_yBa_{1-x-y}Nb_2O_6$ by nominal ratios of CBN28 and SBN61 (which also solidifies congruently from the melt) over the range of x from < 0.07 to 0.21 and y from < 0.15 to 0.45. The $T_{C/M}$ of CSBN is dependent on a linear relationship between the compositional ratio of CBN28 and SBN61, increasing with increasing Ca content. Whilst ε_r-Max (and T_M) become increasingly frequency dependant with increasing Sr content, as shown in Figure 32.

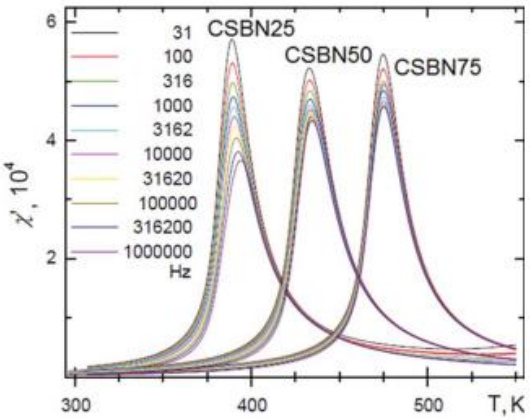

Figure 32. Permittivity-temperature profiles of CSBN ceramics labelled according to the nominal compositional ratio of CBN28 and SBN61, i.e. CSBN25 corresponds to $(Ca_{0.28}Ba_{0.72})_{0.25}(Sr_{0.61}Ba_{0.39})_{0.75}Nb_2O_6$. Taken from [Malyshikna, O. 2017].

A single research group have produced a variety of doped CBN28-based single phase ceramics, for which they have reported dielectric and ferroelectric analysis, as summarised immediately below and in the "Recent work" section. Isovalent, donor and acceptor A site doping has been performed as well as co-doping with acceptor A site and isovalent B site doping. Some ceramics were produced

by the low-level inclusion (0.1 - 0.6 wt.%) of dopant oxides to a $Ca_{0.28}Ba_{0.72}Nb_2O_6$ mix prior to calcination (without charge balanced ionic substitution), whilst other doping was performed by synthesis according to charge balanced, nominal formulations.

4.6.2 Non-Sr isovalent A site doping

The doping of CBN28 ceramics by CuO addition (0.1 - 0.4 wt.%), without charge balanced substitution, caused a minor reduction in T_C and significant variation in ε_r-Max. Initially, up to 0.2 wt.%, ε_r-Max increased to a high of ~3400 before decreasing to a low of 2400 at 0.4 wt.%, when measured at 1 kHz (Figure 33(a)) [Wei, L. 2014-Feb]. Copper oxide can be employed as a sintering aid that allows the use of lower sintering temperatures. Increasing CuO levels from 0.1 - 0.4 wt.% did not reduce the sinter temperature required for each composition's maximum relative density (1300 ^oC). However, the rate of decrease in relative density with decreasing sinter temperature was reduced between 0.2 and 0.4 wt.% (Figure 33(b)). Maximum densities were achieved around 1300 ^oC, which is lower than previously reported CBN28 ceramic sinter temperatures (1330-1350 ^oC).

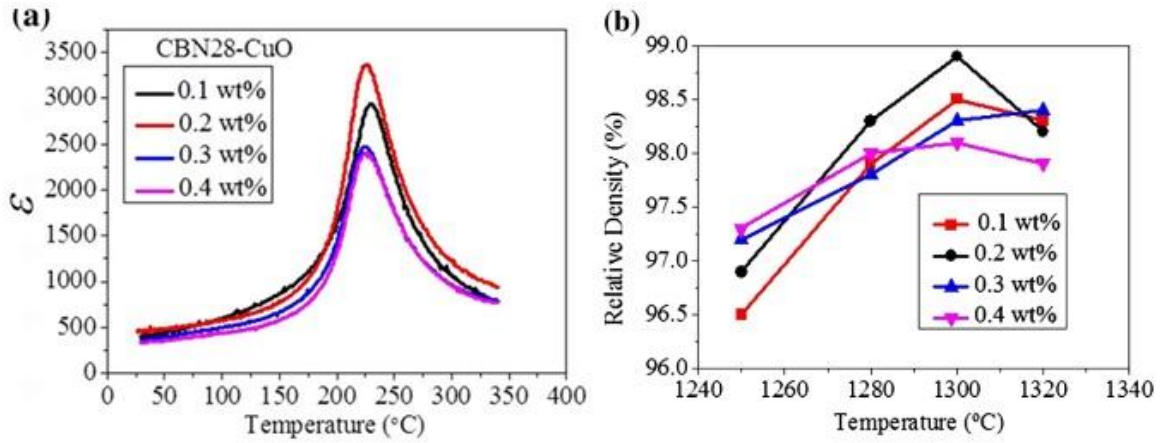

Figure 33. In (a), The permittivity-temperature responses of CBN28 ceramics with the addition of 0.1 - 0.4 wt.% CuO, measured at 1 kHz and, in (b), the measured density of Cu:CBN28, sintered for 4 h at 1250 - 1325 ^oC. Taken from [Wei, L. 2014-Feb].

4.6.3 Donor A site doping

The doping of CBN28 ceramics by Ce^{4+} and La^{3+} was performed by Ce_2O_3 and La_2O_3 addition (0.1 - 0.6 wt.%) [Wei, L. 2014-May]. No charge balancing was performed (no inclusion of A site vacancies in the nominal formula), ceramic densities were high (97.5+ %) and no unambiguous secondary phase peaks were identified by XRD.

The effects on dielectric properties were similar to that of donor doped single crystal CBN [Niemer, A. 2012], with $T_{C/M}$ reducing with dopant addition and peak diffusivity increasing. This combination

resulted in higher permittivity around room temperature, for the doped samples. The ε_r-Max of Ce doped CBN28 was initially higher and decreased with increasing Ce content whilst La doped CBN showed a lesser range of ε_r-Max values and had a less consistent trend between La content and ε_r-Max (see Figure 34). The Ce doped CBN28 (0.5 wt.%) showed near temperature stable permittivity (ε_r ~1780 ±15 %) from ~160 to ~230 ^{o}C. The La doped CBN (0.5 wt.%) showed a comparable range of temperature stability (ε_r ~2070 ±15 %) from ~150 to ~210 ^{o}C. The effects of frequency on permittivity were not presented for all samples, but only a minor variation (< ~5 °C) in the temperature of ε_r-Max occurred in La doped CBN (0.4 wt.%) when measuring at 1 and 100 kHz.

The (room temperature) P-E responses of the Ce doped CBN samples remained comparable whilst La doped CBN showed some increase in maximum polarisation (P_{Max}) with La content, matching the greater observed variation in room temperature permittivity for these samples.

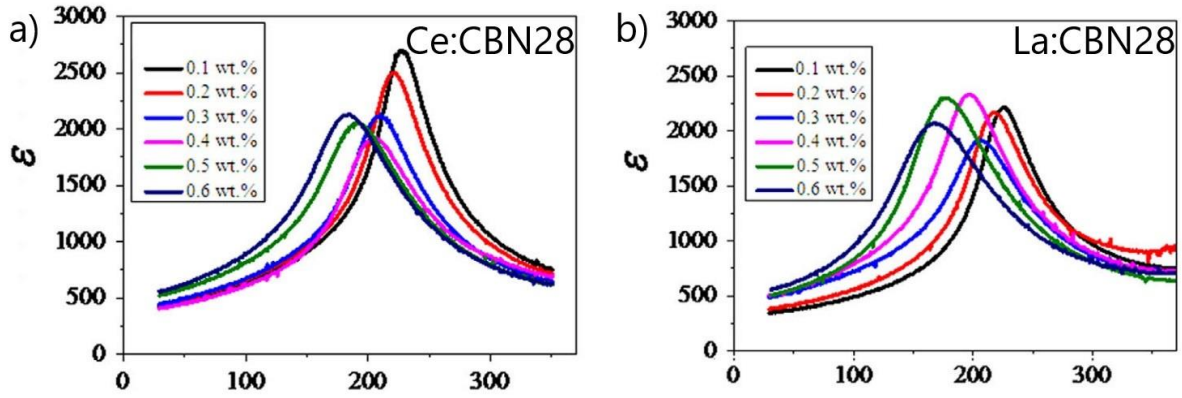

Figure 34. The permittivity-temperature responses of CBN28 ceramics, sintered at for 4 h at 1330-1350 ^{o}C, with the addition of 0.1 to 0.6 wt.% CeO_2, in (a), and La_2O_3, in (b). Taken from [Wei, L. 2014-May].

4.6.4 Acceptor A site doping

The inclusion of Na^+ and K^+, according to the nominal formulas $(Ca_{0.28}Ba_{0.72})_{2.5-0.5x}Na_xNb_5O_{15}$ ($0 \leq x \leq 1.0$) and $(Ca_{0.28}Ba_{0.72})_{2.5-0.5x}K_xNb_5O_{15}$ ($0 \leq x \leq 0.6$), produced single-phase unfilled TBs with presumed lower levels of A site vacancies and a nominally filled TB in Na doped CBN (x = 1.0) [Yang, B. 2015-May] and [Yang, B. 2015-Dec]. Co-doping with Na and K was also performed, according to the formula $(Ca_{0.28}Ba_{0.72})_{2.5-0.5x}(Na_{0.5}K_{0.5})_xNb_5O_{15}$ ($0 \leq x \leq 0.4$) [Yang, B. 2016].

With increasing Na content, from x = 0 to x = 1.0, T_C increased linearly, from ~250 to 350 ^{o}C. The ε_r-Max, measured at 100 kHz, varied only slightly from x = 0.2 to x = 0.8 (ε_r-Max = ~2500 to ~2300), but did increase at lower frequencies [Yang, B. 2015-May]. This low frequency increase in ε_r-Max

coincided with high-temperature, low-frequency dielectric loss peaks, see Figure 35(a). High bulk conductivity at high temperature, possibly due to the movement of oxygen vacancies or other charge carrying defects up to structural (grain) boundaries may have caused these effects. The volatile loss of Na and K (oxides) is known to promote vacancy defects in perovskites and TBs and may explain these observed features [Ketchum, J. L. 1983]. A discontinuation in the trends of increasing T_C, P_r and measured density was observed when transitioning from an unfilled (x = 0.8) to a filled (x = 1.0) TB.

Similar trends in T_C and P_r were observed when doping with increasing levels of K^+, from x = 0 to x = 0.6. The ε_r-Max remained relatively constant, varying from ~1700 to ~1900 [Yang, B. 2015-Dec], see Figure 35(b). High-temperature, low frequency tan δ peaks were also observed, but these were less severe than in the high Na content CBN. Low temperature ($T < T_C$), frequency dispersed tan δ peaks were more pronounced. These peaks increase in magnitude with increasing frequency. However, no frequency variation of T_C was observed.

In Na and K co-doped CBN, T_C increased to ~300 ^oC with increasing x, up to x = 0.3. Sample x = 0.4 showed apparent high-temperature bulk conductivity, similar to that seen in solely Na doped CBN [Yang, B. 2016]. For the non-lossy samples ($0 \leq x \leq 0.3$) ε_r-Max increased slightly from ~1700 to ~2000 with increasing Na and K content, See Figure 35(c). Notably some frequency dispersion of permittivity was observed, with the ε_r-Max of sample x = 0.3 varying from ~1700 to ~2200 as frequency decreased from 1000 to 1 kHz. This frequency dependence of ε_r did not extend to any significant frequency dependence of T_C, with T_C increasing by < 5 °C as frequency decreased from 1000 to 1 kHz.

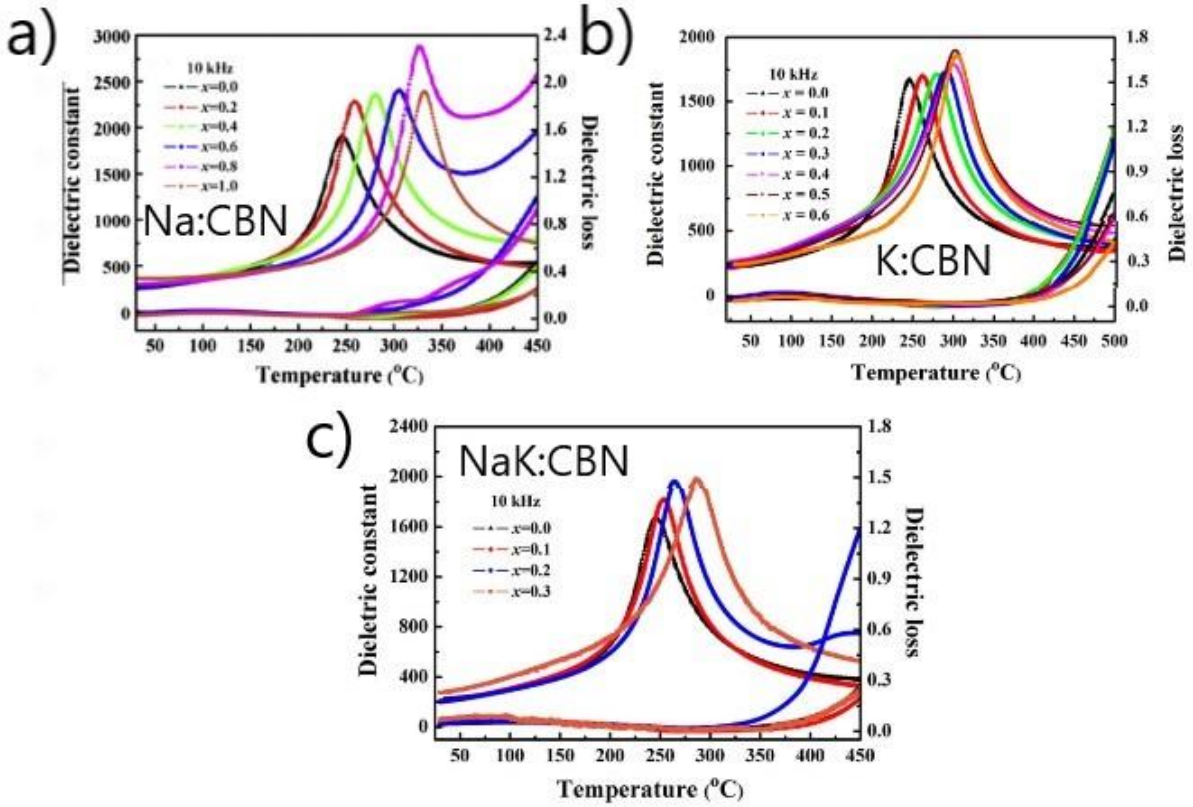

Figure 35. Permittivity- and tan δ- temperature responses for; (a) $(Ca_{0.28}Ba_{0.72})_{2.5-0.5x}Na_xNb_5O_{15}$ ($0 \leq x \leq 1.0$), (b) $(Ca_{0.28}Ba_{0.72})_{2.5-0.5x}K_xNb_5O_{15}$ ($0 \leq x \leq 0.6$) and (c) $(Ca_{0.28}Ba_{0.72})_{2.5-0.5x}(Na_{0.5}K_{0.5})_xNb_5O_{15}$ ($0 \leq x \leq 0.4$) ceramics, measured at 10 kHz. Taken and compiled from; (a) [Yang, B. 2015-May], (b) [Yang, B. 2015-Dec] and (c) [Yang, B. 2016].

4.6.5 Acceptor A site and isovalent B site co-doping

Na doped CBN was modified with increasing levels of Ta^{5+} and Sb^{5+} according to the formulas $(Ca_{0.28}Ba_{0.72})_{2.1}Na_{0.8}Nb_{5-x}Sb_xO_{15}$ (CBNNS) and $(Ca_{0.28}Ba_{0.72})_{2.1}Na_{0.8}Nb_{5-y}Ta_yO_{15}$ (CBNNT). It should be noted that Sb is considered toxic.

The Sb inclusion reduced T_C, from ~330 to ~200 °C when increasing x from 0.0 to 0.4, with x = 0.4 showing some frequency dispersion of permittivity below T_C. For samples ($0.6 \leq x \leq 1.0$), ε_r-Max was frequency dispersed and T_M decreased to a low of ~30 °C (measured at 10 kHz) when further increasing Sb content up to x = 1.0. Frequency dispersion of permittivity increased along with increasing $T < T_M$ tan δ peak frequency dispersion. The modified Curie-Wiess law ϒ coefficient for these samples increased from 1.64 to 1.99 as x increased from 0.0 to 1.0. The ϒ coefficient compares the rate of decrease in ε_r at temperatures just above T_M and correlates this to the diffusivity of the phase transition, with typical values varying between 1 and 2 (or sometimes greater than 2). The Sb modified CBN (x = 1.0) showed near temperature stable permittivity over a very wide temperature

range (ε_r = ~820 ±15 % from ~-90 to ~180 ^{o}C, when measured at 10 kHz), See Figure 36(a). Residual polarisations and P_{Max} values decreased significantly when increasing Sb levels from x = 0 to x = 0.8 [Yang, B. 2018].

The Ta inclusion, nominally on the B site, significantly reduced T_C, from ~330 ^{o}C for (x = 0.0) to ~140 ^{o}C for (x = 1.0), see Figure 36(b). Permittivity peak diffusivity and ε_r-Max remained comparable, and no frequency dependence of T_C was found. Residual polarisations and P_{Max} values remained consistent when increasing x from 0.0 to 0.8. At x = 1.0 a slight increase in P_{Max} and a more lossy hysteresis loop was reported [Yang, B. 2018].

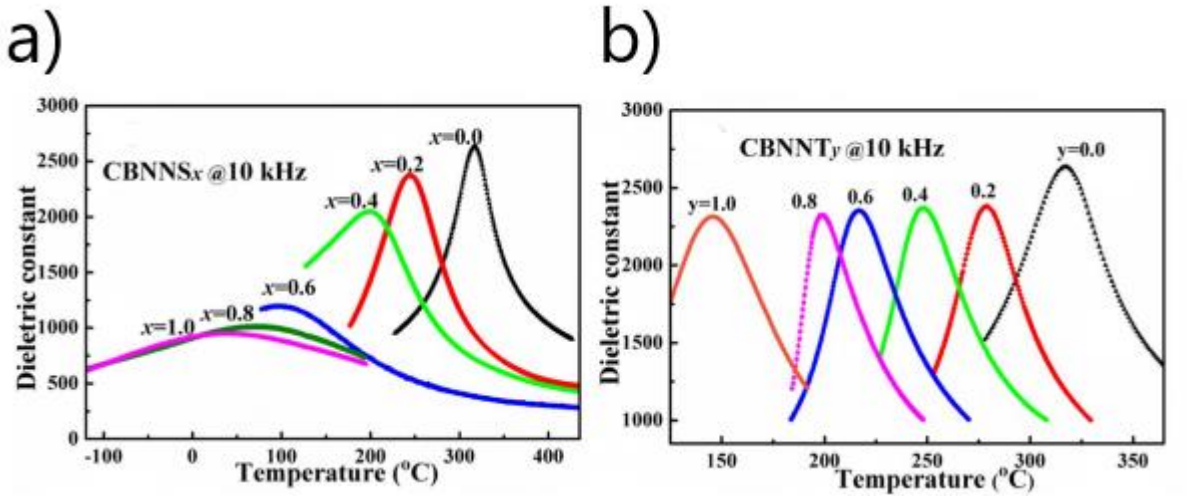

Figure 36. Permittivity-temperature responses for $(Ca_{0.28}Ba_{0.72})_{2.1}Na_{0.8}Nb_{5-x}Sb_xO_{15}$ (CBNNS) and $(Ca_{0.28}Ba_{0.72})_{2.1}Na_{0.8}Nb_{5-y}Ta_yO_{15}$ (CBNNT) ceramics, measured at 10 kHz. Taken from [Yang, B. 2018].

4.7 Recent work

Since the beginning of this PhD project (2019), there has been some shift in the focus of TB research. Increasing attention is being directed towards energy storage and pulsed power, for potential power electronics (i.e. electric vehicle) applications. For these applications relaxor-like polarisation responses are desired (high P_{Max} and very low P_r) alongside very high electrical breakdown strengths and good thermal and cycle (fatigue) stability. In energy storage devices which include ceramic dielectric material, it can be desirable to operate at $T_{C/M} < T < T_B$, where spontaneous polarisation is present but more transient (lower P_r) than when operating under conditions associated with larger ferroelectric domains ($T < T_C$). As such, doping is commonly employed as it has the potential to modify T_C (i.e. to below room or operating temperature) and promote the occurrence of smaller length-scale polar units (with low coercive fields), thus allowing for increased energy recovery.

The co-doping of SBN with Ca, assumed to substitute on the A sites or A1 site, and Ta, assumed to substitute on the B site, was performed [Hou, S. 2022]. Single phase samples with nominal formulations of $Ca_{0.15}(Sr_{0.6}Ba_{0.4})_{0.85}Nb_{2-x}Ta_xO_6$ ($0.0 \leq x \leq 1.2$) were produced by sintering at 1320 °C. For the composition $Ca_{0.15}(Sr_{0.6}Ba_{0.4})_{0.85}Nb_{1.4}Ta_{0.6}O_6$, reasonable energy recovery (1.42 J cm^{-3}) and good efficiency (81.9 %) were reported alongside improved temperature stability of permittivity [Hou, S. 2022].

Very recent donor doping of CBN was achieved by substituting Ca^{2+} with Bi^{3+}, $Pr^{3+ (or\ 4+)}$, Nd^{3+} or Sm^{3+}, with vacancy content increased to ensure charge balance. A series of single phase (by XRD) samples were produced by sintering at 1220 - 1280 °C. They had relatively high dopant levels, R = 0.08, in the formula $Ca_{0.16}R_{0.08}Ba_{0.72}Nb_2O_6$, where R = Bi, Pr, Nd, Sm (or R* = 0.2 when using the $Ca_{0.4}R^*_{0.2}Ba_{1.8}Nb_5O_{15}$ nomenclature).

The permittivity-temperature responses of the samples showed pronounced frequency dependence of permittivity and reduced T_M, to below 150 °C. To varying degrees, a low temperature phase transition, which is not known to have been observed elsewhere, can also be seen at ~-10 °C, in Figure 37.

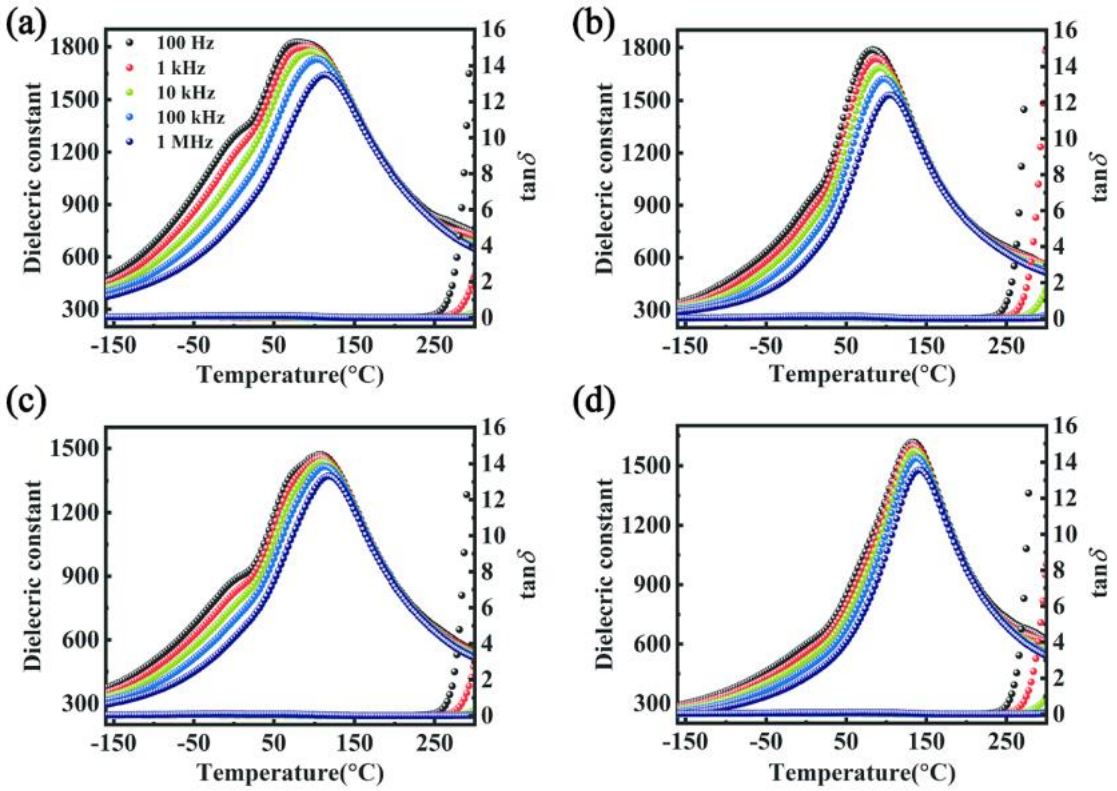

Figure 37. Permittivity- and tan δ- temperature profiles for $Ca_{0.16}R_{0.08}Ba_{0.72}Nb_2O_6$ ceramics, where R = Bi, Pr, Nd, Sm respectively in (a), (b), (c) and (d). Taken from [Cao, L. 2024].

In these samples, strong frequency dependence of permittivity accompanied narrow P-E loops, which allowed for energy recovery efficiencies (η) of 85.3 % in the Pr doped sample, which also showed good total energy recovery (2.59 J cm^{-3}) plus very high dielectric breakdown strengths (> 300 kV cm^{-1}). The polarisation response was also stable (±10 %) from 25 to 160 °C (decreasing from 12.8 to 11.6 µC cm^{-2}). This energy storage performance is comparable to some other TB based materials, see Figure 38.

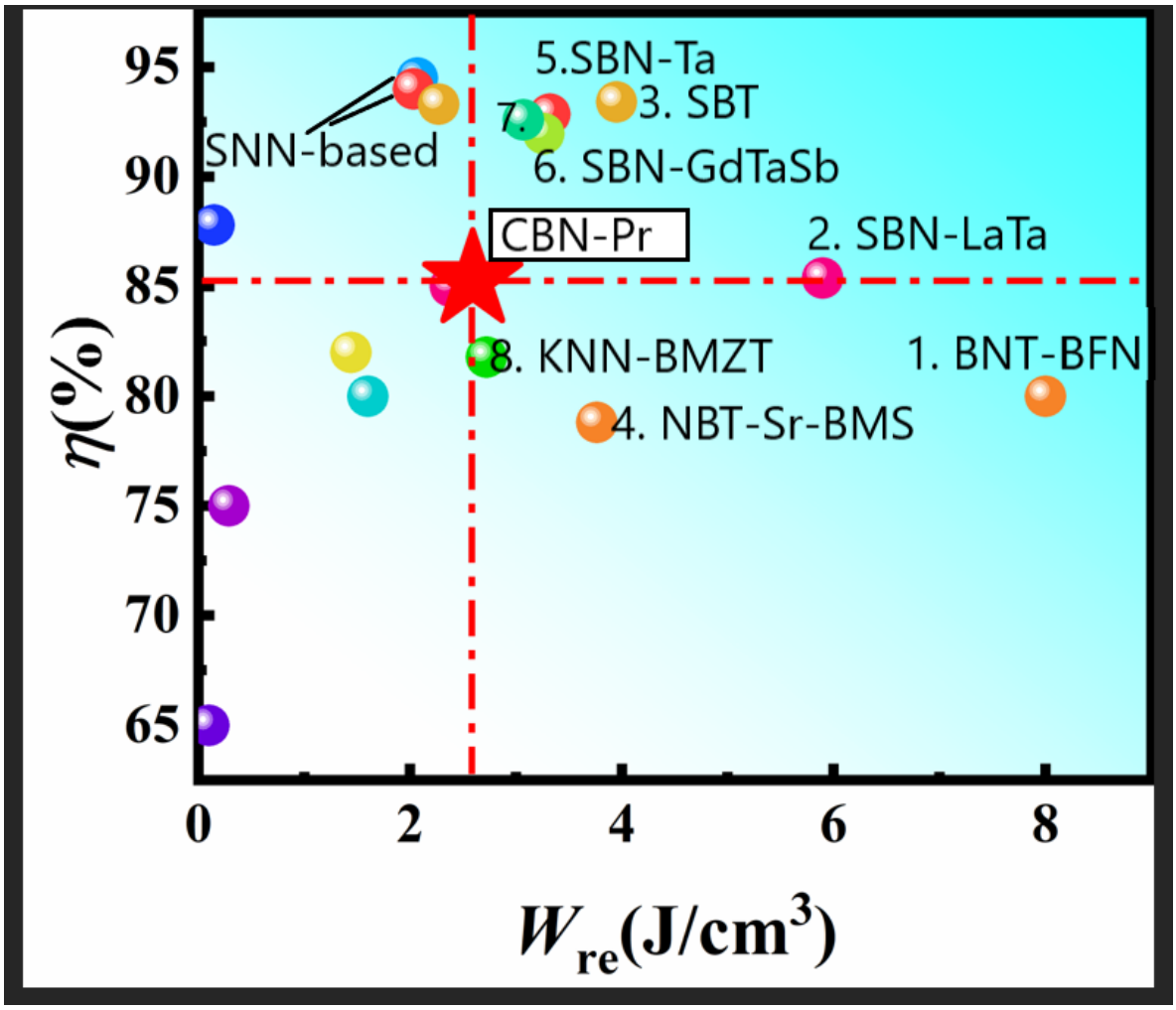

Figure 38. A comparison of the energy recovery efficiency (η) and the total recoverable energy (W_{re}) for Pr doped CBN ($Ca_{0.16}Pr_{0.08}Ba_{0.72}Nb_2O_6$) in comparison to other lead-free perovskite and TB materials, including doped formulations of the following base materials; CBN, SBN, SNN, BNN, potassium sodiun niobate (KNN), sodium bismuth titinate (NBT) and strontium barium titanate (SBT). Taken and adapted from the supplementary information from [Cao, L. 2024].

4.8 Summary of CBN chemical modification

A variety of dopants and styles of doping have been employed to modify the electrical properties of CBN28. With respect to improving the temperature stability of permittivity, donor doping of the A sites shows promise by consistently broadening permittivity peaks whilst also decreasing $T_{C/M}$. High level donor doping also induced strong frequency dependence of permittivity. Acceptor doping, with volatile compounds, appeared to exacerbate the high temperature dielectric losses to which CBN is prone. Whilst less well studied, combined A and B site doping produced the greatest range of near temperature stable permittivity in a CBN based ceramic, in the composition $(Ca_{0.28}Ba_{0.72})_{2.1}Na_{0.8}Nb_{4.2}Sb_{0.8}O_{15}$. Experimental donor doping of CBN28 will be explored in the next Chapter.

4.9 References

Abdelli, F. Boudaya, C. Khemakhem, H. 2016. Microstructure, X-ray diffraction, dielectric and Raman spectroscopy studies of $Ca_xSr_yBa_{1-(y+x)}Nb_2O_6$ ceramics. *J. Alloys Compd*. **683**. 282-291

DOI: https://doi.org/10.1016/j.jallcom.2016.04.189

Beanland, R. Harrison, L. Khan, S. Brown, T. Roncal-Herrero, T. Peirson, H. Milne, S. J. 2023. Temperature dependence of incommensurate modulation in $Ca_{0.28}Ba_{0.72}Nb_2O_6$. *J. App. Phys*. **134**. 064101

DOI: https://doi.org/10.1063/5.0157636

Cao, L. Wang, Y. Yuan, Y. Zhu, J. Barzegar-Bafrooei, H. Mao, M. Liu, B. Li, H. Wang, D. Lu, Z. Wang, G. Song, K. 2024. Low temperature relaxor, polarization dynamics and energy storage properties of $Ca_{0.28}Ba_{0.72}Nb_2O_6$ tungsten bronze ceramics. *J. Chem. Eng*. **479**. 147664

DOI: https://doi.org/10.1016/j.cej.2023.147664

Di, J. Xu, X. Xia, C. Zhou, D. Sai, Q. Xu, J. 2014. Growth and spectral properties of Yb:$Ca_{0.28}Ba_{0.72}Nb_2O_6$ disordered crystal. *Optik*. **125**. 6620-6624

DOI: https://doi.org/10.1016/j.ijleo.2014.08.115

Eßer, M. Burianek, M. Klimm, D. Mühlberg, M. 2002. Single crystal growth of the tetragonal tungsten bronze $Ca_xBa1_{-x}Nb2O6$ (x=0.28; CBN-28). *J. Cryst. Growth*. **240**. 1-5

DOI: https://doi.org/10.1016/S0022-0248(02)00868-0

Eßer, M. Burianek, M. Held, P. Stade, J. Bulut, S. Wickleder, C. Mühlberg, M. 2003. Optical characterization and crystal structure of the novel bronzetype $Ca_xBa_{1-x}Nb_2O_6$ (x = 0.28; CBN-28). *Cryst. Res. Technol*. **38**. 457-464

DOI: https://doi.org/10.1002/crat.200310057

Gao, W. L. Zhang, H J. Xia, S. Q. Huang, B. B. liu, D. Wang, J Y. Jiang, M. H. Zheng, L. M. Wang, J. F. Lu, C. J. 2010. Effect of doping with Nd^{3+} ions on the structural and ferroelectric properties of $Ca_{0.28}Ba_{0.72}Nb_2O_6$ single crystal *Mat. Res. Bull*. **45**. 1209-1212

DOI: https://doi.org/10.1016/j.materresbull.2010.05.024

Graetsch, H. A. Schreuer, J. Burianek, M. Mühlberg, M. 2012. Thermally induced structural changes in incommensurate calcium barium niobate $Ca_{0.28}Ba_{0.72}Nb_2O_6$ (CBN28). *J. Solid State Chem*. **196**. 255-266

DOI: https://doi.org/10.1016/j.jssc.2012.06.028

Han, X. Wei, L. Yang, Z. Zhang, T. 2013. Phase formation, dielectric and ferroelectric properties of $Ca_xBa_{1-x}Nb_2O_6$ ceramics. *Ceram. Int*. **39**. 4853-4860

DOI: https://doi.org/10.1016/j.ceramint.2012.11.078

Hou, S. Xu, S. Yang, L. Liu, X. Wei, L. Chao, X. Wu, Di. Liang, P. Yang, Z. 2022. High energy storage performance of $Ca_{0.15}(Sr_{0.6}Ba_{0.4})_{0.85}Nb_{2-x}Ta_xO_6$ relaxor ferroelectric ceramics. *Ceram. Int*. **48**. 28382-28390

DOI: https://doi.org/10.1016/j.ceramint.2022.06.148

Ismailzade, I. G. 1960. *Title missing*. *Kristallografiya*. **5**. 316–317

DOI: *missing*

Ke, S. Fan, H. Huang, H. Chan, H L W. Yu, S. 2008. Dielectric, Ferroelectric properties, and grain growth of $Ca_xBa_{1-x}Nb_2O_6$ ceramics with tungsten bronzes structure. *J. Appl. Phys*. **104**. 024101

DOI: https://doi.org/10.1063/1.2956615

Ketchum, J. L. Sweeney, K. L. Halliburton, L. E. Armington, A. F. 1983. Vacuum annealing effects in lithium niobate. *Phys. Lett. A.* 1983. **94**. 450-453

DOI: https://doi.org/10.1016/0375-9601(83)90852-6

Krayzman, V. Bosak, A. Playford, H. Y. Ravel, B. Levin, I. 2022. Incommensurate modulation and competing ferroelectric/antiferroelectric modes in tetragonal tungsten bronzes. *Chem. Mater*. **34**. 9989-10002

DOI: https://doi.org/10.1021/acs.chemmater.2c02367

Lin, P. J. Bursill, L. A. 1987. Superlattice structure of ferroelectric barium sodium niobate (BNN). Acta Cryst. B**43**. 504-512

DOI: https://doi.org/10.1107/S0108768187097416

Lu, C. J. Qi, Y. J. 2006. Incommensurate modulation structure in ferroelectric $Ca_{0.28}Ba_{0.72}Nb_2O_6$ single crystals of tungsten bronze structure. *Appl. Phys. Lett*. **89**. 191901

DOI: https://doi.org/10.1063/1.2364840

Malyshikna, O. Ivanova, A. Malyshkin, Y. Folomeeva, A. Shashkov, M. Dec, J. 2017. Effect of Ca, Sr and Ba distribution on the relaxor properties of CSBN single crystals. *Ferroelectrics*. **511**. 76-81

DOI: https://doi.org/10.1080/00150193.2017.1334183

Muehlberg, M. Burianek, M. Joschko, B. Klimm, D. Danilewsky, A. Gelissen, M. Bayarjargal, L. Görler, G. P. Hildmann, B. O. 2008. Phase equilibria, crystal growth and characterization of the novel ferroelectric tungsten bronzes $Ca_xBa_{1-x}Nb_2O_6$ (CBN) and $Ca_xSr_yBa_{1-x-y}Nb_2O_6$ (CSBN). *J. Cryst. growth*. **310**. 2288-2294

DOI: https://doi.org/10.1016/j.jcrysgro.2007.12.023

Niemer, A. Pankrath, R. Betzler, K. Burianek, M. Muehlberg, M. 2012. Dielectric Properties and the Phase Transition of Pure and Cerium Doped Calcium-Barium-Niobate. *World J. Condens. Matter Phys*. **2**. 80-84

DOI: https://doi.org/10.4236/wjcmp.2012.22014

Trubelja, M. P. Ryba, E. Smith, D. K. 1996. A study of positional disorder in strontium barium niobate. *J. Mater. Sci*. **31**. 1435-1443

DOI: https://doi.org/10.1007/BF00357850

Wei, L. Yang, Z. Chao, X. Jiao, H. 2014-May. Structure and electrical properties of $Ca_{0.28}Ba_{0.72}Nb_2O_6$ ceramics with addition of rare earth oxides (CeO_2, La_2O_3). *Ceram. Int*. **40**. 5447-5453

DOI: http://dx.doi.org/10.1016/j.ceramint.2013.10.130

Wei, L. Han, X. Chao, X. Jiao, H. Yang, Z. 2014-Feb. Study on low temperature sintering and electrical properties of CuO-doped $Ca_{0.28}Ba_{0.72}Nb_2O_6$ ceramic. *J. Mater. Sci. Mater. El*. **25**. 1605-1611

DOI: https://doi.org/10.1007/s10854-014-1756-y

Yang, B. Hao, S. Yang, P. Wei, L. Yang, Z. 2018. Relaxor behavior and energy storage density induced by B-sites substitutions in $(Ca_{0.28}Ba_{0.72})_{2.1}Na_{0.8}Nb_5O_{15}$ Tungsten bronze ceramics. *Ceram. Int*. **44**. 8832-8841

DOI: http://dx.doi.org/10.1016/j.ceramint.2018.02.065

Yang, B. Wei, L. Chao, X. Wang, Z. Yang, Z. 2015-May. Role of structural modulation in electrical properties of tungsten bronze $(Ca_{0.28}Ba_{0.72})_{2.5-0.5x}Na_xNb_5O_{15}$ ceramics. *J. Alloys Compd*. **632**. 368-375

DOI: https://doi.org/10.1016/j.jallcom.2015.01.247

Yang, B. Wei, L. Wang, Z. Kang, S. Chao, X. Yang, Z. 2016. Electrical Characterization Induced by Structural Modulation in $(Ca_{0.28}Ba_{0.72})_{2.5-0.5x}(Na_{0.5}K_{0.5})_xNb_5O_{15}$ Ceramics. *J. Electron. Mater.* **45**. 104-115

DOI: https://doi.org/10.1007/s11664-015-4157-y

Yang, B. Yang, P. Wei, L. Wang, Z. Yang, Z(henyu). Chao, X. Yang, Z(upei). 2015-Dec. Structural modulation and electrical properties in ferroelectric niobates $(Ca_{0.28}Ba_{0.72})_{2.5-0.5x}K_xNb_5O_{15}$ ($0.0 \leq x \leq 0.6$) ceramics. *Ceram. Int*. **41**. 13988-13997

DOI: https://doi.org/10.1016/j.ceramint.2015.07.011

Zhao, J-H. Zhang, H-X. Yi, L-L. Guo, G-T. Guan, J. 2018. The properties of planar Na:CBN waveguide with “well” + “barrier” type by multiple energy helium ion implantation. *Nucl. Instrum. Methods Phys. Res. B*. **435**. 331-335

DOI: https://doi.org/10.1016/j.nimb.2018.08.012

5. Results 1: Grain evolution of $Ca_{0.28}Ba_{0.72}Nb_2O_6$ (CBN28) and chemical modification with yttrium and tantalum

5.1 Summary

This chapter initially concerns the grain evolution of $Ca_{0.28}Ba_{0.72}Nb_2O_6$ (CBN28) ceramics sintered at increasing temperature above 1300 °C, and the sensitivity of CBN28's permittivity and dielectric loss to thermal processing. Also examined is the induction of temperature stable permittivity in the $(Ca_{0.28}Ba_{0.72})_{1-3w/2}Y_wNb_2O_6$ [$0 \leq w \leq 0.20$] system with increasing Y and (assumed) A site vacancy content, and the induction of strong frequency dependence of permittivity in Y, (assumed) A site vacancy and Ta modified $(Ca_xBa_{1-x})_{1-3w/2}Y_wNb_{1.8}Ta_{0.2}O_6$ [x = 0.28, w = 0.02 and 0.04] (CBN) ceramics.

CBN28 ceramics were produced by calcining for 20 h at 1200 ^oC and sintering for 4 or 6 h at 1300 to 1400 ^oC. Measured density remained relatively constant (98 - 96 %), when sintering for 4 h at 1325 to 1400 ^oC. High-temperature, low-frequency dielectric losses were observed in this long calcined CBN28 when sintered at and below 1350 ^oC. Cyclical heating, to 400 and 300 ^oC, reduced but did not remove these losses. Such losses were less present in CBN28 which was calcined for only 4 h.

A significant increase in ε_r-Max, from 2520 to 3420, was observed when increasing sinter temperature from 1375 to 1400 ^oC. The origin of this permittivity increase could not be identified from the grain morphologies or XRD-derived lattice parameters, which differed only marginally.

The $(Ca_{0.28}Ba_{0.72})_{1-3w/2}Y_wNb_2O_6$ [$0.01 \leq w \leq 0.20$] system was single phase up to yttrium additions of w = 0.04, with Rietveld refinement-derived theoretical densities decreasing slightly from 5.31 g cm^{-3} to 5.28 g cm^{-3}, for CBN28 to w = 0.04, due to vacancy inclusion. This density decrease occurred despite a contraction in the c-axis, from 7.90 Å to 7.88 Å, causing a reduction in unit cell volume across this composition range. A slight transition in ferroelectric character and a large increase in the temperature-stability of permittivity was observed between w = 0.02 (ε_r = 2055 ±15 % from 166 to 211 ^oC) and w = 0.04 (ε_r = 1143 ±15 % from 71 to 210 ^oC), with the latter exhibiting weak relaxor behaviour, characterised by slight frequency variation of T_M, which ranged from 146 to 151 ^oC, when measured between 1 and 1000 kHz. Permittivity peak suppression increased up to w = 0.20 (ε_r = 470 ±15 % from -38 to 208 ^oC), with modified Curie-Weiss law ϒ coefficients increasing from CBN28 (1.73) to w = 0.10 (2.11).

A slight reduction in ferroelectric character was also observed in the P-E responses, with w = 0.04 possessing a narrower hysteresis loop and lower P_r (1.5 µC cm^{-2}) than w = 0.02 (2.3 µC cm^{-2}) and CBN28 (2.4 µC cm^{-2}), under a maximum applied field of 30 kV cm^{-1}. Disruption to polar ordering was

also evidenced by the P-E response-derived Rayleigh coefficients which showed a reduction in the field-dependant domain wall contributions to ε_r' and ε_r'', with increasing Y and vacancy content. Secondary phases, primarily $CaNb_2O_6$, were present at higher Y levels ($w \geq 0.05$). The composition was then modified to only substitute-out Ca for Y ($Y_rCa_{0.28-3r/2}Ba_{0.72}Nb_2O_6$). In the modified composition, secondary phase $CaNb_2O_6$ content remained absent at low Y levels ($r < 0.05$) and was significantly reduced at $r = 0.05$.

Three CBNs, with Y additions, (assumed) A-site vacancy and Ta modification, $(Ca_xBa_{1-x})_{1-3w/2}Y_wNb_{1.8}Ta_{0.2}O_6$ [$x = 0.28$, $w = 0.02$ and 0.04] and [$x = 0.22$, $w = 0.04$], were produced with comparable densities (95 to 96 %). They expressed strong frequency dependence of permittivity, with T_M varying (when measured at 1 and 1000 kHz) from 91 to 103 ^oC for [$x = 0.28$, $w = 0.02$, Ta = 0.20] (ε_r = 1482 ±15 % from 46 to 144 ^oC). The substitution of Ta for Nb also decreased T_M whilst appearing to have only a minor influence on the Y and vacancy induced transition to permittivity-temperature stability. Ceramic sample $x = 0.28$, $w = 0.04$, Ta = 0.20 (ε_r = 954 ±15 % from -58 to 110 ^oC) contained secondary phases, which were absent when reducing the Ca:Ba ratio ([$x = 0.22$, $w = 0.04$, Ta = 0.20] (ε_r = 972 ±15 % from -9 to 166 ^oC)). Overall, modified CBN shows promise for potential electronics applications achieving temperature stable permittivity (±15 %) over wide temperature ranges and narrow P-E loops, with the maximum temperature of stable permittivity being tailorable by Ca:Ba ratio.

5.2 Grain evolution of $Ca_{0.28}Ba_{0.72}Nb_2O_6$

An understanding of the effects of thermal processing on the density and microstructure of ferroelectrics allows for the optimisation of dielectric properties. High densities (> 95 %) and fine grain sizes (~1 μm) and so finer domain sizes allow for increased permittivity [Jiang, B. 2019] and [Kittel, C. 1946]. A fine-grained uniform microstructure may also reduce conductive losses and increase dielectric breakdown strengths [Cao, L. 2024] and [Hou, S. 2022].

Sinter temperature (1300 - 1400 °C) and time (4 or 6 h) were varied with a view to understanding the sensitivity of CBN28's microstructure to thermal processing. These experiments chronologically followed the Y doping of CBN28, in Section 5.3. Secondary phases were sometimes identified in those samples, which were calcined for 4 h prior to sintering. As such a prolonged calcination, of 20 h, was employed here to minimise any effects of secondary phase presence during sintering.

5.2.1 Microstructure and density

Ceramics of composition $Ca_{0.28}Ba_{0.72}Nb_2O_6$ were calcined at 1200 ^oC for 20 h then sintered at 1300 - 1400 ^oC for either 4 or 6 h respectively. Measured ceramic densities were recorded in relation to maximum theoretical density, which was calculated from XRD data, presented in Figure 39 and

summarised in Table 6. Scanning electron micrographs show the microstructure of the sintered ceramics in Figures 40 and 41. Grain-size distributions, taken from a 100-grain sample, are shown for all samples in Figure 42 and the permittivity-temperature responses of CBN28 ceramics sintered for 4 h at 1325 - 1400 ^{o}C are shown in Figure 43. The CBN28 samples in this sub-chapter are abbreviated according to the sinter conditions, which ranged from 1300 - 1400 ^{o}C and 4-6 h, for example "1300/4" is where CBN28 has been sintered at 1300 ^{o}C for 4 h.

XRD diffraction patterns of 1375/4 and 1400/4 are shown in Figure 39 and indexed against ICCD 05-001-0283. All detectable peaks can be ascribed to CBN. Table 6 details the results of a simple lattice parameter refinement, performed using Highscore software. For this refinement, lattice parameters were derived by indexing the measured CBN28 XRD peaks to a reference pattern for CBN28 (with known lattice parameters). Systematic differences between the measured and reference patterns, in terms of peak positions and relative intensities, are interpreted by the software as variations in lattice parameter. A reference ".CIF" file was imported from the Crystallographic Open Database in order to do this refinement. This XRD reference pattern file was taken from a CBN28 single-crystal journal publication [Graetsch, H. A. 2012-Dec].

In Table 6, R_{wp} "goodness of fit" values were comparable and low (< 5 %). A slight decrease in the *c* parameter, and so unit cell volume, resulted in the theoretical density increasing from 5.31 g cm^{-3} to 5.32 g cm^{-3} between 1375/4 and 1400/4. These values accord with those reported elsewhere for CBN28 (5.29-5.33) [Graetsch, H. A. 2012-Apr] and [Eßer, M. 2002]. For the comparison to measured geometrical densities, a theoretical density of 5.31 g cm^{-3} was assumed, in Figure 40(f) and 41(d). This value is consistent with the XRD derived ρ for sample 1375/4 and was also ascertained from a full pattern Rietveld refinement of a different CBN28 ceramic, whose thermal processing conditions are detailed in Section 5.3.1.

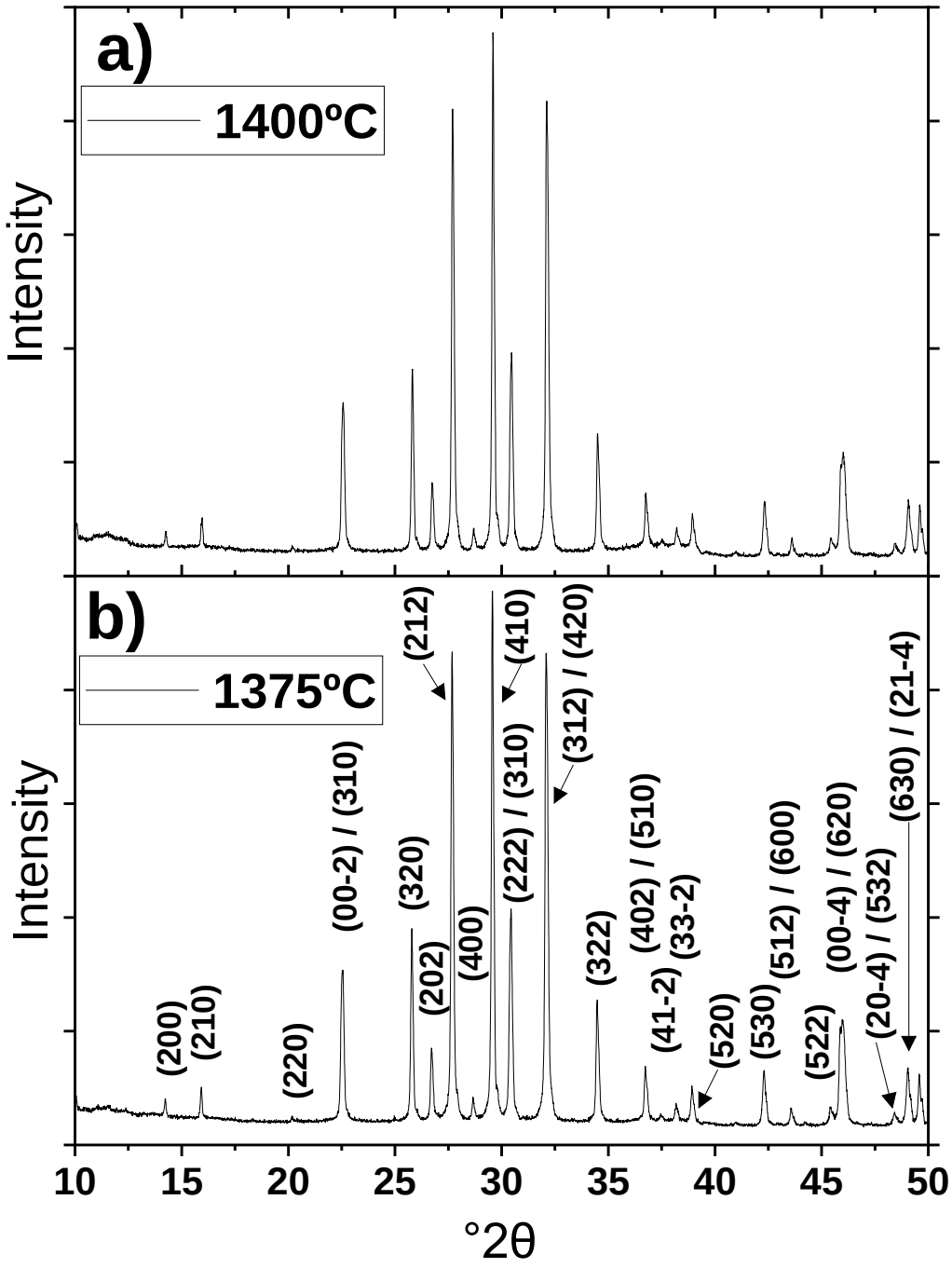

Figure 39. X-ray diffraction patterns of $Ca_{0.28}Ba_{0.72}Nb_2O_6$ crushed sintered pellets, calcined at 1200 ^oC for 20 h, sintered for 4 h at, (a), 1400 ^oC and, (b), 1375 ^oC. Indexed according to P4bm structure, ICCD 05-001-0283.

Table 6. Summary of (pseudo) tetragonal lattice parameters, R_{wp} "goodness of fit" and theoretical densities (ρ) from the unit cell refinement of $Ca_{0.28}Ba_{0.72}Nb_2O_6$ sintered for 4 h at 1375 and 1400 ^oC. Lattice parameter errors (in brackets) were provided by the Highscore software.

Sample Code	a (Å)	c (Å)	Volume ($Å^3$)	R_{wp} (%)	Theoretical ρ (g cm^{-3})
1375/4	12.45 (1)	7.90 (1)	1225.7	4.09	5.31
1400/4	12.45 (1)	7.89 (1)	1223.1	3.26	5.32

Measured densities and measured-density standard deviations are shown in Figure 40(f) and Figure 41(d), they were calculated via the geometric method from a minimum of 5 ceramic pellets. The lowest measured densities occurred in samples at either extreme of the thermal processing, 1300/4 (93 %) and 1400/6 (89 %), all other samples had densities between 94 and 98 % of the theoretical density. The highest measured density was achieved when sintering for 4 h at 1325 ^oC (98 %), density then decreased only slightly, to 96 %, as temperature increased to 1400 ^oC. Measured density for the 6 h-sintered samples peaked at 1300 ^oC (96 %) and decreased with increasing temperature to a low of 89 %. Measured-density standard deviations were relatively low, being < ±1 % of the theoretical density, except for sample 1325/4 which was ± ~2.5 %.

The line-intercept method was used to populate the grain size samples from polished SEM cross sections, see Figures 40 and 41. The furthest distance between grain boundaries was recorded from the polished SEM cross sections, from this "raw" data the maximum measured grain size for each sample was found. This value is likely to be an underestimation of the actual measured grain size, due to two factors; firstly the finite number of grain measured (100), and secondly the limitations of cross-sectional measurements (i.e. the measurement of grain segments that happen not to correspond to the largest section of the grain). This distribution of measured grain segments sizes (relative to the maximum segment size for each grain) infers a size distribution for the measured grains, this clouds the interpretation of grain size variation with sinter condition. The underestimation of grain sizes due to cross-sectional imaging has been modelled [Mendelson, M. I. 1969]. For nontextured grains with a normal size distribution, multiplication of the measured grain size by a factor of 1.56 gives the actual grain size. Using this factor the average calculated grain sizes for the samples was found. It should be noted that ant variation in grain size distributions for the samples may result from variations in grain morphology as well as actual variations in the size distributions of the grains.

Observing the 4 h-sintered samples, at 1300 ^{o}C (Figure 40(a)) the maximum measured grain size was 3.7 µm, with an average calculated grain size of ~3 µm. At 1325 ^{o}C (Figure 40(b)), some evidence of selective grain growth may be found in the wider grain-size distribution, when compared with samples 1300/4 and 1350/4, although the natural distribution of measured grain sizes that results from polished cross-section grain measurements reduces the validity of this assertion. Maximum measured grain size did increase to 9.4 µm for 1325/4. The average calculated grain size of ~6 µm for 1325/4 was comparable to that of 1375/4 and 1400/4, see Table 7.

Sample 1375/4 had the largest measured grains, with no evidence of grain pull out during polishing (which was present at lower sinter temperatures) but with some intra- and inter-granular cracks. A slight decrease in maximum grain size occurred between 1375/4 (10.0 µm) and 1400/4 (7.9 µm) whilst average calculated grain sizes were roughly comparable (~6 µm). Although, grain size measurements for 1400/4 may have been affected by the presence of extensive micro-cracking. Amorphous darker contrast spots in the micrographs of 1300/4 and 1350/4 (Figure 40(a) and (c)) are believed to be caused by contamination by the conductive paint used to prevent charging during the SEM session.

Average calculated grain size increased from ~3 µm to ~6 or ~5 µm respectively, when sintering at both 1300 and 1350 ^{o}C for longer (4 h vs 6 h), as can be seen in Figure 41 and Table 7. The maximum measured grain size of 1300/6 was significantly larger (8.7 µm) than 1300/4 (3.7 µm). Average calculated grain sizes for 1400/4 and 1400/6 where more comparable (~6 µm) although maximum measured grain size increased significantly with the increase in sinter time (7.9 µm and 14.0 µm, respectively). Assessment of grain size for 1400/6 was partially obscured by its appearance, which differed from the other samples in that grain boundaries were less well-defined, see Figure 41(c). In this micrograph, the contrast between the grains and grain boundaries was possibly reduced by the presence of two large (> 1 µm), and darkly contrasted, pores.

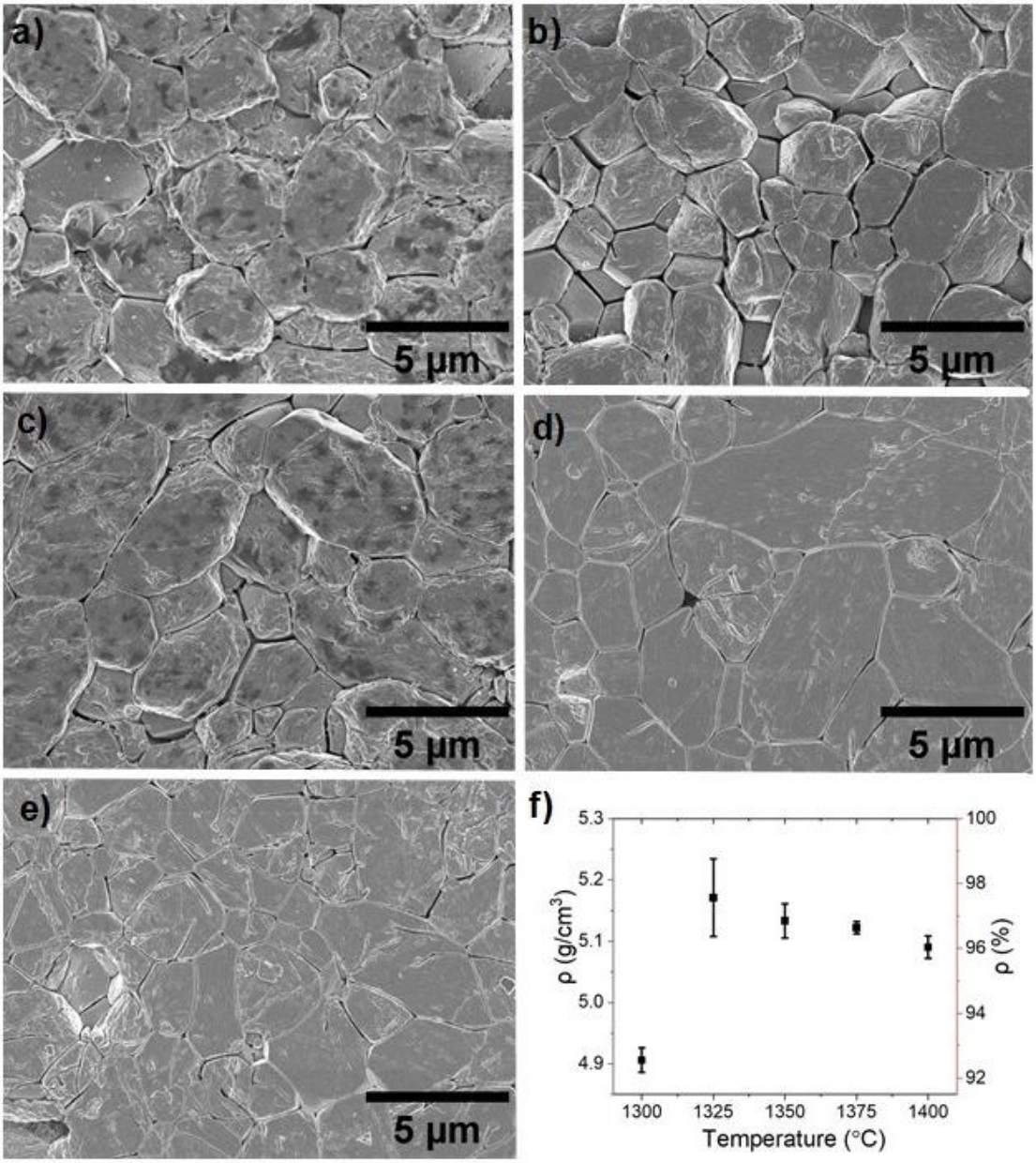

Figure 40. SEM secondary electron micrographs of $Ca_{0.28}Ba_{0.72}Nb_2O_6$ sintered for 4 h at; (a) 1300 ^{o}C, (b) 1325 ^{o}C, (c) 1350 ^{o}C, (d) 1375 ^{o}C, (e) 1400 ^{o}C, and (f) measured densities (g cm^{-3}), on the left-hand axis, and as a % of the theoretical density (5.31 g cm^{-3}), on the right-hand axis. Micrographs were taken at 5 kx magnification.

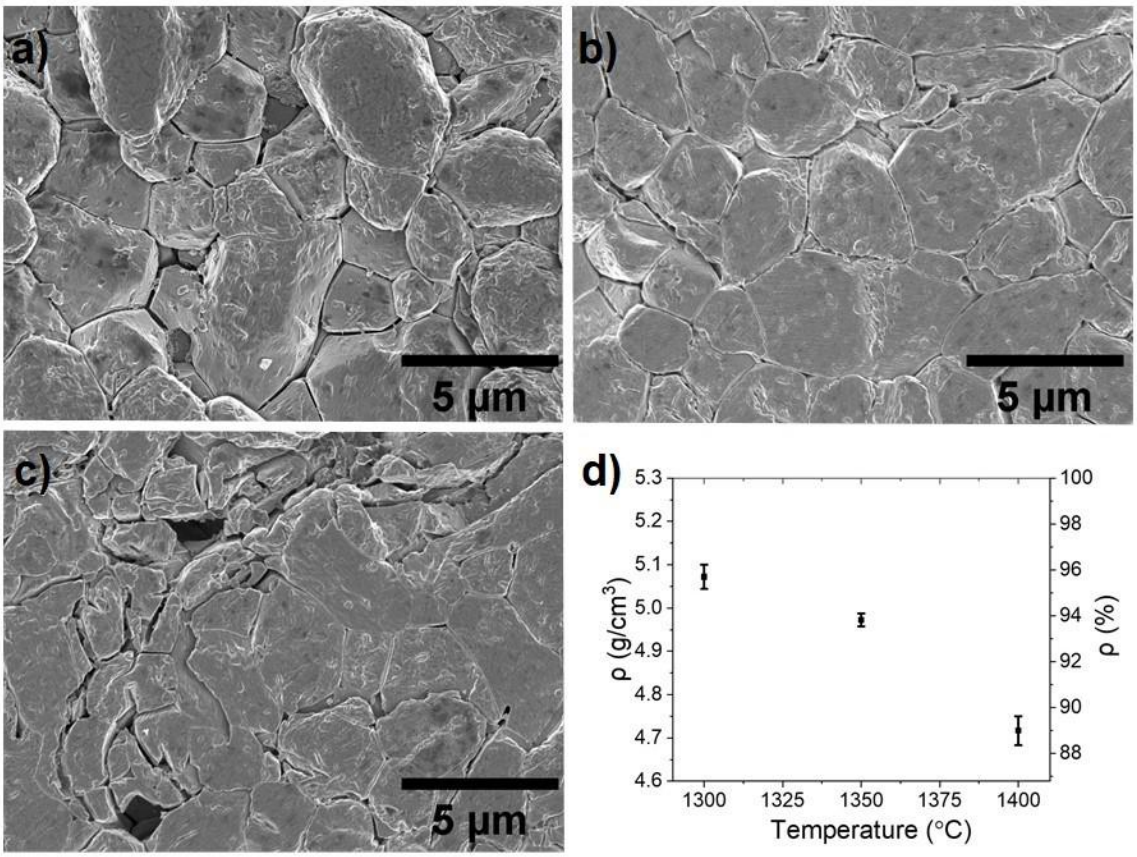

Figure 41. SEM secondary electron micrographs of $Ca_{0.28}Ba_{0.72}Nb_2O_6$ sintered for 6 h at; (a) 1300 ^{o}C, (b) 1350 ^{o}C, (c) 1400 ^{o}C and (d) measured density (g cm^{-3}), on the left-hand axis, and as a % of theoretical density (5.31 g cm^{-3}), on the right-hand axis. Micrographs were taken at 5 kx magnification.

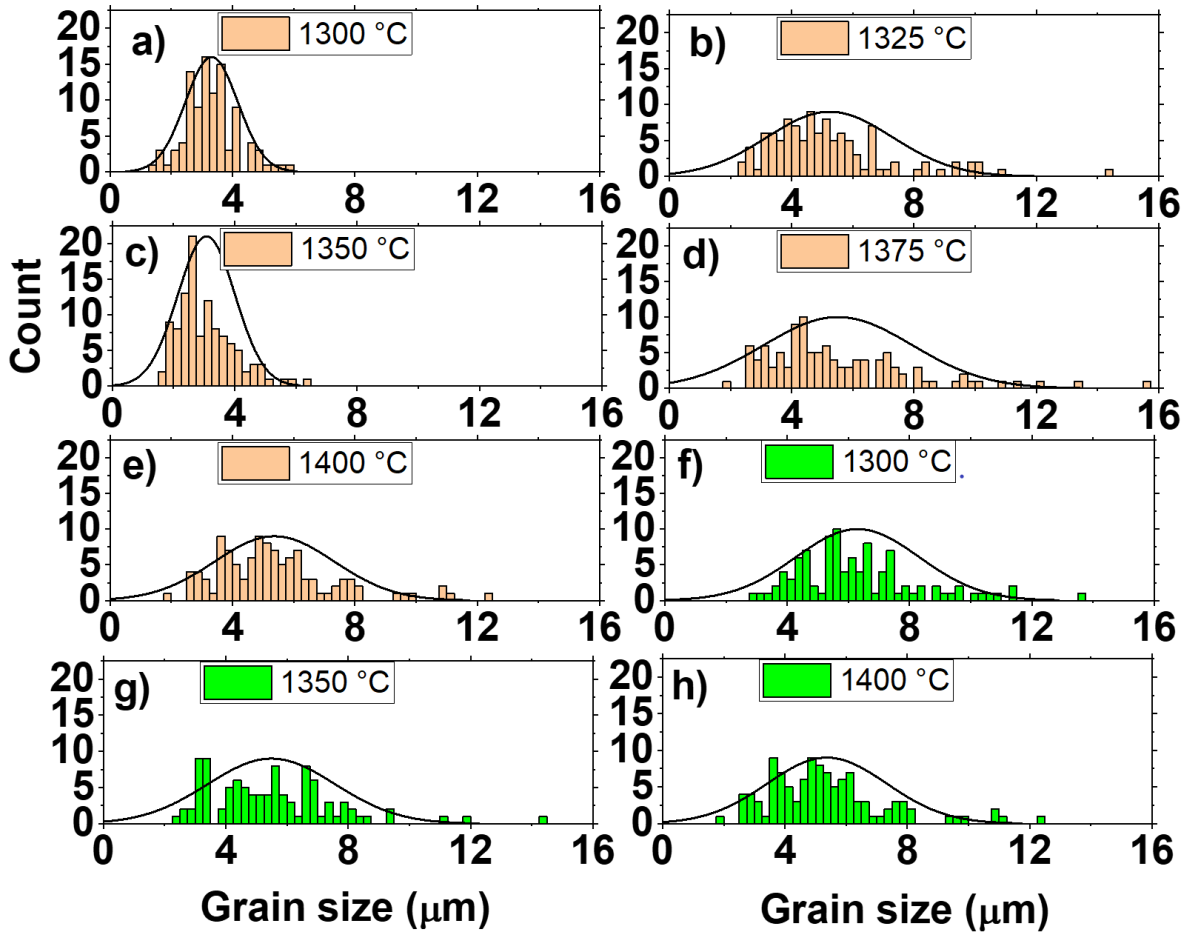

Figure 42. Grain size distributions for $Ca_{0.28}Ba_{0.72}Nb_2O_6$ ceramics sintered at various temperatures for 4 h at; (a) 1300°C, (b) 1325 °C, (c) 1350 °C, (d) 1375 °C, (e) 1400 °C (orange), and 6 h at; (f) 1300 °C, (g) 1350 °C, (h) 1400 °C (green). Data from 100-grain samples. Grain sizes estimated by multiplying measured grain size by a factor of 1.56, to account for underestimation due to cross-sectional imaging [Mendelson, M. I. 1969].

Table 7. Summary of grain size data for $Ca_{0.28}Ba_{0.72}Nb_2O_6$ ceramics sintered at various temperatures for 4 or 6 h. Data from a 100-grain samples. Average grain size values calculated by multiplying measured grain sizes by a factor of 1.56, to account for grain size underestimation related to cross-sectional imaging [Mendelson, M. I. 1969].

Sample Code	Avg. grain size (µm) [S.D]	Max. measured grain size (µm)	**Sample Code**	Avg. grain size (µm) [S.D]	Max. measured grain size (µm)
1300/4	3	3.7	**1300/6**	6	8.7
1325/4	6	9.4			
1350/4	3	6.4	**1350/6**	5	9.3
1375/4	6	10.0			
1400/4	6	7.9	**1400/6**	6	14.0

Sintering for 4 h, rather than 6 h, allowed for the synthesis of high density (98 - 96 %) ceramics over a relatively wide temperature range of 1325-1400 °C. Of these high-density ceramics (> 95 %), sample 1350/4 had the finest grain size, which may benefit its dielectric properties. However, whilst average grain sizes were generally around 6 µm, clear trends in the evolution of CBN28 microstructure with sinter temperature were absent. Due to this inconsistent behaviour, four high density CBN28 samples were chosen to be dielectrically analysed in search of the optimum processing conditions for high permittivity and low dielectric losses.

5.2.2 Dielectric properties

For the comparably dense samples (98 - 96 %), sintered for 4 h at 1325 - 1400 ^{o}C, the temperature at the permittivity maxima varied slightly, decreasing with increasing sinter temperature from T_C = 232 ^{o}C at 1375 ^{o}C to T_C = 226 ^{o}C at 1400 ^{o}C, when measured at 1000 kHz, see Figure 43. These values differed from that of CBN28 calcined for 4 h at 1200 ^{o}C (T_C = 268 ^{o}C), which had some secondary phase $CaNb_2O_6$, shown in Section 5.3. Typical reported temperatures for the ε_r-Max of CBN28 ceramics vary from 235-255 ^{o}C, when measured at 1 kHz [Han, X. 2013] and [Yang, B. 2015-May]. For 1325/4 and 1350/4 (Figure 43(a) and (b)), high losses at and above T_C appear in conjunction with frequency dependence of ε_r-Max. Similar lossy features have been observed by other authors and are particularly acute when doping CBN with volatiles such as K and Na [Yang, B. 2015-Dec] and [Yang, B. 2016]. At and above 1375 ^{o}C, Figure 43(c) and (d), lesser increases in low-frequency

dielectric loss are present only above ~250 °C, which coincide with only minor increases in low-frequency (1 kHz) permittivity at 350 °C. Below T_M, a tan δ peak was observed at 200 °C that increased in magnitude with increasing frequency. Both these features have been observed elsewhere in CBN [Han, X. 2013] and [Ke, S. 2008].

The ε_r-Max of 1375/4, measured at 1 kHz, was 2520 with some frequency dependence, decreasing to 2240 when measured at 1000 kHz. The frequency dependence of T_C was very minor, varying from 229 to 232 °C across this range, see Figure 43(c). The 1000 kHz permittivity maxima values for the samples were variable with sintering temperature, being broadly comparable for 1375/4 and 1325/4 (2400), lower for 1350/4 (1990) and significantly higher for 1400/4 (3420), see Figure 43. Typical values for the ε_r-Max of CBN28 ceramics range from 1800 - 2700 (measured at 1 or 10 kHz) [Yang, B. 2015-Dec] and [Wei, L. 2014-May].

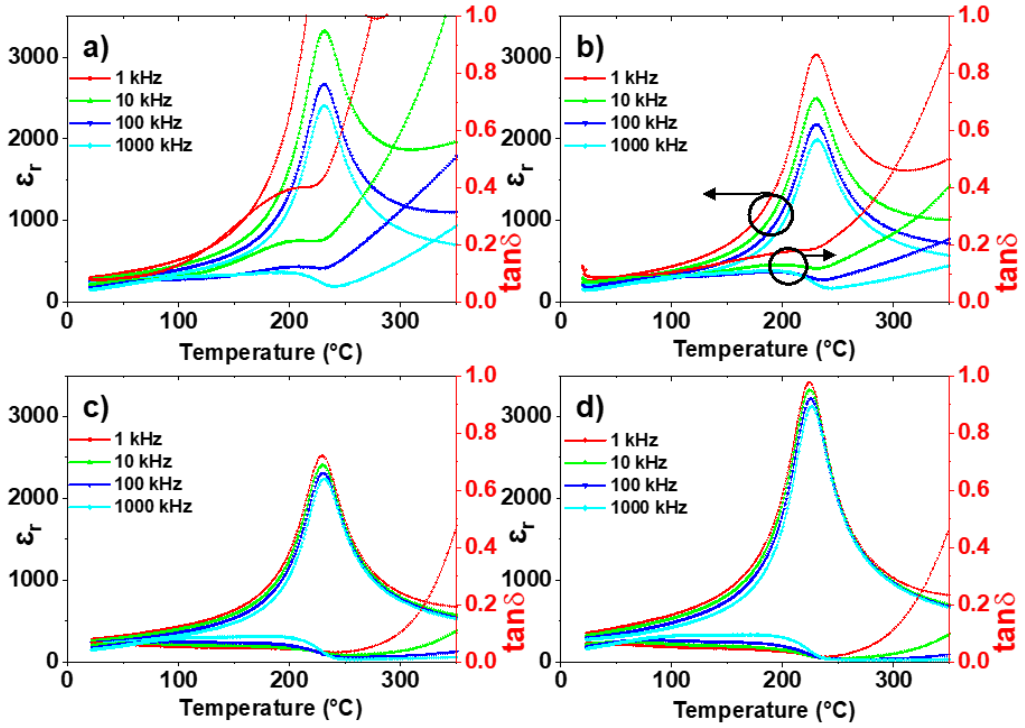

Figure 43. Relative permittivity- and tan δ- temperature responses, on the left-hand axis and right-hand axis respectively, for $Ca_{0.28}Ba_{0.72}Nb_2O_6$ ceramics sintered for 4 h at; (a) 1325 °C, (b) 1350 °C, (c) 1375 °C and (d) 1400 °C, measured at 1 to 1000 kHz.

The observed high frequency (1000 kHz) ε_r-Max values for these samples were variable, though samples 1325/4, 1350/4 and 1375/4 were within the range reported by other authors [Yang, B. 2015-Dec] and [Wei, L. 2014-May]. The ε_r-Max of sample 1400/4 was more comparable to that of very low dopant content CBN28, such as CBN28 with the addition of 0.2 wt.% Cu (ε_r-Max also > 3000) [Wei, L. 2014-Feb]. This raises the possibility of contamination of the sample, possibly from the

alumina crucible. However, no other samples beyond this batch were sintered at such high temperatures and the presence of very low-level contamination, whilst dielectrically significant, would be difficult or impossible to identify by techniques such as SEM EDX or XRD.

The presence of high losses, which are particularly apparent above 250 °C when measured at low frequencies such as 1 kHz, required further investigation. The origin of these losses is discussed later in Section 5.5. It was speculated that factors such as the time between sintering (high temperature exposure) and subsequent heating, during dielectric analysis, may influence the observed losses. Hence, a sample was found which had been dielectrically analysed and then left at room temperature for 12+ months. This sample underwent cyclical heating to compare its dielectric properties upon initial heating and cooling (after 12+ months) and immediate subsequent heating and cooling.

5.2.3 Dielectric loss and thermal treatment

A CBN28 sample was calcined for 1200 ^{o}C for 12 h and sintered at 1350 ^{o}C for 4 h. Henceforth it is referred to as CBN28-12h. Its relative permittivity- and tan δ- temperature response was analysed up to ~400 °C, prior to storage at room temperature for 15 months. Subsequent cyclical heating, up to 400 °C, and cooling, to 130 ^{o}C, was performed for 3 cycles. This heating and cooling curve data, recorded at 1 to 1000 kHz, are displayed in Appendix 1. Select dielectric data from this experiment are tabulated in Appendix 3.

Low-frequency (1 kHz), high-temperature (> 250 °C) dielectric losses were present in CBN28-12h shortly after it was sintered, see H0 in Figure 44 (tan δ(1 kHz) = ~0.18 at 300 ^{o}C), but these were lower than in a 20 h-calcined CBN28 1350/4, see Figure 43(b) (tan δ(1 k Hz) = ~0.45 at 300 ^{o}C). Values of 1 kHz-ε_r at 300 ^{o}C were also lower in CBN28-12h (~1150 compared to ~1750). Hence dielectric loss (ε_r'') values were ~60 % lower in the CBN28-12h sample.

After standing at room temperature for 15 months, low-frequency, high-temperature dielectric losses were higher upon the initial cycle of heating, see H1 in Figure 44 (1 kHz tan δ ~0.40 at 300 ^{o}C). These losses, recorded at 300 °C, declined to tan δ = ~0.29 and ~0.18 upon subsequent heating, in H2 and H3 respectively. This represents a reduction of losses to levels comparable to H0. However, this thermal cycling, or annealing, did not eliminate the presence of elevated low frequency losses at high temperature. A 20 kV cm^{-1} sinusoidal current was applied, in a P-E analyser, prior to measurement Post P-E in Figure 44, This further reduced, but did not eliminate, the loss feature (tan δ(1 kHz) = ~ 0.08 at 300 ^{o}C).

At low temperature (< 250 °C), highlighted in the insert in Figure 44, losses for H2 were higher than for H1. This suggests that some degree of thermal disturbance or activation occurred upon initial

heating to 400 °C and the activity of the loss causing features persisted after cooling and upon secondary heating. The reduced gradient of loss increase, with temperature, in H2 compared to H1, may indicate that, alongside activation, some degree of annealing out of the loss causing features also occurred after initial heating and continued to occur upon further heating. The likelihood of this lossy feature being caused by oxygen vacancies is discussed later in section 5.5. This high temperature, low frequency loss feature is presumed to be distinct from the low temperature ($T < T_{C/M}$), high frequency (1000 kHz) loss feature discussed in Figure 45, below.

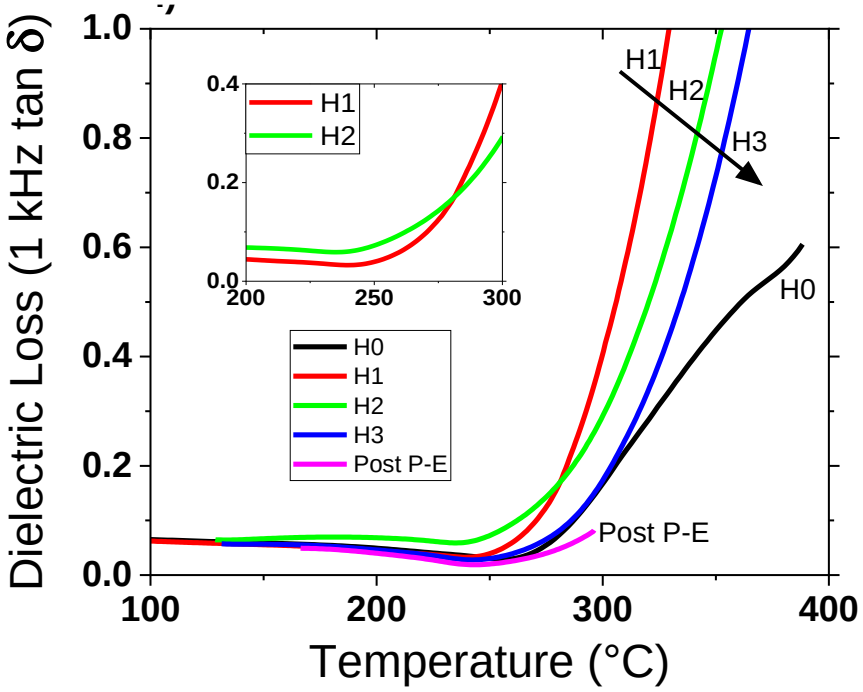

Figure 44. The 1 kHz tan δ-temperature responses for $Ca_{0.28}Ba_{0.72}Nb_2O_6$ calcined for 12 h at 1200 °C and sintered at 1350 °C for 4 h. After the initial heating curve measurement (H0), this sample was left untouched for 15 months before dielectric measurements were performed under cyclical heating, up to 400 °C (H1, H2 and H3), and cooling. Polarisation-electric field analysis was then performed, ostensibly to exercise the domain walls, prior to a final heating curve measurement up to 300 °C (Post P-E). The 1000 kHz relative permittivity- and tan δ- temperature responses for the heating (and cooling) curves that correspond to H1, H2 and H3 are shown in Figure 45. In the Appendix 1(a) to 1(h), the respective relative permittivity- and tan δ- temperature responses for all eight heating and cooling curves are shown, having been measured from 1 to 1000 kHz.

The 1000 kHz ε_r-Max values for CBN28-12h were broadly comparable to the 20 h-calcined 1400/4 sample, in Figure 43(d), with ε_r values on heating and cooling exceeding 3000, see Appendix 3. Upon initial heating (H1) ε_r-Max was lower (3006) than subsequent heating cycles, which were comparable (3074 for H2 and 3076 for H3). These ε_r-Max values were all lower than the cooling curve values, which were also comparable (3184, 3182 and 3182 for C1, C2 and C3), where C refers to the cooling curve data. The hysteresis of T_C, when comparing heating and cooling, showed some apparent variation, however heating measurements were recorded at ~1 °C intervals and so the ΔT_C (i.e. between H1 and C1, or Hx and Cx) variations of 7, 4 and 6 °C for cycles 1, 2 and 3 respectively are likely insignificant. Values of 1000 kHz ε_r-Max for the cooling curve data, in Figure 45, were highly consistent whilst heating curve data showed a slight increase (~2 - 3 %) between initial and subsequent heating. This was independent of the gradual reduction in low-frequency ε_r-Max and losses, seen in Figure 44. It is notable that both the time between subsequent heating (15 months prior compared with immediately) and the temperature from which the sample was heated (from room temperature compared with from 130 °C) may contribute to the variation in ε_r-Max between H1 and H2/H3.

Values of 1000 kHz tan δ increased when cooling below T_C, plateauing below ~180 ^oC, where ε_r'' peaked, whilst showing similar hysteresis to that seen when comparing T_C upon heating and cooling. These losses were also lower in the initial heating cycle when compared with H2/H3, see Figure 45(a). The variation in 1000 kHz tan δ-Max and ε_r-Max showed a near-linear correlation, as seen in Figure 45(d). These dielectric experiments were partly inspired by the identification, by TEM, of a hysteresis of the domain structure in CBN28 [Beanland, R. 2023]. The identification of this hysteresis of dielectric properties in CBN28 is complimentary to those structural investigations, given the links between dielectric properties such as high frequency tan δ or ε_r-Max and domain size [Xu, R. 2014]. Further detail in the Appendix 2, suggests that this correlation between 1000 kHz tan δ-Max and ε_r-Max holds across different CBN28 samples.

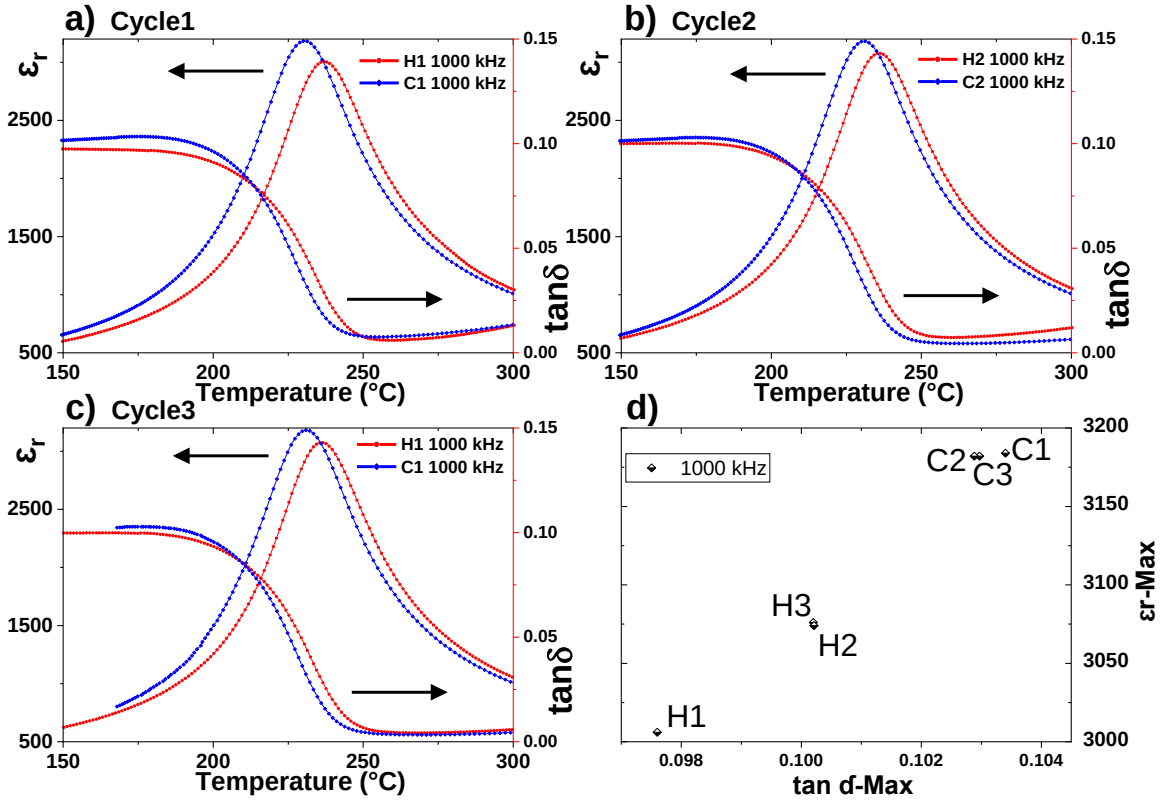

Figure 45. The 1000 kHz relative permittivity- and tan δ- temperature responses for $Ca_{0.28}Ba_{0.72}Nb_2O_6$, synthesised by calcination for 12 h at 1200 °C and then sintering at 1350 °C for 4 h before standing at room temperature for 15 months. Cyclically heating, up to 400 °C, and cooling, to 130 °C, occurred in the sequence; (a), (b) and then (c), with heating data corresponding to the 1 kHz heating data shown in Figure 44 (H1, H2 and H3). The correlation between 1000 kHz ε_r-Max and tan δ-Max on heating (H) and cooling (C) is shown in (d).

To summarise, a high temperature (T > ~250 °C), low frequency loss feature was identified in CBN28. This feature responded to, but was not removed by, thermal cycling. A high frequency, low temperature ($T < T_C$) loss feature was also identified which appeared to correlate with observed values of high frequency ε_r-Max.

5.3 Chemical modification of $Ca_{0.28}Ba_{0.72}Nb_2O_6$ with yttrium

Donor doping of CBN28 ceramics, with increasing levels of Y^{3+}, was performed with a view to improving temperature stable permittivity in a single-phase ceramic. The nominal formulation of the ceramics, $(Ca_{0.28}Ba_{0.72})_{1-3w/2}Y_wNb_2O_6$ [$0 \leq w \leq 0.20$], was derived from the charge balanced substitution-in of 2 Y^{3+} ions for 3 total $Ca^{2+}$and Ba^{2+} ions. This infers the addition of an A site vacancy to the structure with each addition of two Y ions.

5.3.1 Phase and microstructural analysis

XRD patterns for the Y doped CBN28 ceramics, $(Ca_{0.28}Ba_{0.72})_{1-3w/2}Y_wNb_2O_6$ [$0 \leq w \leq 0.20$], are shown in Figure 46. Henceforth $(Ca_{0.28}Ba_{0.72})_{1-3w/2}Y_wNb_2O_6$ [$0 \leq w \leq 0.20$] ceramics are abbreviated according to their Y levels, "w". e.g. "w = 0.05" refers to $(Ca_{0.28}Ba_{0.72})_{1-3w/2}Y_wNb_2O_6$ [w = 0.05] or $(Ca_{0.28}Ba_{0.72})_{0.925}Y_{0.05}Nb_2O_6$. The precursor powders were calcined for 4 h at 1200 ^oC and sintered according to a 2-stage sinter regime: either being heated to 1350 ^oC and then immediately cooled to 1200 ^oC for a dwell time of 4 h ([$0 \leq w \leq 0.02$]); or heated to 1325 ^oC then cooled to 1250 ^oC for a dwell time of 4 h ([$0.03 \leq w \leq 0.20$]). XRD patterns for w = 0 (CBN28) and w = 0.05 powders, calcined at 1200 ^oC for 12 h, are shown in Figure 47, as well as patterns for $Y_rCa_{0.28-3r/2}Ba_{0.72}Nb_2O_6$ (r = 0.04 and r = 0.05). For the latter compositions, the substitution-in of Y solely for Ca was performed to assess the role of (assumed) A1 site competition and thermal processing (calcination time) on the presence of secondary phases in Y doped CBN28.

A full pattern Rietveld refinement of w = 0.04 is shown in Figure 48. This sample was chosen for refinement as it was single phase and displayed a transformed (much broader) permittivity peak around T_M, when compared with CBN28. Unit cell parameters, refined from the XRD data in Figure 46 are presented in Table 8. All five full pattern Rietveld refinements were performed by Dr. Yizhe Li, of the University of Manchester. Data corresponding to these refinements can be found in Figure 48 and Table 8.

Microstructural (SEM) analysis for [$0 \leq w \leq 0.05$] is shown in Figure 49, grain-size data for [$0 \leq w \leq 0.10$] are shown in Figure 50 and summarised in Table 9. Microstructural and phase analysis of w = 0.10, by FIB-SEM EDX and TEM EDX, shown in Figures 51 and 52.

CBN28 calcined for 4 h at 1200 ^oC and then sintered was not single phase, with orthorhombic $CaNb_2O_6$ (ICCD 00-011-0619) identified from the XRD pattern shown in Figure 46(a). Low level Y doped CBNs [$0.01 \leq w \leq 0.04$] were single phase, whilst w = 0.05 possessed a variety of secondary phases including orthorhombic $CaNb_2O_6$, tetragonal $Ba_3Nb_5O_6$ (ICCD 00-031-0158), and a cubic structure whose composition is comparable to either Ba_2YNbO_6 (ICCD 00-024-1042) or $Ba_2Ca_{0.79}Nb_{1.08}O_{5.68}Y_{0.13}$ (ICCD 04-021-7855). CBN28 and the single-phase Y doped compositions had

measured densities above 5 g cm^{-3} (5.07 - 5.18 g cm^{-3}) whilst w = 0.05 had a lower density of 4.96 g cm^{-3}. Only orthorhombic $CaNb_2O_6$ secondary phase was identified in w = 0.10, although FIB SEM-EDX (Figure 51) revealed Y-rich and Nb-deficient grains, most likely Y_2O_3 (ICCD 00-005-0574). The Y_2O_3 phase likely could not be identified by XRD due to the highest intensity (222) Y_2O_3 peak, occurring at 29.2 $^{o}2\theta$, being obscured by the CBN (410) peak. The measured density of w = 0.10 was 4.98 g cm^{-3}. Samples w = 0.15 and w = 0.20 appeared to be significantly outside the single-phase region, their measured densities were low (4.85 and 4.72 g cm^{-3}) and they contained multiple secondary phases, some of which were unidentified.

CBN28 and w = 0.05 powders were calcined for 12 h at 1200 ^{o}C, their XRD patterns are shown in Figure 47(c) and (a). No secondary phase was identified in this CBN28, suggesting that the secondary phase identified in the 4 h calcined CBN28 (Figure 46) was present due to insufficient thermal treatment resulting in the incomplete reaction of the precursor compounds. The 12 h-calcined w = 0.05 powder showed $CaNb_2O_6$ and Barium-Yttrium-(Calcium-)Niobate secondary phases, suggesting that this composition is outside of the single-phase region (Figure 47(a)). Modification of the composition to $Y_rCa_{0.28-3r/2}Ba_{0.72}Nb_2O_6$ ($0.03 \leq r \leq 0.05$) maintained the absence of secondary phases at low Y levels of $r/w < 0.05$ (Y at.% < 0.56), when calcining for 12 h at 1200 ^{o}C. Only a minor presence of $CaNb_2O_6$ was detected at r = 0.05 by lab XRD (Figure 47(b)), with the assumed $CaNb_2O_6$ peak manifesting as only slightly distinct from the CBN peak, as a shoulder. However, permittivity-temperature measurements for $Y_rCa_{0.28-3r/2}Ba_{0.72}Nb_2O_6$ ceramics sintered at 1325 ^{o}C for 4 h showed variable and unexplained suppression of permittivity, see Appendix 4.

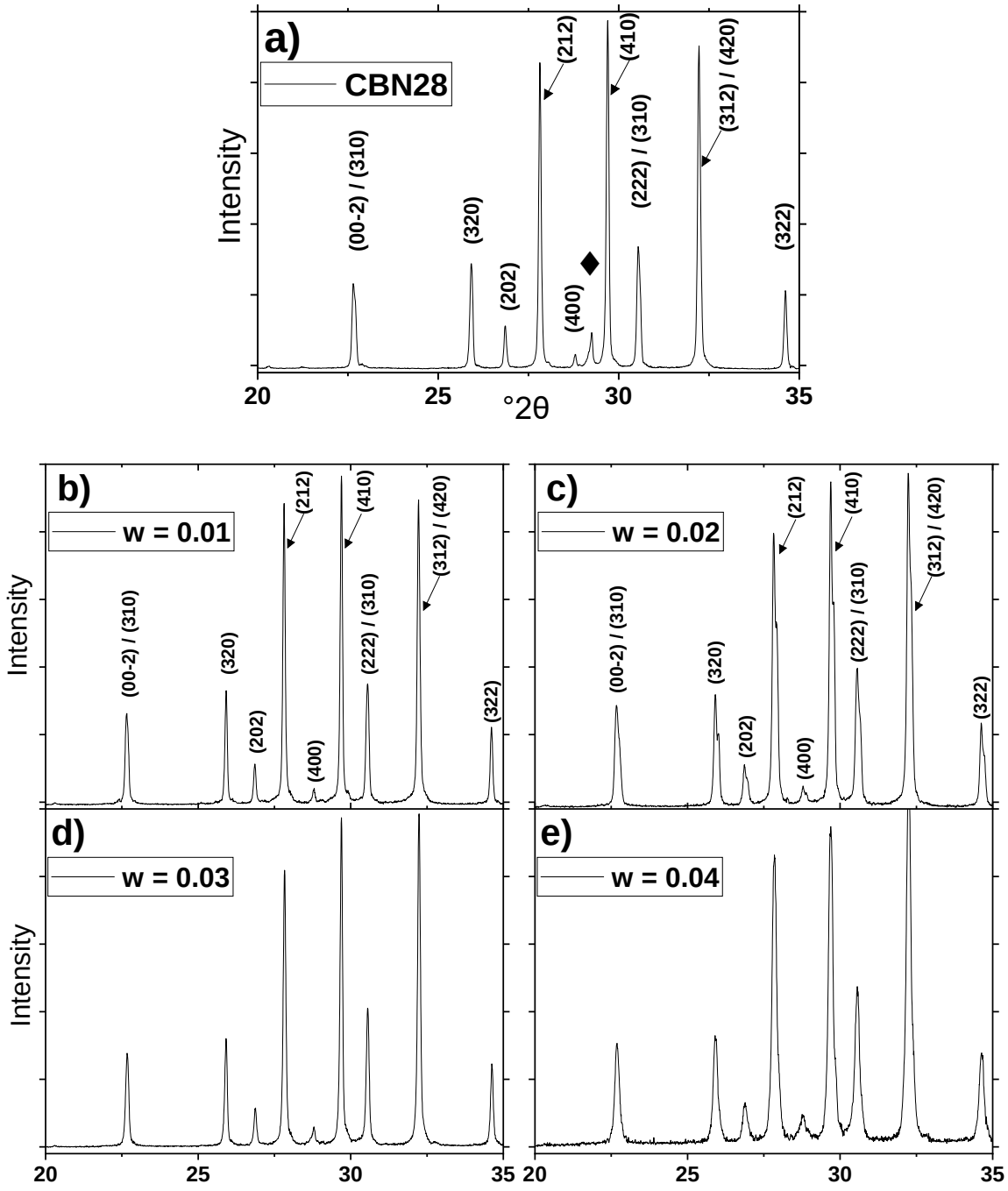
a)
CBN28
Intensity
(00-2) / (310)
(320)
(202)
(400)
(212)
(410)
(222) / (310)
(312) / (420)
(322)
20
25
30
35
°2θ
b)
w = 0.01
c)
w = 0.02
d)
w = 0.03
e)
w = 0.04

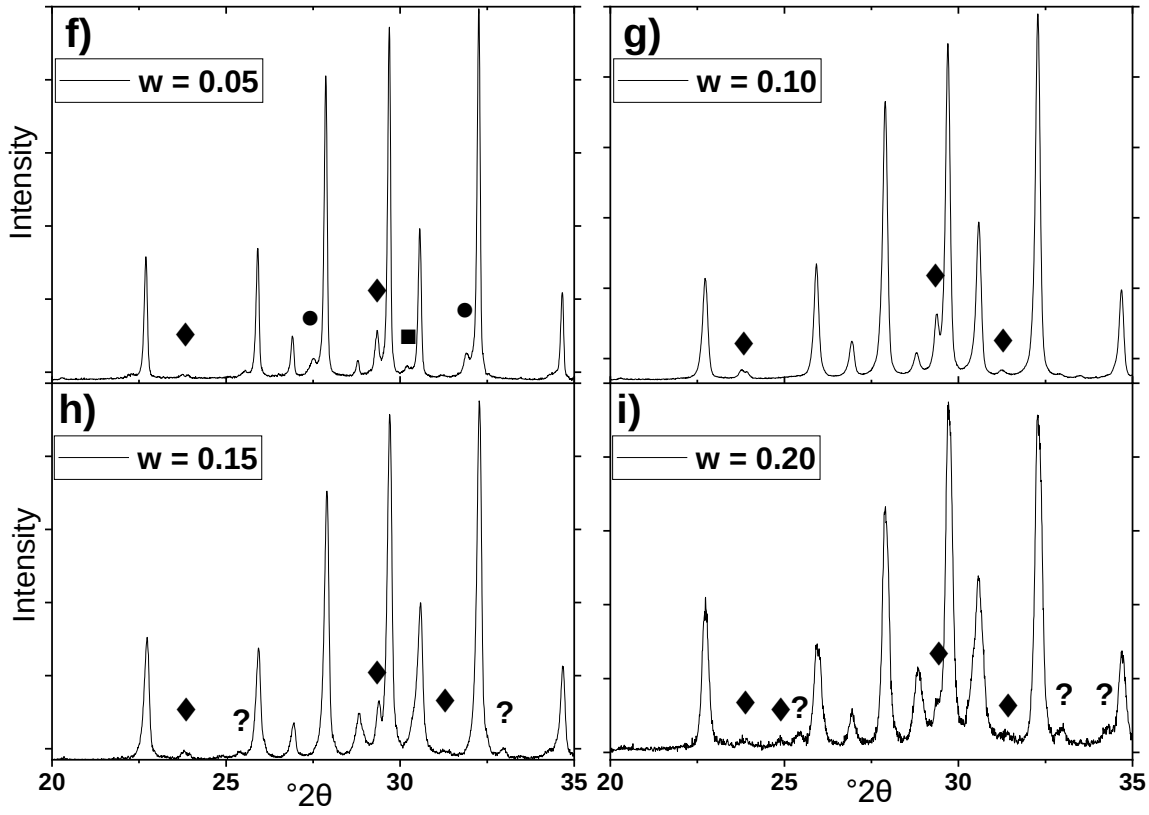

Figure 46. X-ray diffraction patterns of $(Ca_{0.28}Ba_{0.72})_{1-3/2w}Y_wNb_2O_6$ [$0 \leq w \leq 0.20$] crushed sintered pellets, indexed according to P4bm structure, ICCD 05-001-0283. Samples were calcined for 4 h at 1200 ^oC and sintered according to a 2-stage sinter regime, either being heated to 1350 ^oC and then immediately cooled to 1200 ^oC for a dwell time of 4 h ([$0 \leq w \leq 0.02$]) or heated to 1325 ^oC then cooled to 1250 ^oC for a dwell time of 4 h ([$0.03 \leq w \leq 0.20$]). ♦ represents orthorhombic $CaNb_2O_6$ (ICCD 00-011-0619), ● represents tetragonal $Ba_3Nb_5O_6$ (ICCD 00-031-0158) and ■ corresponds to a 100% R.I. peak in a cubic structure whose composition is comparable to either Ba_2YNbO_6 (ICCD 00-024-1042) or $Ba_2Ca_{0.79}Nb_{1.08}O_{5.68}Y_{0.13}$ (ICCD 04-021-7855). ? indicates an unidentified peak.

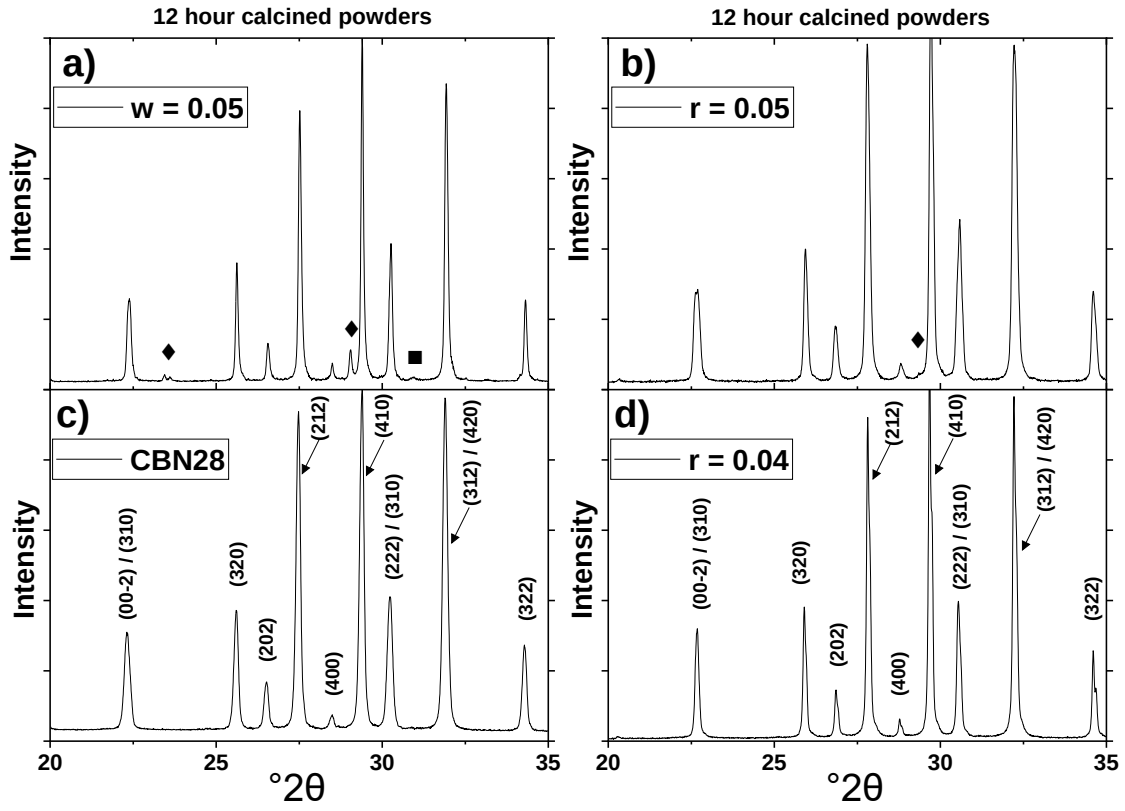

Figure 47. X-ray diffraction patterns of $(Ca_{0.28}Ba_{0.72})_{1-3/2w}Y_wNb_2O_6$ [w = 0 and 0.05], (c) and (a), and $Y_rCa_{0.28-3r/2}Ba_{0.72}Nb_2O_6$ [r = 0.04 and r = 0.05], (d) and (b), powder calcined for 12 h at 1200 ^oC, indexed according to P4bm structure (ICCD 05-001-0283). ♦ represents orthorhombic $CaNb_2O_6$ (ICCD 00-011-0619) and ■ corresponds to a 100% R.I. peak of a cubic structure whose composition is comparable to either Ba_2YNbO_6 (ICCD 00-024-1042) or $Ba_2Ca_{0.79}Nb_{1.08}O_{5.68}Y_{0.13}$ (ICCD 04-021-7855).

Figure 48 shows the Rietveld refinement and difference plot for w = 0.04, all peaks can be ascribed to CBN (ICCD 05-001-0283). This sample was chosen for display as it has the highest Y content of the single-phase samples. Its dielectric response is different to that of CBN28, but as shown here its average structure remains comparable and indexable to the P4bm structure. Similar Rietveld refinements were performed for sample CBN28, w = 0.02, w = 0.05 and w = 0.10. These Rietveld refinements were performed by Dr. Yizhe Li of the University of Manchester using TOPAZ 5.0 software (Bruker AXS, Karlsruhe, Germany). Here, the peak shape function was determined by the X-ray diffractometer geometry, and fundamental background parameters. Lattice constants, scale factor, atomic coordination and occupancy were refined. A simpler lattice refinement protocol, detailed in section 5.2, was undertaken for the remaining samples, with the derived data presented in Table 8. For the simple refinement protocol, Y doped CBN28 samples were compared to a CBN28 reference pattern. The higher R_{wp} values for the five more complete Rietveld refinements likely reflect the lesser use of structural constraints.

For the five Rietveld samples, the *a* lattice parameter varied only slightly between 12.45 and 12.46 Å, with no structural trend with respect to Y-content. For the simply refined compositions that were within the single-phase limit (w = 0.01 and w = 0.03) *a* parameter values were slightly lower, both being 12.44 Å. A clear trend of decreasing *c* parameter with Y addition can be seen for the Rietveld compositions with *c* parameter decreasing from 7.90 to 7.88 and 7.86 Å for CBN28, w = 0.04 and w = 0.10 respectively. Likewise, a trend can be seen between the simply refined w = 0.01 and w = 0.03 (7.92 and 7.89 Å), with the latter value according well with the Rietveld refinement data for w = 0.02 and 0.04. Trends in $CaNb_2O_6$ secondary phase content are likewise consistent between the two refinement approaches. $CaNb_2O_6$ was absent from [0.01 ≤ w ≤ 0.04], then increased in content from w = 0.05 and w = 0.10 (6.7 and 8.3 %) to w = 0.15 and w = 0.20 (10.7 and 14.9 %). Vacancy and Y inclusion reduced the unit cell mass such that theoretical density decreased from 5.31 g cm^{-3} (CBN28) to 5.27 g cm^{-3} (w = 0.05) despite a corresponding, but small, decrease in unit cell *c*-axis and volume. A more significant decrease in theoretical density occurred when increasing Y- (and secondary phase) content from w = 0.10 (5.23 g cm^{-3}) to w = 0.20 (5.06 g cm^{-3}). For samples w = 0.15 and w = 0.20, nominal composition varied significantly from the ascribed CBN28 reference pattern, reducing the accuracy of any structurally based comparisons. Here, calculated *a* and *c* lattice parameters were higher and out of trend with Rietveld refined data, this is reflected in the observed sharper decrease in theoretical density.

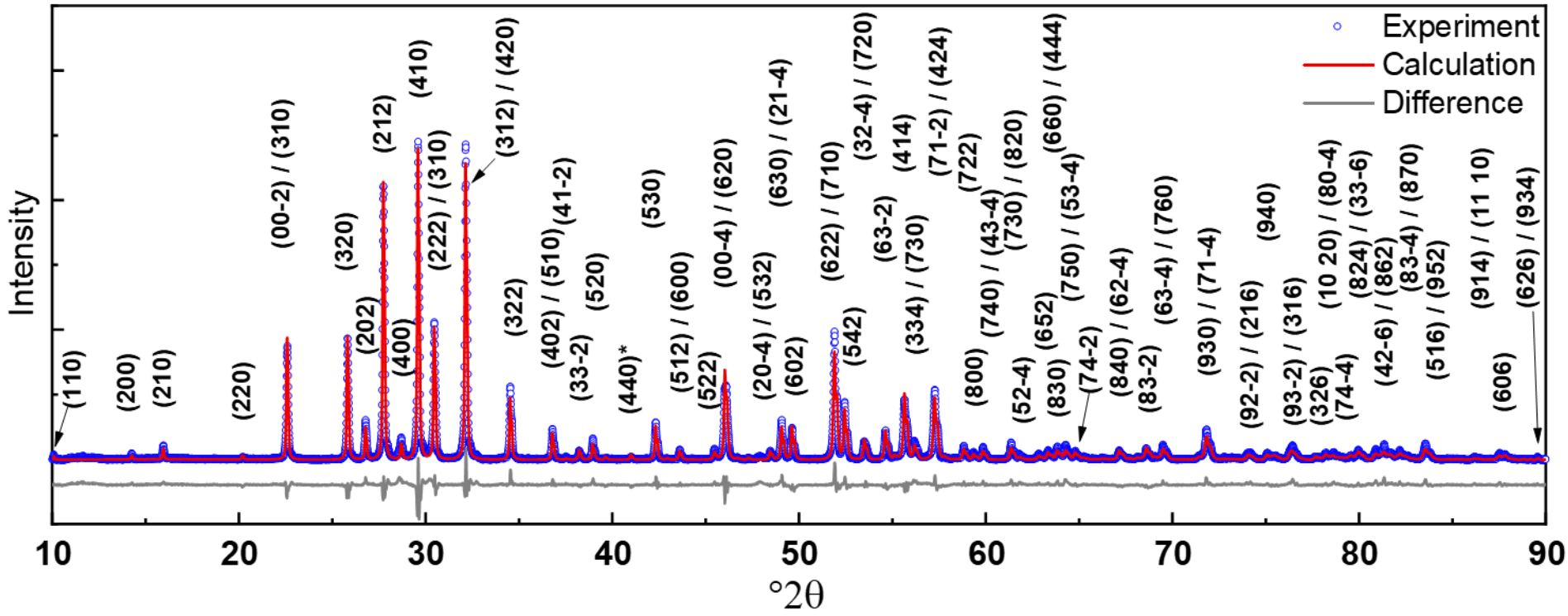

Figure 48. Full pattern Rietveld refinement for $(Ca_{0.28}Ba_{0.72})_{1-3/2w}Y_wNb_2O_6$ [w = 0.04], indexed according to P4bm structure, ICCD 05-001-0283. The refinements R_{wp} value of 9.9% indicates a very good fit to the data. Refinement was performed by Dr. Yizhe Li, of the University of Manchester.

Table 8. Summary of (pseudo) tetragonal lattice parameters from the unit cell refinement of $(Ca_{0.28}Ba_{0.72})_{1-3/2w}Y_wNb_2O_6$ [$0 \leq w \leq 0.20$] ceramics. Samples in **bold** were subject to full pattern Rietveld refinement (performed in TOPAZ 5.0), the remaining samples underwent a simple lattice parameter refinement (performed in Highscore). "Goodness of fit", R_{wp}, calculated maximum theoretical densities (ρ), measured density and $CaNb_2O_6$ content are presented. Lattice parameter error values (in brackets) were provided by Highscore or TOPAZ 5.0 software. Measured density standard deviations [in square brackets] were calculated from a minimum of 5 ceramic pellets.

Sample Code	a (Å)	c (Å)	Volume (Å^3)	R_{wp} (%)	Theoretical ρ (g cm^{-3})	Measured ρ (g cm^{-3}) [S.D.]	$CaNb_2O_6$ (wt.%)
CBN28	**12.4574 (2)**	**7.8976 (1)**	**1225.52 (2)**	**9.81**	**5.31**	5.11 [0.03]	**5.3**
w = 0.01	12.44 (1)	7.92 (2)	1224.9	5.01	5.30	5.17 [0.04]	0
w = 0.02	**12.4538 (1)**	**7.8901(1)**	**1223.74 (1)**	**9.85**	**5.30**	5.18 [0.04]	**0**
w = 0.03	12.44 (1)	7.89 (1)	1221.4	4.73	5.30	5.07 [0.02]	0
w = 0.04	**12.4555 (1)**	**7.8881(2)**	**1223.75 (3)**	**9.93**	**5.28**	5.14 [0.03]	**0**
w = 0.05	**12.4589 (2)**	**7.8762 (7)**	**1222.52 (2)**	**10.06**	**5.27**	4.96 [0.05]	**6.7**
w = 0.10	**12.4572 (2)**	**7.86562 (7)**	**1220.54 (2)**	**10.23**	**5.23**	4.98 [0.04]	**8.3**
w = 0.15	12.47 (1)	7.92 (1)	1232.1	4.14	5.13	4.85 [0.03]	10.7
w = 0.20	12.49 (6)	7.92 (6)	1235.3	4.95	5.06	4.72 [0.01]	14.9

Samples CBN28, w = 0.01 and w = 0.02 were calcined for 4 h at 1200 ^{o}C and sintered by heating to 1350 ^{o}C and then immediately cooling to 1200 ^{o}C for a dwell time of 4 h. They had comparable grain morphologies and micro-cracking (Figure 49) as well as similar average calculated grain sizes ~7-8 µm, see Figure 50 and Table 9. Maximum measured grain sizes were also comparable for CBN28 and the single-phase Y doped CBNs (11.4 to 13.1 µm) before decreasing in w = 0.05 and w = 0.10, to 8.4 and 4.1 µm respectively. The change to a more thermally intensive sinter regime, from w = 0.02 to w ≥ 0.03, resulted in a lower measured density (5.07 g cm^{-3}) and a porous microstructure for w = 0.03, see Figure 49. Average-calculated and maximum-measured grain size decreased to a low of ~3 µm and 4.1 µm respectively for w = 0.10, which contained secondary phases. Microstructural pores and secondary phase grains in w = 0.10 can be seen in Figure 51(a).

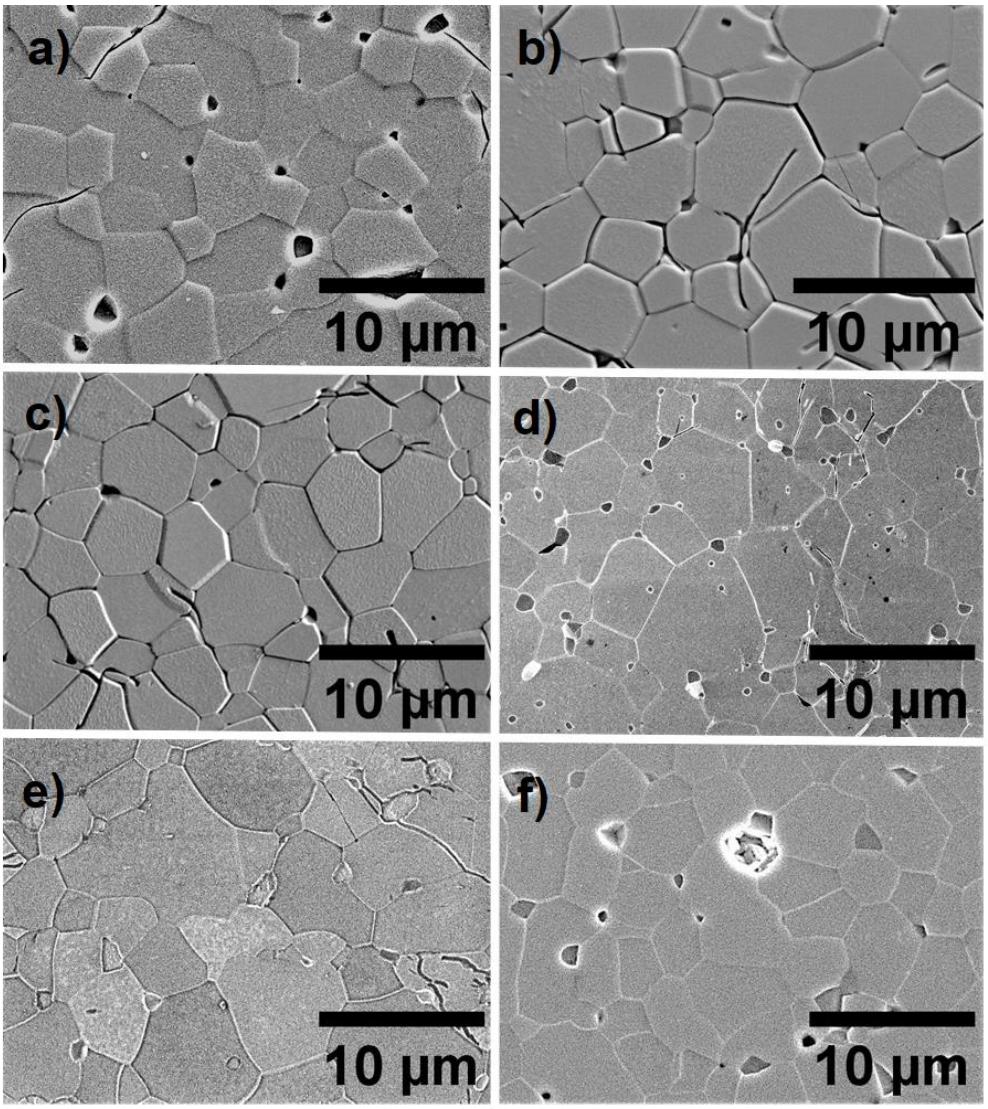

Figure 49. SEM secondary electron micrographs of $(Ca_{0.28}Ba_{0.72})_{1-3w/2}Y_wNb_2O_6$ [0 ≤ w ≤ 0.05]; (a) CBN28, (b) w = 0.01, (c) w=0.02, (d) w = 0.03, (e) w = 0.04 and (f) w = 0.05. Micrographs were taken at 5 kx magnification. The microstructure of w = 0.10 can be seen in Figure 51.

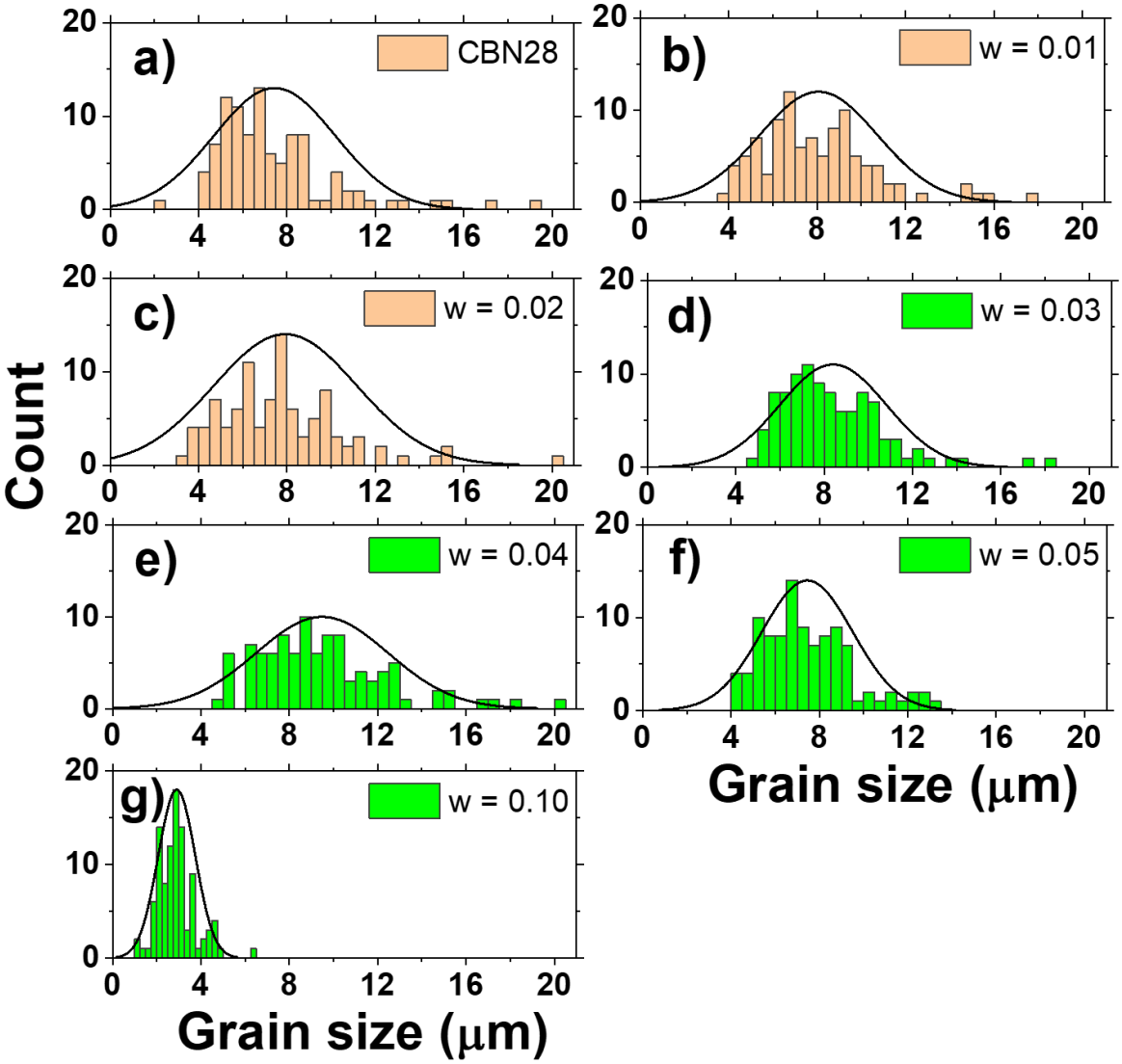

Figure 50. Grain size distributions for $(Ca_{0.28}Ba_{0.72})_{1-3/2w}Y_wNb_2O_6$ [$0 \leq w \leq 0.10$] ceramics; (a) CBN28, (b) w = 0.01, (c) w = 0.02, (d) w = 0.03, (e) w = 0.04, (f) w = 0.05 and (g) w = 0.10. Data from 100-grain samples. Grain sizes estimated by multiplying measured grain size by a factor of 1.56, to account for underestimation due to cross-sectional imaging [Mendelson, M. I. 1969].

Table 9. Summary of grain size data for $(Ca_{0.28}Ba_{0.72})_{1-3/2w}Y_wNb_2O_6$ [$0 \leq w \leq 0.10$] ceramics. Data from 100-grain samples. Average grain size values calculated by multiplying measured grain sizes by a factor of 1.56, to account for grain size underestimation related to cross-sectional imaging [Mendelson, M. I. 1969].

Sample Code	Avg. grain size (µm)	Max. measured grain size (µm)
CBN28	7	12.2
w = 0.01	8	11.4
w = 0.02	8	13.0
w = 0.03	8	11.8
w = 0.04	9	13.1
w = 0.05	7	8.4
w = 0.10	3	4.1

To summarise, the addition of Y in the single-phase ceramics resulted in relatively consistent average calculated grain sizes (7-9 µm) and maximum measured grain sizes (11.4 to 13.1 µm). Further addition of Y above w = 0.05, coinciding with the presence of secondary phases, caused a significant reduction in average calculated grain size and maximum measured grain size, to 3 and 4.1 µm respectively.

5.3.2 Secondary phase analysis

FIB-SEM EDX of w = 0.10 is shown in Figure 51(a), surface scratches may have been caused by the pull-out of material during polishing or the failure to remove scratches from initial sample grinding, during the final-stage polishing. Many Ba-deficient and Ca-rich grains can be seen in the elemental maps, these correspond to the $CaNb_2O_6$ phase identified by XRD in Figure 46(f). Y-rich and Ba/Nb-deficient grains can also be seen, which weren't identified by XRD, these likely correspond to Y_2O_3 inclusions. Figure 51(b) is taken from the upper right quadrant of the micrograph in 51(a), the yellow and red arrows indicate $CaNb_2O_6$ and (presumed) Y_2O_3 grains respectively. HAADF STEM and STEM-EDX of w = 0.10 is shown in Figure 52, no evidence of secondary phases at the grain boundaries between CBN grains, or any "core-shell" structured compositional inhomogeneities was identified. The lighter contrast grain boundaries, found in w = 0.10 and to a lesser extent in w = 0.05 by SEM in Figure 49, are therefore believed to be an etching affect, rather than an indication of grain boundary secondary phases. Higher concentrations of Y are, however, detected between the $CaNb_2O_6$ grain and the deposited Pt layer (Figure 52, top left). The characteristic X-rays of Y (La α) and Pt (M) have comparable energies (1.92 and 2.05 KeV) [AMETEK Inc. 2022]. Hence, in the EDX spectrum, X-rays originating from Pt atoms may have been incorrectly assigned as originating from Y.

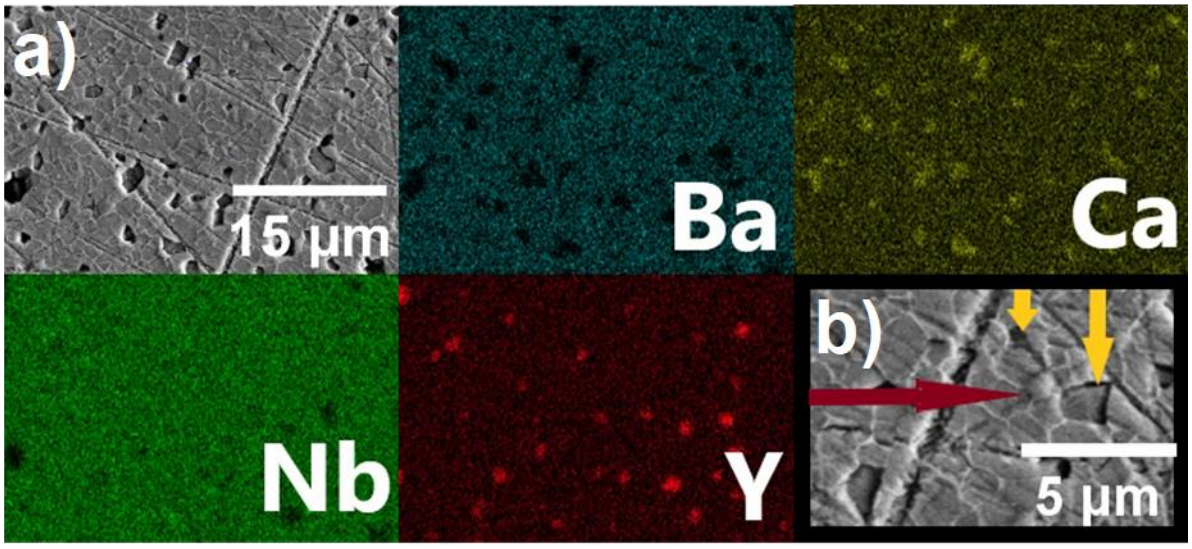

Figure 51. FIB-SEM of $(Ca_{0.28}Ba_{0.72})_{1-3/2w}Y_wNb_2O_6$ [w = 0.10] and FIB-SEM-EDX elemental maps of Ba, Ca Nb, and Y. Showing Y rich grains deficient in Ba and Nb, and Ca rich grains deficient in Ba. In (b), Yellow and red arrows indicate 3 Ba deficient grains, present in the top right quadrant of the FIB-SEM image (a), which are respectively Ca-rich (x2 in yellow) and Y-rich (and Nb deficient, in red).

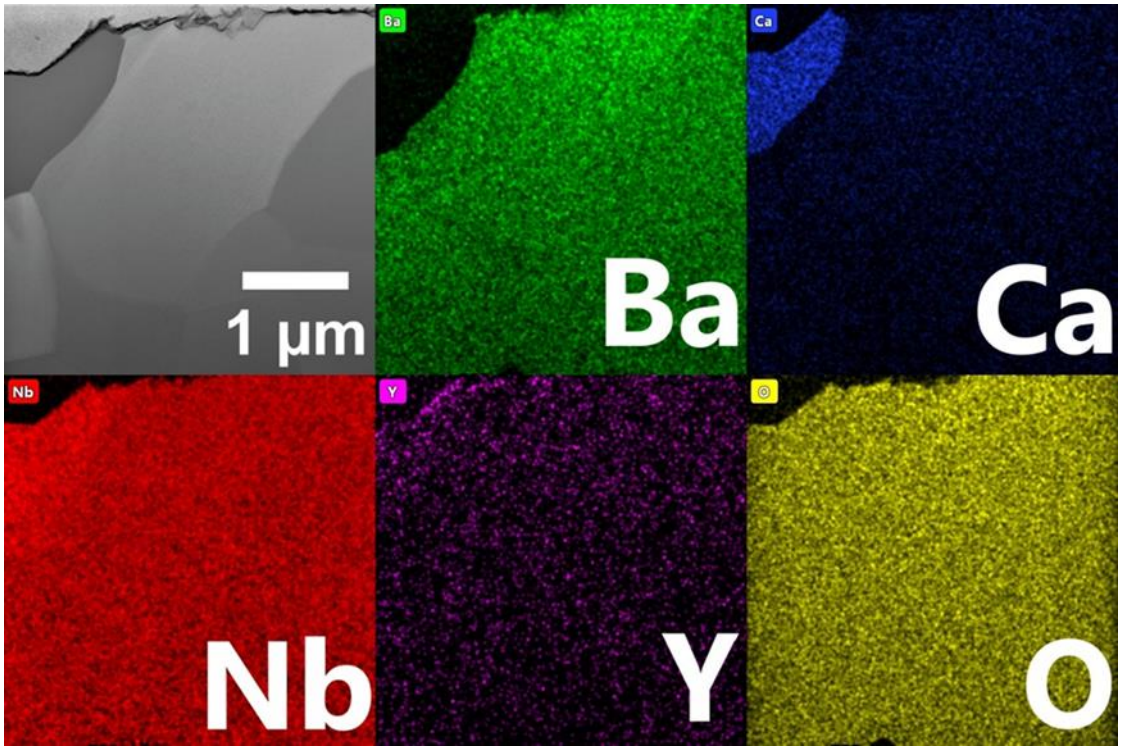

Figure 52. HAADF STEM of $(Ca_{0.28}Ba_{0.72})_{1-3/2w}Y_wNb_2O_6$ [w = 0.10] and STEM-EDX elemental maps of Ba, Ca, Nb, Y and O. Showing a Ca-rich and Ba-deficient grain and no evidence of secondary phases at the grain boundaries between CBN grains or any "core-shell" structured compositional inhomogeneities. An apparent increase in Y concentration is seen between the $CaNb_2O_6$ grain and the deposited Pt (top left).

No core-shell structured compositional inhomogeneities or grain boundary secondary phases were identified by FIB-SEM of STEM-EDX in Y doped CBN. When present, these micron-scaled variations in composition have been linked to broader permittivity peaks, as discussed later in section 5.5.

5.3.3 Dielectric and ferroelectric properties

The permittivity- and tan δ -temperature responses of CBN28s with $0 \leq w \leq 0.15$ are shown in Figure 53, with Curie-Weiss law ϒ coefficients, derived from this data, shown in Figure 54. Polarisation-Electric field loops for $0 \leq w \leq 0.20$ are shown in Figure 55, at various maximum field strengths. Table 10 and Table 11 summarise, respectively, the dielectric and ferroelectric properties of $0 \leq w \leq 0.20$. Table 12 presents Rayleigh analysis, calculated from the P-E data-derived real (ε_r') and imaginary (ε_r'') components of permittivity for CBN28, w = 0.02, w = 0.04 and w = 0.05 (Figure 56).

P-E measurements were performed by Dr. Yizhe Li and Dr. Juncheng Pan, both from the University of Manchester. Rayleigh analysis was performed Dr. David Hall, also from the University of Manchester.

Plots of relative permittivity and dielectric loss with respect to temperature are shown in Figure 53. The ε_r-Max of CBN28 was 2090, occurring at 268 ^oC, when measured at 1 kHz. For CBN28, T_C was not

frequency dependent and the permittivity peak was relatively non-diffuse, with the temperature range of stable permittivity (±15 %) being approximately 26 ^{o}C (Table 12). From CBN28 to w = 0.01, T_C reduced significantly to 220 ^{o}C. High-temperature, low-frequency losses at and above T_C were elevated and likely related to the frequency dependence of ε_r-Max in this sample. The permittivity peaks of w = 0.01 and w = 0.02 and 0.03 remained narrow, with the temperature range of stable permittivity (±15 %) being approximately 40 ^{o}C for [0 ≤ w ≤ 0.02] and nearer 50 ^{o}C-wide for w = 0.03. Values of T_C reduced further over this range to a low of 182 ^{o}C, measured at 1 kHz, or 186 ^{o}C when measured at 1000 kHz.

Values of ε_r-Max increased from CBN28 to w = 0.02 (up to 2360, measured at 1 kHz). Despite the permittivity peaks being of comparable profile, the permittivity maxima then decreased between w = 0.02 and w = 0.03 (2130), possibly due to the latter's lower measured density. The frequency dispersion of dielectric loss at temperatures just below T_C, at around 150 to 200 °C, was more pronounced in samples w = 0.02 and w = 0.03 than in CBN28. This elevated 1000 kHz tan δ peak, observed in w = 0.02 and w = 0.03, decreased sharply on approach to T_C when compared with the more diffuse $T < T_c$ 1000 kHz tan δ peaks of w ≥ 0.04.

Between w = 0.03 and w = 0.04 a change in dielectric response and a slight change in ferroelectric character was observed. The permittivity peaks of the w ≥ 0.04 samples were much more diffuse, showing temperature stable permittivity (±15 %) from 71 to 209 ^{o}C and 37 to 218 ^{o}C for w = 0.04 and w = 0.05, respectively. A decrease in, and slight frequency dependence of, ε_r-Max was also seen with the T_M of w = 0.05 varying from 141 to 150 ^{o}C, when measured at 1 to 1000 kHz. This frequency dependence is consistent with weak relaxor behaviour. The ε_r-Max for w = 0.05, when measured at 1 kHz, was 1040. Values of ε_r-Max became increasingly suppressed with further Y addition to 540 (ε_r = 470 ±1 5% from -27 to 236 ^{o}C) for w = 0.15. The decrease in ε_r-Max, with respect to Y content, somewhat limited any further increases in the range of temperature stable permittivity (±15 %), despite absolute variation in permittivity, with respect to temperature, decreasing significantly across this range, see Table 10.

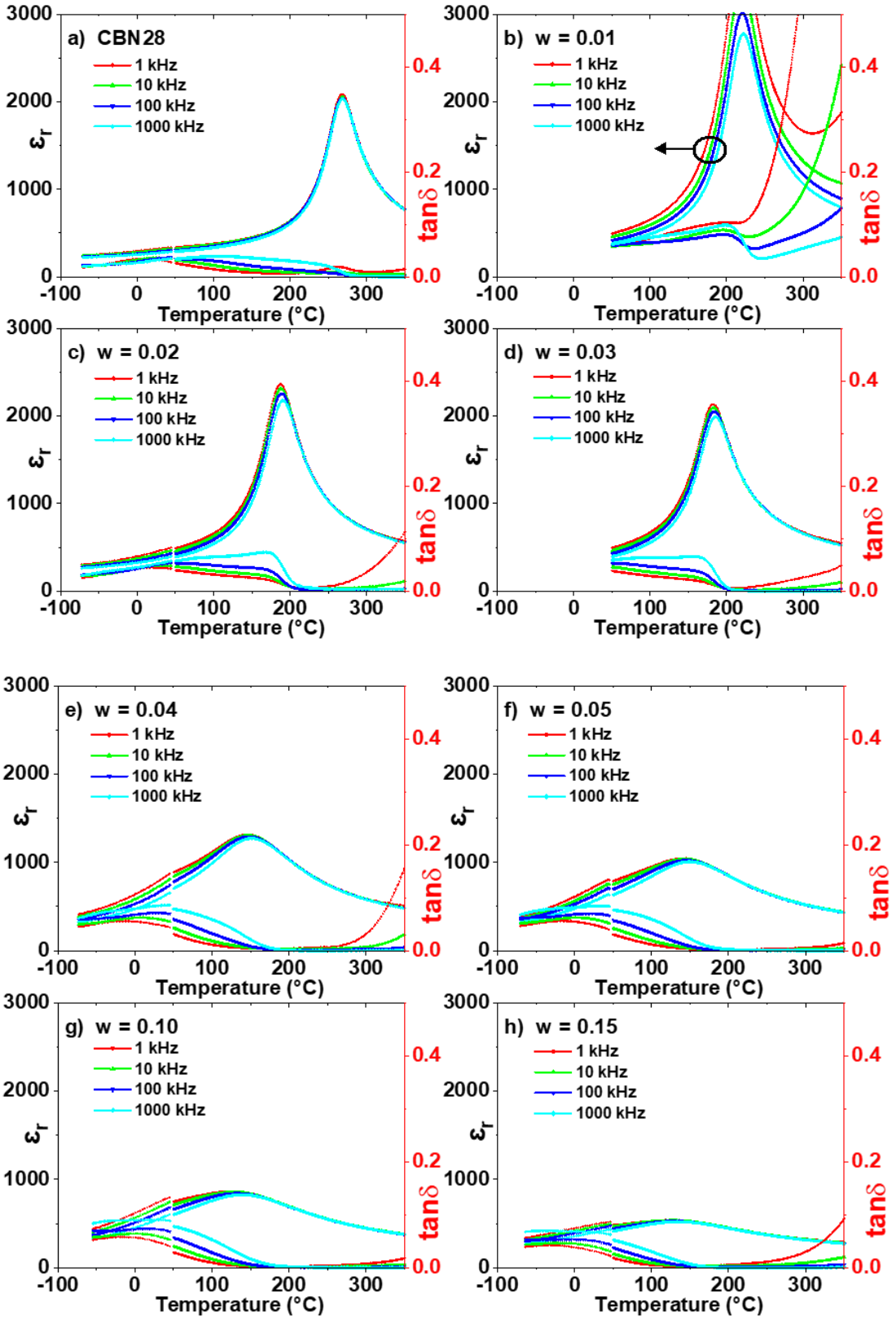

Figure 53. Relative permittivity- and tan δ- temperature responses for $(Ca_{0.28}Ba_{0.72})_{1-3/2w}Y_wNb_2O_6$ [0 ≤ w ≤ 0.15] ceramics, measured at 1 to 1000 kHz. (a) CBN28, (b) w = 0.01, (c) w = 0.02, (d) w = 0.03, (e) w = 0.04, (f) w = 0.05, (g) w = 0.10 and (h) w = 0.15.

Modified Curie-Weiss law ϒ coefficients for $(Ca_{0.28}Ba_{0.72})_{1-3w/2}Y_wNb_2O_6$ [0 ≤ w ≤ 0.15] ceramics are shown in Figure 54, these values correspond to the rate of reduction in permittivity just above T_M and this reflects the diffusivity of the ferroelectric phase transition. CBN28 had a ϒ coefficient of 1.72, comparable to values reported by Han, X. *et al*. [2013]. The ϒ coefficients were stable from [0 ≤ w ≤ 0.02], before increasing slightly to 1.85, for w = 0.03. This increase corresponds to a very minor increase in permittivity stability, see Table 12. The ϒ coefficients then increased further from w = 0.03 to w = 0.10, to a maximum of 2.11, before decreasing to 1.97 for w = 0.15.

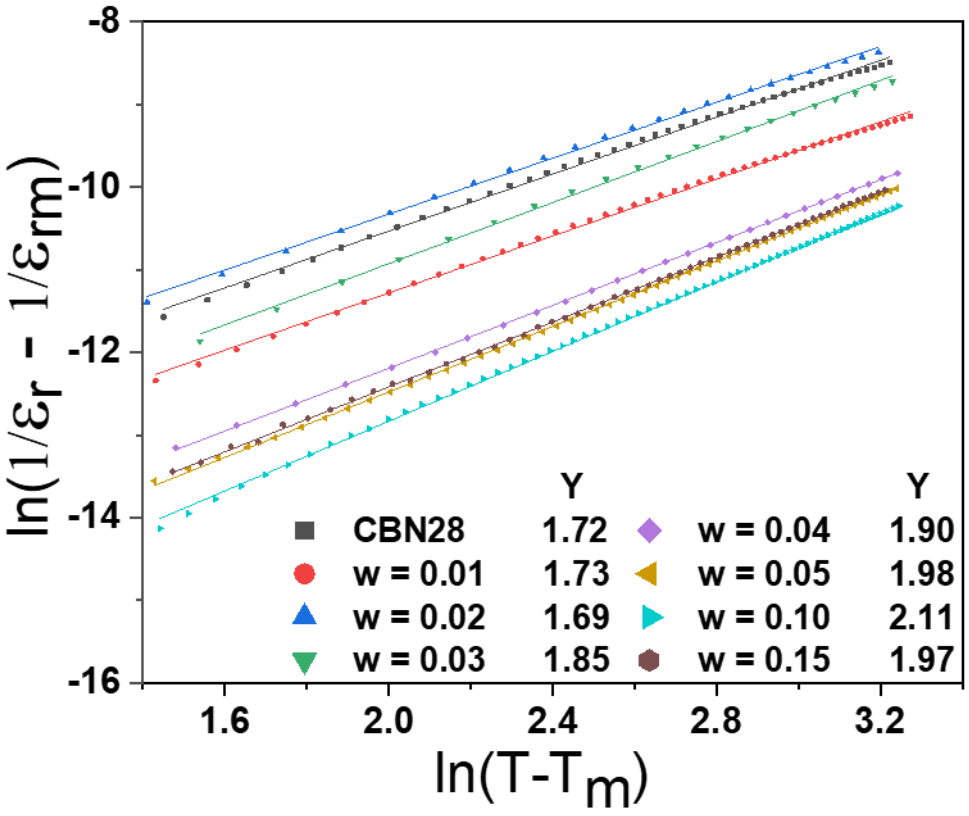

Figure 54. Modified Curie-Weiss law ϒ coefficients for $(Ca_{0.28}Ba_{0.72})_{1-3w/2}Y_wNb_2O_6$ [0 ≤ w ≤ 0.20] ceramics, measured at a frequency of 1 kHz.

Table 10. Summary of dielectric properties for $(Ca_{0.28}Ba_{0.72})_{1-3w/2}Y_wNb_2O_6$ [$0 \leq w \leq 0.20$] ceramics. Values measured at 1 kHz unless otherwise stated. Temperature range values in **bold** and without decimal places indicate the limit of measured temperature.

Sample Code	Nominal formula	T_M at 1 kHz (°C)	T_M at 1000 kHz (°C)	ε_r-max	$\Delta\varepsilon_r$ FWHM (°C) [ε_r at FWHM]	Curie-Weiss law ϒ coefficient	ε_r ±15 % temperature range (°C) [ε_r median]	tan δ < 0.2 temperature range (°C)
CBN28	$Ca_{0.28}Ba_{0.72}Nb_2O_6$	*268*	*269*	2090	*240 to 306 [1210]*	*1.72*	*250 to 290 [1810]*	***-70*** *to* ***350+***
w = 0.01	$(Ca_{0.28}Ba_{0.72})_{0.985}Y_{0.01}Nb_2O_6$	*220*	*222*	3760	*194 to 260 **[1640]*	*1.73*	*203 to 245 [2420]*	***22*** *to 311*
w = 0.02	$(Ca_{0.28}Ba_{0.72})_{0.97}Y_{0.02}Nb_2O_6$	*188*	*191*	2360	*154 to 228[1330]*	*1.69*	*166 to 211 [2060]*	***-70*** *to* ***350+***
w = 0.03	$(Ca_{0.28}Ba_{0.72})_{0.955}Y_{0.03}Nb_2O_6$	*182*	*186*	2130	*152 to 22 [1310]*	*1.85*	*160 to 207 [1860]*	***22*** *to* ***350+***
w = 0.04	$(Ca_{0.28}Ba_{0.72})_{0.94}Y_{0.04}Nb_2O_6$	*147*	*152*	1320	*57 to 219 [910]*	*1.90*	*71 to 209 [1140]*	***-70*** *to* ***350+***
w = 0.05	$(Ca_{0.28}Ba_{0.72})_{0.925}Y_{0.05}Nb_2O_6$	*141*	*150*	1040	*30 to 225 [740]*	*1.98*	*37 to 218 [910]*	***-70*** *to* ***350+***
w = 0.10	$(Ca_{0.28}Ba_{0.72})_{0.85}Y_{0.1}Nb_2O_6$	*126*	*140*	860	*4 to 234 [620]*	*2.11*	*7 to 219 [750]*	***-70*** *to* ***350+***
w = 0.15	$(Ca_{0.28}Ba_{0.72})_{0.775}Y_{0.15}Nb_2O_6$	*126*	*135*	540	*-21 to 224 [410]*	*1.97*	*-27 to 236 [470]*	***-70*** *to* ***350+***
w = 0.20	$(Ca_{0.28}Ba_{0.72})_{0.7}Y_{0.2}Nb_2O_6$	*122*	*-****	540	*-29 to 199 [420]*	-	*-38 to 208 [470]*	***-70*** *to 223*

*Measured permittivity appears elevated, in conjunction with high losses above the permittivity maxima, ε_r-Max at 1000 kHz = 2780

**Values calculated from 1000 kHz data.

***Absence of 1000 kHz data. T_M at 100 kHz = 127 °C.

At sub-coercive field levels (5 kV cm^{-1}) all polarisation-electric field loops possessed elliptical forms (Figure 55(a)), as is seen in perovskite ferroelectrics [Hall, D. A. 1998]. The P_{Max} values were low (< 0.5 μC cm^{-2}), appearing to increase with Y content from CBN28 to w = 0.04, corresponding to an increase in room temperature permittivity, associated with a reduction in $T_{C/M}$ and, for w = 0.04, significant broadening of the permittivity-temperature peak (Figure 53). Values of P_{Max} decreased slightly from w = 0.04 to w = 0.10, and then significantly between w = 0.10 and w = 0.15/0.20, corresponding to suppression of permittivity in these samples. Sample w = 0.01 possessed a broader, more lossy P-E ellipse at a maximum field level of 10 kV cm^{-1}, prior to dielectric breakdown at 18 kV cm^{-1}. When increasing the applied field to 30 kV cm^{-1}, Increases in P_r were higher in the lower Y content compositions (CBN28, w = 0.02 and w = 0.03), with the P_r of w = 0.03 being 0.5 μC cm^{-2}, for the 10 kV cm^{-1} maximum field loop, and 2.0 μC cm^{-2} for the 30 kV cm^{-1} loop. Increases in the P_r values for the higher Y content compositions (w ≥ 0.04) were lower (1.5 μC cm^{-2} for w = 0.04, at maximum field levels of 30 kV cm^{-1}), see Figure 55(f). Characteristic ferroelectric loops were observed for samples 0 ≤ w ≤ 0.10, with samples w = 0.15 and w = 0.20 remaining elliptical and to some extent lossy, at both E_{Max} = 30 and 50 kV cm^{-1}.

The change in dielectric response, observed in the permittivity-temperature plots with increasing Y content (Figure 53), is paired with the observed reduction in remnant polarisations (P_r) and coercive field (E_C) levels in Table 11, measured at maximum applied field of 50 kV cm^{-1}. Here, P_r remained roughly constant and E_C decreased between CBN28 (3.0 μC cm^{-2} and 17.0 kV cm^{-1}) and w = 0.03 (3.0 μC cm^{-2} and 13.0 kV cm^{-1}), before both sharply decreased in sample w = 0.05 (1.0 μC cm^{-2} and 6.5 kV cm^{-1}). The P_r continued to decrease from w = 0.05 to w = 0.20 (0.5 μC cm^{-2}), whilst E_C increased to 10.0 kV cm^{-1}. This increase in E_C is likely due to a reduction in the polarisation response with respect to applied field for these samples.

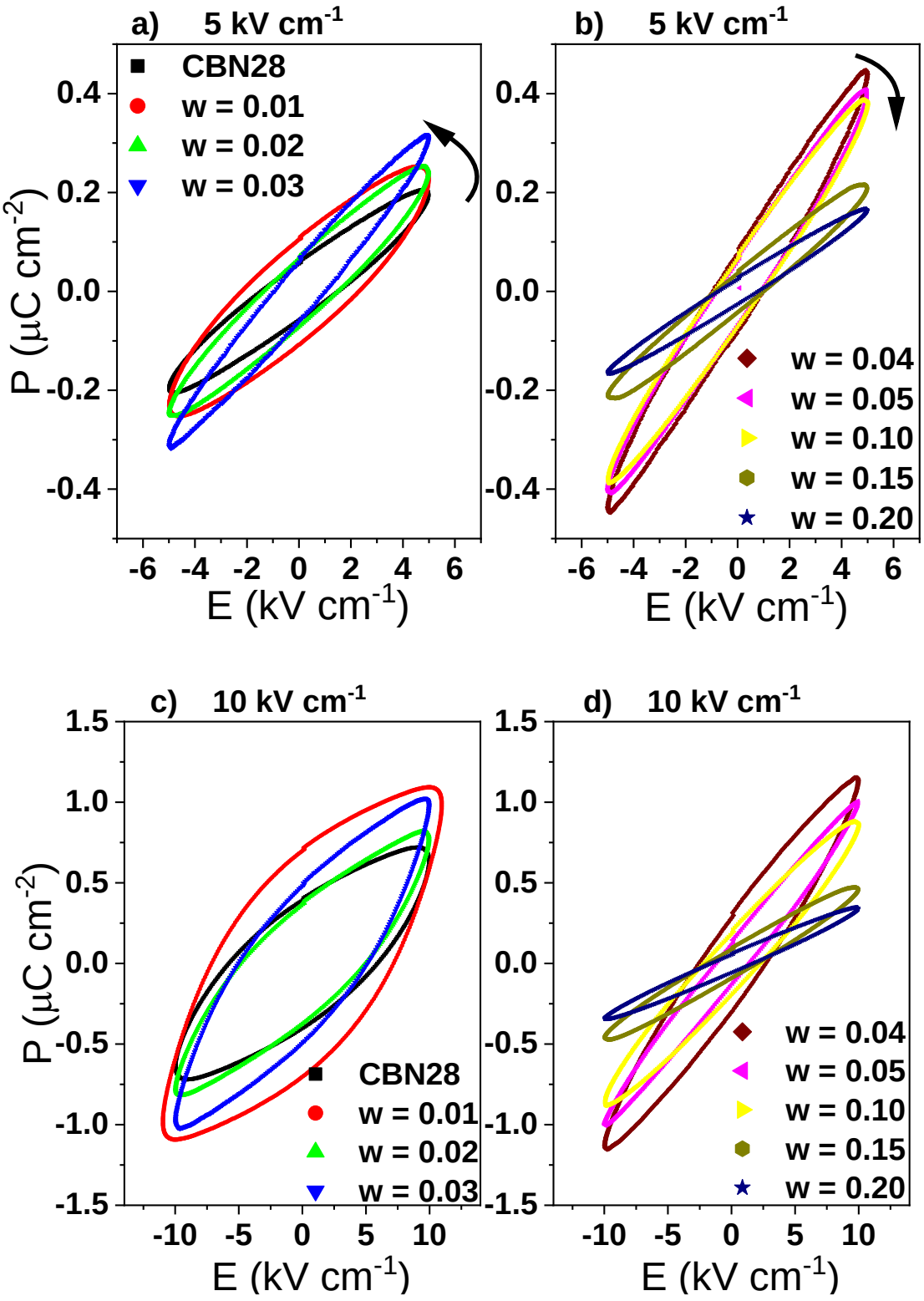
a) 5 kV cm-1
CBN28
w = 0.01
w = 0.02
w = 0.03
b) 5 kV cm-1
w = 0.04
w = 0.05
w = 0.10
w = 0.15
w = 0.20
c) 10 kV cm-1
d) 10 kV cm-1
P (µC cm-2)
E (kV cm-1)

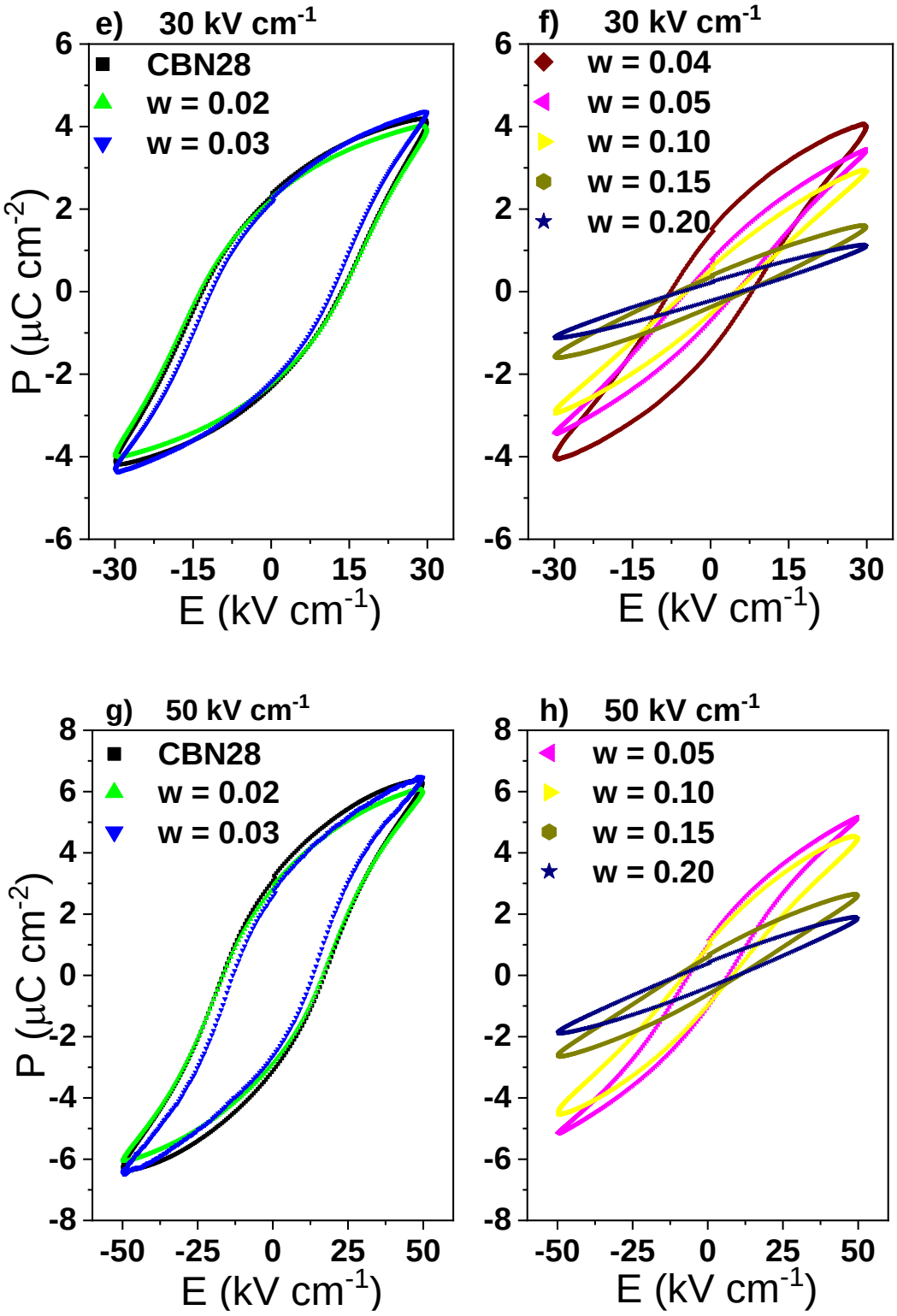

Figure 55. Comparison of P-E loops for $(Ca_{0.28}Ba_{0.72})_{1-3w/2}Y_wNb_2O_6$ [$0 \leq w \leq 0.20$] ceramics, measured at; (a) and (b) 5 kV cm^{-1}, (c) and (d) 10 kV cm^{-1}, (e) and (f) 30 kV cm^{-1}, (g) and (h) 50 kV cm^{-1}. Sample w = 0.01 broke down at 18 kV cm^{-1}. Sample w = 0.04 broke down at 36 kV cm^{-1}. P-E data obtained by Dr. Yizhe Li and Dr. Juncheng Pan, both of the University of Manchester.

Table 11. Summary of ferroelectric properties for $(Ca_{0.28}Ba_{0.72})_{1-3w/2}Y_wNb_2O_6$ [$0 \leq w \leq 0.20$] ceramics. Maximum polarisation (P_{Max}), residual polarisation (P_r) and coercive field (E_C) were measured under a maximum applied field of (+)50 kV cm^{-1}. P-E data obtained by Dr. Yizhe Li and Dr. Juncheng Pan, both of the University of Manchester.

Sample Code	Nominal formula	P_{Max} (μC cm^{-2}) (±0.5)	P_r (μC cm^{-2}) (±0.5)	E_C (kV cm^{-1}) (±0.5)
CBN28	$Ca_{0.28}Ba_{0.72}Nb_2O_6$	6.5	3.0	17.0
w = 0.01	$(Ca_{0.28}Ba_{0.72})_{0.985}Y_{0.01}Nb_2O_6$	-	-	-
w = 0.02	$(Ca_{0.28}Ba_{0.72})_{0.97}Y_{0.02}Nb_2O_6$	6.0	3.0	16.5
w = 0.03	$(Ca_{0.28}Ba_{0.72})_{0.955}Y_{0.03}Nb_2O_6$	6.5	3.0	13.0
w = 0.04	$(Ca_{0.28}Ba_{0.72})_{0.94}Y_{0.04}Nb_2O_6$	-	-	-
w = 0.05	$(Ca_{0.28}Ba_{0.72})_{0.925}Y_{0.05}Nb_2O_6$	5.0	1.0	6.5
w = 0.10	$(Ca_{0.28}Ba_{0.72})_{0.85}Y_{0.1}Nb_2O_6$	4.5	1.0	8.0
w = 0.15	$(Ca_{0.28}Ba_{0.72})_{0.775}Y_{0.15}Nb_2O_6$	3.0	0.5	10.5
w = 0.20	$(Ca_{0.28}Ba_{0.72})_{0.7}Y_{0.2}Nb_2O_6$	2.0	0.5	10.0

The response of the real (ε_r') and imaginary (ε_r'') parts of permittivity for CBN28, w = 0.02, w = 0.04 and w = 0.05, are shown in Figure 56(a) and (b), they roughly correspond to the P-E loop gradient and loop area (hysteresis loss), respectively. At low electric field levels ε_r'-E_0 and ε_r'-E_0 responses were minor, then between 5 and 15 kV cm^{-1} linear relationships were established, before levelling off again above 15 kV cm^{-1}. The gradients of the linear (Rayleigh) regions, for the ε_r'-E_0 and ε_r''-E_0 plots, are the Rayleigh coefficients $\alpha^{/}$ and $\alpha^{//}$, calculated here by Dr. David Hall, they represent the extrinsic ferroelectric domain wall contributions to dielectric permittivity and loss [Eitel, R. A. 2007], see Table 12. A decrease in $\alpha^{/}$ from CBN28 (0.7 x10^{-3} m V^{-1}) to w = 0.05 (0.3 x10^{-3} m V^{-1}) and a more consistent decrease in $\alpha^{//}$ over this range, from 0.8 to 0.1 x10^{-3} m V^{-1}, is observed. The reduction in these coefficients indicates a disruption to, and decrease in, ferroelectric ordering with increasing Y content.

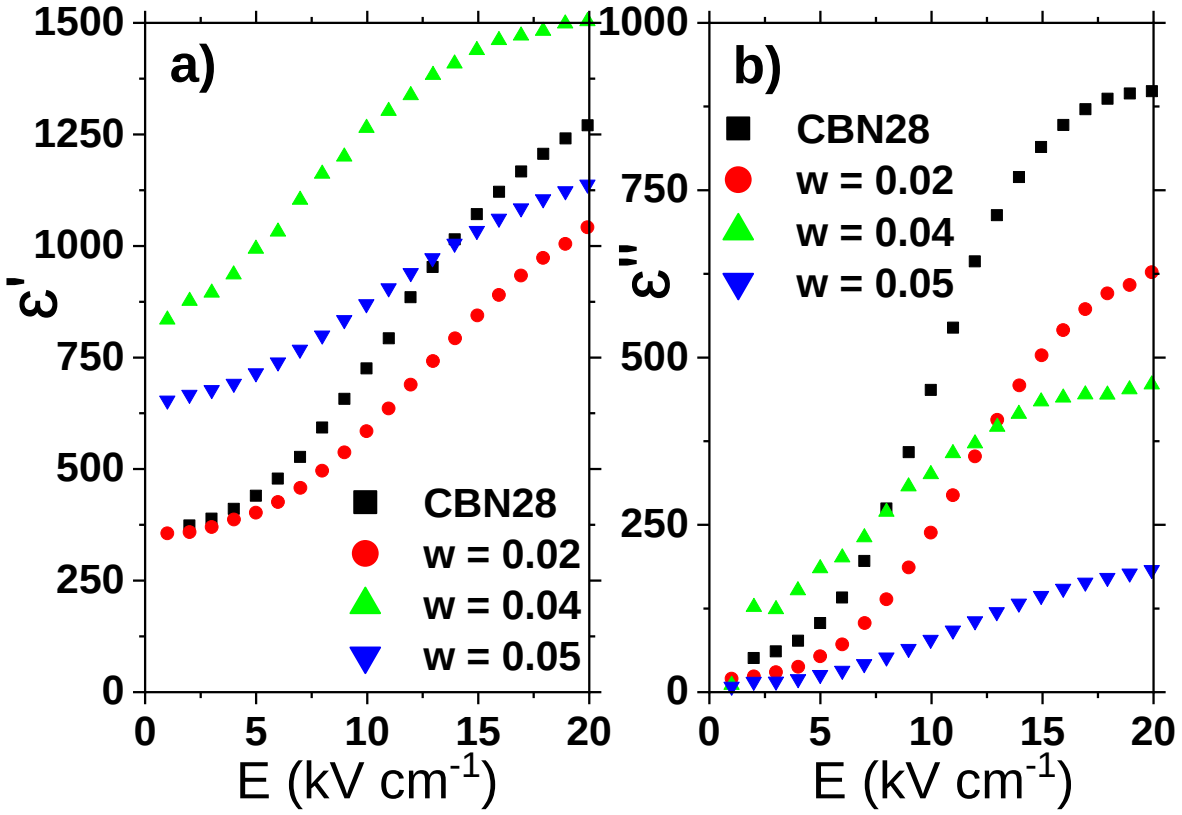

Figure 56. Variation in (a) real, ε_r', and (b) imaginary, ε_r'', parts of the permittivity as a function of electric-field amplitude for select $(Ca_{0.28}Ba_{0.72})_{1-3w/2}Y_wNb_2O_6$ ceramics.

Table 12. Rayleigh coefficients for select $(Ca_{0.28}Ba_{0.72})_{1-3w/2}Y_wNb_2O_6$ ceramics, obtained from nonlinear field-dependent dielectric properties. Rayleigh coefficients calculated by Dr. David Hall, of the University of Manchester.

Sample Code	Nominal formula	α' (10^{-3} m V^{-1})	α'' (10^{-3} m V^{-1})
CBN28	$Ca_{0.28}Ba_{0.72}Nb_2O_6$	0.7	0.8
w = 0.02	$(Ca_{0.28}Ba_{0.72})_{0.97}Y_{0.02}Nb_2O_6$	0.5	0.5
w = 0.04	$(Ca_{0.28}Ba_{0.72})_{0.94}Y_{0.04}Nb_2O_6$	0.5	0.3
w = 0.05	$(Ca_{0.28}Ba_{0.72})_{0.925}Y_{0.05}Nb_2O_6$	0.3	0.1

To summarise, the charge balanced donor doping of CBN28 with Y^{3+} resulted in an increase in the frequency dependence of the temperature of ε_r-Max and elevated low temperature ($T < T_{C/M}$), frequency dispersed (high frequency) losses. These represent a slight shift to weak relaxor behaviour at dopant levels of $w \geq 0.04$ in the formulation $(Ca_{0.28}Ba_{0.72})_{1-3w/2}Y_wNb_2O_6$. A reduction in the samples ferroelectric response accompanied this shift in dielectric character, with P_r and E_C significantly reducing with Y content above $w = 0.03$. However, these P-E responses, whilst narrower, remained characteristically non-linear (ferroelectric and lossy).

5.4 Yttrium and tantalum modification of $Ca_xBa_{1-x}Nb_2O_6$

The improvement in the temperature stability of permittivity for CBN28 with Y^{3+} doping, and assumed A site vacancy increase, motivated further investigation into the chemical modification of CBN. This was performed with the ambition of inducing strong relaxor behaviour and attaining temperature stable permittivity (±15 %) from -55 to 250+ °C.

Co-doping of CBN with Y and Ta, where Ta^{5+} is assumed to substitute isovalently on the B site, was performed according to the formulations $(Ca_xBa_{1-x})_{1-3w/2}Y_wNb_{1.8}Ta_{0.2}O_6$ [x = 0.28, w = 0.02 and 0.04] and [x = 0.22, w = 0.04]. The reduction in the Ca:Ba ratio, in sample x = 0.22 and w = 0.04, was performed to counteract any further reduction in $T_{C/M}$ that may accompany further doping and thus allow for the attainment of higher permittivity at high temperatures (250+ °C). The level of Y content, substituted in place of Ca and Ba, was chosen as it was comparable in level to w = 0.04, in solely Y doped CBN28 which showed no secondary phases. The inconsistent dielectric properties found when solely substituting Y for Ca, in the formulation $Y_rCa_{0.28-3r/2}Ba_{0.72}Nb_2O_6$ [$0.03 \leq r \leq 0.05$], dissuaded further investigation with that base composition. This is despite a reduction in secondary phase presence at r = 0.05.

5.4.1 Summary

XRD patterns for the $(Ca_xBa_{1-x})_{1-3w/2}Y_wNb_{1.8}Ta_{0.2}O_6$ [x = 0.28, w = 0.02 and 0.04] and [x = 0.22, w = 0.04] ceramics are contained in Figure 57, with XRD-derived unit cell refinements and theoretical and measured densities presented in Table 13. Permittivity-temperature, tan δ-temperature responses and modified Curie-Weiss law Ɣ coefficients are presented in Figure 58, with the dielectric data summarised in Table 14. The P-E responses are present in Figure 59, with ferroelectric data summarised in Table 15. These ceramics are henceforth abbreviated with respect to Ca, Y and Ta content e.g. “28Y02 Ta20” for $(Ca_xBa_{1-x})_{1-3w/2}Y_wNb_{1.8}Ta_{0.2}O_6$ [x = 0.28, w = 0.02].

5.4.2 Phase analysis

XRD patterns for the yttrium and tantalum doped CBN ceramics are shown in Figure 57, samples were calcined for 12 h at 1200 ^oC and sintered for 4 h at 1350 ^oC. The patterns for samples 22Y04 Ta20 and 28Y02 Ta20 had no secondary phase peaks. For the 28Y04 Ta20 ceramic, two peaks at 28.3 $^o2\theta$ and 31.5 $^o2\theta$ did not belong to CBN (ICCD 05-001-0283) and were unidentified. Unit cell parameters, simply refined from the XRD data, are presented in Table 13. There was a large increase in *c* parameter with increasing Y content from 28Y02 Ta20 to 28Y04 Ta20, from 7.88 Å to 7.93 Å, which resulted in a decrease in measured density from 5.55 to 5.49 g cm^{-3}. This change was much more significant than the change in density between $(Ca_{0.28}Ba_{0.72})_{1-3w/2}Y_wNb_2O_6$ samples of w = 0.02 and w = 0.04. The simple refinement approach, used here, referenced the measured patterns against the compositionally dissimilar CBN28, possibly introducing significant error despite

comparable and low R_{wp} (%) values. The theoretical density of 22Y04 Ta20 was highest (5.58 g cm^{-3}) owing to the higher Ba content in the unit cell. Measured densities, shown in Table 13, were comparable (95 - 96 %) for the samples.

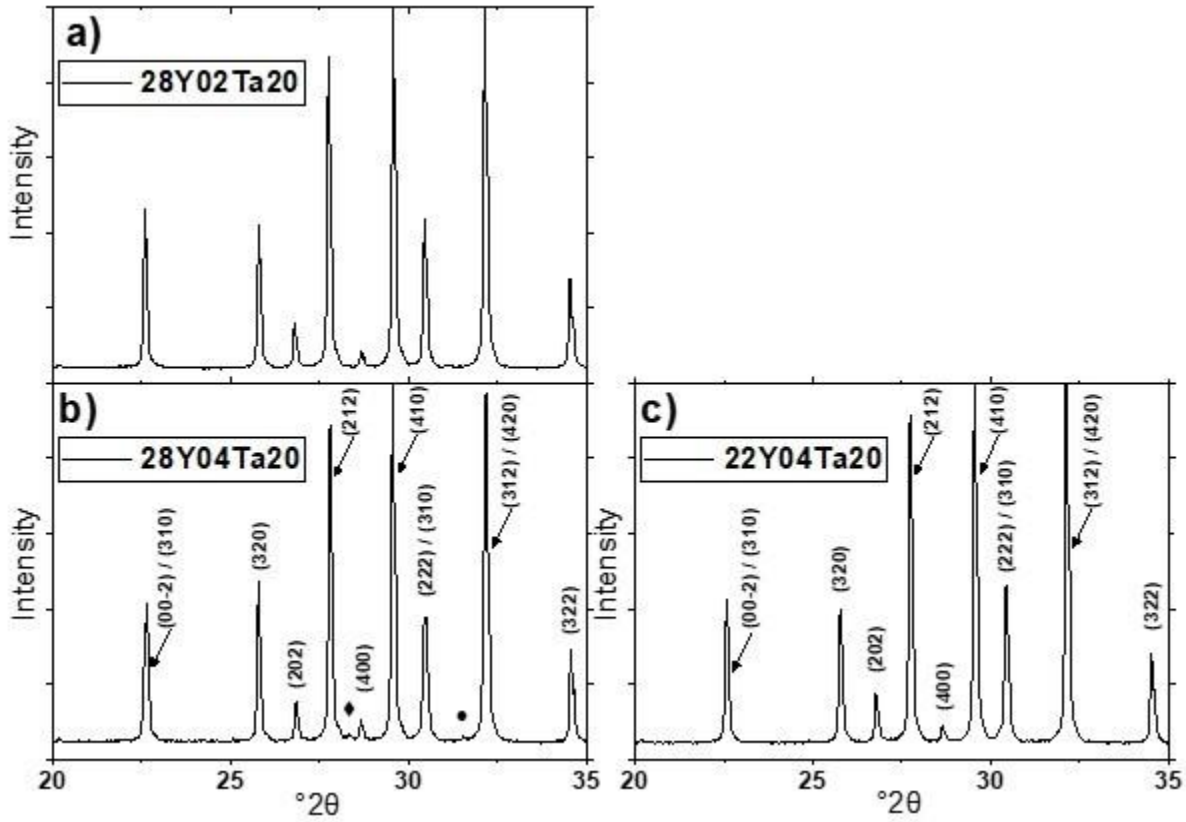

Figure 57. X-ray diffraction patterns of $(Ca_xBa_{1-x})_{1-3w/2}Y_wNb_{1.8}Ta_{0.2}O_6$ for samples of x = 0.28, w = 0.02 and 0.04 and a sample of x = 0.22 and w = 0.04 crushed sintered pellets, indexed according to P4bm structure (ICCD 05-001-0283). Samples were calcined for 12 h at 1200 ^oC and sintered for 4 h at 1350 ^oC. Samples are abbreviated to 28Y02 Ta20, 28Y04 Ta20 and 22Y04 Ta20, respectively. ♦ and ● represent unidentified peaks, possibly corresponding to a $Ca_2Nb_2O_7$ phase.

Table 13. Summary of (pseudo) tetragonal lattice parameters from the unit cell refinement of $(Ca_xBa_{1-x})_{1-3w/2}Y_wNb_{1.8}Ta_{0.2}O_6$ for the samples of x = 0.28, w = 0.02 and 0.04, and the sample of x = 0.22 and w = 0.04, crushed sintered pellets. Lattice parameter error values (in brackets) were provided by Highscore software. Measured density standard deviations [in square brackets] were calculated from a minimum of 5 ceramic pellets.

Sample Code	Nominal formula	a (Å)	c (Å)	Volume (Å^3)	R_{wp} (%)	Theoretical ρ (g cm^{-3})	Measured ρ (g cm^{-3})
28Y02 Ta20	$(Ca_{0.28}Ba_{0.72})_{0.97}Y_{0.02}Nb_{1.8}Ta_{0.2}O_6$	12.45 (1)	7.88 (1)	1222.1	5.27	5.55	5.27 [0.05]
28Y04 Ta20	$(Ca_{0.28}Ba_{0.72})_{0.94}Y_{0.04}Nb_{1.8}Ta_{0.2}O_6$	12.45 (1)	7.93 (1)	1230.2	6.05	5.49	5.24 [0.03]
22Y04 Ta20	$(Ca_{0.22}Ba_{0.78})_{0.94}Y_{0.04}Nb_{1.8}Ta_{0.2}O_6$	12.46 (1)	7.89 (1)	1225.4	5.31	5.58	5.36 [0.03]

5.4.3 Dielectric and ferroelectric properties

The T_M of 28Y02 Ta20 ranged from 91 to 103 ^oC when measured at 1 to 1000 kHz, with ε_r-Max decreasing from 1700 to 1460 over this range, see Figure 58(a). When compared to $(Ca_{0.28}Ba_{0.72})_{1-3w/2}Y_wNb_2O_6$ for w = 0.02 (T_C = 188 and 191 ^oC, measured at 1 and 1000 kHz), the substitution of Nb for Ta caused a significant reduction in the temperature of ε_r-Max and induced much more pronounced frequency dependence of permittivity. This frequency dependence was present in all Y and Ta doped samples in addition to characteristic relaxor-like dielectric losses, which were frequency dispersed at low temperatures. The decrease in 1000 kHz tan δ values on approach to T_M was sharpest in 28Y02 Ta20 which also had a narrower range of temperature stable permittivity (ε_r = 1482 ±15 % from 46 to 144 ^oC), when compared to the higher Y content 28Y04 Ta20 (ε_r = 955 ±15 % from -58 to 110 ^oC). The addition of significant levels of Ta, in $(Ca_{0.28}Ba_{0.72})_{0.94}Y_{0.04}Nb_{1.8}Ta_{0.2}O_6$, resulted in only a minor increase in permittivity-peak broadening over solely Y doped CBN28 (w = 0.04).

Sample 22Y04 Ta20 showed highly comparable degrees of permittivity peak diffusivity (ε_r = 972 ±15 % from -9 to 166 ^{o}C) when compared with 28Y04 Ta20. For 28Y04 Ta20, T_M ranged from 13 to 46 ^{o}C when measured from 1 to 1000 kHz. The T_M for 22Y04 Ta20 was higher (73 ^{o}C, measured at 1 kHz) due to the higher $T_{C/M}$ of unmodified CBN22 [Han, X. 2013]. Frequency dispersion of T_M was less pronounced in 22Y04 Ta20 (T_M at 1000 kHz = 99 ^{o}C) when compared with 28Y04 Ta20.

The T_M (at 1 kHz) of 28Y04 Ta20 was significantly lower than that of solely Y doped CBN, $(Ca_{0.28}Ba_{0.72})_{1-3w/2}Y_wNb_2O_6$ at w = 0.04, and the frequency dispersion of T_M was significantly greater, with the latter exhibiting T_M values of 147 and 152 ^{o}C, when measured at 1 and 1000 kHz. This transition from weak relaxor behaviour in the Y doped CBN28s [w ≥ 0.04] to much more pronounced frequency dependence of permittivity in Y and Ta doped CBN28 did translate into a slightly increased range of temperature stability for 28Y04 Ta20, compared with $(Ca_{0.28}Ba_{0.72})_{1-3w/2}Y_wNb_2O_6$ at w = 0.04 (ε_r = 914 ±15 % from 57 to 219 ^{o}C). High-temperature (T > 250 °C), low-frequency tan δ peaks were present in Y and Ta doped CBN. Similarly to solely Y doped CBN (excluding w = 0.01), no or only very minor increases in high-temperature ($T \geq T_M$), low-frequency permittivity values corresponded to these losses. Figure 44 (Section 5.2) showed that these minor losses could likely be reduced, but not removed, by annealing.

Modified Curie-Weiss law ϒ coefficients increased from 1.88 to 1.94 with increasing Y content, from 28Y02 Ta20 to 28Y04 Ta20, Figure 58(d). A much higher ϒ coefficient of 2.44 was calculated for 22Y04 Ta20 with the ε_r just above T_M decreasing non-linearly, initially remaining closer to ε_r-Max. This is evidenced by the ln(ε_r - ε_r-Max) values deviating from the linear trend line, of gradient 2.44, in Figure 58(d).

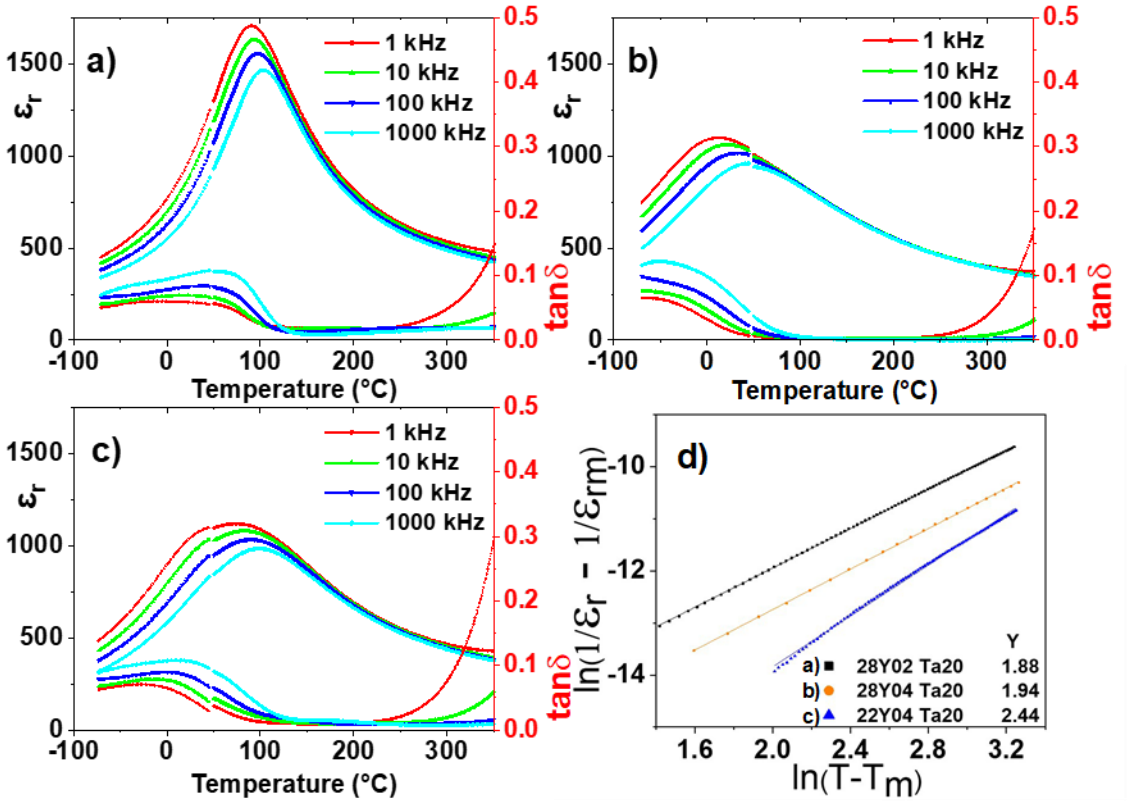

Figure 58. Relative permittivity- and tan δ- temperature responses for $(Ca_xBa_{1-x})_{1-3w/2}Y_wNb_{1.8}Ta_{0.2}O_6$ samples of x = 0.28, w = 0.02 and 0.04 and of x = 0.22, w = 0.04 ceramics, measured at 1 to 1000 kHz, (a) 28Y02 Ta20, (b) 28Y04 Ta20, (c) 22Y02 Ta20, and (d) modified Curie-Weiss law Y coefficients, measured at a frequency of 1 kHz. Samples are abbreviated to 28Y02 Ta20, 28Y04 Ta20 and 22Y04 Ta20, respectively.

Table 14. Summary of dielectric data for $(Ca_xBa_{1-x})_{1-3w/2}Y_wNb_{1.8}Ta_{0.2}O_6$ [x = 0.28, w = 0.02 and 0.04] and [x = 0.22, w = 0.04] ceramics, permittivity values measured at 1 kHz unless otherwise stated. Temperature range values in **bold** and without decimal places indicate the limit of measured temperature.

Sample Code	Nominal formula	T_M at 1 kHz (°C)	T_M at 1000 kHz (°C)	ε_r-Max	$\Delta\varepsilon_r$ FWHM (°C) [ε_r at FWHM]	Curie-Weiss law ϒ coefficient	ε_r ±15 % temperature range (°C) [ε_r median]	tan δ < 0.2 temperature range (°C)
28Y02 Ta20	$(Ca_{0.28}Ba_{0.72})_{0.97}Y_{0.02}Nb_{1.8}Ta_{0.2}O_6$	*91*	*103*	1700	*36 to 156 [1110]*	*1.88*	*46 to 144 [1480]*	***-70** to **350+***
28Y04 Ta20	$(Ca_{0.28}Ba_{0.72})_{0.94}Y_{0.04}Nb_{1.8}Ta_{0.2}O_6$	*13*	*46*	1100	***-70** to 134 [740]*	*1.94*	*-58 to 110 [950]*	***-70** to **350+***
22Y04 Ta20	$(Ca_{0.22}Ba_{0.78})_{0.94}Y_{0.04}Nb_{1.8}Ta_{0.2}O_6$	*71*	*99*	1120	*-17 to 179 [770]*	*2.44*	*-9 to 166 [970]*	***-70** to 330.7*

At sub-coercive field levels, Figure 59(a), P-E loops for the Y and Ta doped CBN ceramics took narrow elliptical forms. Sample 28Y02 Ta20 broke down at 15 kV cm^{-1}. The 28/22Y04 Ta20 hysteresis loops remained narrow up to 40 kV cm^{-1}, although they did take characteristic ferroelectric (non-linear) forms. At this maximum applied field level, the remnant polarisation (P_r) values for 22Y04 Ta20 and 28Y04 Ta20 were low (both ~0.5 µC cm^{-2}), which coincides with strong frequency dependence of permittivity (Figure 58), as is seen elsewhere in relaxor ferroelectrics [Hou, S. 2022].

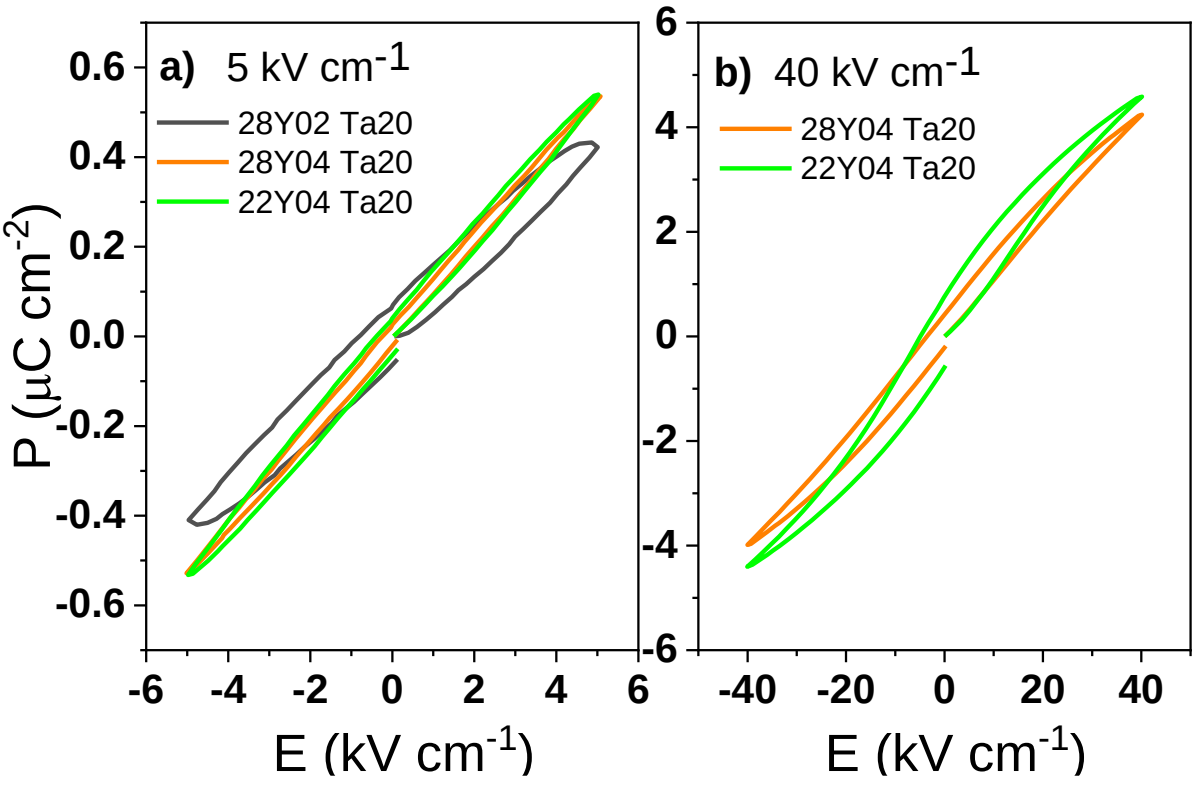

Figure 59. Comparison of P-E loops for $(Ca_xBa_{1-x})_{1-3w/2}Y_wNb_{1.8}Ta_{0.2}O_6$ samples of x = 0.28, w = 0.02 and 0.04 and of x = 0.22, w = 0.04 ceramics, measured at; (a) 5 kV cm^{-1} and (b) 40 kV cm^{-1}.

Table 15. Summary of ferroelectric data for $(Ca_xBa_{1-x})_{1-3w/2}Y_wNb_{1.8}Ta_{0.2}O_6$ samples of x = 0.28, w = 0.02 and 0.04 and of x = 0.22, w = 0.04 ceramics. Maximum polarisation (P_{Max}), residual polarisation (P_r) and coercive field (E_C) were measured under a maximum applied field of (+)40kV cm^{-1}.

Sample Code	Nominal formula	P_{Max} (µC cm^{-2}) (±0.5)	P_r (µC cm^{-2}) (±0.5)	E_C (kV cm^{-1}) (±0.5)
28Y02 Ta20	$(Ca_{0.28}Ba_{0.72})_{0.97}Y_{0.02}Nb_{1.8}Ta_{0.2}O_6$	-	-	-
28Y04 Ta20	$(Ca_{0.28}Ba_{0.72})_{0.94}Y_{0.04}Nb_{1.8}Ta_{0.2}O_6$	4.0	0.5	3.0
22Y04 Ta20	$(Ca_{0.22}Ba_{0.78})_{0.94}Y_{0.04}Nb_{1.8}Ta_{0.2}O_6$	4.5	0.5	3.0

To summarise, secondary phases, possibly containing Ca, were identified in $(Ca_{0.28}Ba_{0.72})_{0.94}Y_{0.04}Nb_{1.8}Ta_{0.2}O_{6.}$ These phases were not identified when the Ca:Ba ratio was reduced, in sample $(Ca_{0.22}Ba_{0.78})_{0.94}Y_{0.04}Nb_{1.8}Ta_{0.2}O_6$. Improvements in the temperature stability of permittivity were only marginal in the Y and Ta co-doped CBN28 samples, when compared with solely Y doped CBN28. A reduction in the Ca:Ba ratio resulted in a significant increase in T_M. The addition of Ta to Y doped CBN resulted in pronounced frequency dependence of permittivity and significantly narrower P-E loops. Importantly, this strong relaxor character may be useful for energy storage applications.

5.5 Discussion

5.5.1 CBN Microstructure and phase purity

CBN28 ceramics, calcined for 20 h and sintered for 4 h, had high measured densities (98 - 96 %) when sintering at a wide range of temperatures (1325 - 1400 ^{o}C), see Figure 40. Typically, CBN28 sintering occurs between 1330 - 1350 ^{o}C after much shorter calcination times, although CuO (0.4 wt.%) has been used as a sintering aid to produce ceramics of high density (97.25 - 98.25 %) at a wide range of reduced temperatures (1240 - 1320 ^{o}C) [Wei, L. 2014-Feb]. One reason for the typically narrow range of reported sinter temperatures may be a propensity for abnormal grain growth fuelled by suspected partial liquid phase sintering at higher temperatures [Ke, S. 2008], which becomes more acute in CBN as Ca content increases. High Ca content ($Ca_xBa_{1-x}Nb_2O_6$, $x \geq 0.28$) has been linked to $CaNb_2O_6$ secondary phases in calcined CBN powders [Han, X. 2013] and in SBN the presence of similar secondary phases is associated with abnormal grain growth and liquid phase sintering [Kim, M-S. 2002] and [Lee, H-Y. 1998]. It is possible that the presence of secondary phases post calcination necessitates sintering CBN at finely controlled conditions and that extending the calcination time, and so presumably reducing the secondary phase content, allows for the extension of sintering conditions to higher temperatures.

Micro-cracking was present in CBN28 sintered at higher temperatures (1375+ ^{o}C), see Figure 40(d) and (e). Such inter- and intra-granular cracks are largely absent in the CBN literature. Rather, grains are either small (~2 µm measured diameter) and nearly equiaxed or, more often, show a pillar-type morphology with measured grain lengths sometimes exceeding 10 µm. This pillar type morphology is presumed to be due to the (0 0 1) growth habit of tungsten bronzes [Glass, A. M. 1969]. Some micro-cracks were present in CBN28 which was calcined for 4 h and sintered at 1350 ^{o}C (Section 5.3, Figure 43). Whilst increasing the calcination time to 20 h and sintering at 1350 °C (in Figure 40(c)), resulted in the absence of micro-cracking. Micro-cracking was also relieved when doping with Y $(Ca_{0.28}Ba_{0.72})_{1-3w/2}Y_wNb_2O_6$, $w \geq 0.03$. Micro-cracking has been reported in CSBN, where it was associated with "abnormal grain growth" [Abdelli, F. 2016]. Micro-cracking in CBN may be associated with sintering at higher than optimal temperatures, given its presence in this work when sintering at higher temperatures and its association with abnormal grain growth in the work of others [Abdelli, F. 2016]. Further experiments, examining the Vickers hardness of Y doped CBN28, via measuring the length of mechanically induced micro-cracks, may help explain the reduction in micro-cracking with Y doping.

Apart from the relieving of micro-cracks, the influence of increasing Y addition in single-phase CBN grain morphology was negligible. Although maximum measured grain size for the Y doped samples was consistent (varying from 11.4 to 13.1 µm, Table 9), more so than undoped CBN28 calcined for 20 h and sintered at 1350 - 1400 °C, (which varied from 6.4 to 10.0 µm, Table 7). This consistency,

despite variations in composition and sintering temperature, may indicate that Y doping inhibits exaggerated grain growth.

Secondary phases, associated with doping at Y level of w ≥ 0.05, did result in much smaller grain sizes, with average calculated grain size decreasing from ~7 µm in CBN28 to ~ 3 µm in sample w = 0.10 (maximum grain sizes were 8.4 and 4.1 µm respectively), see Table 9. The pinning of grain boundaries by secondary phases is known to limit grain size and is likely responsible for the reduction in grain size observed here [Cao, H. 2006] and [Kang, S-J. L. 2004]. The presence of secondary phases was reduced but not removed when solely substituting Y for Ca in the composition, r = 0.05, see Figure 47. The similar ionic radii of Y (1.075 Å, CN9) and Ca (1.18 Å, CN9) (1.34 Å, CN12) likely resulted in increased competition for the A1 site, over the Ba (1.61 Å, CN12) containing A2 site, and promoted the presence of Ca-containing secondary phases in w = 0.05. Whilst these secondary phases were partly addressed by solely substituting Y for Ca, in r = 0.05, dielectric results were less promising, see Appendix 4.

The presence of low-level Y and assumed A site vacancy inclusion promoted single phase synthesis, likely by improving sintering kinetics. As seen when comparing CBN28 to low Y content CBN28s (Figure 46(a) and (b) to (e)). The addition of vacancies to filled TBs is known to improve atomic diffusion rates and it is possible that the further addition of vacancies to an already unfilled TB would also improve atomic diffusion [Jang, C-Y. 2004]. A possible lowering of the melting point, with low level dopant inclusion, may also improve sinter kinetics.

5.5.2 Low frequency, high temperature dielectric losses and thermal processing in CBN

When calcined for 4 h, CBN28 had a significantly different T_C (268 ^oC, measured at 1 kHz) to that of CBN28 calcined for 20 h and also sintered at a maximum temperature of 1350 ^oC (232 ^oC, measured at 1000 kHz), with typical reported values of CBN28 T_C ranging from 235 - 255 ^oC. The presence of secondary phase $CaNb_2O_6$ in 4 h-calcined CBN28 may have reduced the ratio of Ca:Ba in the parent phase, resulting in elevation of the T_C [Han, X. 2013]. However, a not insignificant decrease in single-phase CBN28 T_C occurred when increasing sinter temperature from 1375 to 1400 ^oC (T_C ~232 - 226 ^oC), see Figure 43. This suggests that thermal treatment does play some role in the destabilisation of the ferroelectric phase. This decrease in T_C, when sintering at 1400 °C is accompanied by a sharp increase in ε_r-Max, not dissimilar to the reduction in T_C and an increase in ε_r-Max associated with the low-level doping of CBN, for example with Cu [Wei, L. 2014-Feb]. Sintering at very high temperatures in Alumina crucibles, which had previously contained compounds other than CBN precursors, may have caused low-level (but dielectrically significant), contamination of this sample. The absence of significant T_C reduction, when increasing sinter temperature from 1325 to 1375 °C, suggests that

these samples were less effected by the proposed contamination, when comparing 1000 kHz data in which (low frequency) losses were absent (T_C at 1000 kHz varied from 235 to 232 °C), see Figure 43.

The presence of high temperature, low frequency dielectric loss peaks can be found in CBN28 as well as Y and Y + Ta doped CBNs (Figures 53 and 58). This feature appeared to vary independently of composition and was particularly apparent in CBN28 calcined for 20 h and sintered at ≤ 1350 ^{o}C, where it is observed in conjunction with frequency dispersion of ε_r-Max and high temperature, low frequency permittivity peaks (Figure 43). Other authors have also reported these dielectric loss peaks in CBN, and they also often vary independently to compositional trends, apart from when doping with volatile compounds (Na and K doping), where they are exacerbated [Yang, B. 2016].

The combination of elevated low-frequency dielectric loss and elevated permittivity is suggestive of a particular kind of loss mechanism; the intragranular motion of charge defects (bulk-conductivity) [Lee, J-H. 2022]. Here, the conduction of charge carrying defects up to an insulating grain boundary produces a capacitor-like affect, increasing permittivity. The effect is more apparent at low frequencies as the motion of these defects is reduced at higher frequencies. The observed loss mechanism is thermally activated, often becoming noticeable above 250 or 300 ^{o}C. Once activated or disturbed, by initial heating, the losses may be higher (at first) upon subsequent heating, see Figure 44.

Oxygen vacancies are known to cause similar thermally activated losses in perovskites as proximate pairs of vacant cation and (oxygen) anion sites, termed a Schottky defects, become mobile at temperatures around 250 ^{o}C and contribute to low frequency dielectric loss [Lee, J-H. 2022] and [Viola, G. 2013]. In Na and K doped CBN [Yang, B. 2018], which exhibits significant low-frequency, high-temperature losses, oxygen vacancies might be expected due to the presence of volatile Na- and K- oxides during sintering. The volatile loss of these cations promotes the presence of charge compensating oxygen vacancies in the structure [Stiener, S. 2019].

In undoped CBN the volatility of precursor carbonates and oxides is sufficiently low that site vacancies due to volatile loss is considered unlikely. However, site vacancies are not required for the promotion of oxygen vacancies. The reduction of cation valency can also be paired with charge balancing oxygen vacancies. Such reduction, of some Nb^{5+} to Nb^{4+}, is known to occur in compositions such as $LiNbO_3$ and $SrNbO_3$ [Ketchum, J. L. 1983] and [Ofoegbuna, T. 2019]. This cation reduction has been linked to oxygen vacancies and is promoted by sintering in low oxygen partial pressures. The reduction of Nb ions is also promoted at high temperatures [Ziolek, M. 2003]. Prolonged calcination, may, therefore, promote Nb ion reduction and oxygen vacancy presence, even at 1200 ^{o}C which is lower than the conventional sinter temperature for CBN28. However, uncertainties with regards to

the valency states of Nb in CBN and the mechanisms of high-temperature dielectric loss require further study by Raman spectroscopy, X-ray Photoelectron spectroscopy (XPS) or TEM based electron energy loss spectroscopy (EELS).

Low-frequency, high-temperature dielectric losses appeared to decrease with increasing sinter temperature to 1375 or 1400 ^{o}C in Figure 43. However, the heating curve data (H0 and H1) in Figure 44 shows that similar losses increase after standing at room temperature (from 1 kHz tan δ at 300 ^{o}C = ~ 0.3 to 1 kHz tan δ at 300 ^{o}C = ~ 0.4). Lower 1 kHz tan δ values were observed between 200 and 300 ^{o}C upon initial heating when compared with subsequent heating (H1 and H2 in Figure 44). This suggests that the species responsible for the losses was 'locked-in' after standing untouched for 15 months and required thermal disturbance or activation by heating above 300 ^{o}C. Annealing, which occurred during cyclical heating to temperatures of 300 to 400 ^{o}C, reduced these 1 kHz losses to tan δ = 0.18 (at 300 ^{o}C) after 3 thermal cycles between 130 ^{o}C and 400 ^{o}C and to 1 kHz tan δ = 0.084 (at 295 ^{o}C) after the application of a sinusoidal current up to a maximum field of 20 kV cm^{-1} and a further 3 cycles between 200 and 300 ^{o}C.

It is possible that the decrease in high-temperature dielectric losses, observed when increasing sinter temperature for the 20 h-calcined CBN28's (in Figure 43), were caused by other thermal processing factors like the time left standing untouched at room temperature (i.e. the time between the application of electrodes, at 550 ^{o}C, and dielectric measurement). A more systematic study of the onset and annealing-out of high-temperature, low-frequency dielectric loss is required, which may also serve to elucidate the mechanism responsible for these affects in CBN. If oxygen vacancies are identified then doping with a variable valency ion, such as $Mn^{2\text{ to }4+}$, may reduce this lossy feature. In Mn doped $BiFeO_3$, a reduction in the density of oxygen vacancies was observed [Yoneda, Y. 2012].

5.5.3 High frequency, low temperature dielectric losses, their hysteresis and dependence on polar ordering

At temperatures below $T_{C/M}$ CBN-based compositions (and also CBN28) show high frequency dielectric loss peaks. The magnitude and diffusivity of these loss peaks appears to be linked to composition, initially increasing in magnitude with Y content from w = 0.00 to w = 0.03 then becoming more diffuse in its decline on approach to T_M for w ≥ 0.04, see Figure 53. Such peaks are common in relaxor ferroelectrics and have been ascribed to the relaxation and hysteresis motion of domain boundaries [Chen, I-W. 1998] and [Lee, J-H. 2022]. At higher frequencies the rate of domain wall motion and the accumulation of loss is greatest, provided that the domains are small and mobile enough to follow the high frequency AC. Depolarisation on approach to $T_{C/M}$ causes these losses to reduce. The diffusivity of the reducing loss-peak, likewise with the diffusivity of the

permittivity peak around $T_{C/M}$, gives an indication of the increased diffusivity of phase transition. Single crystal CBN28 has been shown, by second harmonic generation (SHG) of light, to have a domain-size dependant T_C [Heine, U. 2009]. This k-space spectroscopy linked increased SHG of light that was traveling along the c-axis and increased on approach to $T_{C,}$ with finer domain size.

Repeated thermal cycling of CBN28-12h (Calcined for 12 h at 1200 ^{o}C, sintered at 1350 ^{o}C for 4 h) gave 1000 kHz ε_r-Max values that varied by 2 - 3 % in a near-linear correlation with tan δ-Max values, see Figure 45(d). Smaller domains, and higher domain wall densities have been linked to higher values of permittivity and may therefore explain this correlation [Xu, R. 2014]. A recent structural investigation on a CBN28 ceramic (produced by the author) was performed by TEM [Beanland, R. 2023]. In that report, hysteresis of the domain structure was evidenced by the hysteresis of incommensurate structuring, derived from electron diffraction. The incommensurability factor, σ, was linked to the presence of domains and found to differ between the initial measurement and the measurement performed after heating and cooling. Reported here, dielectric hysteresis is complimentary to that interpretation of domain-size hysteresis in CBN28. However, dielectric analysis offers only indirect observations regarding the hysteresis of domain size-distribution in CBN28.

5.5.4 The diffuse ferroelectric to weak relaxor transition in Y modified CBN

The inclusion of the smaller Y ion and the addition of vacancies, both on the A sites, resulted in a reduction in lattice tetragonality (*c*/*a*) and $T_{C/M}$, see Table 8 and Table 10. This correlation between *c*/*a* and $T_{C/M}$ has previously been observed in TBs [Gardener, J. 2014]. In that report, vacancy concentration was controlled and smaller A site ions were associated with increased tetragonality.

Filled niobate TB's have the general formula $AS_3Nb_5O_{15}$, where AS refers to the occupied A site. In unfilled TB's some vacancies are present in the formula $VS_{0.5}AS_{2.5}Nb_5O_{15}$ (= $VS_{0.2}AS_1Nb_2O_6$), where VS refers to the vacant A site. The addition of further vacancies at half the concentration of Y presence results in the formula $VS_{0.2+w/2}AS_{1-w/2}Nb_2O_6$. For w = 0.02 in Y modified CBN28, $VS_{0.21}AS_{0.99}Nb_2O_6$, a 5 % increase in the nominal number of vacant A sites is assumed.

An increase in ε_r-Max to 2360 was observed with low level of Y modification (w = 0.02), and of an assumed A site vacancy inclusion in, CBN28 (ε_r-Max = 2070), see Figure 53. Such permittivity increases may occur as dopant ions reduce the size of domains without inducing a significantly diffuse phase transition in the material [Xu, R. 2014]. Here, the presence of additional A site vacancies may have promoted octahedral tilting and further disrupted polar ordering [Cao, L. 2022] and [Gardener, J. 2016]. The increase in 1000 kHz dielectric losses below T_C indicates this reduction

in domain size. The sharp decrease in 1000 kHz tan δ on approach to T_C suggests that depolarisation (phase transition) occurred over a narrow temperature range in samples w = 0.02 and w = 0.03.

A different dielectric character was observed in sample w = 0.04, permittivity and high frequency tan δ peaks were much more diffuse, although frequency dispersion of T_M, when comparing the temperature of ε_r-Max at 1 and 1000 kHz, was relatively minor (ΔT = 5 °C). This ΔT had increased linearly between CBN28, where it was insignificant (ΔT = 1 °C), and w = 0.04. Sample w = 0.05 showed a greater frequency dispersion of T_M, which ranged from 141 to 150 ^{o}C as frequency increased from 1 to 1000 kHz. Polarisation-Electric field loops also showed a slight transition in ferroelectric character, with apparent polar structures initially showing no significant decrease in mobility between CBN28 and w = 0.03 (P_r = 3.0 μC cm^{-2} for both) before residual polarisation decreased in w = 0.05 to 1.0 μC cm^{-2} (max field strengths = 50 kV cm^{-1}), see Figure 54. Coercive field strengths decreased more linearly with Y addition. It can be concluded that Y modification of CBN, in the formulation $(Ca_{0.28}Ba_{0.72})_{1-3w/2}Y_wNb_2O_6$ for$0 \leq w \leq 0.20$, results in a transition from a slightly diffuse ferroelectric ($w \leq 0.03$) to a more diffuse and possibly weak relaxor character with significantly improved temperature stability of permittivity. Although P-E loops, whilst narrower, remained lossy and characteristically ferroelectric whilst frequency dependence of permittivity was minor.

Microstructural elemental analysis by TEM-EDX of sample w = 0.10 showed no core-shell structured chemical inhomogeneities (Figure 52), such compositional distributions have been the cause of broader permittivity-temperature profiles in some $BaTiO_3$-based compositions [Burn, I. 1976]. For such materials, these micron-scaled variations in composition offer an explanation for the occurrence of a diffuse phase transitions in the bulk material, but this is not the case for Y modified CBN.

The primary cause of the improved temperature stability of permittivity in Y modified CBN and the slight transition in ferroelectric character is likely to be due to the increased atomic disorder on the A1 site and vacancy presence on the A1 or A2 sites. Atomic site disordering results in variations of the local chemical environment and electrical fields and promotes diffuse phase transition in the bulk, associated with a broader range of local (unit cell level) phase transition temperatures. Vacancies on the A1 site have induced varied tilting of the B_2O_6 octahedra in the isostructural unfilled TB SBN [Paściak, M. 2019]. This disordered tilting is likewise associated with disruption to the ordering of chains of like-polarised unit cells within the c-axis. Strong frequency dependence of permittivity is observed in SBN, whose A site cations are also less segregated by ion size and site occupancy. The presence of A1 site vacancies may have been supressed in Y modified CBN28, given

the increased competition for the A1 site, when doping with Y and substituting out both Ca and Ba. Paściak *et al*. [2019] found that A2 site vacancies did not induce the same degree of octahedral tilting. It is possible that this A1 site competition inhibited the development of strong relaxor behaviour in Y doped CBN, given that very recent donor doping of CBN, by solely substituting out Ca, at levels comparable to twice that of w = 0.04 (w = 0.08) did produce single-phase samples with strong frequency dependence of permittivity [Cao, L. 2024]. Interestingly, the temperature range of stable permittivity was greater in Y doped CBN (w = 0.04) produced here than in the recent donor doped CBNs (w = 0.08) of Cao, L *et al*. [2024]. These recent CBNs had potential energy storage applications, rather than high temperature capacitor applications.

Despite limited frequency dependence of permittivity, some disruption to polar ordering with Y and vacancy addition is evidenced here by a reduction in the Rayleigh coefficients of the P-E loops (Figure 56, Table 12) and reduced residual polarisations and coercive fields. Presumably, this disruption did not disorder the polar units significantly enough to induce strong relaxor behaviour, which is associated with finer, less cohesive, transient nano-scaled polar structures and near linear P-E responses.

5.5.5 Relaxor behaviour in Y and Ta modified CBN

XRD data for Y and Ta modified CBN showed a large, and unexpected, increase in *c* parameter with Y addition, from 28Y02 Ta20 to 28Y04 Ta20, see Figure 57 and Table 13. This may be due to the simplistic parameter refinement which used a CBN28 reference pattern. This reference pattern may have been too dissimilar to the nominal compositions for an unchanged assessment of lattice parameters to be made. Although, *a* parameters appeared consistent, increasing slightly from 12.45 to 12.46 Å with an increase in Ba content from 28Y04 Ta20 to 22Y04 Ta20. This is consistent with the Ba ion being larger than the Ca ion. A secondary phase in 28Y04 Ta20, possibly Ca containing such as $Ca_2Nb_2O_7$, was eliminated by reducing Ca content in 22Y04 Ta20.

The dielectric properties of all Ta doped compositions showed strong frequency dispersion of permittivity and minor broadening of the permittivity peaks around T_M, when compared with solely Y doped compositions (compare Figures 53 and 58). The temperature of ε_r-Max was also significantly reduced by Ta inclusion. Comparable Ta doping of Na modified CBN has also shown limited broadening of the permittivity peak, though without frequency dispersion of permittivity at T_C [Yang, B. 2018].

The Ta^{5+} ion has a highly comparable ionic radius to the isovalent Nb^{5+} ion (0.64 Å, CN6), which may explain the limited influence of Ta inclusion on structural disordering and permittivity-peak broadening. Although Ta inclusion does significantly reduce T_M. For contrast, the dissimilarly sized

Sb^{5+} (0.60 Å, CN6) ion does induce significant permittivity peak broadening in Na doped CBN [Yang, B. 2018]. A combination of A1 site vacancies and Ta B site atomic disordering is shown here to be required for the induction of strong frequency dependence of permittivity in CBN. A similar induction of relaxor properties was achieved by doping CSBN with Ta [Hou, S. 2022]. There, Ta addition was linked to a reduction in domain/polar unit size and a reduction in P-E loop coercive field strength. Both the Ta doped CSBN reported by Hou, S *et al*. [2022] and, the Y and Ta doped CBN reported here in Figure 59, show narrow (low loss) P-E loops that could indicate potential energy storage applications.

Varying the Ca:Ba ratio in Y and Ta modified CBN had a very minor effect on the range of temperature stability of permittivity (ε_r = 950 ±15 % from -58 to 110 for 28Y04 Ta20 and ε_r = 970 ±15 % from -9 to 166 for 22Y04 Ta20). However, T_M increased significantly with increasing Ba content, as observed in undoped CBN [Han, X. 2013]. The tailoring of T_M in modified CBNs is therefore shown to be possible.

Y and Ta modified CBNs show near temperature stable permittivity (±15 %) over wide temperature ranges, though not as wide a range as Na and Sb modified CBN (~-90 to ~180 ^oC). The limited effect of Ta inclusion on permittivity peak broadening suggests that doping the B site with ions more dissimilar to Nb^{5+} than Ta^{5+}, in terms of ionic radii and valence, should be trailed to achieve improved permittivity-temperature stability. Furthermore, the use of lower Ca content CBNs as base compositions could counteract the significant reduction in T_M associated with B site doping, allowing for temperature-stable permittivity up to high temperatures. However, for energy storage applications, a reduction in T_M to below operating temperature may be beneficial. This is due to the more transient polar structures present in relaxors at $T > T_M$, which allow for the avoidance of high frequency, low temperature ($T < T_M$) dielectric loss peaks, which have been identified and discussed earlier.

This work's observed propensity for Ca containing secondary phases in Y- (A site) doped CBN28 could also be counteracted by a reduction in the Ca:Ba ratio of the base composition. As is shown in lower Ca-content Y and Ta doped CBN (22Y04 Ta20). Whilst still present, $CaNb_2O_6$ secondary phase content was also reduced in lower Ca-content Y doped CBN (r = 0.05), when compared with w = 0.05, where the substituting-out of Ca and Ba, for Y, occurred.

5.6 Conclusions

Prolonging the calcination time of CBN28 from 4 h to 12 or 20 h allowed for the synthesis of single-phase ceramics whose T_C was 232 °C, when sintering for 4 h at 1375 °C. Prolonging calcination also improved the stability of measured densities to variations in sinter temperature, possibly due to a reduction in the presence of secondary phases upon the initiation of sintering, which are associated with exaggerated grain growth.

The presence of a low frequency, high temperature loss mechanism in CBN28 was examined and found to vary inconsistently with thermal processing conditions, and to decrease slightly after annealing (cyclical heating) at temperatures between 300 and 400 ^{o}C. These losses, appearing similar to those caused by the thermal activation of oxygen vacancies, require further investigation.

The Y-doped CBN28 system, $(Ca_{0.28}Ba_{0.72})_{1-3w/2}Y_wNb_2O_6$ for samples of $0 \leq w \leq 0.20$, was single-phase up to w = 0.04. At w = 0.04 weak-relaxor behaviour and improved temperature-stable permittivity was exhibited (ε_r = 1143 ±15 % from 71 to 210 ^{o}C). Additional B site substitution, of Ta for Nb, reduced T_M significantly and induced strong frequency dependence of permittivity in the novel Y and Ta doped $(Ca_xBa_{1-x})_{1-3w/2}Y_wNb_{1.8}Ta_{0.2}O_6$ at compositions of x = 0.28 and w = 0.04. The transition to flatter permittivity-temperature responses, with Y and assumed A site vacancy inclusion, was largely unaffected by this B site substitution, occurring between w = 0.02 and w = 0.04, for both the solely Y doped and the Y and Ta co-doped CBN28's.

Values of P_r decreased with Y and vacancy inclusion, from 2.4 µC cm^{-2} for CBN28 to 1.4 µC cm^{-2} for w = 0.04 (E_{Max} = 30 kV cm^{-1}). Although, the P-E loops remained characteristically ferroelectric and lossy except when Y doping at levels well beyond the single-phase limits. With Ta substitution, P_r reduced further to ~0.5 µC cm^{-2} (E_{Max} = 40 kV cm^{-1}), indicating possible energy storage applications.

Secondary phases in the novel Y and Ta doped $(Ca_xBa_{1-x})_{1-3w/2}Y_wNb_{1.8}Ta_{0.2}O_6$ composition of x = 0.28, and w = 0.04 (ε_r = 954 ±15 % from -58 to 110 ^{o}C) were alleviated by reducing the Ca:Ba ratio to x = 0.22, whilst the stability of permittivity, with respect to temperature, remained relatively constant (ε_r = 972 ±15 % from -9 to 166 ^{o}C). The T_M of CBN based compositions is therefore shown to be tailorable by Ca:Ba ratio.

The development of temperature-stable, high temperature dielectrics by modification of CBN requires further study. This work suggests a combination of donor doping on the A site and doping of the B site with ions more dissimilar to Nb^{5+} than Ta^{5+} is required to achieve temperature stable permittivity over a very wide temperature range (-55 to 250+ °C). The substitution out of some, primarily A2 site occupying, Ba may improve the temperature stability of permittivity, even when doping with cations that preferentially occupy the A1 site. Although, the synthesis of single-phase

ceramics is promoted by substitution based on nominal site occupancy, which is typically derived from ionic radii.

In a CBN with temperature stable permittivity over very wide temperature ranges, the significant presence of A site vacancies and B site disorder would reduce T_M and likely necessitate the use of a low Ca content base composition so as to achieve temperature stable permittivity above 250 ^oC. However, for a CBN with strong frequency dependence of permittivity and near linear P-E loops, suitable for energy storage applications, a reduction in T_M to below operational temperatures may be preferable as it would avoid the high frequency loss peak observed in relaxors at $T < T_M$.

5.7 References

Abdelli, F. Boudaya, C. Khemakhem, H. 2016. Microstructure, X-ray diffraction, dielectric and Raman spectroscopy studies of $Ca_xSr_yBa_{1-(x+y)}Nb_2O_6$ ceramics. *J. Alloys Compd*. 683. 282-291

DOI: https://doi.org/10.1016/j.jallcom.2016.04.189

AMETEK Inc. 2022. Periodic Table. [Accessed online 11 November 2023] [Accessed from]: [https://www.edax.com/resources/periodic-table]

Beanland, R. Harrison, L. Khan, S. Brown, T. Roncal-Herrero, T. Peirson, H. Brown, A. P. Milne, S. J. 2023. Temperature dependence of incommensurate modulation in $Ca_{0.28}Ba_{0.72}Nb_2O_6$. *J. Appl. Phys*. **134**. 064101.

DOI: https://doi.org/10.1063/5.0157636

Burn, I. 1976. Temperature-stable Barium Titanate Ceramics Containing Niobium Pentoxide. *Act. Passiv. Electron. Compon.* **2**. 947096

DOI: https://doi.org/10.1155/APEC.2.241

Cao, H. Min, J. Y. Wu, S. D. Xian, A. P. Shang, S. K. 2006. Pinning of grain boundaries by second phase particles in equal-channel angularly pressed Cu–Fe–P alloy. *Mater. Sci. Eng. A*. **431**. 86-91

DOI: https://doi.org/10.1016/j.msea.2006.05.081

Cao, L. Yuan, Y. Meng, X. Li, E. Tang, B. 2022. Ferroelectric-Relaxor Crossover and Energy Storage Properties in $Sr_2NaNb_5O_{15}$-Based Tungsten Bronze Ceramics. *ACS Appl. Matter. Inter*. 9318-9329

DOI: https://doi.org/10.1021/acsami.1c23673

Cao, L. Wang, Y. Yuan, Y. Zhu, J. Barzegar-Bafrooei, H. Mao, M. Liu, B. Li, H. Wang, D. Lu, Z. Wang, G. Song, K. 2024. Low temperature relaxor, polarization dynamics and energy storage properties of $Ca_{0.28}Ba_{0.72}Nb_2O_6$ tungsten bronze ceramics. J. Chem. Eng. **479**. 147664

DOI: https://doi.org/10.1016/j.cej.2023.147664

Chen, I-W. Wang, Y. 1998. A domain wall model for relaxor ferroelectrics. *Ferroelectrics.* **206**. 245-263

DOI: https://doi.org/10.1080/00150199808009162

Eitel, R. A. 2007. Rayleigh Law Response in Ferroelectric Ceramics: Quantifying Domain Wall Dynamics and Structural Relationships. *Sixteenth IEEE International Symposium on the Applications of Ferroelectrics*, Nara, Japan. 319-323

DOI: https://doi.org/10.1109/ISAF.2007.4393253

Eßer, M. Burianek, M. Klimm, D. Mühlberg, M. 2002. Single crystal growth of the tetragonal tungsten bronze $Ca_xBa_{1-x}Nb_2O_6$ (x = 0:28; CBN-28). J. Cryst. Growth. **240**. 1-5

DOI: https://doi.org/10.1016/S0022-0248(02)00868-0

Gardener, J. Yu, F. Tang, C. Kockelmann, W. Zhou, W. Morrison, F. 2016. Relaxor-to-Ferroelectric Crossover and Disruption of Polar Order in "Empty" Tetragonal Tungsten Bronzes. *Chem. Mater.* **28**. 4616–4627

DOI: **https://doi.org/10.1021/acs.chemmater.6b01306**

Gardener, J. Morrison, F. 2014. A-site size effect in a family of unfilled ferroelectric tetragonal tungsten bronzes: $Ba_4R_{0.67}Nb_{10}O_{30}$ (R = La, Nd, Sm, Gd, Dy and Y). *Dalton Trans*. **43**. 11687-11695

DOI: **https://doi.org/10.1039/C4DT00126E**

Glass, A. M. 1969. Investigation of the electrical properties of $Sr_{1-X}Ba_xNb_2O_6$ with special reference to pyroelectric detection. *J. Appl. Phys*. **40**. 4699–4713

DOI: https://doi.org/10.1063/1.1657277

Graetsch, H. A. Pandey, C. S. Schreuer, J. Burianek, M. Mühlberg, M. 2012 (April). Incommensurate modulation of calcium barium niobate (CBN28 and Ce:CBN28). *Acta Cryst*. B**68**. 101-106

DOI: https://doi.org/10.1107/S0108768111054863

Graetsch, H. A. Schreuer, J. Burianek, M. Mühlberg, M. 2012 (December). Thermally induced structural changes in incommensurate calcium barium niobate $Ca_{0.28}Ba_{0.72}Nb_2O_6$ (CBN28). *J. Solid State Chem*. **196**. 255-266

DOI: https://doi.org/10.1016/j.jssc.2012.06.028

Hall, D. A. Ben-Omran, M. M. Stevenson, P. J. 1998. Field and temperature dependence of dielectric properties in $BaTiO_3$-based piezoceramics, *J. Phys.: Condens. Matter*. **10**. 461–476.

DOI: https://doi.org/10.1088/0953-8984/10/2/025

Han, X. Wei, L. Yang, Z. Zhang, T. 2013. Phase formation, dielectric and ferroelectric properties of $Ca_xBa_{1-x}Nb_2O_6$ ceramics. *Ceram. Int.* **29**. 2853-2860

DOI: https://doi.org/10.1016/j.ceramint.2012.11.078

Heine, U. Voelker, U. Betzler, K. Burianek, M. Muehlberg, M. 2009. The ferroelectric phase transition of calcium barium niobate: experimental evidence of Smolenskii's model for diffuse phase transitions?. *New J. Phys*. **11**. 083021

DOI: https://doi.org/10.1088/1367-2630/11/8/083021

Hou, S. Xu, S. Yang, L. Liu, X. Wei, L. Chao, X. Wu, D. Liang, P. Yang, Z. 2022. High energy storage performance of $Ca_{0.15}(Sr_{0.6}Ba_{0.4})_{0.85}Nb_{2-x}Ta_xO_6$ relaxor ferroelectric ceramics. *Ceram. Int*. **48**. 28382-28390

DOI: https://doi.org/10.1016/j.ceramint.2022.06.148

Jang, C-Y. Lee, J-H. Kim, J-J. Cho, S-H. Lee, H. 2004. Phase Stability of Tungsten-Bronze-Structured KLN Ceramics: Effect of Excess Nb2O5. *J. Electroceram*. **13**. 847-850

DOI: https://doi.org/10.1007/s10832-004-5202-z

Jiang, B. Locozzia, J. Zhao, L. Zhang, H. Harn, Y-W. Chena, Y. Lin, Z. 2019. Barium titanate at the nanoscale: controlled synthesis and dielectric and ferroelectric properties. *Chem. Soc. Rev*. **48**. 1194-1228

DOI: **https://doi.org/10.1039/C8CS00583D**

Kang, S-J. L. 2004. Sintering: Densification, Grain Growth and Microstructure. *7. GRAIN BOUNDARY SEGREGATION AND GRAIN BOUNDARY MIGRATION*. Oxford: Elsevier

URI: https://www.elsevier.com/books/sintering/kang/978-0-7506-6385-4

Ke, S. Fan, H. Huang, H. Chan, H. L. W. Yu, S. 2008. Dielectric, Ferroelectric properties, and grain growth of $Ca_xBa_{1-x}Nb_2O_6$ ceramics with tungsten bronzes structure. *J. Appl. Phys*. **104**. 024101

DOI: https://doi.org/10.1063/1.2956615

Ketchum, J. L. Sweeney, K. L. Halliburton, L. E. Armington, A. F. 1983. Vacuum annealing effects in lithium niobate. *Phys. Lett. A.* 1983. **94**. 450-453

DOI: https://doi.org/10.1016/0375-9601(83)90852-6

Kim, M-S. Lee, J-H. Kim, J-J. Lee, H. Y. Cho, S-H. 2002. Origin of Abnormal Grain Growth in Tungsten Bronze Structured Ferroelectric $Sr_xBa_{1-x}Nb_2O_6$ Ceramics. *Jpn. J. Appl. Phys.* **41**. 7048

DOI: http://doi.org/10.1143/JJAP.41.7048

Kittel, C. 1946. Theory of the structure of ferromagnetic domains in films and small particles. *Phys. Rev*. **70**. 965-971

DOI: https://doi.org/10.1103/PhysRev.70.965

Lee, H-Y. Freer, R. 1998. Abnormal grain growth and liquid-phase sintering in Sr0.6Ba0.4Nb2O6 (SBN40) ceramics. *J. Mat. Sci.* **33**. 1703–1708

DOI: https://doi.org/10.1023/A:1004312128588

Lee, J-H. Lee, G-J. Hoang, A-P. Frömling, T. Pham, T-L. Lee, J-S. Jo, W. 2022. Suppression of high-temperature dielectric loss by designed thermal annealing treatment in $(Bi_{1/2}Na_{1/2})TiO_3$ ceramics. *J. Eu. Ceram. Soc*. **42**. 1388-1395

DOI: https://doi.org/10.1016/j.jeurceramsoc.2021.12.029

Mendelson, M. I. 1969. Average Grain Size in Polycrystalline Ceramics. *J. Am. Ceram. Soc*. **52**. 443-446

DOI: **https://doi.org/10.1111/j.1151-2916.1969.tb11975.x**

Ofoegbuna, T. Darapaneni, P. Sahu, S. Plaisance, C. Dorman, J A. 2019. Stabilizing the B-site oxidation state in ABO_3 perovskite nanoparticles. *Nanoscale*. **30**. 14303-14312

DOI: https://doi.org/10.1039/C9NR04155A

Paściak, M. Ondrejkovic, P. Kulda, J. Vaněk, P. Drahokoupil, J. Steciuk, G. Palatinus, Welberry, L. Fischer, H. Hlinka, J. Buixaderas, E. 2019. Local structure of relaxor ferroelectric $Sr_xBa_{1-x}Nb_2O_6$ from a pair distribution function analysis. *Phys. Rev. B*. **99**. 104102

DOI: https://doi.org/10.1103/PhysRevB.99.104102

Steiner, S. Seo, I-T. Ren, P. Li, M. Keeble, D. J. Frömling, T. 2019. The effect of Fe-acceptor doping on the electrical properties of $Na_{1/2}Bi_{1/2}TiO_3$ and 0.94 $(Na_{1/2}Bi_{1/2})TiO_3$–0.06 $BaTiO_3$. *J. Am. Ceram. Soc*. **102**. 5295-5304.

DOI: https://doi.org/10.1111/jace.16401

Viola, G. Ning, H. Wei, X. Deluca, M. Adomkevicius, A. Khaliq, J. Reece, M. J. Yan, H. 2013. Dielectric relaxation, lattice dynamics and polarization mechanisms in $Bi_{0.5}Na_{0.5}TiO_3$-based lead-free ceramics. *J. Appl. Phys*. **114**. 014107

DOI: https://doi.org/10.1063/1.4812383

Wei, L. Han, X. Chao, X. Jiao, H. Yang, Z. 2014-Feb. Study on low temperature sintering and electrical properties of CuO-doped $Ca_{0.28}Ba_{0.72}Nb_2O_6$ ceramic. *J. Mater. Sci. Mater. El*. **25**. 1605-1611
DOI: https://doi.org/10.1007/s10854-014-1756-y
Wei, L. Yang, Z. Chao, X. Jiao, H. 2014-May. Structure and electrical properties of $Ca_{0.28}Ba_{0.72}Nb_2O_6$ ceramics with addition of rare earth oxides (CeO_2, La_2O_3). *Ceram. Int*. **40**. 5447-5453
DOI: http://dx.doi.org/10.1016/j.ceramint.2013.10.130

Xu, R. Karthik, J. Damodaran, A. R. Martin, L. W. 2014. Stationary domain wall contribution to enhanced ferroelectric susceptibility. *Nat. Commun.* **5**. 3120
DOI: https://doi.org/10.1038/ncomms4120

Yang, B. Hao, S. Yang, P. Wei, L. Yang, Z. 2018. Relaxor behavior and energy storage density induced by B-sites substitutions in $(Ca_{0.28}Ba_{0.72})_{2.1}Na_{0.8}Nb_5O_{15}$ Tungsten bronze ceramics. *Ceram. Int*. **44**. 8832-8841
DOI: http://dx.doi.org/10.1016/j.ceramint.2018.02.065

Yang, B. Wei, L. Wang, Z. Kang, S. Chao, X. Yang, Z. 2016. Electrical Characterization Induced by Structural Modulation in $\square(Ca_{0.28}Ba_{0.72})_{2.5-0.5x}(Na_{0.5}K_{0.5})_xNb_5O_{15}$ Ceramics. *J. Electron. Mater*. 45. 104-115

DOI: https://doi.org/10.1007/s11664-015-4157-y

Yang, B. Wei, L. Chao, X. Wang, Z. Yang, Z. 2015 (May). Role of structural modulation in electrical properties of tungsten bronze $(Ca_{0.28}Ba_{0.72})_{2.5-0.5x}Na_xNb_5O_{15}$ ceramics. *J. Alloys Compd*. **632**. 368-375

DOI: https://doi.org/10.1016/j.jallcom.2015.01.247

Yang, B. Yang, P. Wei, L. Wang, Z. Yang, Z(henyu). Chao, X. Yang, Z(upei). 2015 (Dec). Structural modulation and electrical properties in ferroelectric niobates $(Ca_{0.28}Ba_{0.72})_{2.5-0.5x}K_xNb_5O_{15}$ ($0.0 \leq x \leq 0.6$) ceramics. *Ceram. Int*. **41**. 13988-13997

DOI: https://doi.org/10.1016/j.ceramint.2015.07.011.

Yoneda, Y. Kitanaka, Y. Noguchi, Y. Miyayama, M. 2012. Electronic and local structures of Mn-doped $BiFeO_3$crystals. *Phys. Rev. B.* **86**. 184112

DOI: https://doi.org/10.1103/PhysRevB.86.184112

Ziolek, M. 2003. Niobium-containing catalysts—the state of the art. *Catal. Today*. **78**. 47–64

https://doi.org/10.1016/S0920-5861(02)00340-1

6. Particle aerosol deposition (PAD) for electroceramic applications, a review

Particle aerosol deposition (PAD) is a coating technique that typically employs ceramic and metal powders and substrates. The resultant films are of µm-scale thickness and are often highly dense (95+ %) with uniform microstructures and nanometre-scaled crystallinity [Akedo, J. 2004]. The PAD method is comparable to Cold Spraying, although it operates at room temperature and reduced pressures [Akedo, J. 2008]. The densification mechanism that occurs in Cold Spraying relies on the deformation of ductile material, whilst PAD achieves densification by a combination of plastic deformation and also brittle fracture and re-bonding [Akedo, J. 2006] and [Handft, D. 2015]. This shock-consolidation, or room temperature impact consolidation (RTIC) mechanism, is, however, not fully understood [Hanft, D. 2015].

Room temperature conditions allow for the integration of thermally dissimilar material. As such, PAD offers an alternative to the co-firing of metals and ceramics in the fabrication of capacitor and other electroceramic components [Nam, S-M. 2004] and [Šadl, M. 2021]. Co-firing occurs at temperatures around 1000 ^{o}C, which can promote undesired oxidation of an electrode material, especially when the combination of dielectric material (oxide) and electrode (metal) facilitates some degree of electrode oxidation (as occurs when employing Bi-containing oxides and Ni metal electrodes) [Stratton, P. 2013]. Whilst ostensibly a room-temperature process, some thermal treatment (annealing) of deposited films is required for electroceramic applications to recover polarisation response [Zhou, F. 2022]. During deposition, GPa impact forces reduce crystallite size to the nm-scale and induce high levels of microstrain (~0.2 %) both of which can cause a reduction in polarisation response [Nazerenus, T. 2022].

The PAD method is a platform technology with varied potential applications. It is capable of general consolidation-based protective coatings, whilst also inducing properties specific to shock-consolidation or RTIC. The particle size reduction inherent to the process allows for the deposition of transparent layers with retained crystalline order at length scales below that of visible light [< 400 nm], [Apetz, R. 2003] and [Lebedev, M. 2008]. Microstrains and fine crystallite sizes can modify ceramic phase transitions and ferroelectric character. These strains can be reduced, and the crystallite size increased, by annealing, allowing for the tailoring of a film's ferroelectric character and the removal of charged defects that may arise during RTIC [Eckstein, U. 2022]. This is of particular interest to this PhD project since deposition and annealing may be required to induce high but temperature stable permittivity and linear P-E responses in CBN-based material for high-temperature capacitor and energy storage applications.

The PAD method originated in the 1980's in connection with the Gas deposition method. Other names for the technique include aerosol deposition (AD) and the aerosol deposition method (ADM). A 2015 review, by Hanft, D. *et al*. stated that 90 % of research papers on the topic originated from Japan and South Korea, with the Japanese-based author Akedo, J. producing notable research since the 1990's [Hanft, D. 2015]. This research includes the use of PAD for electroceramic (PZT) films [Akedo, J. 1999]. More recently, academic interest in PAD has increased in Germany and the rest of Europe as well as in the USA.

This brief review of PAD has covered its origin and shall cover its categorisation amongst other coating technologies, the conditions employed, the equipment set-up and the proposed RTIC mechanism. Also covered are the desired properties and preparation of the input materials, and the subsequent properties of the produced films as well as their post deposition processing. Special attention will be given to the deposition of ceramic powders onto metallic substrates, for electroceramic applications.

6.1 Categorisation amongst other coating technologies

The surface coating of materials can be employed to protect a bulk material from the environment, provide a different surface finish, integrate the properties of two dissimilar materials and fabricate complex components. Coatings may be thick (>> 100 µm) or thin (<< 10 µm) and can be produced by adhesive or reactive processes which are achieved by chemical and/or mechanical methods. The conditions employed allow for the categorisation of coating techniques, often they infer distinct processing dependant properties into the product.

Figure 60 compares the typical particle sizes and velocities used in deposition by Particle Aerosol Deposition (PAD) to other techniques that achieve coating or alloying by the collision of solid-state particles [Akedo, J. 2008]. The PAD method produces an aerosol by the mixture of µm- or nm-scaled particles within a carrier gas. These primary particles may be constituted within aggregates (hard/ strongly bonded particle clusters) or agglomerates (soft/weakly bonded particle clusters). The aerosol is accelerated to form a jet of high, but typically subsonic, velocity particles on passing from an aerosol generation chamber (AGC) to a vacuum or deposition chamber (VC) via a nozzle. A vacuum pump serves to maintain a pressure gradient throughout the rig and maintains low (< 20 mbar) pressure within the VC. The gas source, AGC, VC, and vacuum pump comprise the main components of a PAD system. Within the VC, the substrate is moved relative to the nozzle to allow for area coating.

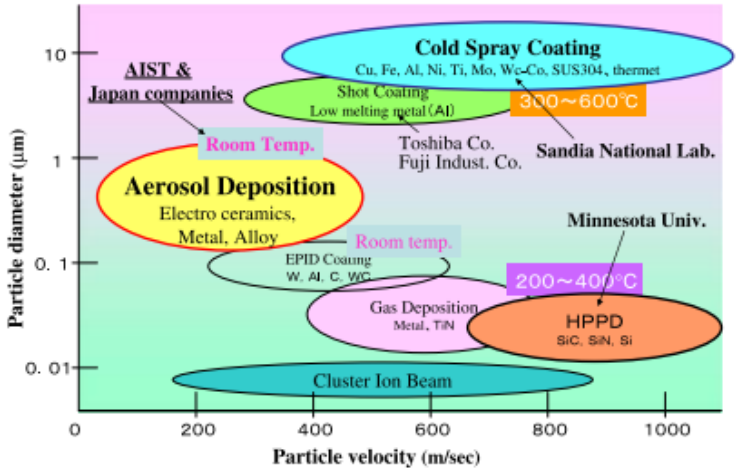

Figure 60. The particle diameters (μm) and velocities (m s^{-1}) employed in various particle collision-based consolidation techniques. Taken from [Akedo, J. 2008].

Table 16 details the typical operational conditions for the PAD method. The conditions affecting aerosol flow are discussed directly below Table 16.

Table 16. Typical operational parameters for the PAD method. Taken from [Hanft, D. 2015].

Parameters	Reported data from [7,15–21]
Pressure in deposition chamber	0.2 – 20 mbar
Pressure in aerosol chamber	60 – 1066 mbar
Nozzle geometry	Slit nozzle 2.5 x 0.2 up to 25 x 0.8 mm^2
Carrier gas	Air, N_2, O_2, Ar, He
Gas flow rate	1 l/min - 30 l/min
Sweep speed	0.05 – 10 mm/s
Stand-off distance nozzle – target	0.5 – 50 mm

6.2 Pressure dynamics and the nozzle

The maintenance of a pressure gradient between the AGC (~60 to ~1000 mbar) and the VC (< 20 mbar) is essential for ensuring the acceleration of the aerosol and the particles within it. Low pressures in the VC also ensures the retention of high momentum in the fine (μm-scaled) particles upon impact during deposition. Variations in impact momentum are also likely to be reduced by the maintenance of low pressure, allowing for more homogeneous or defect free films. Pressure bows, caused by stagnation of the jet directly above the substrate, reduce particle momentum, particularly at the centre point of the jet-substrate interaction. Such effects are common to jet-based deposition

[Benchaita, M. 1983]. The jet travels in a direction normal to the substrate and is deflected on approach to a substrate, causing the angle of particle-substrate impaction to increasingly vary from 90^{o} with increasing radial distance from the centre, see Figure 61(a). This jet-substrate interaction also has an effect on the erosion of a substrate. Figure 61(b) models the erosion of a substrate via a water jet. Initially, as radial distance from the centre increases so does the rate of erosion, due to a reduction in the shielding effect from the stagnated buffer region directly above the central impact point of the jet on the substrate. However, with increasing radial distance, the proportion of momentum that is normal to the substrate decreases and erosion decreases also [Benchaita, M. 1983]. This inherent radial variation in impact momentum, when translated across a substrate by the relative motion of the nozzle, may produce defect tracks in PAD films. To minimise this effect the bow pressure, or local variation in pressure across the substrate surface, must be reduced by the maintenance of general vacuum conditions (< 20 mbar).

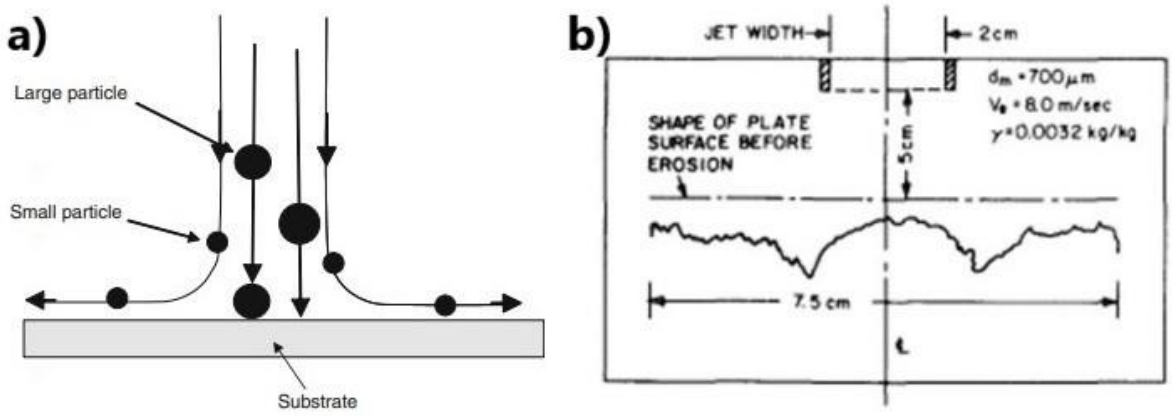

Figure 61. The travel and deflection of an aerosol, and the size dependant deflection of particles within the aerosol upon approach to the substrate in PAD is shown in (a), taken from [Akedo, J. 2008]. The radial variation in substrate erosion due to interaction with a water jet is shown in (b), taken from [Benchaita, M. 1983].

The nozzles employed in PAD systems typically have slit-like dimensions to allow for the covering of a greater area perpendicular to the nozzles motion (relative to the substrate). The aerosol in the AGC is compressed upon or prior to the entrance of the nozzle and then decompressed and accelerated on passing through it. Typically diverging nozzles are employed, the importance of sufficient nozzle divergence upon the jet acceleration (exit velocity) is shown in the schematic of Figure 62, where the white (top) section is the body of the nozzle and the jet is passing downwards. Converging-diverging (de Laval) nozzles are also employed [Naoe, K. 2013].

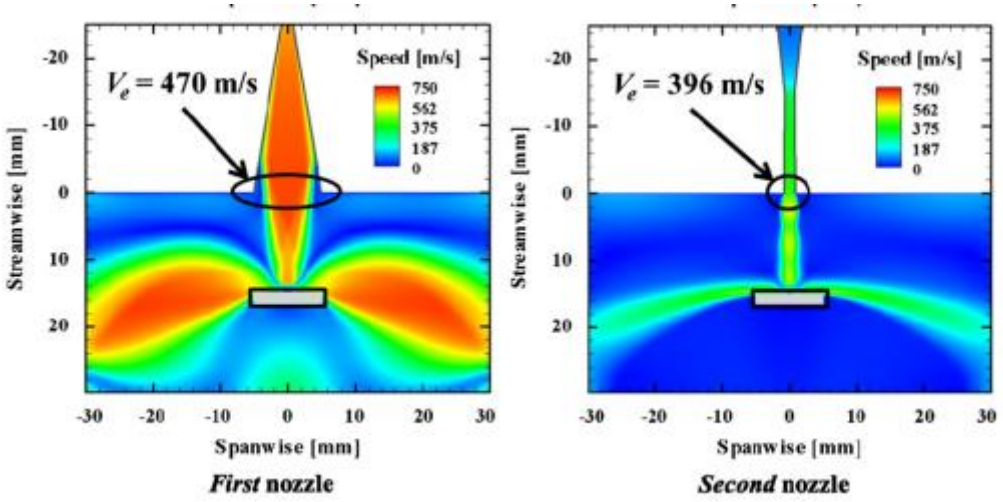

Figure 62. The variability of jet exit velocity (m s^{-1}) and substrate impaction velocity on the divergence of the nozzle interior. The adequately diverged (first) nozzle achieves higher velocities. Taken from [Lee, M. W. 2011].

Figure 62 shows schematics of a modelled velocity of a jet that interacts with a substrate. However, in aerosols, the acceleration and velocity of the particles within the jet must also be considered. Particles, i.e. µm-scaled ceramic particles, have masses greater than the molecules that comprise the carrier gas and so they may experience lesser acceleration. Increasing the nozzle stand-off distance (z), which is the distance between the nozzle and substrate, can facilitate higher velocity particles, provided that the jet velocity does not decrease to below the velocity of the aerosolised particles over this greater distance of travel. The sweep-speed or scan-speed of the nozzle (velocity of travel of the nozzle relative to the substrate) is inversely proportional to the exposure time of the substrate to deposition, or to the exposure time of the already deposited film to subsequent impactions. Deposition typically occurs via multiple scans of the nozzle over the same area. The beneficial role of subsequent impactions, or hammering, to the densification of films is discussed in the mechanism section below. However, as deposition time increases deterioration of the powder (agglomeration of the aerosolized µm-scaled particles due to van de Waals forces) may increase, see Figure 65 and the discussion later [Handft, D. 2018].

6.3 Carrier gas species and consumption

Species such as N_2, O_2, H_2 and (dry) air have been employed as carrier gasses to produce aerosols in PAD. Experimentally, mixtures of the gasses have also been employed [Schuber, M. 2014]. Under comparable conditions, the carrier gas species and its consumption (m^3), or flowrate ($m\ s^{-1}$), determine the aerosol velocity, as seen in Figure 63(a). Gasses with lower molecular weights are less compressible (adiabatically). Hence, at comparable flowrates, lower molecular weight gasses will expand/accelerate more and attain higher velocities. This affect can be seen, for Al_2O_3 and PZT aerosols, in Figure 63(a). The acceleration of aerosolised particles within the gas may be reduced by the possibly lower momentum of the lighter gases, necessitating greater nozzle-substrate stand-off distances. An increase in particle impaction force with lower molecular weight carrier gasses is implied by the work of Schubert, M. *et al* [2014]. Here, levels of substrate strain were found to decrease when mixing a H_2 (molecular weight = ~2 g mol^{-1}) or N_2 (molecular weight = ~28 g mol^{-1}) carrier gases with increasing concentrations of O_2 (which is of greater molecular weight, ~32 g mol^{-1}), see Figure 63(b).

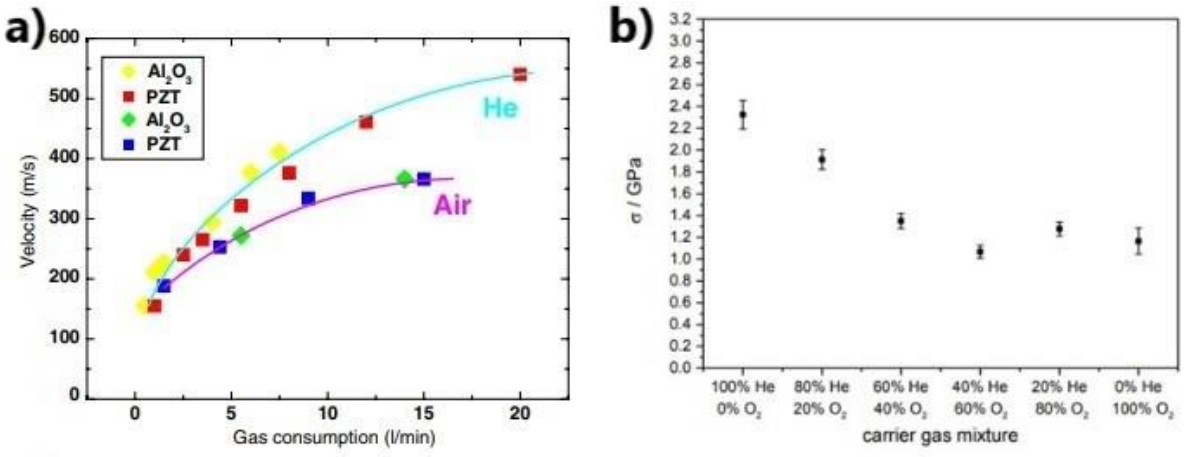

Figure 63. The relationship between impact particle velocity and gas consumption for different gasses is shown in (a), taken from [Akedo, J. 2008]. The resultant strain in films produced by varying carrier gas composition at a controlled flowrate is shown in (b), taken from [Schuber, M. 2014].

6.4 PAD system set-up and variants

A schematic of a typical PAD system is shown in Figure 64. The system is comprised of a gas source, AGC, VC and a vacuum pump. The nozzle allows for the generation of a jet whilst various ancillary components control the flow of carrier gas (mass flow controller) and the size and agglomeration state of the particles in the aerosol (filter and classifier). A (X-Y-Z) stage allows for the movement of the nozzle relative to the substrate.

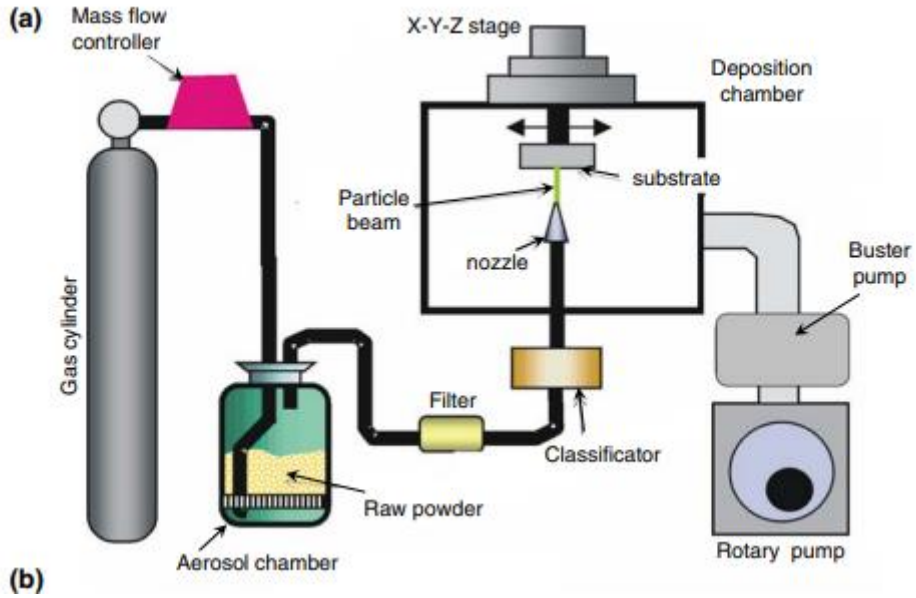

Figure 64. A diagram of a PAD system. Taken from [Akedo, J. 2008].

In addition to the inclusion of ancillary components, variations to the AGC, VC and vacuum pump are common. The low (< 1 wt.%) deposition efficiency of PAD has prompted modification of the VC to include troughs for the collection and subsequent recycling of non-deposited powder. The vacuum pump, typically a rotary pump, must be commissioned to maintain suitable pressure (< 1 - 20 mbar) and gas consumption (m^3). Of particular interest here is the AGC. Successful deposition requires the controlled production of an ideally consistent aerosol. Several modifications to the traditional manner of aerosolization, by addition of a vibrating powder bed, have been demonstrated [Mihara, K. 2009] and [Handft, D. 2018].

In a traditional AGC the carrier gas passes through a bed of loose powder, generating an aerosol. Vibration of the AGC helps fluidise the bed and promotes aerosolization. However, the µm-scaled ceramic powders typically employed in PAD can be prone to agglomeration due to van de Waals forces [Francis, L. F. 2015]. Any agglomerates produced accumulate with increasing deposition time and are deleterious to a successful uniform film deposition. Agglomerates may hinder the formation of dense films due to dissipation of kinetic energy, which is spent on (partial) disintegration as opposed to brittle fracture and re-bonding [Nam, S-M. 2004]. Figure 65 shows the reduction in deposition rate with time when employing a fluidised bed aerosol generator. The mass flow within the aerosol (i.e. concentration of particles) also lacks control, being determined by the uplift from the carrier gas. At high carrier gas flowrates front-loading, or a high initial mass flow, may occur.

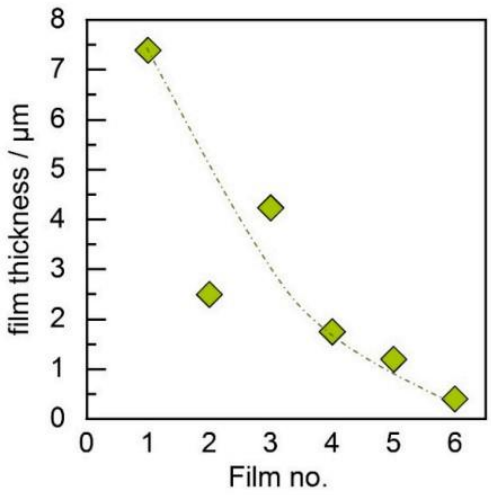

Figure 65. The reduction in deposition rate with time (film number) when employing a fluidised bed aerosol generator. Taken from [Handft, D. 2018].

A modified vibrating bed system was proposed to improve the control of mass flow, in which a lower flowrate uplifting gas aerosolised the bed and carried it upwards into a high flowrate carrier gas stream traveling perpendicular to the uplift stream [Mihara, K. 2009].

The brush aerosol generator similarly controls mass flow, though in the absence of an uplifting stream. Here, a loosely compacted powder bed is situated within a tube. The bottom of the tube is raised at a controlled rate, pushing the powder out of the tube and into a rotating brush. The rotation of the brush may be caused by the carrier gas stream and the brush serves to disperse the powder within the stream [Handft, D. 2018].

6.5 Mechanism of consolidation

The mechanism of room temperature impact consolidation (RTIC), proposed by Akedo, J. [2008], is not fully understood. Bulk ceramics are known to fail mechanically due to brittle fracture, which tends to occur at the site of existing structural defects [Griffiths, A. A. 1921]. However, sub-micron ceramic powders tend to lack defects or cracks of a critical length for fracture, they have been shown to have increased toughness, and in the correct conditions they can accumulate deformation without fracture, perhaps analogously to the behaviour seen in more ductile materials such as metals, in which defects (primarily dislocations) accumulate into structural boundaries [Hellstern, E. 1989]. Ceramic particle size reduction, to nm-scales, may, therefore, facilitate high levels of plastic deformation during densification. Dissimilarly to Cold Spraying, this plastic deformation is accompanied by extensive fracture and particle size reduction, which is believed to also promote bonding and consolidation [Lee, D-W. 2011].

A minimum size of the impacting particles is required to achieve sufficiently high impact forces for the deposition of particles. An upper size limit is required to ensure that the process is net-additive, rather than net-erosive [Handft, D. 2015]. The accelerated particles require sufficient inertia (size) to maintain a trajectory normal (90^{o}) to the substrate whilst the carrier gas is deflected parallel to the substrate (or stage, Figure 61(a)). The impacting particles, and agglomerates or aggregates, can then be categorised into having low, medium and high momentums, as seen in Figure 66. The dissipation of kinetic energy associated with the (partial) break-up of agglomerates may hinder consolidation and densification [Nam, S-M. 2004]. Aggregated (strongly bonded) primary particles, in contrast to agglomerates, have been shown to improve deposition, provided that these aggregates readily fracture upon impact [Mihara, K. 2009]. Aggregates (e.g. granules) may provide high momentum impacts whilst still transferring their kinetic impact forces into fracture, for example in the fracture of the necks between the primary particles.

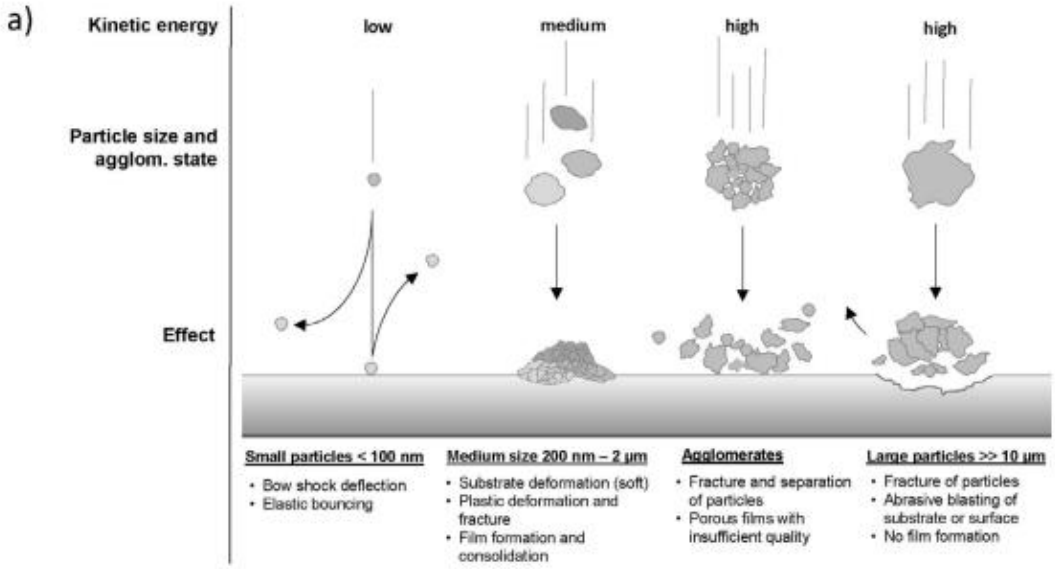

Figure 66. The size dependence of particle-substrate interactions, taken from [Handft, D. 2015].

During deposition high stresses (sometimes > 10 GPa) induce local temperatures increases, which have been shown by single-particle impact modelling to exceed 500 ^{o}C, See Figure 67. Experimental results also indicate the presence of stresses of this order of magnitude (~10 GPa) [Cicconi, M. R. 2020]. Here, residual bond compression in a deposited silicate glass was analysed by Raman spectroscopy and correlated to a minimum pressure of 10.5 (±1.5) GPa during deposition [Cicconi, M. R. 2020]. These stresses result in defects and strains that are associated with the induction of nanocrystallinity in the resulting films as well as particle size reduction, see Figure 68. No significant

melting of the particles, even in metals, is believed to occur [Akedo, J. 2006]. The exposure of fresh and active surfaces, due to fracture, may promote fresh chemical bonding.

In other mechanical-impact processes, such as the milling of ceramic particles, the processes of particle/crystallite size reduction and strain accumulation have been shown to be intimately entwined [Delogu, F. 2006]. The mutual processes of plastic deformation and brittle fracture (and re-bonding), required for successful PAD, appear similarly entwined but they require further study.

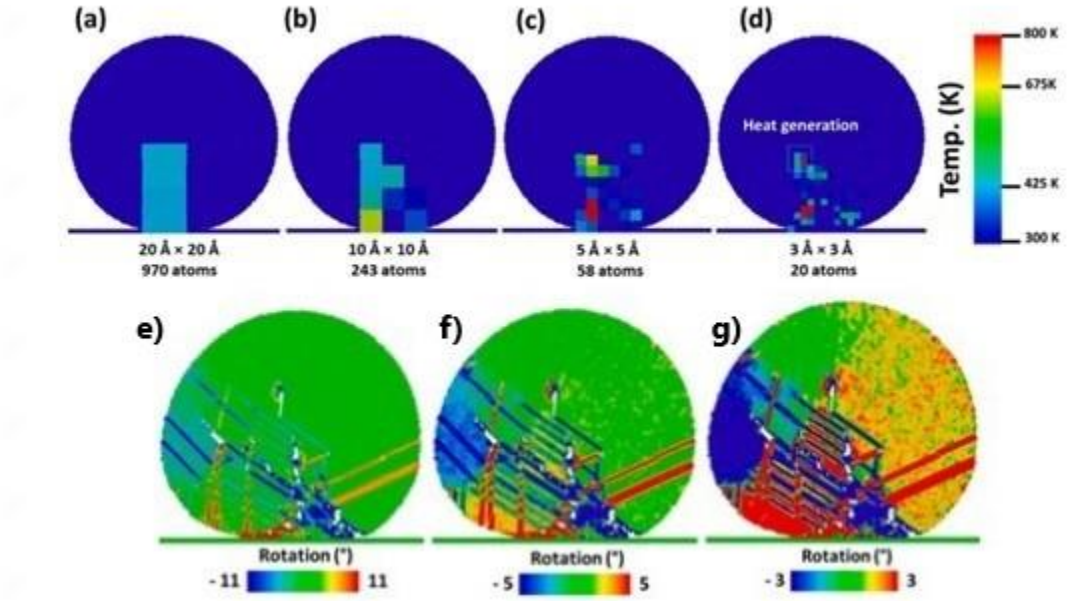

Figure 67. In (a) - (d), the effect of increasing the resolution (reducing the model box/domain size), during 2-D molecular dynamic modelling, on accurately assessing maximum local temperatures during the deposition of a 33 nm TiO_2 particle at impaction velocity of 400 m s^{-1}. Local temperatures of or above ~800 K, were calculated using LAMMPS software, they correlated with stresses, parallel to deposition, of up to 32 GPa. In (e) - (g), there are modelled strain fields due to particle rotation on impact in a 33 nm TiO_2 particle at an impaction velocity of 500 m s^{-1}. In (a), high angle (±11°, dark blue and red) rotations are associated by the authors with fractures, in (b) a mixture of fracture and different regions of rotation are evident at medium angle rotations. In (c), lower angle (< ±3°, light blue and yellow) rotations are associated by the authors with induction of nanocrystallisation. Taken and adapted from [Daneshian, B. 2022].

6.6 Stages of deposition

Aerosol deposition occurs in two stages, initially particles interact with the substrate to form an anchor layer. Subsequently, particle-film interactions occur as the film builds up. During the formation of the anchor layer the softer substrate may be damaged or severely deformed, as seen in Figure 68(b). In that report, substrate roughness was shown to increase with increasing carrier gas flowrate. Deformation and damage to the substrate may aid in the mechanical entrapment (interlocking) of particles, thus allowing for subsequent film build-up and densification. However, increased surface roughness has been associated with reduced deposition rates [Naoe, K. 2013]. Deposition rates have also been shown to be reduced in initially rough substrates [Kim, C-W. 2012]. This suggests that the roughening of the exposed substrate, and the subsequent reduction in deposition rate and greater exposure time of the substrate to deposition, is a self-propagating process that is deleterious to film build up. This inhibition of deposition in rough substrates may be caused by varying the angle of impacts (away from 90^{o}) [Naoe, K. 2013].

Heating of a stainless-steel substrate during deposition, up to 500 ^{o}C, was shown to result in films with larger crystallite sizes and lower Vickers hardness [Lebedev, M. 2005]. This is likely due to an increase in the substrate's malleability with temperature, given that harder and less malleable substrates have been shown to promote particle size reduction and hinder the deposition of fine particles [Lee, D-W. 2012]. Whilst substrate- or particle- deformation may promote initial particle interlocking, as has been shown in Cu-Al_2O_3 co-deposition [Cho, M. Y. 2019], this is not its sole function. The substrate also functions "as an anvil" allowing for some degree of particle size reduction, which appears requisite for the formation of dense and well-adhered anchor layers. This size reduction of deposited particles is likely caused by a hammering effect, directly from subsequent particle deposition and also, in thicker films, from the propagation of stresses from the hammered surface through the entire thickness of the film. Crystallite size reduction has been shown to correlate with scan number, and strain level with depth within the film [Lee, D-W. 2011]. Well-adhered anchor layers may also be produced with only minor (< ±100 nm) variations in the substrate surface (slight roughening), see Figure 68(c) [Imanaka, Y. 2013] and [Khansur, N. H. 2018].

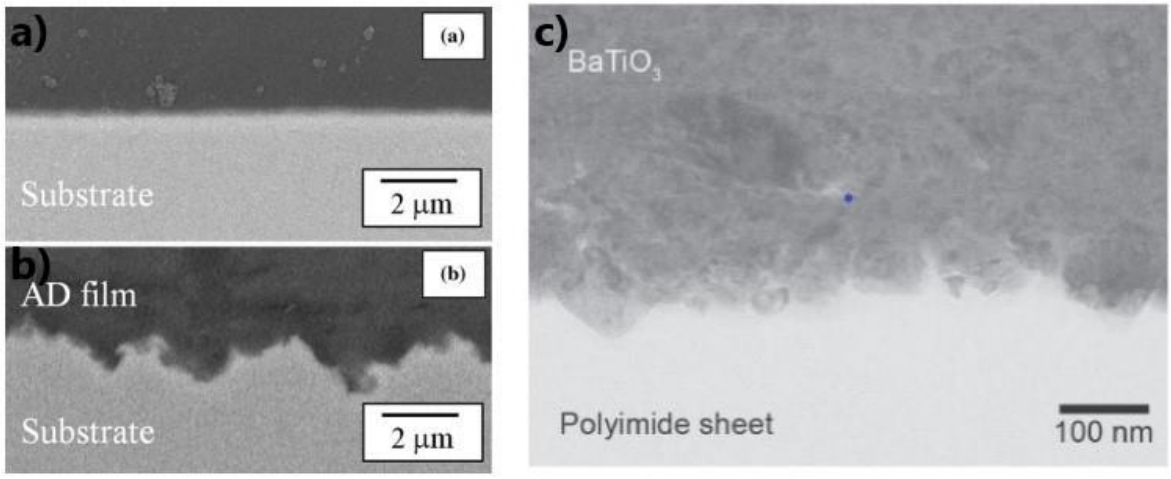

Figure 68. In (a), an increase in substrate height variation (surface roughness) from < ±100 nm to ±~1 μm is shown to occur after deposition of Al_2O_3 on Cu at a N_2 carrier gas flowrate of 8 L min^{-1}. Taken from [Naoe, K. 2013]. The retention of low roughness (substrate height variations of < ±100 nm) is shown for $BaTiO_3$ deposited on a polyimide substrate in (b), taken from [Imanaka, Y. 2013].

Subsequent build-up of a ceramic film relies on the impact of particles onto the already deposited ceramic layer. In comparison to a metallic substrate, the ceramic anchor layer will have a greater Vickers hardness, despite a likely increased in the substrate hardness due to the shot-peening or hammering affect [Gopi, R. 2020]. Particle-layer interactions may be particularly conducive to particle size reduction, given that harder (e.g. sapphire) substrates promote particle size reduction [Lee, D-W. 2012].

6.7 Substrate and deposition material preparation and properties

Preparation of the substrate is largely limited to its polishing. Whilst the sand-blasting effect of the initial particle deposition may serve to clean the substrate of any obstructing dirt, pre-polishing is still required to prevent the deleterious effects of surface roughness on deposition.

The deposition process is critically affected by non-intrinsic powder properties. Particle size reduction (by milling) or the increase in the size of ceramic particles (by annealing) offers a route to the modification of non-intrinsic powder properties [Rice, R. W. 1990]. Particle size, standard deviation of size range, surface area, morphology and primary particle state (aggregated, agglomerated or not) are all controlled by the milling and thermal pre-treatment of powders in the solid state. The wet chemical synthesis of ceramic particles offers fine control of primary particle size, for example via the sol-gel process [Trusova, E. A. 2012]. Granulation or aggregation techniques, such as spray drying (physical process) or spray pyrolysis (wet chemical method), may also be employed.

The milling of ceramic powders is a common particle size reduction and size distribution modification technique. It typically occurs with a powder dispersed in a liquid phase. This promotes particle motion during milling which may otherwise be affected by the particles extrinsic properties (size, agglomeration or aggregation state) or, in the case of mixtures, their intrinsic or chemical properties [Francis, L. F. 2015]. The impact of ceramic particles with milling media, for example in a tumbling or ball mill, causes the breakup of aggregates and agglomerates and a reduction in particle size, largely due to brittle fracture. The rate of particle size decrease is dependent on the frequency and energy of the collisions and this rate decreases exponentially with the number of collisions (time) [Suryanarayana, C. 2001]. As particle size decreases, the presence of flaws of a critical length (for further fracture) also decreases, resulting in a convergence of the particles to a size which is dependent on the energy of the milling impacts [Griffiths, A. A. 1921]. This, given sufficient milling time, causes a narrowing of the powder's particle size distribution. The stresses of mechanical attrition also induce strains in ceramic particles, with strain and size reduction being correlated [Delogu, F. 2006]. The relationship between strain accumulation and fracture is empirically related to a material's melting point (T_M) and Youngs modulus, with both affects being determined by the intrinsic nature and strength of the primary bonds that are present [Koch, C. C. 1997].

The high impact stresses (sometime > 10 GPa) that occur during PAD allow for the further size reduction of powders prepared by milling. Given that fracture and particle size reduction appear requisite for successful PAD, it may be beneficial to promote some regrowth of particles prior to deposition, particularly of the finer fragments produced during milling. This can be achieved by thermal pre-treatment of milled powder. Sintering is enhanced in finer particles (< 1 μm) and their growth is promoted, theoretically allowing for a narrowing of particle size distribution in milled material [Al Rsheed, A. 2021]. However, in practise, other preferential growth conditions, such as Ostwald ripening, may result in a degree of exaggerated grain growth of the larger particles too, resulting in an increase in particle size distribution. Annealing at temperatures several hundred degrees below the sintering temperature (for bulk ceramic densification) limits (exaggerated) grain growth whilst promoting only the initial stages of densification (i.e. the necking of the particles). Damage to particles is also recovered and strains are reduced during such annealing.

The production of necked aggregates by thermal pre-treatment can produce powders capable of high momentum impacts, whilst retaining fine primary particle sizes. The presence of aggregation inhibits uncontrolled agglomeration. Hence aggregation is beneficial to deposition, providing the bonds between the particles are weak enough (i.e. in the form of necks) such that they easily fracture on impact, avoiding excessive expenditure of the kinetic energy of the impact [Mihara, K. 2009].

6.8 Structural and electrical properties of ceramic films produced by PAD and their thermal modification

Ceramic anchor layers, of ~1 or < 1 µm thickness, and ceramic thick films (5+ µm) may be produced by PAD. These films often have high (95+ %) density, reduced particle sizes and high levels of microstrain. Surface and cross-sectional micrographs of a relatively dense $BaTiO_3$ film are shown in Figure 69(a) and (b). Annealing, at 750 ^oC, caused limited grain growth and a reduction in the size of the pores present within the film (see Figure 69(c) and (d)).

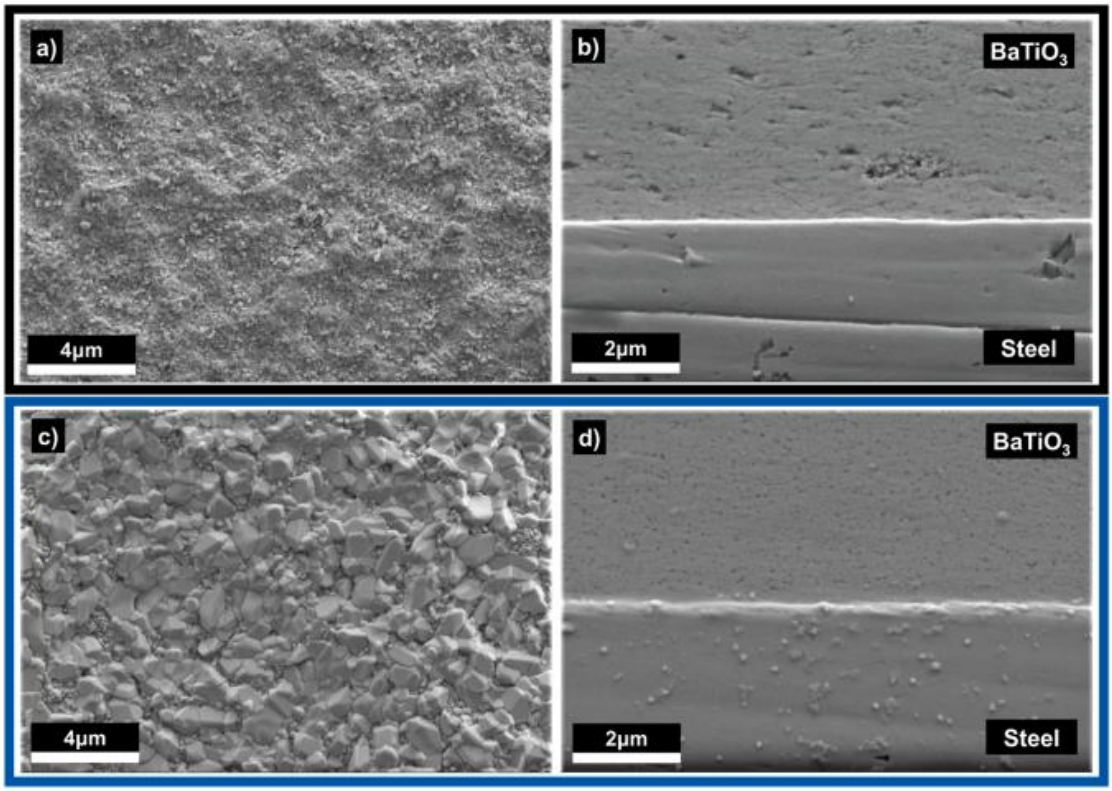

Figure 69. Surface and cross-sectional SEM micrographs of $BaTiO_3$ films deposited on steel are shown in (a) and (b), respectively. The film surface has some roughness and cratering, which is typical of a ceramic deposition. Annealing at 750 ^oC caused limited grain growth, as seen in (c), and some closing of the pores within the film, in (d). Taken from [Bentzen, M. 2023].

Figure 70 shows XRD peak broadening in a $BaTiO_3$ film deposited on steel by PAD, the broadening can be associated with reduced crystallite sizes and high levels of microstrains [Mote, V. D. 2012]. This broadening affect increases as film thicknesses increase from 0.2 µm to 0.5 µm and to 2 µm in Figure 70(a), (b) and (c), suggesting some degree or combination of microstrain increase and crystallite size reduction with increasing film thickness.

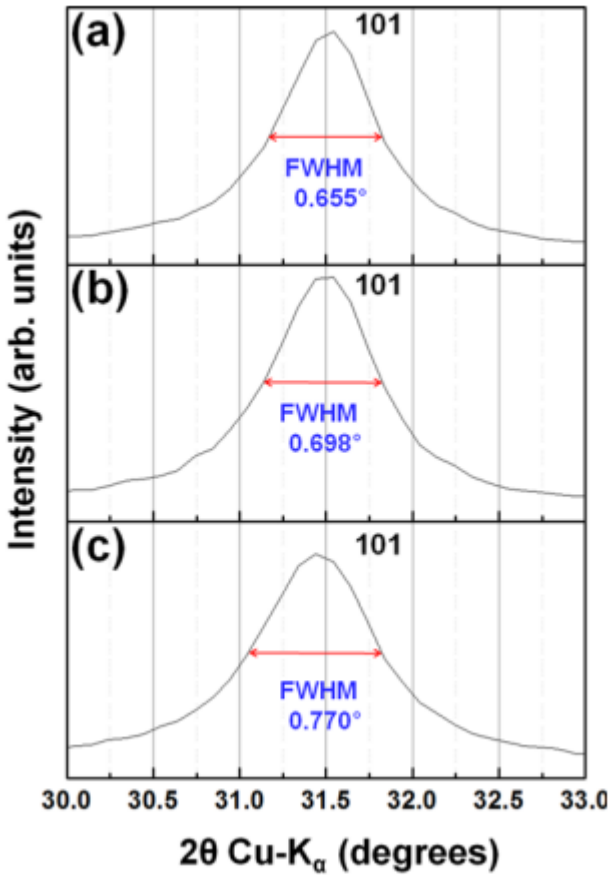

Figure 70. XRD peaks of $BaTiO_3$ (101) Bragg reflections from PAD films with thicknesses of 0.2 µm (a), 0.5 µm (b), and 2 µm (c), showing peak broadening that correlates with film thickness. Taken from [Kim, H-K. 2015].

The TEM micrographs in Figure 71(a) and (b) show an increase in lead magnesium niobate – lead titanate (PMN-PT) crystallite sizes in a PAD film annealed at 500 ^{o}C, in comparison with the as-deposited film. In the electron diffraction patterns in Figure 71(c), a reduction in the intensity of the polycrystalline diffraction rings/bands, upon annealing, indicates a potential reduction in the presence of microstrains as well as the observed increase in crystallite sizes.

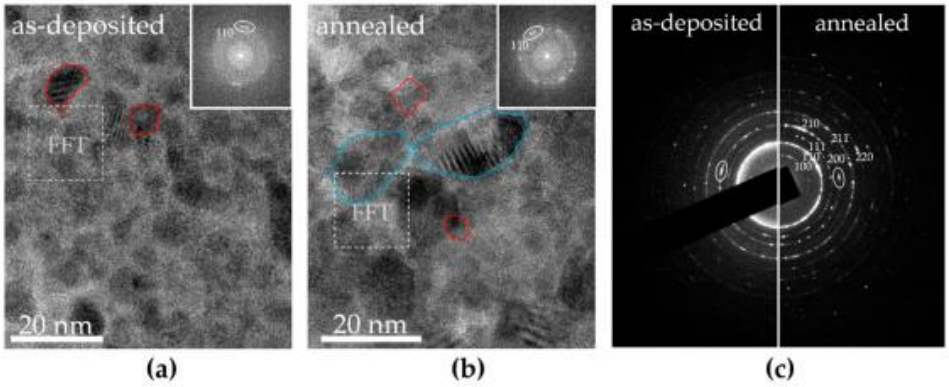

Figure 71. Micrographs showing some larger grains and crystallites in the lead magnesium niobate – lead titanate (PMN-PT) film annealed at 500 ^{o}C, in (b), compared with the as-deposited film, in (a). Electron diffraction patters, in (c), show a reduction in the presence of polycrystalline diffraction ring/band intensity upon annealing. Taken from [Žiberna, K. 2023].

The partial recovery of crystallinity and the potential reduction of strains coincide with some recovery of dielectric and ferroelectric properties. In as deposited films, electrical defects are common, they result in dielectric losses and can be removed by annealing at a critical temperature that is below but related to the materials melting point [Exner, J. 2020]. Figure 72 shows high variability in the relative permittivity of a $BaTiO_3$ PAD film upon initial heating. Subsequent heating cycles yield temperature stable permittivity, which is better than that of the bulk. Figure 73(a) and (b) likewise shows a variation between the permittivity upon initial heating and when measuring permittivity response after annealing at 500 ^{o}C. Some recovery of polarisation response also occurs with annealing, as shown in (c), and XRD peak broadening decreases (see Figure 73(d)).

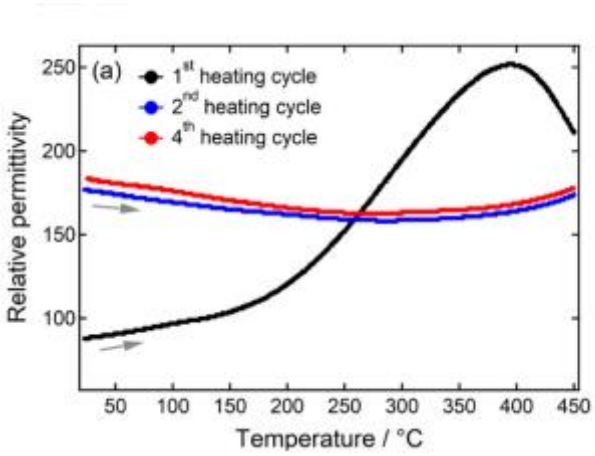

Figure 72. The variation in permittivity for $BaTiO_3$ PAD films between initial and subsequent heating cycles, due to the presence of defects in the as deposited films that recover on annealing. Taken from [Khansur, N. H. 2018].

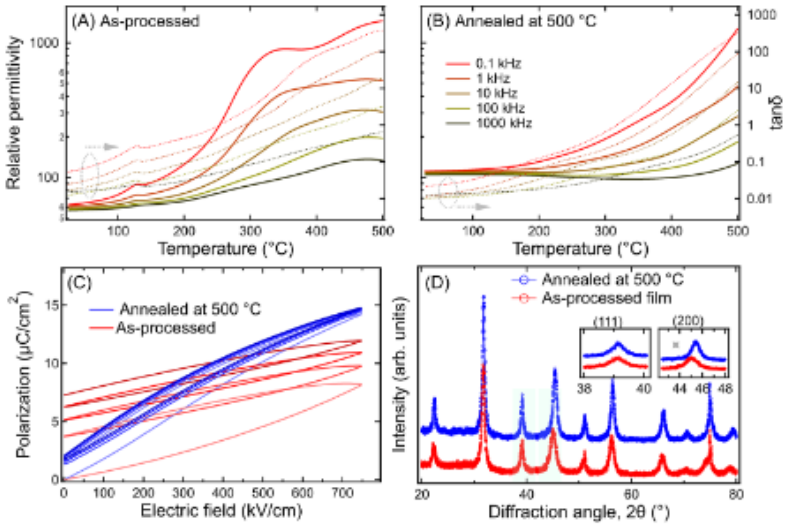

Figure 73. The permittivity- and tan δ- temperature plots for as deposited, in (a), and annealed at 500 ^{o}C, in (b), $BaTiO_3$ PAD films. An increase in P_{Max} is shown to occur after annealing, in (c). Some reduction in XRD peak broadening, with annealing, is also shown to occur in (d). Taken from [Zhou, F. 2022].

6.9 Outlook

The application of the PAD method to the production of electroceramics with processing modified dielectric properties shows promise. The resulting films are dense and have uniform microstructures, ideal for electroceramic applications. A lack of fundamental understanding regarding the RTIC mechanism will necessitate investigation of the role of the various PAD deposition parameters with a view to making dense (95+ %) and thick (5+ µm) films of heavily deformed ceramic suitable for electrical characterisation. Annealing of the films will likely be required to induce some crystallite growth and microstrain reduction in order to recover ferroelectric and dielectric functional properties. This recovery could be tailored in the fabrication of CBN-based films, whose target functional properties are listed in Section 5 (Results chapter 1), promoting their suitability for energy storage (low losses) and high-temperature capacitor (temperature-stable permittivity) applications.

6.10 References

Al Rsheed, A. Aldawood, S. Aldossary, O. M. 2021. The Size and Shape Effects on the Melting Point of Nanoparticles Based on the Lennard-Jones Potential Function. *Nanomater*. **11**. 2916

DOI: https://doi.org/10.3390/nano11112916

Apetz, R. van Bruggen, M. P. B. 2003. Transparent alumina: A light-scattering model. *J. Am. Ceram. Soc*. **86**. 480-486.

DOI: https://doi.org/10.1111/j.1151-2916.2003.tb03325.x

Akedo, J. Lebedev, M. 1999. Microstructure and Electrical Properties of Lead Zirconate Titanate ($Pb(Zr_{0.52}/Ti_{0.48})O_3$) Thick Films Deposited by Aerosol Deposition Method. *Jpn. J. Appl. Phys*. **38**. 5397-5401

DOI: https://doi.org/10.1143/JJAP.38.5397

Akedo, J. 2004. Aerosol deposition method for fabrication of nano crystal ceramic layer. *MSF*. **449–452**. 43-48.

DOI: https://doi.org/10.4028/www.scientific.net/MSF.449-452.43

Akedo, J. 2006. Aerosol deposition of ceramic thick films at room temperature: Densification mechanism of ceramic layers. *J. Am. Ceram. Soc*. **89**. 1834–1839.

DOI: https://doi.org/10.1111/j.1551-2916.2006.01030.x

Akedo, J. 2008. Room Temperature Impact Consolidation (RTIC) of Fine Ceramic Powder by Aerosol Deposition Method and Applications to Microdevices. *J. Therm. Spray Technol.* **17**. 181-198

DOI: https://doi.org/10.1007/s11666-008-9163-7

Benchaita, M. Griffith, P. Rabinowicz, E. 1983. Erosion of Metallic Plate by Solid Particles Entrained in a Liquid Jet. *J. Eng. Ind*. **105**. 215-222

DOI: https://doi.org/10.1115/1.3185891

Bentzen, M. Maier, J. Eckstein, U. He, J. Henss, A. Khansur, N. H. Glaum, J. 2023. Enhanced grain growth and dielectric properties in aerosol deposited BaTiO3. *J. Am. Ceram. Soc*. **43**. 4386-4394

DOI: https://doi.org/10.1016/j.jeurceramsoc.2023.03.012

Cho, M-Y. Lee, D-W. Ko, P-J. Koo, S-M. Kim, J. Choi, Y-K. Oh, J-M. 2019. Adhesive Mechanism of Al2O3/Cu Composite Film via Aerosol Deposition Process for Application of Film Resistor. *Electron. Mater. Lett*. **15**. 227–237

DOI: https://doi.org/10.1007/s13391-018-00111-w

Cicconi, M. R. Khansur, N. H. Eckstein, U. R. Werr, F. Webber, K. G. de Ligny, D. 2020. Determining the local pressure during aerosol deposition using glass memory. *J. Am. Ceram. Soc*. **103.** 2443-2452

DOI: https://doi.org/10.1111/jace.16947

Daneshian, B. Gärtner, F. Assadi, H. Villa Vidaller, M. Höche, D. Klassen, T. 2022. Features of ceramic nanoparticle deformation in aerosol deposition explored by molecular dynamics simulation. *Surf. Coat. Technol*. **429**. 127886

DOI: https://doi.org/10.1016/j.surfcoat.2021.127886

Delogu, F. Cocco, G. 2006. Microstructural refinement of ceramic powders under mechanical processing conditions. *J. Alloys Compd*. **420**. 246-250

DOI: https://doi.org/10.1016/j.jallcom.2005.10.037

Eckstein, U. Exner, J. Golob, A. B. Žiberna, K. Dražić, G. Uršič, H. Wittkämper, H. Papp, C. Kita, J. Moos, R. Webber, K. G. Khansur, N. H. 2022. Temperature-dependent dielectric anomalies in powder aerosol deposited ferroelectric ceramic films. *J. Mater*. **8**. 1239-1250

DOI: https://doi.org/10.1016/j.jmat.2022.05.001

Exner, J. Nazarenus, T. Hanft, D. Kita, J. Moos, R. 2020. What Happens during Thermal Post-Treatment of Powder Aerosol Deposited Functional Ceramic Films? Explanations Based on an Experiment-Enhanced Literature Survey. *Adv. Mater*. **32**. 1908104

DOI: https://doi.org/10.1002/adma.201908104

Francis, L. F. Sadler, B. J. H. Roberts, C. C. 2015. Materials Processing: A Unified Approach to Processing of Metals, Ceramics and Polymers. *Academic Press*. 58

DOI: https://doi.org/10.1016/C2009-0-64287-2

Griffith, A. A. 1921. The phenomena of rupture and flow in solids. *Philos. Trans. R. Soc. Lond*. **A 221**. 163–198

DOI: https://doi.org/10.1098/rsta.1921.0006

Hanft, D. Exner, J. Schubert, M. Stöcker, T. Fuierer, P. Moos, R. 2015. An Overview of the Aerosol Deposition Method: Process Fundamentals and New Trends in Materials Applications. *J. Ceram. Sci. Technol.* **6.** 147-182

DOI: https://doi.org/10.4416/JCST2015-00018

Hanft, D. Glosse, P. Denneler, S. Berthold, T. Oomen, M. Kauffmann-Weiss, S. Weis, F. Häßler, W. Holzapfel, B. Moos, R. 2018. The Aerosol Deposition Method: A Modified Aerosol Generation Unit to Improve Coating Quality. *Mater*. **11**. 1572.

DOI: https://doi.org/10.3390/ma11091572

Gopi, R. Saravanan, I. Devaraju, A. loganathan, G. B. 2020. Investigation of shot peening process on stainless steel and its effects for tribological applications. *Mater. Today*. **22**. 580-584

DOI: https://doi.org/10.1016/j.matpr.2019.08.215

Hellstern, E. Fecht, H. Fu, Z. Johnson, W. 1989. Stability of CsCl-type intermetallic compounds under ball milling. *J. Mater. Res.* **4**. 1292-1295.

DOI: https://doi.org/10.1557/JMR.1989.1292

Imanaka, Y. Amada, H. Kumasaka, F. 2013. Dielectric and Insulating Properties of Embedded Capacitor for Flexible Electronics Prepared by Aerosol-Type Nanoparticle Deposition. *Jpn. J. Appl. Phys*. **52**. 05DA02
DOI: https://doi.org/10.7567/JJAP.52.05DA02

Khansur, N. H. Eckstein, U. Benker, L. Deisinger, U. Merle, B. Webber, K. G. 2018. Room temperature deposition of functional ceramic films on low-cost metal substrate. *Ceram. Int*. **44**. 16295-16301

DOI: https://doi.org/10.1016/j.ceramint.2018.06.027

Kim. C-W. Choi, J-H. Kim, H-J. Lee, D-W. Hyun, C-Y. Nam, S-M. 2012. Effects of interlayer roughness on deposition rate and morphology of aerosol-deposited Al2O3 thick films. *Ceram. Int*. **38**. 5626-5627

DOI: https://doi.org/10.1016/j.ceramint.2012.04.003

Kim, H-K. Lee, S-H. Lee, S-G. Lee, Y-H. 2015. Densification mechanism of BaTiO3 films on Cu substrates fabricated by aerosol deposition. *Electron. Mater. Lett*. **11**. 388–397

DOI: https://doi.org/10.1007/s13391-015-4419-0

Koch, C. C. 1997. Synthesis of nanostructured materials by mechanical milling: problems and opportunities. *J. Nanomater*. **9**. 13-22

DOI: https://doi.org/10.1016/S0965-9773(97)00014-7

Lebedev, M. Akedo, J. Ito, T. 2005. Substrate heating effects on hardness of an α-Al2O3 thick film formed by aerosol deposition method. *J. Cryst. Growth*. **15**. e1301-e1306

DOI: https://doi.org/10.1016/j.jcrysgro.2004.11.109

Lebedev, M. Krumdieck, S. 2008. Optically Transparent, Dense α-Al2O3ThickFilms Deposited on Glass at Room Temperature. *Curr. Appl. Phys*. **8**. 233-236

DOI: https://doi.org/10.1016/j.cap.2007.10.057

Lee, D-W. Kim, H-J. Kim, Y-H. Yon, Y-H. Nam, S-M. 2011. Growth Process of α-Al2O3 Ceramic Films on Metal Substrates Fabricated at Room Temperature by Aerosol Deposition. *J. Am. Ceram. Soc*. **94**. 3131-3138

DOI: https://doi.org/10.1111/j.1551-2916.2011.04493.x

Lee, D-W. Kim, H-J. Kim, Y-H. Jeon, M-S. Nam, S-M. 2012. Substrate hardness dependency on properties of Al2O3 thick films grown by aerosol deposition. *Surf. Coat. Technol*. **209**. 160-168

DOI: https://doi.org/10.1016/j.surfcoat.2012.08.012

Lee, M. W. Park, J. J. Kim, D. Y. Yoon, S. S. Kim, H. Y. Kim, D. H. James, S. C. Chandra, S. Coyle, T. Ryu, J. H. Yoon, W. H. Park, D. S. 2011. Optimization of supersonic nozzle flow for titanium dioxide thin-film coating by aerosol deposition. *J. Aerosol Sci*. **42**. 771-780

DOI: https://doi.org/10.1016/j.jaerosci.2011.07.006.

Naoe, K. Nishiki, M. Yumoto, A. 2013. Relationship Between Impact Velocity of Al2O3 Particles and Deposition Efficiency in Aerosol Deposition Method. *J. Therm. Spray. Tech*. **22**. 1267-1274

DOI: https://doi.org/10.1007/s11666-013-0031-8

Nam, S-M. Mori, N. Kakemoto, H. Wada, S. Akedo, J. Tsurumi, T. 2004. Alumina Thick Films as Integral Substrates Using Aerosol Deposition Method. *Jpn. J. Appl. Phys.* **43**. 5414

DOI: https://doi.org/10.1143/JJAP.43.5414

Nazarenus, T. Schlesier, K. Lebeda, F. Retsch, M. Moos, R. 2022. Microstrain release decouples electronic and thermal conductivity in powder aerosol deposited films. *Mater. Lett*. **322**. 132461

DOI: https://doi.org./10.1016/j.matlet.2022.132461

Mihara, K. Hoshina, T. Takeda, H., Tsurumi, T. 2009. Controlling factors of film-thickness in improved aerosol deposition method. *J. Ceram. Soc. Jpn*. **117**. 868-872

DOI: https://doi.org/10.2109/jcersj2.117.868

Mote, V. D. Purushotham, Y. Dole, B. N. 2012. Williamson-Hall analysis in estimation of lattice strain in nanometer-sized ZnO particles. *J. Theor. Appl. Phys*. **6**. 6

DOI: https://doi.org/10.1186/2251-7235-6-6

Rice, R. W. 1990. Ceramic Processing: An overview. *AlChE J*. **36**. 481-510

DOI: https://doi.org/10.1002/aic.690360402

Šadl, M. Tomc, U. Uršič, H. 2021. Investigating the Feasibility of Preparing Metal–Ceramic Multi-Layered Composites Using Only the Aerosol-Deposition Technique. *J. Mater.* **14**. 4548

DOI: https://doi.org/10.3390/ma14164548

Schubert, M. Exner, J. Moos, R. 2014. Influence of Carrier Gas Composition on the Stress of Al2O3 Coatings Prepared by the Aerosol Deposition *Method. J. Mater*. **7**. 5633-5642

DOI: https://doi.org/10.3390/ma7085633

Stratton, P. 2013. Ellingham diagrams – their use and misuse. *Int. Heat Treat. Surf. Eng*. **7**. 70-73

DOI: https://doi.org/10.1179/1749514813Z.00000000053

Suryanarayana, C. 2001. Mechanical Alloying and Milling. *Prog. Mater. Sc*i. 46.1-184

DOI: http://dx.doi.org/10.1016/S0079-6425(99)00010-9

Trusova, E. A. Vokhmintcev, K. V. Zagainov, I. V. 2012. Wet-chemistry processing of powdery raw material for high-tech ceramics. *Nano. Res. Lett.* **7**. 58

DOI: https://doi.org/10.1186/1556-276X-7-58

Zhuo, F. Eckstein, U. R. Khansur, N. H. Dietz, C. Urushihara, D. Asaka, T. Kakimoto, K-I. Webber, K. G. Fang, X. Rödel, J. 2022. Temperature-induced changes of the electrical and mechanical properties of aerosol-deposited BaTiO3 thick films for energy storage applications. *J. Am. Ceram. Soc.* **105**. 4108-4121

DOI: https://doi.org/10.1111/jace.18377

Žiberna, K. Šadl, M. Drnovšek, A. Dražić, G. Uršič, H. Benčan, A. 2023. Influence of Thermal Treatment on the Cross-Sectional Properties of Aerosol-Deposited Pb(Mg1/3Nb2/3)O3−PbTiO3 Thick Films. *Cryst*. **13**. 536

DOI: https://doi.org/10.3390/cryst13030536

7. Results 2: Particle aerosol deposition (PAD) at Erlangen and Leeds

To acquire an understanding of particle aerosol deposition (PAD), prior to the commission of PAD systems at Leeds and Manchester, the author and Dr. David Hall (of the University of Manchester) travelled to the University of Erlangen-Nuremburg, with various tungsten bronze (TB) ferroelectric powders for deposition. At Erlangen, the author assisted Dr. Neamul Khansur and Dr. Udo Ekstein in the deposition of 2 TB powders from Leeds. Photographs of the produced films can be seen in Appendix 5 and 6.

After commissioning the Leeds system, preliminary experiments with commercial Al_2O_3 were performed. Subsequently, first attempts at the microstructural and electrical characterisation of TB films were made. Prior to the optimisation of powder processing and the deposition of CBN at Leeds and Manchester (in Section 8, Results chapter 3), these experiments provided insight into the importance of powder processing and the need for dense, thick (5+ µm) films for electrical characterisation.

7.1 Microstructural characterisation of tungsten bronze (TB) powders and PAD films

7.1.1 TB powder characterisation

A CBN powder, with a nominal composition $Ca_{0.28}Ba_{0.72}Nb_2O_6$, was produced by the calcination of precursor oxides and carbonates for 2 h at 1150 ^oC, at a ramp rate of 300 $^oC\ h^{-1}$. Subsequent ball milling, for 24 h, produced a powder with irregular morphology and a primary particle size of up to ~5 µm, see Figure 74(a). For milling, ~400 mL bottles were 2/3 filled with milling media (~15 mm diameter yttria stabilised zirconia beads), 80 mL of 2-isopropanol and 50 g of powder. Milling bottles were rotated at 150 rpm. Particle size analysis, shown in Table 17, gave an average particle size, d(50), of 1.2 µm. Maximum particles size, d(90), was 3.6 µm. The properties d(50) and d(90) denote the percentage (50 or 90 %) of particles at or below the recorded size

A SNN powder, with nominal composition of $Sr_2Na_{0.8}Nb_5O_{15}$, was synthesised and provided by Dr. Tom Brown. This calcined powder was similar to the filled TB $Sr_2NaNb_5O_{15}$ in the publication Brown, T. *et al*. [2021]. The 0.8Na SNN powder used here was an unfilled TB as it contained less Na, since this removed any $NaNbO_3$ secondary phase [Brown, T. 2022]. As shown in Figure 74(b), this powder had a regular particle morphology and a primary particle size of approximately 2 - 3 µm. Necked bonds between the primary particles produced aggregates of 50+ µm in size. Particle size analysis, via a Mastersizer 3000, gave an average particle size of 2.3 µm, after planetary milling for 4 h (see Table 17). This milling was performed on a powder sample to reduce the presence of aggregates and aid the accuracy of size analysis. The minimum, d(10), and maximum, d(90), particle size values for

SNN in Table 17 were taken from the initial SNN size analysis prior to planetary milling. The bulk of the SNN powder, which was used for deposition and SEM imaging, underwent no planetary milling because it was believe the aggregates may aid deposition.

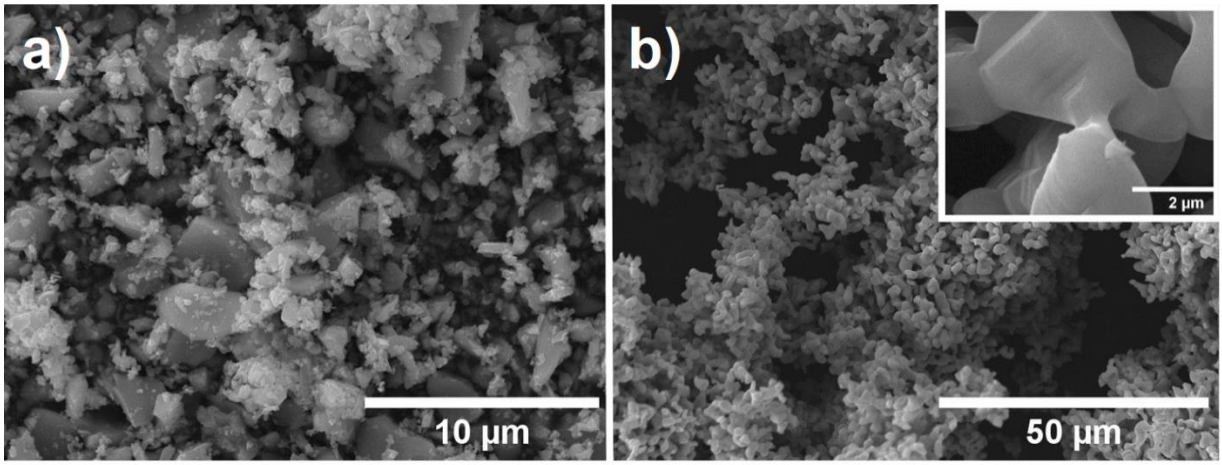

Figure 74. SEM secondary electron micrographs of, (a), CBN powder at 10 kx magnification, showing irregular particle size, and (b), SNN powder at 2.5 kx magnification, showing the aggregation of uniform particles. Inserted in (b) is a 50 kx magnification image showing the necked bonding between the SNN particles. Micrographs courtesy of the University of Erlangen-Nuremburg.

Prior to deposition, 5 - 10 g of powder was dried for 12+ h at 200 ^{o}C within the detachable aerosol generation chamber of the Erlangen PAD system. During deposition, vacuum chamber pressure was kept below 10 mbar. The N_2 carrier gas flowrate was controlled by inlet pressure and nozzle scan speed was 5 mm s^{-1}. The diverging nozzle used on this system became the basis for the design of the nozzle in the Leeds system, see Figure 85. The aerosol generation chamber of the PAD system was situated atop a vibrating bed, which aided in the aerosolization of the powder bed. More detail on the specifications of this rig can be found in the following journal publications, in which comparable deposition parameters are used [Khansur, N. H. 2019] and [Eckstein, U. 2022].

Table 17. Experimental conditions for the deposition of CBN and SNN powders via PAD at Erlangen. Particle size estimated using a Mastersizer 3000 particle size analyser.

Sample code	Avg. Powder size d(50) (µm)	Min. Powder size d(10) (µm)	Max. powder size d(90) (µm)	Substrate	Gas inlet flowrate (L m^{-1})	Inlet pressure (mbar)	Number of scans
CBN-2L	1.2	0.4	3.6	Stainless steel (SUS304)	2	115	10
CBN-8L	1.2	0.4	3.6	Stainless steel (SUS304)	8	316	10
SNN-4L	6.5 (2.3*)	2.2	50.9	Stainless steel (SUS304)	4	180	25
SNN-Ti	6.5 (2.3*)	2.2	2.2	Ti-Alloy (Ti-4V-6Al)	4	180	~25**

*Planetary milling of the SNN powder, for 4 h to reduce the presence of aggregates, produced a powder with an average particle size d(50) of 2.3 µm. Initial measurements, skewed by the presence of aggregates, gave an average particle size of 6.5 µm.

**Deposition was programmed for 150 scans, to deplete all the powder in aerosol generation chamber. Deposition ceased when the powder was depleted or only the fraction that could not be aerosolised at these conditions remained, this was estimated to occur somewhere around 25 scans.

7.1.2 CBN PAD film topography, microstructure and defects

During the deposition of CBN the vibration of the bed, and the motion induced by the aerosolising carrier gas, caused severe agglomeration of the CBN powder within the aerosol generation chamber. Judging by eye, these agglomerates were up to several mm in diameter. Often, they failed to aerosolise, a large fraction (> 50%) of the powder remained within the aerosol generation chamber post-deposition. If aerosolised, the agglomerated powder sometimes resulted in clogging of the nozzle. The carrier gas cleared these build-ups, or blockages, resulting in sudden bursts of high-mass rate powder deposition. As shown in Appendix 5(f) and (a), a thicker band of film was produced by a deposition burst, and a rougher texture was produced in the film deposited for 30 rather than 10 scans (in which the agglomeration was exacerbated by the extended run-time). The phenomenon of uncontrolled agglomeration served to reduce the consistency of the aerosol resulting in a snow-globe or blizzard-like appearance within the aerosol generation chamber, rather than the desired uniform mist (aerosol). The CBN films produced tended to be visibly thick and rough. They were white in appearance, matching the powder. They possessed low mechanical strength, exhibiting some disintegration when surface shearing the deposited film with a spatula. See the top of Appendix 5(d) for the damage caused by shearing.

Profilometry data from a CBN28 film deposited at 2 L min^{-1} on steel (SUS304), obtained from confocal microscopy, revealed an approximately 11 mm diameter film which was thickest 2 - 3 mm from its edge and more uniform in thickness at the centre, see Figure 75. The film was 85 µm at its thickest point, with a centre-region of thickness ~25 (±5) µm.

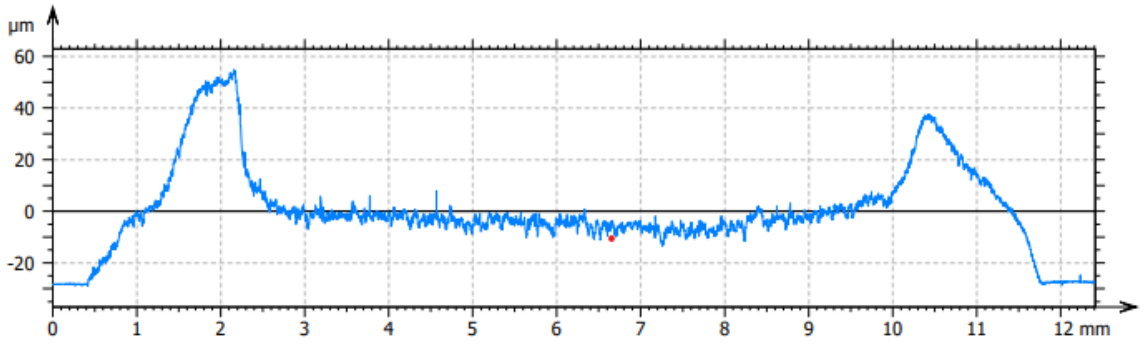

Figure 75. Profilometry of a CBN28 film deposited at 2 L min^{-1} on steel (SUS304). Data obtained from topographical imaging via a confocal microscope (Carl Zeiss, LSM800).

The influence of carrier gas flowrate (2 vs 8 L min^{-1}) on CBN28 PAD film properties and surface defects was assessed by optical microscopy and scanning electron microscopy.

Observed via optical microscopy, which has a limited depth of focus, macro-roughness of the films was apparent. Neighbouring regions of the films had differing degrees of resolution, when employing the same focusing conditions, indicating a dissimilar distance between themselves and the objective lens, see Figure 76. Darker contrasted pinholes were observed in CBN28 films deposited at both carrier gas flowrates, of 2 and 8 L min^{-1}. Larger pinholes (> 5 µm) were more numerous in the 8 L min^{-1} film, see Figure 76(b).

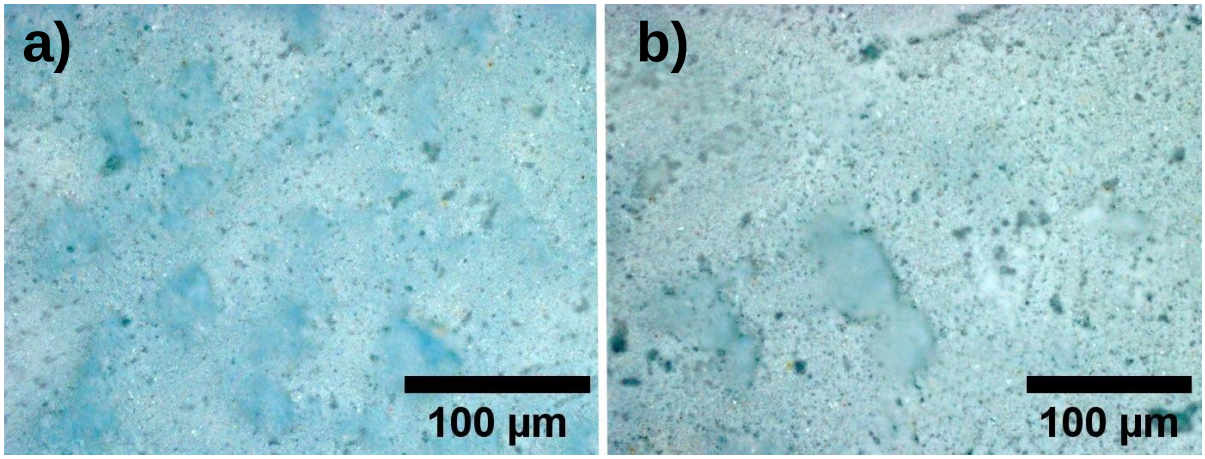

Figure 76. Optical micrographs of CBN28 films deposited at N_2 flowrates of 2 and 8 L min^{-1}, in (a) and (b), respectively, showing macro-roughness, evidence by regions out of the range of focus, and the presence of darker contrasted pin-holes.

Secondary electron SEM of the CBN28 films was performed using lower and upper angle electron detectors, with the latter providing more topographical information. When deposited at 2 L min^{-1}, particles of up to 2 µm in diameter could be seen in the micrographs in Figures 77(a) and (b), produced by lower and upper angle detectors respectively. No extensive plastic deformation of these surface particles was evident, given the sharp and well-defined particle edges.

Larger particles, up to ~4 µm in diameter, were present in the CBN film deposited at 8 L min^{-1}, see Figures 77(c) and (d). This film also lacked any clear evidence of plastically deformed particles.

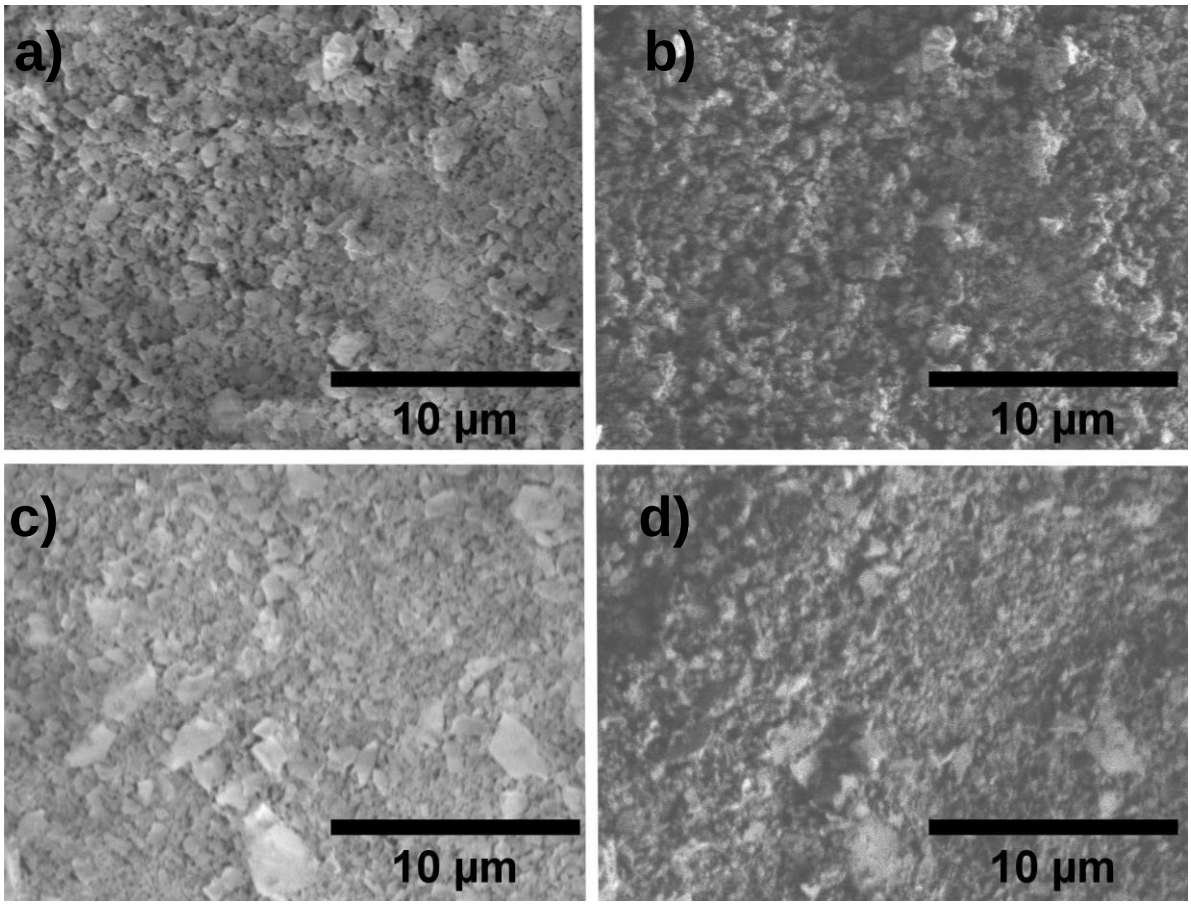

Figure 77. Secondary electron micrographs from SEM of CBN films deposited on steel (SUS304) at 2 L min^{-1}, (a) and (b), and 8 L min^{-1}, (c) and (d), at 5 kx magnification. Secondary electrons in images (a) and (c) were captured by a lower angle detector, giving more topographical information.

To summarise, the CBN28 powder was prone to agglomeration in the aerosol generation chamber during deposition. There was a lesser presence of surface defects (pinholes) in the CBN28 film deposited at lower carrier gas flowrates (2 vs 8 L min^{-1}). Due to this, the 2 L min^{-1} film was chosen for phase and electrical analysis, which is shown in Section 7.4.

7.1.3 Strontium sodium niobate (SNN) PAD film microstructure, phase identification, crystallinity, and deformation

The SNN powder experienced no, or very little, uncontrolled agglomeration during deposition. The aerosol produced was of the “uniform mist”-type and during the deposition of SNN, onto the Ti-alloy substrate, over 90% of the powder was depleted after approximately 25 scans. The SNN films produced were dark and uniform in appearance, in contrast to the white SNN powder. The films possessed no visible thickness and were judged to be well adhered to the substrate, due to their resistance to being scraped-off by sheering (using the edge of a fresh substrate). See Appendix 6 for photographs of the SNN PAD films.

Optical microscopy of the SNN films was inconclusive as characterisation of the film's features required higher resolution EM. See Appendix 7 for the SNN optical micrographs. The XRD patterns for SNN, deposited on SUS304 stainless steel and Ti-alloy, gave little indication to the presence of a tungsten-bronze structure, suggesting that the films were of sub-micron thickness- assuming that the TB structure was retained at all in the material post-deposition. See Appendix 8 for XRD patterns of SNN on steel and Ti-alloy. Electrical analysis of the films was not possible, due to their high conductivity, suggesting that the SNN films had perforations or areas of the substate were exposed.

Secondary electron micrographs of the SNN films, deposited at a carrier gas flowrate of 4 L min^{-1}, on SUS304 stainless steel and Ti-4V-6Al Ti-alloy, are shown in Figure 78. Micrographs, from Lower angle SE detectors, show an apparently continuous film with extensive deformation at the film surface when deposited on both stainless steel (Figure 78(a)) and Ti-alloy (Figure 78(c)). The visually dark appearance of the films may be caused by the specular scattering of light upon the films surface, which possessed micro-roughness. Similar (high deformation) Al_2O_3 films, seen in Figure 88, were also visually dark. Individual grains are difficult to identify from the lower angle micrographs.

The contrasted outlines of features with irregular morphology and diameters of ~1 µm can be seen in the upper angle micrographs, Figure 78(b) and (d). These features are presumably deformed fragments from the 2 - 3 µm primary particles in the SNN powder. They may also be impact craters on a consolidated layer. Darker contrasted regions, at the bottom-left and bottom-middle, in Figure 78(d) are inferred to be exposed substrate. To a lesser extent these features are also present in 78(b).

The Ti-alloy and the stainless steel substrates are reported to have Vickers hardness of ~300 and ~150 respectively [Ma, X. 2017] and [Lu, C-J. 2023]. Despite this variation, apparent anchor layers were formed on both substrates. The SNN-Ti alloy film was visibly darker, see Appendix 6. In leu of any other thickness estimates, the darker film was presumed to be thicker and chosen for further EM characterisation.

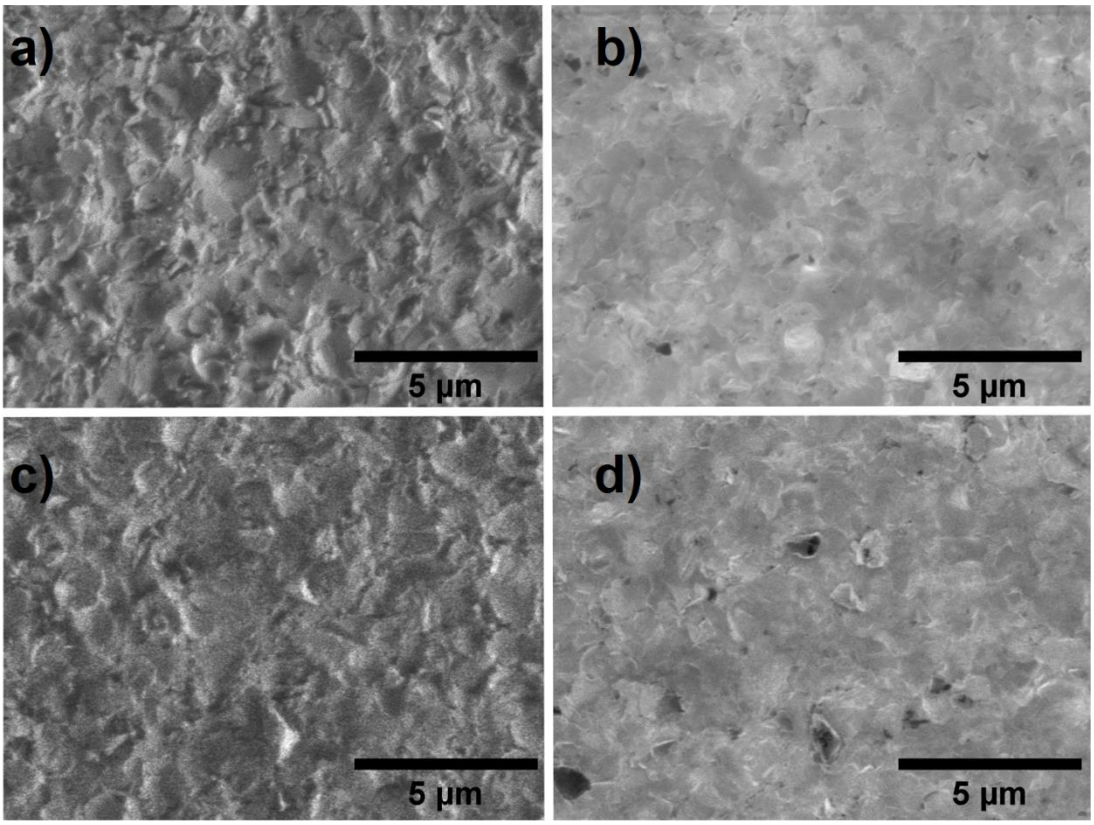

Figure 78. Secondary electron micrographs from SEM of SNN deposited on SUS304 stainless steel, (a) and (b), and Ti-4V-6Al Ti-Alloy substrates at 4 L min^{-1}, (c) and (d), at magnifications of 10 kx. Secondary electron micrographs (a) and (c) were captured by a lower angle detector and give more topographical information, but less contrast between the deposited particles and the (darker) exposed (higher conductivity) substrate.

Cross-sectional STEM and STEM-EDX of the SNN film deposited on Ti-alloy was performed by Prof. Andy Brown and is shown in Figure 79. Preparation of the thin film cross-section, via Ga ion-focused ion beam milling, was performed by John Harrington. A high-density/nonporous Sr, Na, Nb and O containing (SNN) layer of irregular thickness, of up to 400 nm, was identified. A protective Pt coating was applied to the film prior to ion milling, to prevent charging and surface damage. Some Ga, from the ion beam, is assumed to have deposited into this protective layer during excavation. The apparent presence of Na in the Pt layer is assumed to be mischaracterised Ga, given the comparable energies of the Na(-K_α) = 1.041 keV and the Ga(-L) = 1.18 keV characteristic X-rays and the overlap of the lines associated with these species in the EDX spectra [AMETEK Inc. 2022].

Deformation of the underlying substrate is apparent, although no comparable EM of the substrate prior to deposition was available. No clear distinction between the individually deposited particles can be made in the high-density film. Deformation, possibly extensive and plastic flow-like, is

apparent in the SNN layer. This deformation is further observed in the micrograph in Appendix 9, which corresponds to the site of further TEM analysis shown in Figure 80(a).

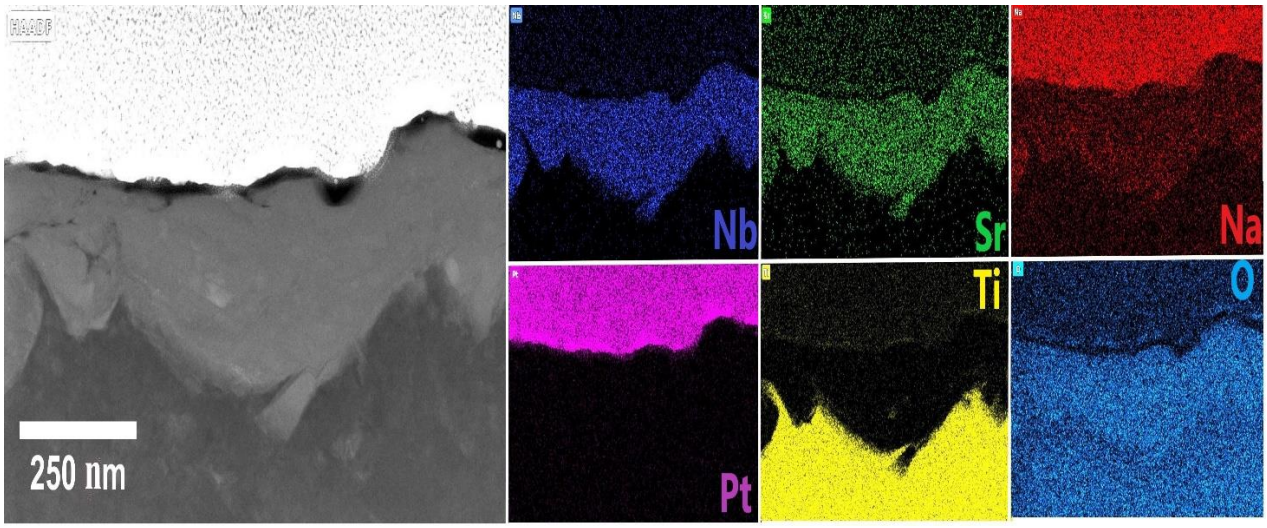

Figure 79. HAADF STEM and STEM-EDX elemental maps for SNN deposited on a Ti-Al alloy substrate. Some Ga was likely deposited into the Pt layer during Ga-ion beam milling of the cross-section. The characteristic X-rays emitted by the Ga during EDX have energies of (L) = 1.18 keV, comparable to the energies of the Na(-K_α) X-rays = 1.041 keV, likely resulting in the misidentification of Ga as Na in the elemental map [AMETEK Inc. 2022]. The micrograph and elemental maps were captured by Prof. Andy Brown.

The SNN film Bright Field TEM micrographs, in Figure 80, show a speckled contrast which may indicate a nanocrystalline nature to the film. In materials with crystalline order, the transmission or diffraction of electrons is orientationally dependent. A greater intensity of diffraction occurs when the electron beam is appropriately aligned with a plane of atoms. In Figure 80(b), contrasting regions are typically < 50 nm in scale.

In Figure 80(a) a larger region (250+ nm) of darker contrast, with a well-defined upper left edge, can be seen. It is highlighted by a blue circle, which indicates the selected area for the corresponding electron diffraction pattern. This electron diffraction pattern is symmetric and shows planes of uniform lattice spacing, indicating the retention of long-range crystalline order in this single crystal particle fragment. An average diffraction pattern spacing of ~3.3 nm^{-1}, between the centre plane of diffraction points and parallel planes, corresponds to a d spacing of 3.03 Å. These diffraction points most likely correspond to the (410) plane of SNN, which has d spacing of 3.02 Å (ICCD 00-059-0894),

although measurement errors of up to 5% allow for other planes to be responsible for the pattern, i.e. the (330) plane or the (400) plane, with respective lattice spacings of 2.93 and 3.11 Å.

The (blue) electron diffraction pattern from the film in Figure 80(b) shows diffraction rings, indicating a distribution of atomic plane spacing over the, 100's of nm, range of the ED aperture. This indicates polycrystallinity over this length scale with diffraction spots corresponding to individual crystals. The diffraction ring is continuous, not solely consisting of numerous diffraction spots, indicating significant distortions of the common lattice spacing, i.e. deformation, in the SNN layer. This corroborates the possible flow-like deformation seen in Figure 79. See Appendix 9 for further evidence of deformation, from a lower magnification image of the site in Figure 80(a). The (orange) diffraction patterns in Figure 80(a) and (b), originating from the substrate material, likewise show variation in crystal distortion and likely levels of microstrain.

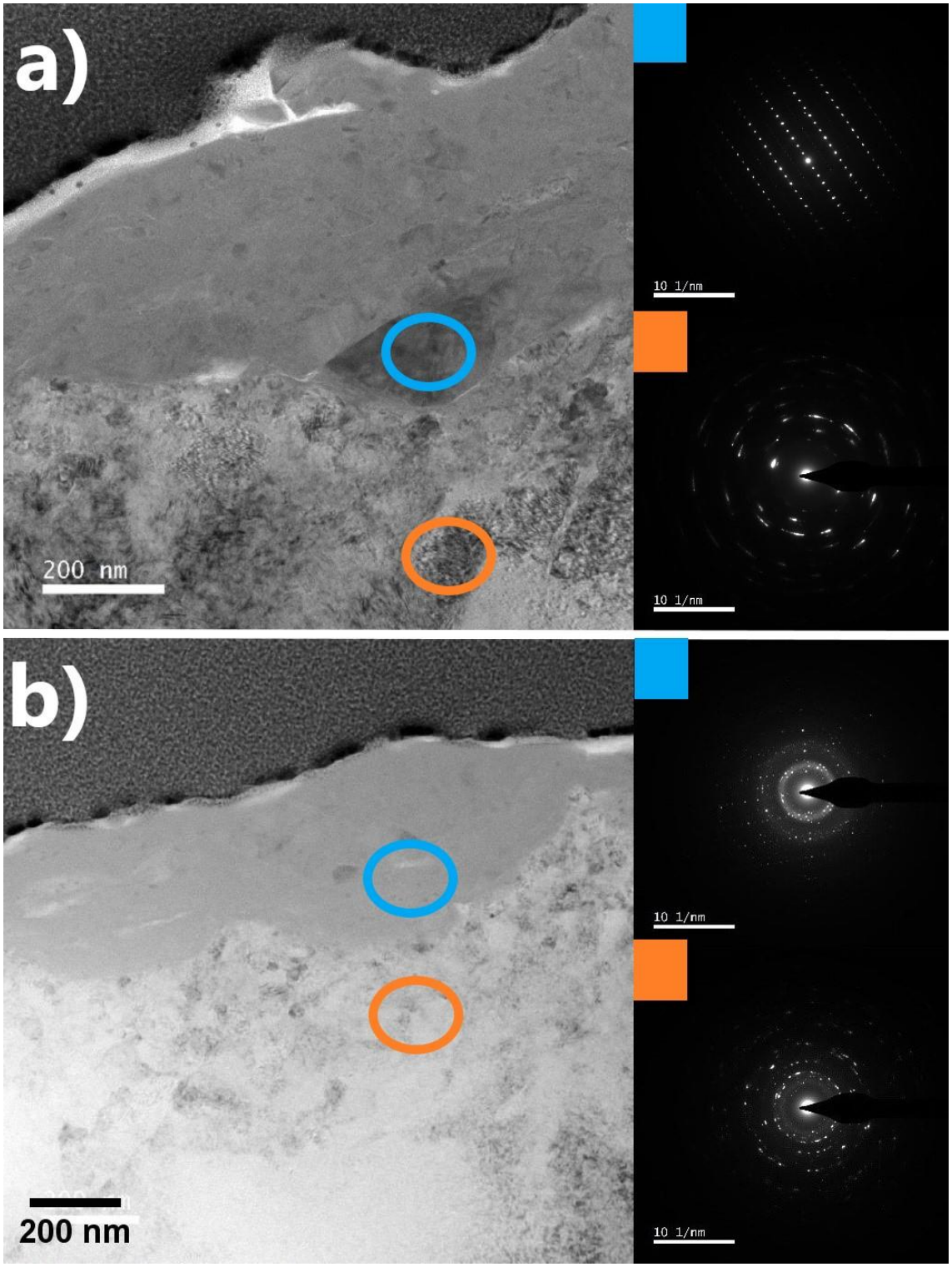

Figure 80. Bright Field TEM and electron diffraction patterns for SNN deposited on Ti-alloy. Blue and orange rings indicate the selected areas from which the corresponding electron diffraction patterns originate. Electron diffraction patterns show a single crystal SNN grain (fragment) with ordered lattice spacing, in (a) (blue), and a highly deformed and nanocrystalline region, in (b) (blue). Electron diffraction from the substrate (orange) also indicated varied degrees of deformation. These micrographs were captured by Prof. Andy Brown.

To summarise, aggregated SNN particles did not agglomerate during aerosol generation or deposition and did form apparent anchor layers on metal substrates. A high-density submicron anchor layer of SNN on Ti-alloy substrate was confirmed, and shown, by ED, to possess high levels of deformation. These films were not suitable for electrical testing due to conductivity, likely due to perforations of the < 400 nm anchor layer.

7.2 Leeds PAD set up and preliminary testing

The commissioning of the Leeds PAD system was undertaken by the author with the extensive support of Rob Simpson, Dr. Thomas Hooper and Prof. Nik Kapur. The rig was an in-house design. The nozzle and vibrating aerosol generation chamber were inspired by the Erlangen PAD system. The Leeds system was commissioned with a combination of pre-purchased parts and in-house engineering. The functionality of the Leeds system was tested using commercial Al_2O_3 powders.

7.2.1 Leeds PAD system set up

The key physical components of the Leeds PAD system are listed below, with numbers corresponding to the schematic in Figure 81. The system principally operates by the establishment of a pressure gradient between the aerosol generation chamber (AGC) and the vacuum chamber (VC). A carrier gas and vacuum pump establish this gradient. The carrier gas also aerosolises micrometre-scaled ceramic particles. A nozzle accelerates the aerosol into the vacuum chamber, allowing for high momentum impacts with the substrate and the consolidation of the particles into continuous, high-density films.

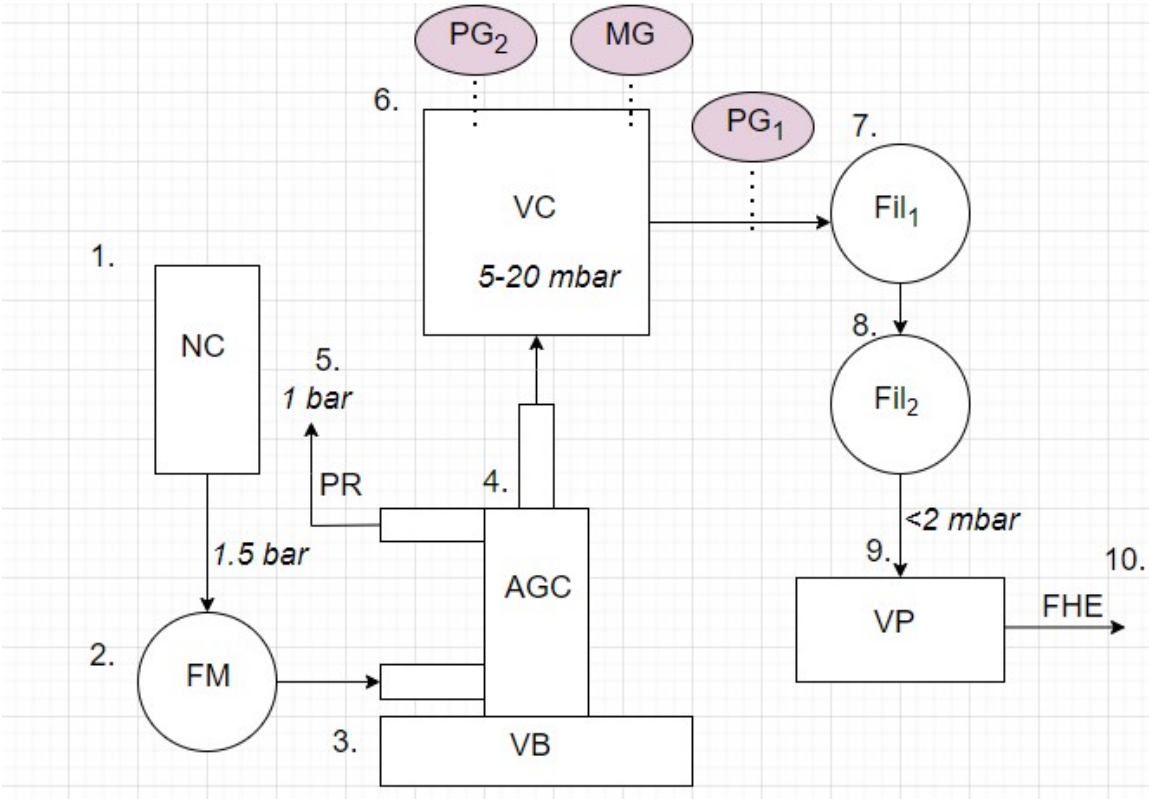

Figure 81. A schematic of the Leeds PAD system that shows the pressure gradient from the nitrogen cannister (NC) to the vacuum chamber (VC) and vacuum pump (VP). The nature and specifications of each listed component are described below, as well as that of the removable sample stage (RSS) and nozzle, which operated within the VC. The components include a flow meter with a flow control dial (FM), a vibrating bed (VB), an aerosol generation chamber (AGC), a pressure release valve (PR), Pirani gauges (PG_1 and PG_2), a manual pressure gauge (MG), filters (Fil_1 and Fil_2) and, surrounding the PAD system, a fume-hood exhaust system (FHE).

1. The N_2 gas cannister (NC) was fitted with a regulator which limited the inlet pressure of the carrier gas to 1.5 bar. The NC is not pictured in Figure 82.

2. The manual flow controller and flowmeter (FM) had a maximum flowrate (at atmospheric pressure) of 12 L min^{-1}. During operation, the rigs closed-circuit vacuum conditions exerted a vacuum pull that resulted in a (presumed) greater flow of carrier gas. This pull also (artificially) raised the widget that indicated flowrate, thus recalibration was required. To ensure consistent operational flowrate the control dial was marked at intervals that corresponded to gas flowrates of 2, 4, 6, 8, 10 and 12 L min^{-1} at atmospheric pressure. Operational flowrates were therefore consistent but likely higher than indicated.

3. The KS 130 basic vibrating bed (VB) (IKA England LTD, UK) operated up to 500 RPM and was typically set to 300 RPM to avoid excessive or resonant vibration of the AGC.

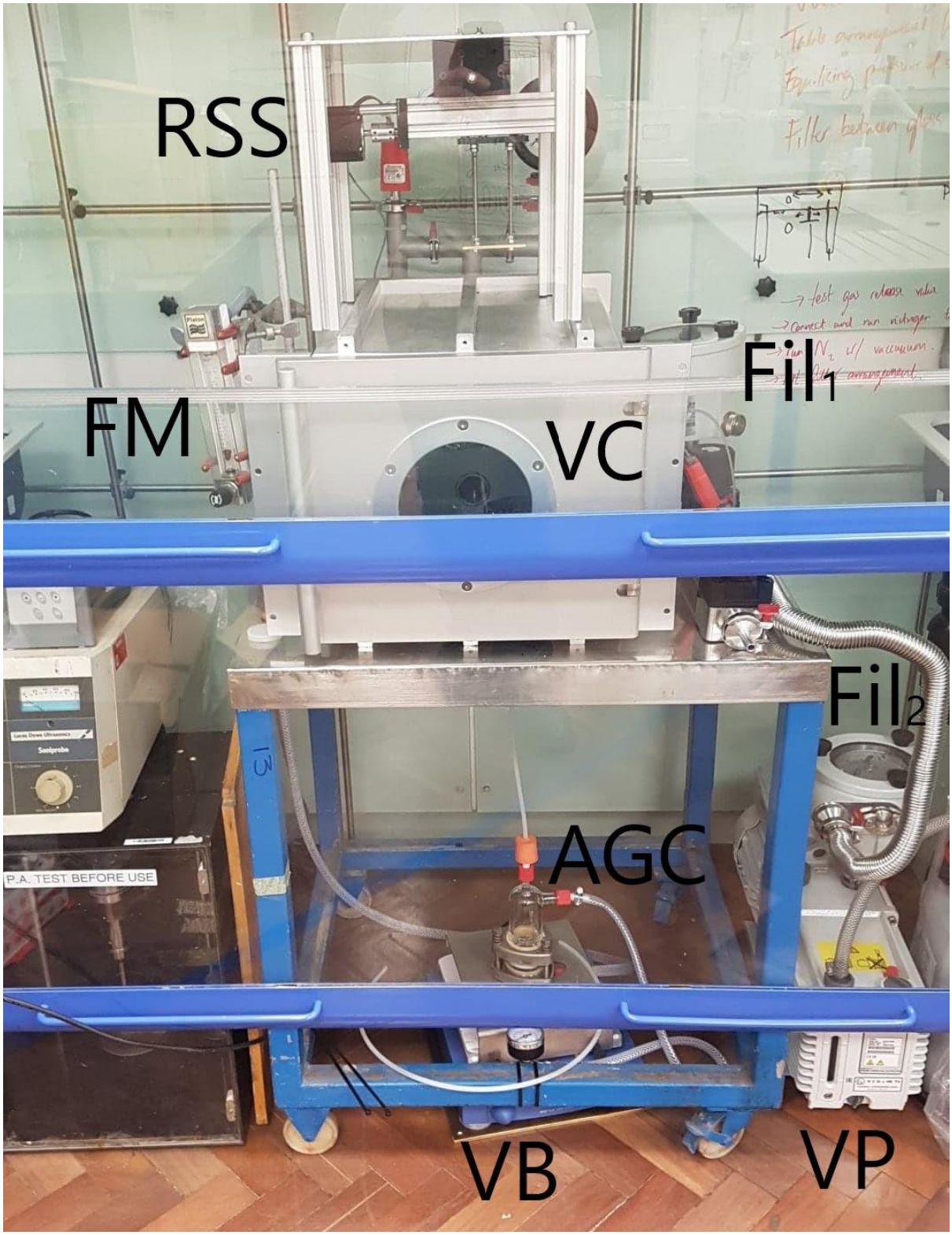

Figure 82. A photograph of the Leeds PAD system, within the fume-hood. The removable sample stage is positioned atop the vacuum chamber. All abbreviations are detailed in the caption of Figure 81.

4. The borosilicate aerosol generation chamber (AGC) was of bespoke design and was purchased from Asynt Ltd. (Cambridgeshire, UK), see Figure 83. Typically, Durapore™ filter papers from Merk Millipore **(**Darmstadt, Germany), were sandwiched between the two halves of the AGC and served as a bed for the powder. In addition to an inlet and an outlet (numbered 1 and 2 in Figure 83(b)), a pressure relief outlet (numbered 3 in Figure 83(b)) limited the pressure in the AGC to 1.5 bar. The AGC was fastened to the vibrating bed by a weighted (steel) plate, which served to prevent any travel of the AGC during vibration/operation.

5. The pressure relief valve (PR), set to 1.5 bar, exhausted into the fume-hood (FHE).

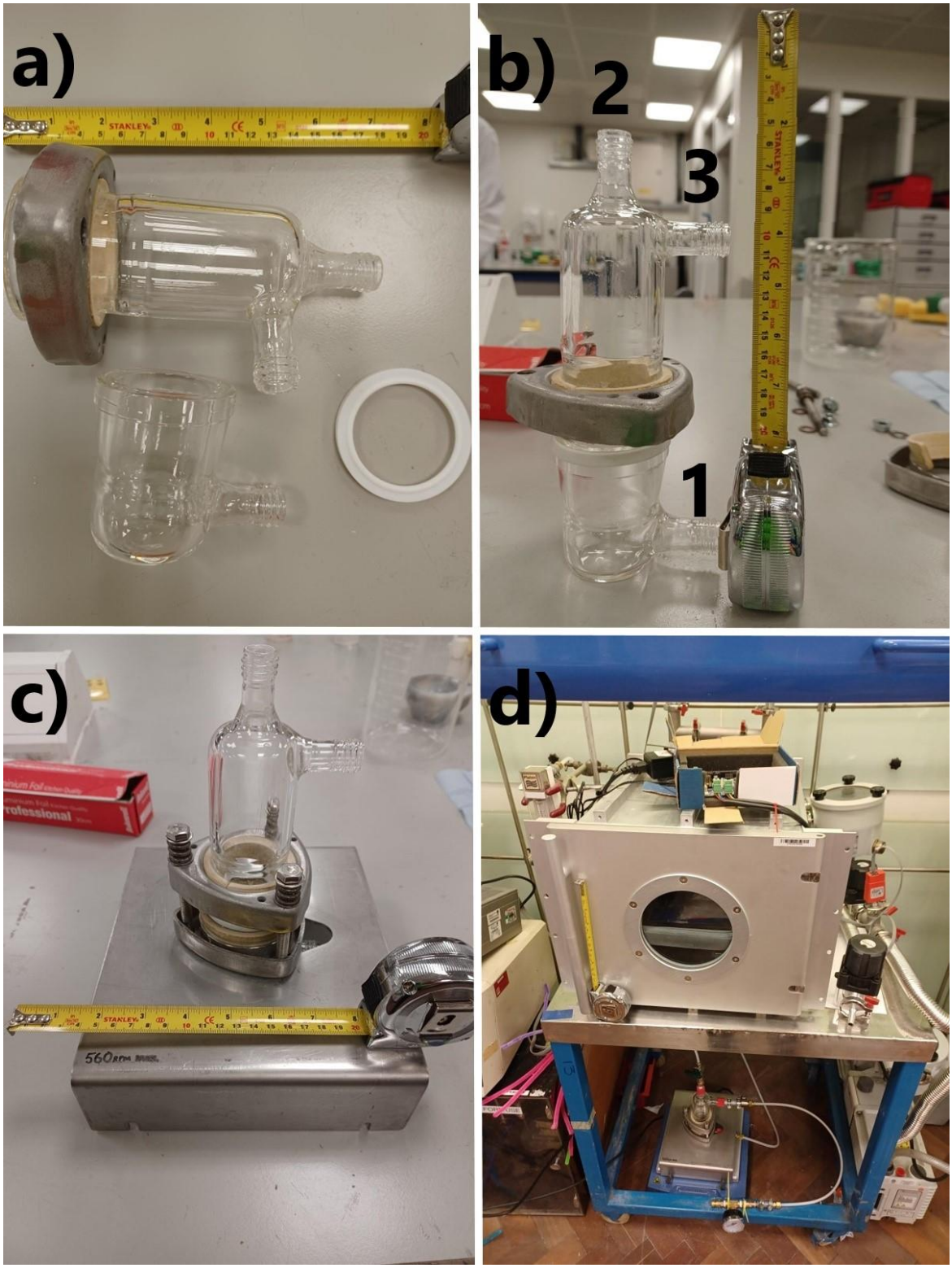

Figure 83. The aerosol generation chamber is shown disassembled in (a), assembled in (b), attached to the weighted vibrating bed mount in (c), and *in situ* in (d). The numbers 1, 2 and 3 in (b) correspond to the inlet, outlet and pressure relief outlet, respectively. A filter paper, typically Durapore™ (Merk Millipore), was inserted between the halves of the AGC to serve as a filter-bed for the powder.

6. The stainless steel vacuum chamber (VC) was purchased from Diener electronic (Ebhausen, Germany). In addition to an inlet (from the AGC) and an outlet (to the vacuum pump), various other inlets and ancillary parts were installed. Pirani gauges (PG_1 and PG_2) recorded pressure, to a precision of 0.1 mbar, inside the VC and between the VC and the vacuum pump. A manual gauge also recorded VC pressure. A venting inlet (not labelled) is visible to the right of the VC in Figure 85. It allowed for chamber re-pressurisation, post-deposition. The electronics which controlled the removable sample stage (RSS) actuators entered through a port at the back of the VC. The RSS can be seen atop the VC in Figure 82 and is also shown disassembled and assembled in Figure 84(a) and (b). A Perspex shield prevented powder-contamination of the actuators during deposition. A window in the shield allowed for the movement of the sample holding X-Y stage and a loosely attached waste bag prevented any powder contamination via the window. Foam insulation, around the edges of the shield, produced a non-airtight seal, allowing for pressure equalisation in the chamber. A Duet 3D control board (Duet3D Ltd, UK), visible atop the VC in Figure 83(d), was programmed using G code, it allowed for control of the sample stages motion in the X- and Y- directions, in terms of speed, distance and direction. Typically, the X-Y stage scanned at 20 mm s^{-1} traveling from its origin to +40 mm in the x direction and then returning to the origin, this scan cycle was repeated 3 times during a ~12 s deposition.

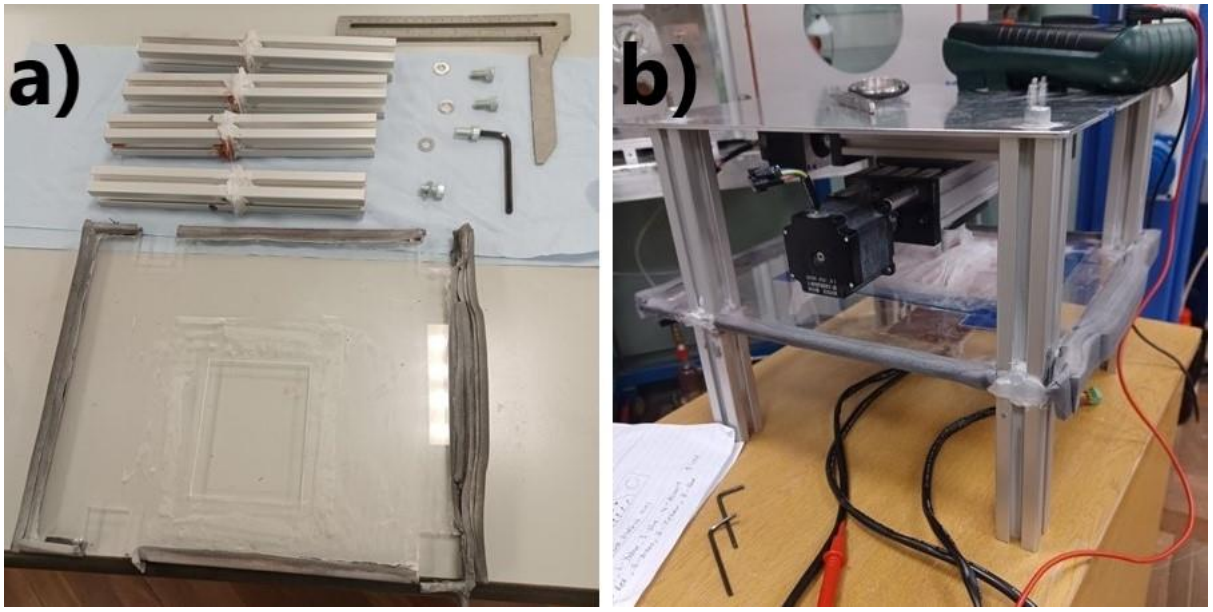

Figure 84. The removable sample stage is shown disassembled in (a) and assembled with the addition of x- and y- actuators in (b). These actuators allowed for controlled motion of the sample stage. A Duet 3D control board was programmed, using G code, to control the sample stage's travel in terms of distance and rate, in the x- and y- directions. The brass X-Y stage, onto which the substrates were attached, is positioned below the Perspex and is more clearly visible in Figure 85(c).

7. A carbon filter (Fil_1) from Edwards vacuum (London, UK) is visible to the back and right of the VC in Figure 83(d), it has black turn-screws to allow for replacement of the filter cartridge. Most powder was filtered prior to Fil_1 by a disposable foam shield which covered the VC outlet and is visible (in orange) at the back of Figure 85(c).
8. A second carbon filter (Fil_2) protected the vacuum pump.
9. The Edwards direct-drive rotary vane vacuum pump (VP) (Edwards vacuum (London, UK)) was cost efficient, although operational pressures in the VC were higher than desired (sometimes 20+ mBar). Powder clogging of the disposable foam shield in the VC was partly responsible for these higher pressures. Pressure-flow charts for the Leeds PAD system are shown in Figure 86, for dry runs at 2, 4, 8 and 12 L min^{-1} (Figure 86(a)) and for the deposition of an Al_2O_3 powder at 4 L min^{-1} (Figure 86(b)).
10. The diverging nozzle, whose design was based on the nozzle used in the Erlangen PAD system. It was part-designed by Prof. Nik Kapur and machined in-house. Figure 85(d) shows a schematic of the nozzle, which was produced by Rob Simpson. The nozzle is shown disassembled and assembled in Figure 85(a) and (b) as well as fixed within the VC in 85(c).

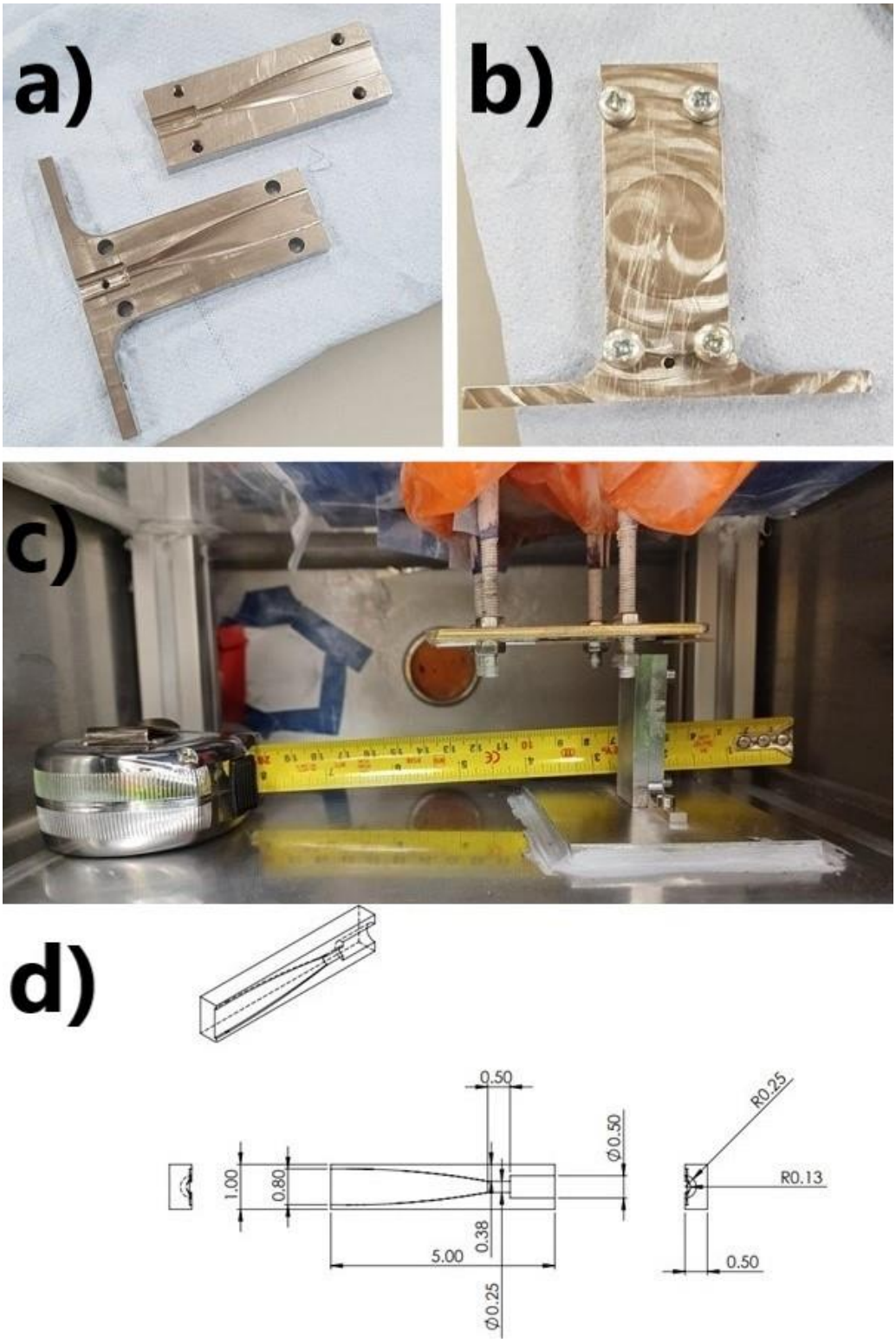

Figure 85. Photographs of the diverging nozzle, disassembled in (a), assembled in (b) and attached to the base of the vacuum chamber in (c). The brass X-Y stage, to which the substrates are mounted, can be seen in the foreground and ~7 mm above the nozzle in (c). The partial schematic of the nozzle in (d) shows dimensions in cm and is provided courtesy of Rob Simpson.

7.2.2 Leeds set up preliminary testing and deposition protocol

Initial testing of the rig, without any powder, showed that it could not maintain pressures below 10 mbar when depositing for 10+ s at 2+ L min^{-1} flowrate, see Figure 86(a). Pressure could be maintained below 20 mbar when depositing at or below 4 L min^{-1} for 40 s. Chamber pressure plateaued, or increased only marginally, when depositing at these flowrates after 10 or 20 s. Further testing with a commercial Al_2O_3 powder saw chamber pressure increase more rapidly, up to ~50 mbar after 25 s. However, during this static deposition onto a SEM sample-stub, a dark (anchor) layer was observed to have formed. Profilometry of this film indicated no discernible thickness, with the original texture of the stubs surface remaining, see Appendix 10.

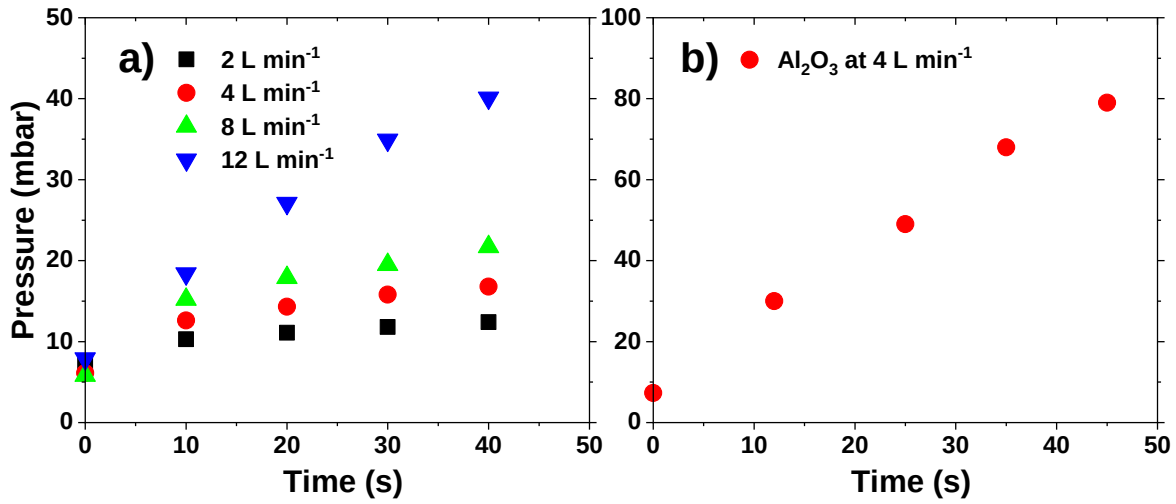

Figure 86. Pressure-time charts for the Leeds PAD system when operating with no powder (dry) at 2-12 L min^{-1} in (a), and, in (b), with Al_2O_3 powder deposited at a carrier gas flowrate of 4 L min^{-1}.

Thus, the construction of a relatively low-budget PAD system in Leeds had been achieved. Despite a direct 8-month delay, due to the school's Covid-related closure, and further delays due to Covid-related work restrictions, the system became operational and provided practical insights into the PAD process, prior to the completion of a more substantial PAD system in Manchester (detailed in Section 8, Results chapter 3). The Leeds system could reach VC pressures of ~5 mbar, which is typically sufficient for deposition [Akedo, J. 2008]. However, sustaining low pressures (< 20 mbar) during powder deposition was challenging.

Following the apparent successful deposition of an Al_2O_3 anchor layer on to an Al SEM stub, further testing using Al_2O_3 powder of known particle sizes was performed (see below, Section 7.3), with a view to optimising system operation prior to the deposition of in-house synthesised CBN powders, see Section 8, Results chapter 3.

7.3 Deposition and microstructure of Al_2O_3 anchor layers at Leeds

Four Al_2O_3 powders, sourced by Bingying Xie of the University of Manchester, are detailed in terms of size and specific surface area in Table 18. These powders were deposited using the Leeds system at carrier gas flowrates of 4 L min^{-1} on SUS304 stainless steel substrates. In practice, flowrates above 4 L min^{-1} tended to produce an initial aerosol burst of high mass flowrate, which depleted the powder rapidly. Flowrates of 2 L min^{-1}, or less, were insufficient to aerosolise the majority of the powder promptly. This resulted in a large fraction of the powder (sometime > 50 %) remaining in the AGC, and unwanted agglomeration over time, due to the action of the vibrating table or VB (and the carrier gases flow through the AGC). Higher flowrates, up to 8 L min^{-1}, produced films that were visually comparable to those deposited at 4 L min^{-1}. However, these high flowrate films often had fine pinholes that exposed the underlying substrate, presumably these were caused by high momentum particle impacts. Hence a N_2 carrier gas flowrate of 4 L min^{-1} was judged to be the general optimum, for this PAD system. A more quantitative appreciation of the relationship between flowrate, film density, thickness and deposition-rate, was hindered by the (sub-)micron thickness of the films produced, which required cross-sectional EM to accurately characterise. The preparation for which was time-consuming. Continuous deposition, at 4 L min^{-1}, often resulted in VC pressure exceeding 20 mbar. To limit the deposition-time spent at higher pressure, a multi-stage deposition protocol was undertaken. Table 19 details the start (Pst) and end (Pe) pressures for each deposition stage, for the Al_2O_3 powders. Each deposition stage had a duration of ~12 s.

7.3.1 Properties and deposition of Al_2O_3 powders

The four Al_2O_3 powders, sourced by Bingying Xie of the University of Manchester (Table 18) were deposited at carrier gas flowrates of 4 L min^{-1} on SUS304 stainless steel substrates according to the protocol described below. The powders ranged in average size, d(50), from 0.5 to 2.3 µm. Particle size distribution, judged by comparing d(50) to d(90), also varied with the largest known particle size distribution occurring in powder “CT 530 SG”. The specific surface areas, S_{BET}, of the powders also varied from 0.6 to 6.6 $m^2 g^{-1}$. Higher S_{BET} values may indicate the presence of smaller particles and increased particle porosity or surface roughness. The presence of necked bonds between primary particles would also increase S_{BET}.

Table 18. The size properties of Al_2O_3 powders as purchased from Almatis. The properties d(50) and d(90) denote the percentage (50 or 90%) of particles at or below the recorded size. The low specific surface area of "CL 3000", S_{BET}, may indicate the presence of larger particles, d(90) data for this powder is missing. Data taken from Almatis [Almatis. 2023] and sourced by Bingying Xie, of the University of Manchester.

Al2O3 powder code	d(50) (µm)	d(90) (µm)	S_{BET} (m^2 g^{-1})
CT 3000 SG	0.5	2.1	6.6
CL 3000	2.3	N/A	0.6
CT 1200 SG	1.3	2.9	2.8
CT 530 SG	1.7	5.1	5.0

A three-stage deposition protocol was employed to increase the deposition time spent at low chamber pressures. The start (Pst) and end (Pe) pressures from each deposition stage are listed in Table 19. No clear trends between the powder sizes, in Table 18, and Pe or subsequent-stage Pst values could be determined. Later Pst values were higher than Pst-1 values due to (assumed) clogging of the chamber filter, given that the reduced chamber pressure was judged to be stable/equilibrated for ~20 s to 30 s post deposition.

Table 19. Deposition conditions for Al_2O_3 powders at Leeds. To reduce operational pressures, deposition was performed in 3x ~12 s bursts, with ~30 s pauses between each deposition, to allow for the reduction of VC pressure to a lower stable condition. The VC pressure at the start (Pst) and end (Pe) of each deposition burst is recorded.

Sample code	Substrate	Gas inlet flowrate (L min^{-1})	Pst-1 (mbar)	Pe-1 (mbar)	Pst-2 (mbar)	Pe-2 (mbar)	Pst-3 (mbar)	Pe-3 (mbar)
CT 3000 SG	SUS304	4	5.8	33	7.2	24	7.3	30
CL 3000	SUS304	4	6.5	35	7.4	35	8.2	38
CT 1200 SG	SUS304	4	6.3	25	6.7	27	6.8	30
CT530 SG	SUS304	4	6.5	19	6.8	21	6.9	23

7.3.2 Microstructure of Al_2O_3 PAD anchor layers

Secondary electron micrographs for the four Al_2O_3 films are shown in Figure 87. The films had a black appearance and lacked any visible thickness, similar to the SNN films deposited in Erlangen, except for the CL 3000 film, which was matt-silver in appearance- similar in colour to the original substrate. The CL 3000 powder had an intermediate particle size and the lowest S_{BET}, see Table 18. Cross-sectional FIB-SEM, in Figures 88(b), showed that no film was deposited by the CL 3000 powder. All FIB-SEM was performed by John Harrington. Surface SEM (Figure 87(b)) showed high levels of plastic deformation and cratering on this substrate, likely due to the hammering-effect of particle impact. The remaining powder films had comparable surface micrographs, consisting of a textured layer with embedded or resting particle fragments (or small particles), see Figure 87(a), (c) and (d).

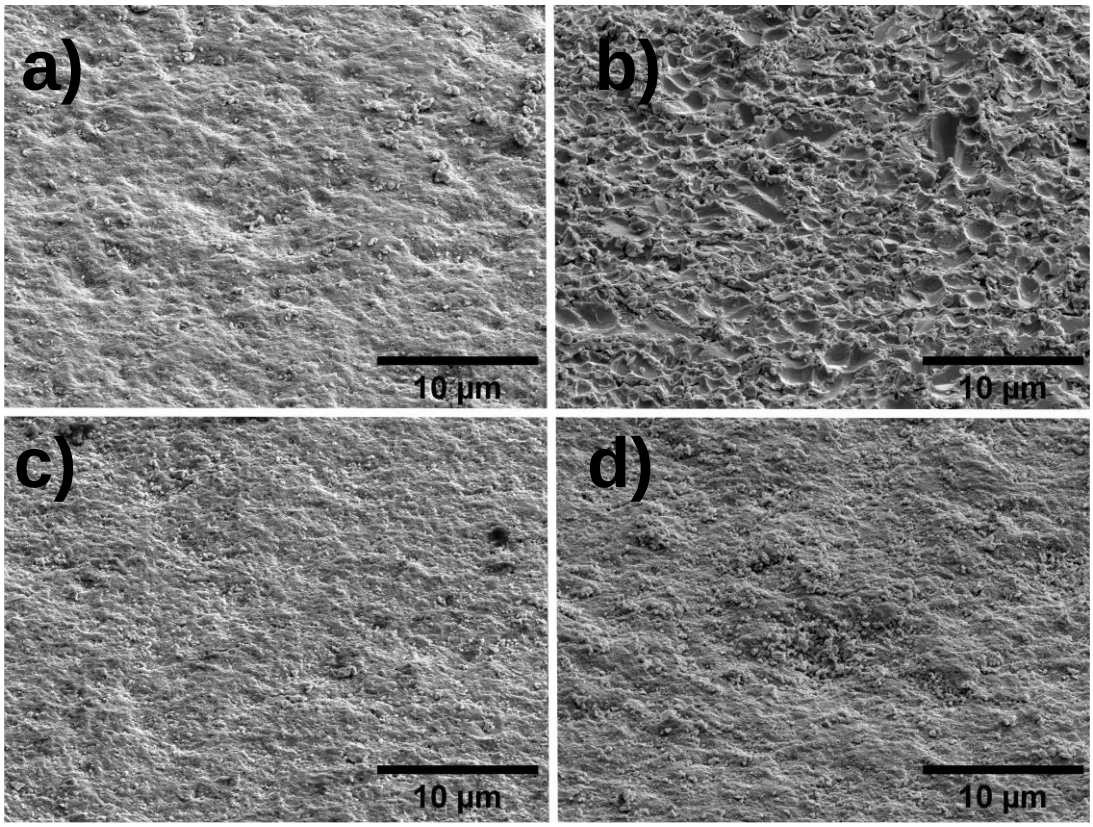

Figure 87. Lower angle secondary electron micrographs, at a magnification of 10 kx, for various Al_2O_3 films; (a) CT 3000 SG, (b) CL 3000, (c) CT 1200 SG, (d) CT 530 SG. The highly cratered surface in (b) is shown to be the exposed SUS304 stainless steel substrate in Figure 88(b). Surface SE micrographs were captured by John Harrington.

Cross-sectional FIB-SEM ion-beam micrographs (i.e. ion beam illumination and electron detection) of the four Pt-coated AL_2O_3 films are shown in Figure 88. A darker contrasted Al_2O_3 layer can be observed below a white Pt coating in Figure 88(a), (c) and (d). See Figure 89 for EDX conformation of the layer's composition. The CT 1200 SG powder in Figure 88(c) produced a sub-micron layer whilst CT 3000 SG and CT 530 SG powders, in (a) and (d) respectively, produced films which were several microns thick in places. A ~1 µm grain can be seen embedded in the mostly exposed substrate in Figure 88(b) and is indicated by a red arrow.

The micrographs were produced by capturing the electrons emitted on illumination by the Ga-ion beam. Secondary and some backscatter electrons are presumed to have been detected, with this backscatter element allowing for greater compositional and structural (crystal)-orientational contrast. The substrates in Figure 88 show grains and grain boundaries, between contrasting regions. These regions are larger, often 1+ µm, in the body of the substrate and fine, << 1µm, at the substrate surface. In Figure 88(b), and where no overlying particle film formed to shield the substrate, this high deformation layer extends deepest into the substrate.

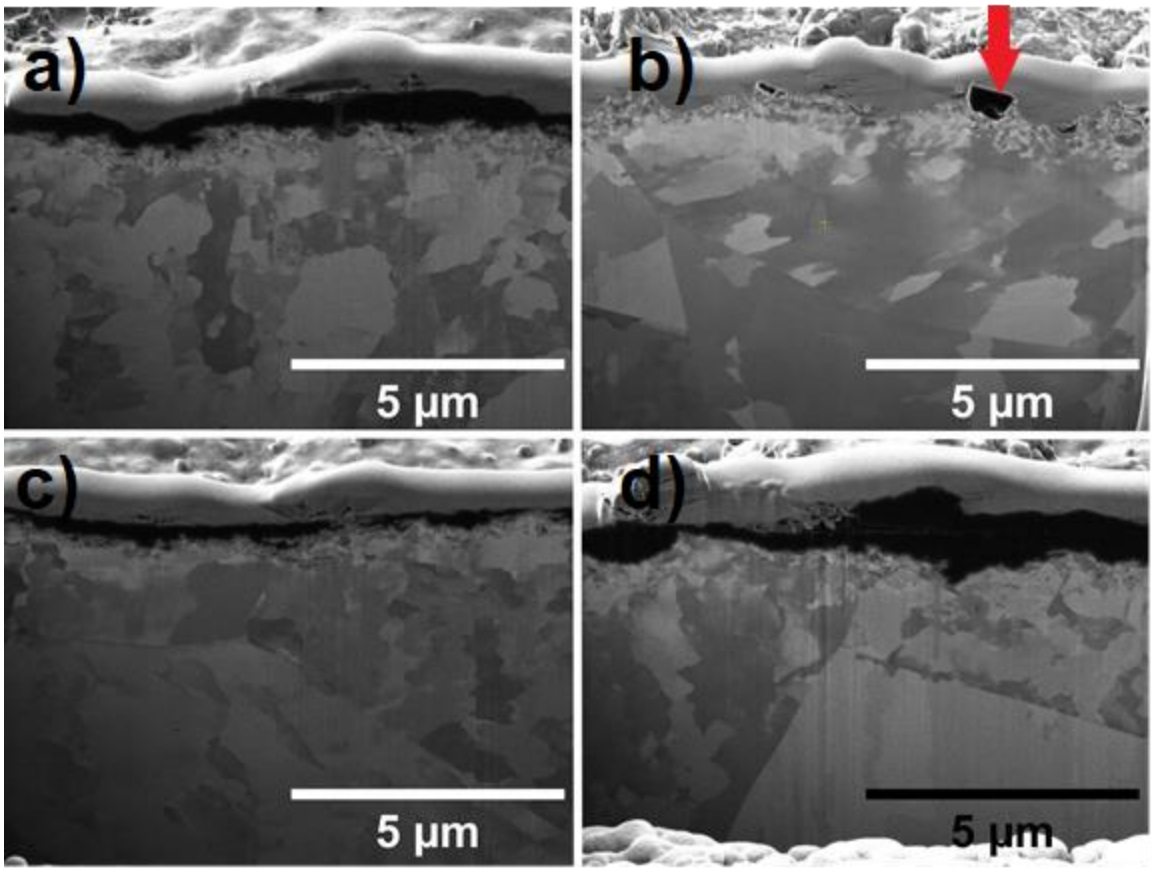

Figure 88. Cross-sectional FIB-SEM micrographs of various Pt-coated AL_2O_3 films, at a magnification of 35 kx; (a) CT 3000 SG, (b) CL 3000, (c) CT 1200 SG, (d) CT 530 SG. The higher density Al_2O_3 appears black and the conductive Pt coating, added to prevent charging, appears in white. Imaging and slight etching, with a Ga-ion beam (i.e. Ga illumination and electron detection), revealed the grain structure of the substrate. Smaller grains, or grains with internal defects (deformation boundaries), can be observed near the surface of the substrate, particularly in (b) where no film was deposited to shield the substrate. The particle films in (a) and (d) were over 1 µm thick in places, whilst the particle film in (c) was submicron. A micron-sized grain can be seen embedded in the substrate, in (b), and is indicated by a red arrow. Lateral cracking, of the CT 530 SG film can be seen in Figure 89(c), where it is indicated by a green arrow. These micrographs were captured by John Harrington.

The micrographs and EDX maps in Figure 89(a), (b) and (c) correspond to higher magnification areas of the micrographs in Figure 88(a), (c) and (d), respectively. No EDX was performed on the CL 3000 “film” in Figure 88(b), due to the absence of a continuous particle layer. The elemental maps confirm the presence of an Al and O signal in the particle layer on a Fe containing substrate.

The CT 530 SG film in Figure 89(c) shows a 3+ µm lateral crack. Comparable film delamination has been noted elsewhere and associated with the presence of rougher substrates [Naoe, K. 2013]. The substrate in Figure 88(c) does show the greatest roughness, judged by absolute variation in height over the ~10 µm range. This roughening may have been caused by the impact of larger particles, given that the CT 530 SG had the largest known particles, d(90) = 5.1 µm (see Table 18).

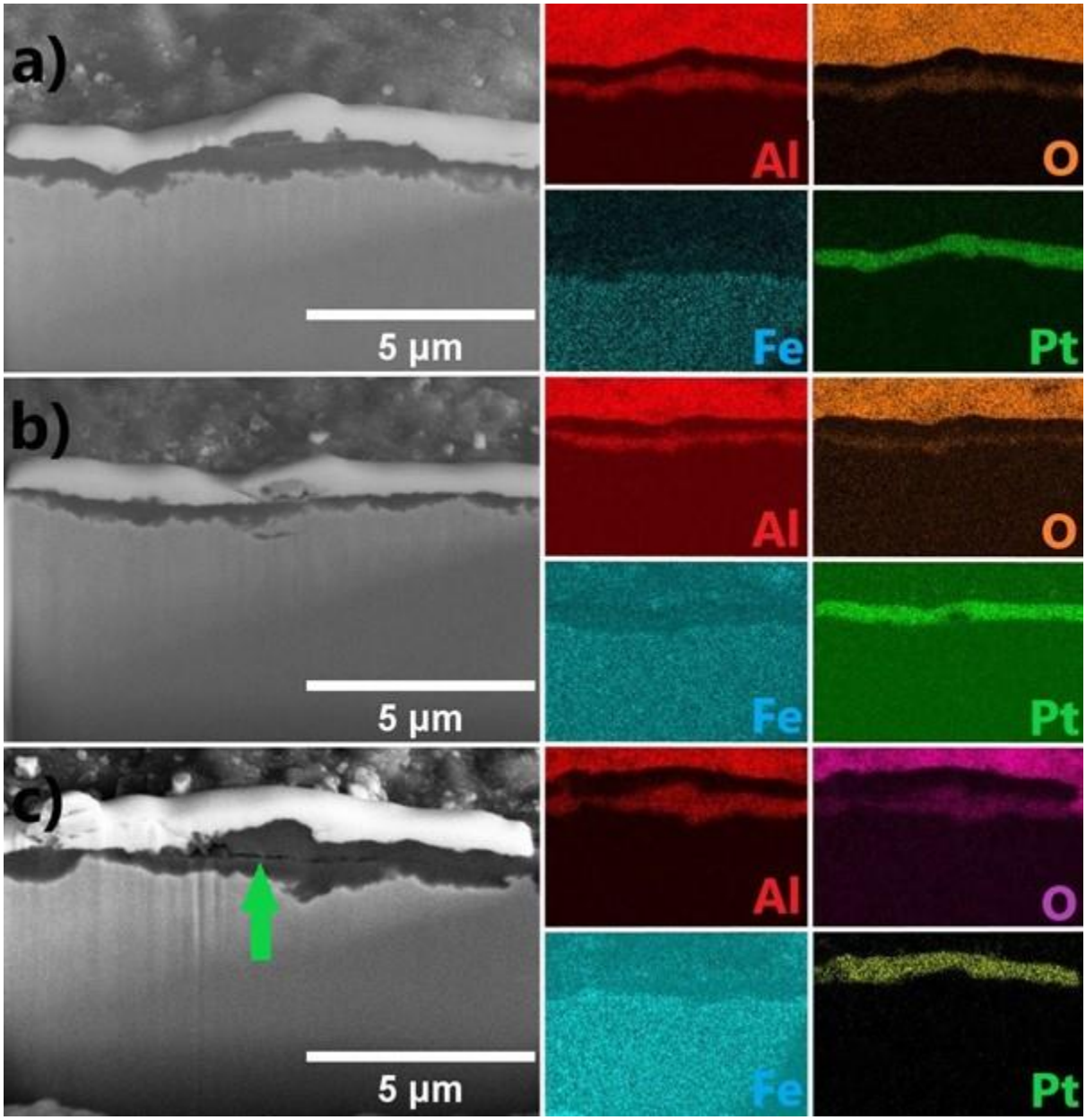

Figure 89. FIB-SEM micrographs and EDX elemental maps of (a) CT 3000 SG, (b) CT 1200 SG and (c) CT 530 SG. All powders were deposited on SUS304 stainless steel substrates, and imaging at a magnification of 35 kx, confirms the presence of Al and O in the deposition layers. The apparent absence of Fe in the bottom right of the elemental map for (c) is due to a shadowing affect (caused by the detector). Lateral cracking of the CT 530 SG film in (c) is indicated by a green arrow. These micrographs and elemental maps were captured by John Harrington.

To summarise, a multi-stage deposition protocol was established when using the PAD system designed and built at Leeds. This protocol allowed for production of Al_2O_3 particle anchor layers, which were dense, possessing high levels of apparent deformation and sometimes of multi-micron thickness. Anchor layers were produced from powders whose average particle size, d(50), varied from 0.5 to 2.3 µm. A powder with a low specific surface area, S_{BET} = 0.6 $m^2 g^{-1}$, did not form a continuous film. Damaged to the substrate, during deposition, was evidenced by a reduction in grain size near the surface.

7.4 Phase and electrical characterisation of CBN PAD films from Erlangen

First attempts at phase analysis by XRD and electrical characterisation were made on a CBN28 film deposited in Erlangen at 2 L min^{-1} on stainless steel (SUS304). Profilometry, OM and SEM of this film are shown in Figures 75, 76 and 77.

Patterns from a 12 h, 10 to 90 $^{o}2\theta$, XRD scan of the CBN film deposited at 2 L min^{-1} are shown in Figure 90. Most peaks can be attributed to CBN (ICCD 05-001-0283). A peak at ~51 $^{o}2\theta$, indicated by ♦ in Figure 90(a), is consistent with the SUS304 stainless steel substrate. A shoulder to the (410) CBN peak, indicated by ● in Figure 90(b), is consistent with an orthorhombic $CaNb_2O_6$ phase (ICCD ICCD 00-011-0619). The overlap of the CBN and assumed $CaNb_2O_6$ peaks may indicate broadening of the peaks in the film, in comparison to the bulk ceramic (in which the peaks were distinct, see Section 5, Results chapter 1 Figure 46(a)). No $BaNb_2O_6$, or similar Ba containing precursor, phase was identified. Hence, the parent CBN phase may have a higher Ba content than that of the nominal (CBN28) composition, assuming that $BaNb_2O_6$, if present in the powder, was not resistant to deposition.

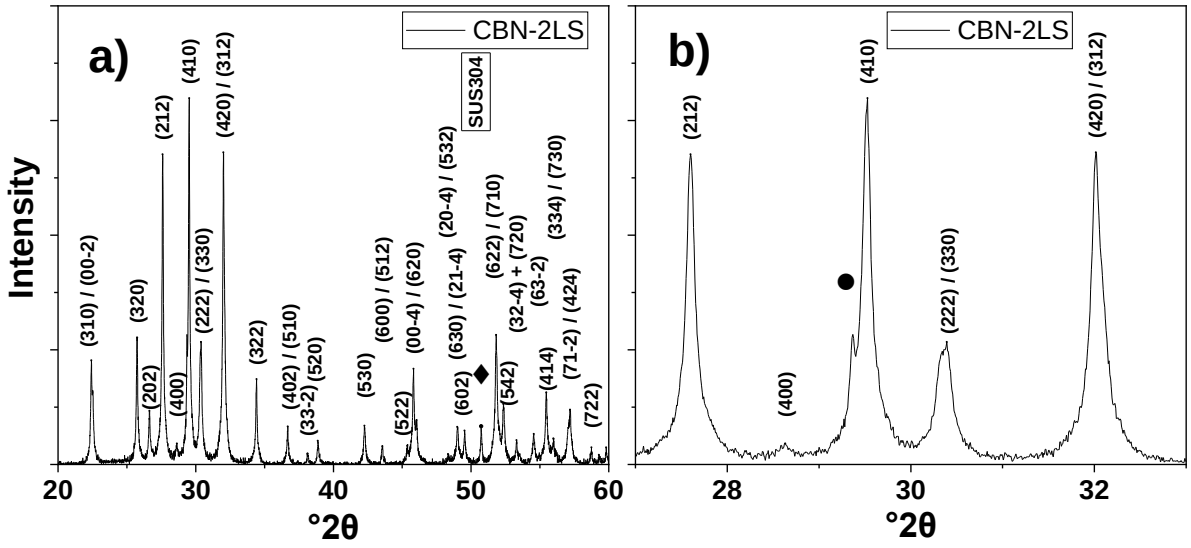

Figure 90. The X-ray diffraction pattern of a CBN28 PAD film, deposited at 2 L min^{-1} on SUS304 stainless steel. A peak associated with the SUS304 stainless steel substrate is indicated by ♦, at ~51 $^{o}2\theta$ in (a). Augmentation of the (530) peak, at ~43 $^{o}2\theta$, by a coinciding substrate peak may also be present. In (b), a 29.3 $^{o}2\theta$ shoulder to the 29.7 $^{o}2\theta$ (410) peak is indicated by ● and is consistent with orthorhombic $CaNb_2O_6$ (ICCD 00-011-0619). Primary phase peaks were indexed according to P4bm structure, ICCD 05-001-0283. Prior to deposition, the CBN28 powder was calcined at 1150 ^{o}C for 2 h. See Appendix 11, for the XRD pattern of the substrate, courtesy of the University of Erlangen-Nuremburg.

Permittivity-temperature profiles of the CBN film, deposited at 2 L min^{-1}, and a bulk ceramic CBN28 sample are shown in Figure 91(a) and (b), respectively. Prior to sintering for 4 h at 1350 ^{o}C, the bulk ceramic was calcined at 1200 ^{o}C for 4 h, it may also possess minor amounts of secondary phases (see Section 5, Results chapter 1, Figure 46(a) Chapter R1 for XRD of a comparably calcined bulk ceramic). The permittivity maximum, of ε_r = 1960 at 1 kHz, occurred at 278 ^{o}C in the bulk ceramic. This maximum was 5-6 times the magnitude of the permittivity at room temperature (ε_r = ~350). Dielectric losses were low (tan δ < 0.05) across the measurement range.

The calcined powder used to produce the CBN film underwent lesser thermal processing than for the bulk material described above, the former being calcined for only 2 h at 1150 ^{o}C. The film's permittivity-temperature response was measured by Dr. Yizhe Li, of the University of Manchester. The (high-temperature ~250 ^{o}C) 1 kHz permittivity maxima of the film (ε_r = ~57) was ~1/30th of that of the bulk material and 1.5x the magnitude of the films permittivity at 50 ^{o}C (ε_r = 44). At low-temperatures, below 50 ^{o}C, a spike in losses and permittivity was observed. This spike can be attributed to the presence, and disturbance, of water vapour within the film's pores, suggesting that the film was of low-density [Caballero, A. C. 1999]. The (high-temperature) permittivity maxima occurred at 258 ^{o}C, 20 ^{o}C below that of the bulk ceramic. A peak in 1 kHz permittivity at 190 ^{o}C corresponds to frequency-dependant peaks in dielectric loss at 190 ^{o}C and also at 210 ^{o}C (for the 10 kHz data). These peaks are broadly consistent with the T_C of $Ca_{0.3}Ba_{0.7}Nb_2O_6$, which may indicate incomplete thermal processing in this powder [Han, X. 2013].

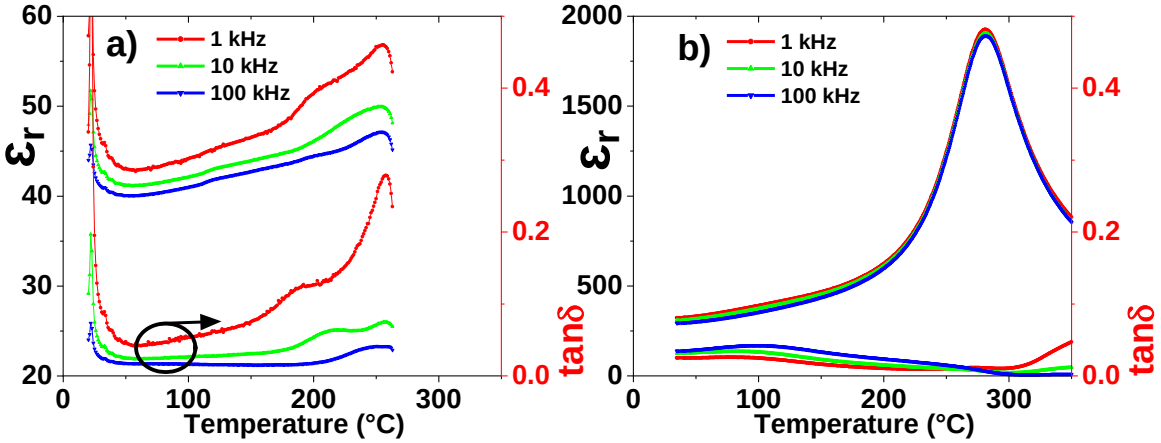

Figure 91. The permittivity-temperature response of a CBN28 AD film, deposited at 2 L min^{-1} on stainless steel (SUS304), is shown in (a), and compared to the bulk ceramic CBN28, calcined for 4 h at 1200 ^{o}C and sintered for 4 h at 1350 ^{o}C, in (b). A peak in permittivity and dielectric loss, seen in (a), coincides with the Curie-temperature of $Ca_{0.3}Ba_{0.7}Nb_2O_6$ [Han, X. 2013], which may be present due to incomplete thermal processing. Measurement of the film's permittivity-temperature response was performed by Dr. Yizhe Li, of the University of Manchester.

The film's polarisation-electric field response was measured by Dr. Yizhe Li, of the University of Manchester, and is shown in Figure 92(a). The P_r-Max, measured at 50 kV cm^{-1}, of the film was ~0.3 µC cm^{-2}, approximately 1/20th that of the bulk ceramic. The polarisation response was mostly linear, from -40 to +40 kV cm^{-1}, although lossy. The polarisation-electric field response of a CBN bulk ceramic, calcined for 4 h at 1200 ^{o}C and sintered by heating to 1350 ^{o}C and then immediately cooling to 1200 ^{o}C for a dwell time of 4 h, is shown in Figure 92(b). This polarisation-electric field response is analysed in greater detail in the text preceding Figure 55 in Section 5, Results chapter 1, it is a characteristically ferroelectric response at field levels at and above 30 kV cm^{-1}.

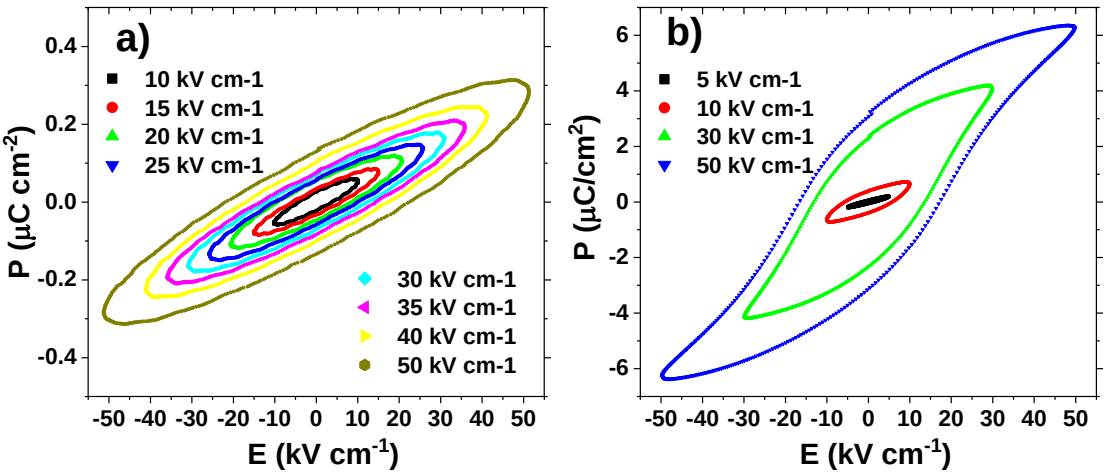

Figure 92. The polarisation-electric field response of a CBN28 PAD film, deposited at 2 L min^{-1} on SUS304, is shown in (a) and compared to the bulk ceramic CBN28, calcined for 4 h at 1200 ^{o}C and sintered for 4 h at 1350 ^{o}C, in (b). Measurement of the film's polarisation-electric field response was performed by Dr. Yizhe Li, of the University of Manchester.

To summarise, a CBN PAD film, deposited in Erlangen, was successfully electrically analysed. The film was not phase pure and had presumed low density, which may have contributed to the increased temperature-stability of permittivity as well as the suppression of the polarisation response. The characterisation of films with densities comparable to that of the bulk ceramic (95+ %) would allow for a more meaningful comparison. However presumed particle deformation in this film, that was observed in SNN and Al_2O_3 PAD films, may be a partial cause of the reduced polarisation response in this CBN PAD film.

7.5 Discussion

The proposed mechanism of room temperature impact consolidation (RTIC) suggests that a combination of particle size reduction and deformation are responsible for the formation of high-density PAD layers [Akedo, J. 2008]. Here, high density anchor-layers were produced from SNN and Al_2O_3 powders. These layers conform to the theory of RTIC in that they show evidence of particle size reduction and deformation. The SNN film shows evidence of particle size reduction in that the film is significantly thinner (<400 nm) than the average size of the SNN primary particles (~2 µm) (compare Figures 74(b) and 79) and TEM shows reduced crystallite sizes in the SNN film (Figure 81). A submicron Al_2O_3 film was also produced from a powder whose average size was > 1 µm, see Figure 88(c) and Table 18. Crystal deformation within the SNN layer is confirmed by ED in Figure 81(b). In the corresponding micrograph, a speckled contrast at length scales below 100 nm indicates nano-crystallinity. The *in situ* examination of deformation accumulation and crystallite size reduction is fundamentally prohibited by the activity of the deposition process. However, modelling and ceramic impact-processing theory have been employed to understand the evolution of these entwined phenomena [Daneshian, B. 2022] and [Delogu, F. 2006]. Alternatively, *in situ* observations of deformation recovery and crystallite growth, during annealing, may elucidate their relationship in PAD films. Such experimentation, within a TEM, is performed in Section 8, Results chapter 3, on a CBN28 film deposited on the Manchester PAD system.

The presence of agglomeration in the aerosol generation chamber, whilst not quantitively assessed, coincided with the formation of a low density, rough CBN28 film during PAD at Erlangen (see Figure 75 and Appendix 5(a)). Elsewhere it has been postulated that the dissipation of kinetic impact energy, upon the disintegration of agglomerates, prevents the consolidation of high-density layers [Nam, S-M. 2004].

7.5.1 Parameter window for the deposition of dense films

For ceramics, appropriate kinetic impact forces are required to achieve a combination of particle size reduction, via brittle fracture, and deformation, likely by accumulated slip. These kinetic impact forces should be sufficiently high (GPa), whilst remaining net additive rather than net erosive [Handft, D. 2015]. Particle size correlates with potential impact momentum. Here, Al_2O_3 powders with a range of average sizes, from 0.5 to 2.3 µm, were found to deposit at a gas flowrate of 4 L min^{-1}. This suggests that the window of particle sizes, for successful deposition, is relatively wide.

A wider particle size distribution will result in a wider range of particle impact momentums. The Al_2O_3 powder with the largest known size distribution produced the thickest film, see Table 18 and Figure 88(d). The powder with the lowest specific surface area (S_{BET}) did not produce a film.

Micrographs of the Al_2O_3 films were only taken when depositing at 4 L min^{-1}, and so the observed trends are specific to this deposition parameter. To allow for a more general understanding, a range of deposition parameters should be analysed. This in turn may require fine control of operational parameters to reduce the flowrate intervals, i.e. to every 0.5 L min^{-1}, whilst retaining reproducible results.

A trend of increasing pin-hole size with increasing flowrate (2 vs 8 L min^{-1}) is observed in the optical micrographs of CBN28 films deposited in Erlangen and shown in Figure 75. Circumstantial evidence of increased pinhole presence in Al_2O_3 films when increasing flowrate from 4 to 8 L min^{-1} was also found. In the thick (20+ µm) CBN28 film deposited in Erlangen pinholes did not prevent electrical measurements, whilst perforations of the SNN anchor layer by presumed pinholes likely resulted in conductivity.

Partial delamination of an Al_2O_3 film was observed, i.e. a lateral crack, that was coincident with increased substrate roughness in Figure 89(c) (and Figure 88(d)). Substrate roughening may have occurred due to the presence of larger particles in this powder, d(90) = 5.1 µm, which damaged the substrate. Elsewhere enhanced substrate roughening and (partial) film delamination have also coincided [Naoe, K. 2013]. Increasing substrate hardness, for example when depositing SNN onto Ti-alloy (Ti-4V-6Al) rather than Stainless steel (SUS304), with respective Vickers hardnesses of ~300 and ~150, did not prevent the formation of an anchor layer. The Ti-alloy film was visibly darker and so possibly thicker (see Appendix 6), but cross-sectional EM of the SNN on steel film would be required to confirm its thickness.

7.5.2 Suitability of PAD anchor layers for electrical testing

The SNN deposited in Erlangen on Ti-alloy was as an anchor layer up to 400 nm thick, and the SNN on stainless steel anchor layer was presumed to be of comparable thickness, see Figure 79. Both these films were too conductive for electrical analysis, likely due to perforations of the film, or regions of very low (< 100 nm) thickness (see Figures 78(d) and 80(b)). Comparably thin $BaTiO_3$ anchor layers (0.2 µm) were also found to be conductive, whilst a 1.5 µm $BaTiO_3$ layer was resistive [Kim, H-K. 2015]. The Al_2O_3 of anchor layer in Figure 88(d), whilst 3+ µm in places, had variable thickness and may also possess low resistivity (conductivity) given that some regions were less than 0.5 µm thick.

In order to produce anchor layers of suitable resistivity for electrical testing, a uniform film thickness and the absence of pin-hole perforations are required. The control of particle size distribution may aid both of these features. Firstly, pinholes are associated with high-momentum impacts and the absence of large particles, aggregates or agglomerates would prohibit such high momentum

impacts. However, some level of controlled aggregation, or granulation, may be beneficial in the prevention of uncontrolled agglomeration (see Figure 74 for the aggregated SNN powder, which did not appear to agglomerate in the aerosol generation chamber). Secondly, larger particles and high momentum impacts are assumed to have caused the enhanced surface roughness in the film in Figure 88(d), given that the powder had the largest known particles (d(90) = 5.1 µm) of the four Al_2O_3 powders tested. Substrate roughness has in turn been linked to increased variation in film thickness [Kim, H-K. 2015].

The low density CBN film produced in Erlangen was sufficiently resistive for electrical analysis to be performed. It was found to have low permittivity and polarisation responses, see Figures 91 and 92. The permittivity maxima of the film was ~1/30th that of the bulk ceramic and the P_{Max}, from the P-E response, was ~1/20th that of the bulk ceramic. The temperature stability of film's permittivity was improved, showing only a 1.5x increase from 50 to ~260 ^{o}C, when compared to the bulk ceramic which showed a ~6 x variation from 50 to ~280 ^{o}C. However, the contribution of low film density to these electrical properties is unknown. High levels of deformation were shown in the SNN and Al_2O_3 films (Figures 81(b) and 88). This deformation is presumed to contribute to polarisation response suppression. The comparison of bulk ceramic dielectric properties to comparably dense (95+ %) films would allow for greater comparability of electrical properties. Alternatively, the comparison of an as deposited film's dielectric properties to an annealed film's response, with reduced microstrain, would illustrate the role of deformation in the suppression of polarisation response. This experiment is performed for a CBN28 film deposited on the Manchester PAD and will be reported in Section 8, Results chapter 3.

7.5.3 Conclusions and next steps

A functioning PAD system was commissioned at Leeds. Initial microstructural and electrical characterisation experiments were conducted on PAD films. The importance of powder properties such as particle size distribution and specific surface area were highlighted during initial testing, but not fully explored. For future CBN PAD film electrical testing and comparison to bulk ceramics, thick (5+ µm) and high-density (95+ %) films are desired. To achieve electrically characterizable CBN films, in house powder processing shall be explored prior to PAD in the next Section (8, Results chapter 3).

7.6 References

Akedo, J. 2008. Room Temperature Impact Consolidation (RTIC) of Fine Ceramic Powder by Aerosol Deposition Method and Applications to Microdevices. *J. Therm. Spray Technol.* **17**. 181-198

DOI: https://doi.org/10.1007/s11666-008-9163-7

Almatis. 2023. batch-ground-reactive-aluminas. [Accessed Online 12th January 2024]. [Accessed from]: https://www.almatis.com/market-en/ceramics/batch-ground-reactive-aluminas

AMETEK Inc. 2022. periodic-table. [Accessed Online 12th January 2024].

[Accessed from]: https://www.edax.com/resources/periodic-table

Brown, T. Brown, A. P. Hall, D A. Hooper, T. E. Li, Y. Micklethwaite, S. Aslam, Z. Milne, S. J. 2021. New high temperature dielectrics: Bi-free tungsten bronze ceramics with stable permittivity over a very wide temperature range. *J. Eur. Ceram*. Soc. **41**. 3416-3424

DOI: https://doi.org/10.1016/j.jeurceramsoc.2020.10.034

Brown, T. 2022. High-Temperature Dielectrics Based on Tungsten Bronze Structured Niobate Ceramics. 5.5.1 Phase analysis. 118. PhD thesis, University of Leeds.

Accessed from: https://etheses.whiterose.ac.uk/32655/

Caballero, A. C. Villegas, M. Fernandez, J. F. 1999. Effect of humidity on the electrical response of porous $BaTiO_3$ ceramics. *J. Mater. Sci. Lett***. 18**. 1297-1299

DOI: https://doi.org/10.1023/A:1006662805186

Daneshian, B. Gärtner, F. Assadi, H. Villa Vidaller, M. Höche, D. Klassen, T. 2022. Features of ceramic nanoparticle deformation in aerosol deposition explored by molecular dynamics simulation. *Surf. Coat. Technol*. **429**. 127886

DOI: https://doi.org/10.1016/j.surfcoat.2021.127886

Delogu, F. Cocco, G. 2006. Microstructural refinement of ceramic powders under mechanical processing conditions. *J. Alloys Compd*. **420**. 246-250

DOI: https://doi.org/10.1016/j.jallcom.2005.10.037

Eckstein, U. Khansur, N. H. Urushihara, D. Asaka, T. Kakimoto. K-I. Fey, T. Webber, K. G. 2022. Defect modulated dielectric properties in powder aerosol deposited ceramic thick films. *Ceram. Int*. **48**. 33082-33091

DOI: https://doi.org/10.1016/j.ceramint.2022.07.241

Han, X. Wei, L. Yang, Z. Zhang, T. 2013. Phase formation, dielectric and ferroelectric properties of $Ca_xBa_{1-x}Nb_2O_6$ ceramics. *Ceram. Int.* **29**. 2853-2860

DOI: https://doi.org/10.1016/j.ceramint.2012.11.078

Hanft, D. Exner, J. Schubert, M. Stöcker, T. Fuierer, P. Moos, R. 2015. An Overview of the Aerosol Deposition Method: Process Fundamentals and New Trends in Materials Applications. *J. Ceram. Sci. Technol.* **6.** 147-182

DOI: https://doi.org/10.4416/JCST2015-00018

Khansur, N. H. Eckstein, U. Li, Y. Hall, D. A. Kaschta, J. Webber, K. G. 2019. Revealing the effects of aerosol deposition on the substrate-film interface using NaCl coating. *J. Am. Ceram. Soc*. **102**. 5763-5771

DOI: **https://doi.org/10.1111/jace.16489**

Kim, H-K. Lee, S-H. Lee, S-G. Lee, Y-H. 2015. Densification mechanism of BaTiO3 films on Cu substrates fabricated by aerosol deposition. *Electron. Mater. Lett*. **11**. 388–397

DOI: https://doi.org/10.1007/s13391-015-4419-0

Nam, S-M. Mori, N. Kakemoto, H. Wada, S. Akedo, J. Tsurumi, T. 2004. Alumina Thick Films as Integral Substrates Using Aerosol Deposition Method. *Jpn. J. Appl. Phys.* **43**. 5414

DOI: https://doi.org/10.1143/JJAP.43.5414

Naoe, K. Nishiki, M. Yumoto, A. 2013. Relationship Between Impact Velocity of Al2O3 Particles and Deposition Efficiency in Aerosol Deposition Method. *J. Therm. Spray. Tech*. **22**. 1267-1274

DOI: https://doi.org/10.1007/s11666-013-0031-8

Ma, X. Li, F. Cao, J. Li, J. Chen, H. Zhao, C. 2017. Vickers microhardness and microstructure relationship of Ti-6Al-4V alloy under cyclic forward-reverse torsion and monotonic torsion loading. *Mater. Des.* **114**. 271-281

DOI: https://doi.org/10.1016/j.matdes.2016.11.028

Lu, C-J. Yeh, J-W. 2023. Improved Wear and Corrosion Resistance in TiC-Reinforced SUS304 Stainless Steel. *J. Compos. Sci.* **7**. 34

DOI: https://doi.org/10.3390/jcs7010034

8. Results 3: Powder preparation and the dielectric properties of PAD films, with thermal treatment

In this chapter the effect of milling and thermal treatment on the properties of CBN28 powders is assessed, prior to aerosol deposition of these powders on to steel substrates by systems in Leeds and Manchester. The microstructure and electrical properties of anchor-layer type CBN films, produced by the Leeds deposition system are assessed. Thicker CBN films, produced on the Manchester deposition system, are then microstructurally and electrically analysed. Finally, the effects of annealing a ~10 μm thick CBN28 PAD film on the film's microstrain and permittivity is shown.

8.1 The preparation of CBN28 powders, their deposition in Leeds and characterisation

The production of a variety of CBN28 powders, with known and controlled extrinsic properties, was required for further assessing the functionality of the Leeds deposition system developed in Section 7, Results chapter 2, and for producing films suitable for electrical testing.

8.1.1 Powder preparation and deposition

A combination of low- and high- energy ball- and attrition- milling techniques were used by the author to produce CBN28 powders for PAD at Leeds. Thermal "pre-treatment" of high-energy milled powders, i.e. thermal treatment post milling, was also performed by the author. This work built upon the high-energy milling and thermal pre-treatment experiments undertaken by Dr. Thomas Hooper for the EPSRC funded grant, Aerosol Deposition for Manufacturing and Developing Next Generation Dielectric Charge Storage Devices (https://gow.epsrc.ukri.org/NGBOViewGrant.aspx?GrantRef=EP/S029036/1).

Low-energy ball milling

The micrographs in Figure 93 show the evolution of particle size, size-distribution, morphology and agglomeration state, during the calcination and subsequent low-energy ball milling of CBN28 powders made by the mixed oxide route detailed in the Section 3.5 (methodology). For milling, ~400 mL bottles were 2/3 filled with milling media (~15 mm diameter yttria stabilised zirconia beads), 80 mL of 2-isopropanol and 50 g of powder. Milling bottles were rotated at 150 rpm, the tumbling of the milling media within the bottle is believed to be the primary cause of the particle size reducing impacts. Despite ball milling for 24 h, to promote mixing, the precursor powder mix (of $BaCO_3$, $CaCO_3$ and Nb_2O_5) had a range of particle sizes- from < 0.5 to ~2.5 μm, see Figure 93(a). After calcination for 12 h at 1200 ^{o}C, aggregates of the single phase CBN28 primary particles were present (see XRD for 12 h-calcined CBN28 in Section 5, Results chapter 1, Figure 47), these sometimes exceeded 100 μm in diameter, see Figure 93(b). The calcined primary particles were typically slightly elongated, with

an expected <001> growth habit similar to that observed in other CBNs and TBs [Han, X. 2013], see Figure 93(c). These primary particles were of variable size (~0.5 to 2.5 µm). Subsequent low energy ball milling of the calcined powder, for a duration of 8 h, resulted in breakdown of the macro-aggregates, though some of the primary particles remained bonded, see the centre of Figure 93(d). The primary particles mostly retained smooth edges, suggesting that any particle surface damage was limited, despite the presence of additional nano-fragments post-milling, < 0.25 µm in scale. A total of 50 particles or aggregates of bonded particles were measured by the line-intercept method, similarly to the measurements in Section 5.2.1, Results chapter 1. An average particle/small agglomerate size of ~3 µm was calculated with a standard deviation of 1.2 µm.

After low energy ball-milling for 24 h, primary particle size and size distribution were reduced (average particle size ~1 µm, standard deviation = 0.3 µm), excluding < 0.25 µm fragments which were difficult to measure and discern from features on the surface of larger primary particles. The facetted particle edges of the primary particles became progressively more roughened with milling time and additional surface features were present, which were inferred to be fractures or superficial damage, see Figure 93(e). Additional milling, to a total duration of 32 h, did not significantly reduce the average particle size or particle size-distribution further (average particle size = ~1 µm, standard deviation = 0.3 µm), but did result in more roughened particle with apparent surface damage increased.

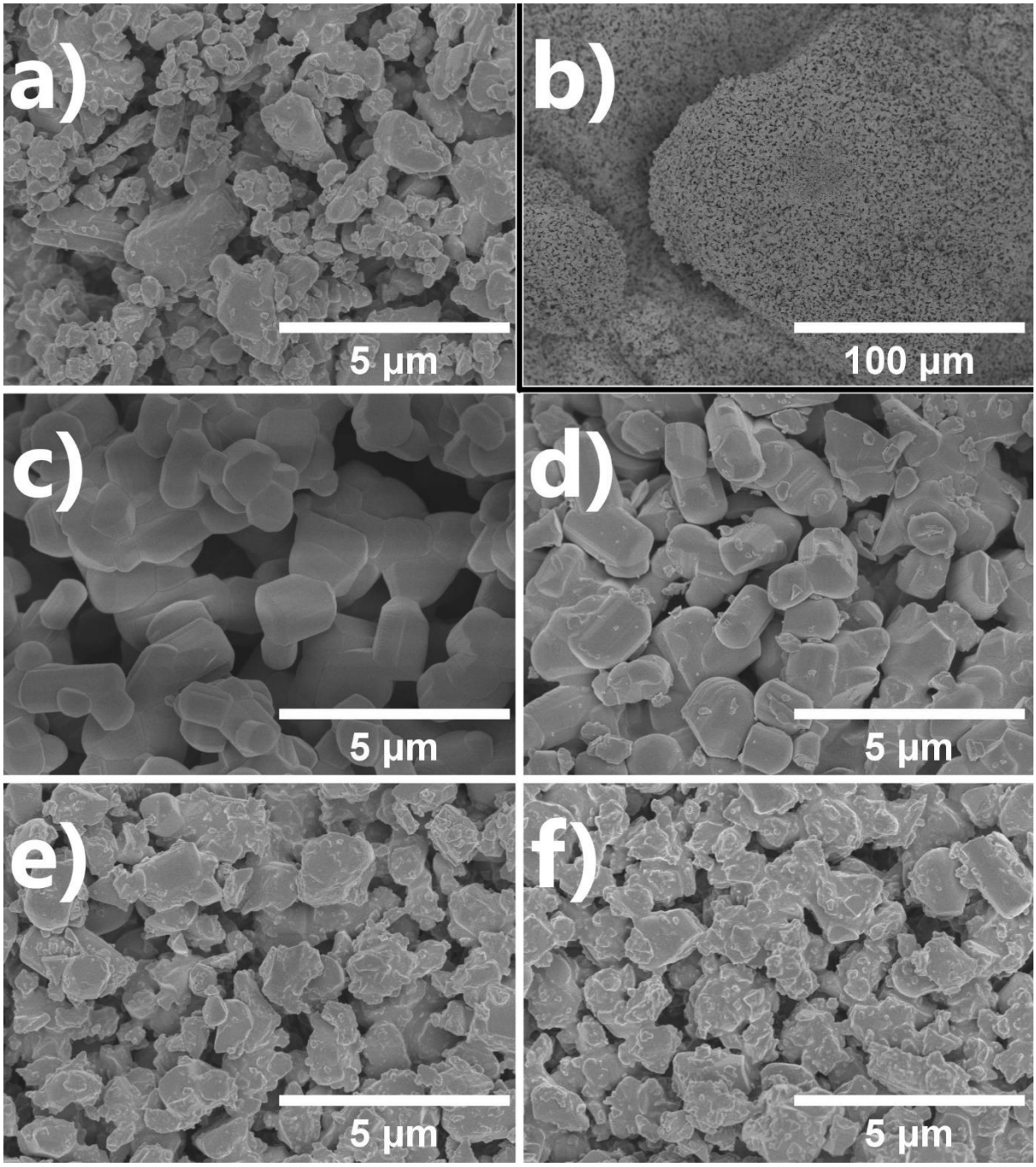

Figure 93. Secondary electron SEM micrographs of CBN28 powders; (a) prior to calcination, after ball milling for 24 h to the promote mixing of precursors, (b) after calcination for 12 h at 1200 ^{o}C at 400 x mag, showing a large aggregate and, (c), at 10 kx mag. Post-calcination ball milled powders are shown in (d), (e) and (f), with respective mill durations of 8, 24 and 32 h. Micrographs taken at 10 kx mag, excluding (b) which was taken at 400 x mag.

High-energy attrition milling

Calcination for 20 h at 1200 ^{o}C produced CBN28 powders from precursor oxides and carbonates, prior to high-energy attrition milling. This further extension of the calcination time was adopted as there was concern that a 12 h calcination may produce powders that appear single phase by XRD, but contain small amounts of secondary phases (< 5 at.%). The potential negative effects of prolonging calcination, namely increasing primary particle size, were judged to be of little consequence given the planned, subsequent high-energy milling of the powders.

The high-energy attrition mill reduced particle size via mechanical impact with yttria-stabilised zirconia beads of variable size (650 µm and 1000 µm). Prior work by Dr. Thomas Hooper indicates that decreasing the size of the milling beads decreased the size of the resultant CBN28 powder and that the rate of size reduction decreased exponentially with time, becoming negligible after 1 h. Approximately 150 g of calcined powder was mixed with 800 mL of iso-propanol and passed through the attrition mill for 1 h, which operated with 1 kg of 650 µm yttria stabilised zirconia beads. The ceramic propellors within the milling chamber agitated the milling bead and powder slurry causing higher energy impacts than can be achieved by (tumbling) ball milling. After drying, the resultant powder was judged to have poor flowability, a result that is atypical, in comparison to the other attrition milled powders, which in turn had reduced flowability in comparison to as-calcined powders. Particle shape is a factor in powder flowability. Non-spherical powders, when agitated or vibrated, are capable of more intimate surface contact/proximity (and so increased adhesive forces), reducing flowability [Kudo, Y. 2020]. It is possible that the variety of particle sizes, seen in this powder in Figure 94(a), allowed for intimate contact and reduced flowability. In general, poor flowability may be caused by the increased agglomeration, due to van de Waals interactions, that takes place in finer powders (average particle size < 1 µm). Agglomerates, or granules, have lower surface area to volume ratios, are typically less cohesive to one another, and have higher flowability [Santomaso, A. 2003].

Analysed later, a SEM secondary electron micrograph (Figure 94(a)) shows that particle size (average = ~1 µm) was comparable or larger than the 12 h-calcined CBN28 that was ball milled for 24 h (Figure 93(c)). The size-distribution of the particles was also larger (standard deviation = 0.5 µm) suggesting incomplete milling. The presence of agglomerates within the piping of the attrition mill, may have limited flowrate and resulted in uneven milling, or else 1 h is insufficient to attrition mill powders straight from calcination into size-reduced particles with narrow size-distributions.

Subsequently, calcined powder was ball milled for 24 h prior to attrition milling with 1000 µm and 650 µm beads and SEM images are shown in Figures 94(b) and 2(c) respectively. Particle sizes for these attrition milled powders averaged ~0.5 µm, particle size standard deviation decreased slightly from 0.3 to 0.2 µm with decreasing milling media size. These milled CBN powders were employed in PAD at Leeds, however they readily formed soft agglomerates during deposition and did not produce mechanically stable films. Rather, the deposited thick, low-density powder-compacts could be removed by surface sheering the films with a spatula, see Appendix 5(d). Annealing (Thermal pre-treatment) of the attrition milled powder (650 µm beads) in Figure 94(c), for 4 h at 1000 ^{o}C with ramp rates of 300 ^{o}C h^{-1}, produced the powder shown in Figure 94(d). Annealing served to recover damage to the particle surface, producing more rounded or less roughened primary particles. Some of these primary particles were also bonded to form hard aggregates. Average particle size and standard deviation increased to ~1 µm and 0.4 µm respectively. This powder was used to produce the PAD film seen in Figure 95.

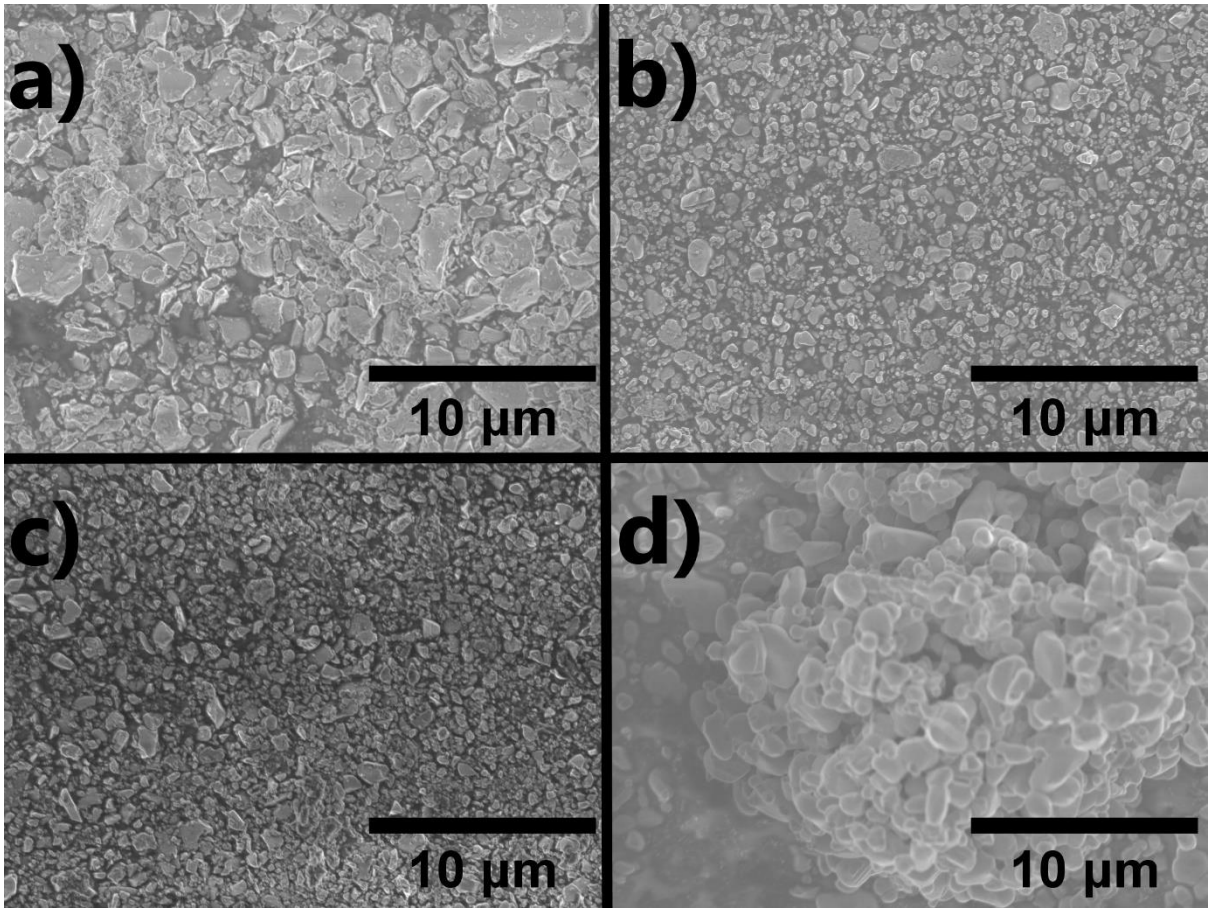

Figure 94. Secondary electron SEM micrographs of CBN28 powders calcined for 20 h at 1200 ^{o}C and, in (a), (high-energy) attrition milled with 650 µm beads for 1 h. The flowability of the powder was unexpectedly low and attrition milling was judged to have been unsuccessful. As such powders (b) and (c) were ball milled for 24 h prior to attrition milling with 1000 µm and 650 µm beads respectively. Thermal pre-treatment (annealing) of the milled powder in (c) was performed at 1000 ^{o}C for 4 h, the resulting powder is shown in (d). Primary particle size was reduced by high-energy milling. Subsequent annealing produced a larger more uniform and rounded set of primary particles of ~1 µm in size in a mix of hard aggregates and non-agglomerated particles.

Deposition of CBN powders at Leeds

Powders with primary particles of differing sizes, size-distributions and states (aggregated or not) were deposited at Leeds. Some calcined powders, with and without post-calcination ball milling, formed films. Low-energy ball milled powders underwent some (presumed) soft agglomeration during deposition but tended to form anchor layer films only (dark and lacking visible thickness). High-energy attrition milled powders, seen in Figure 94(b) and (c), were prone to the formation of agglomerates during aerosolization, this appeared to hinder the deposition of films and promoted the deposition of thicker, low-density powder compacts. Thermal pre-treatment of high-energy attrition milled powder, for example by heating to 1000 ^{o}C for 4 h at a ramp rate of 300 ^{o}C min^{-1},

reduced but did not eliminate the formation of agglomerates during aerosolization. A backscatter electron micrograph of a CBN28 film deposited at Leeds is shown in Figure 95. This film was produced from a thermally pre-treated powder prepared under the same conditions as that in Figure 94(d). A Y-doped CBN film was produced from a similarly processed powder, this film was damaged during the process of mechanical cross sectioning, however it can be seen in Appendix 12. The attrition milled powder, in Figure 94(c) was also granulated by spray drying at Manchester and used to produce films at both Manchester and Leeds. A photograph of the film, resulting from deposition of the spray dried material at Leeds, can be seen in Appendix 13 (white in colour), it was thick (~250 µm) but had poor mechanical stability, i.e. it was a compact rather than a dense film.

During the deposition of CBN, some of the Leeds systems operational conditions were fixed. These included the stand-off distance between the nozzle and the stage (7 mm), nozzle scan speed (20 mm s^{-1}) and carrier gas (N_2). Other operational conditions, such as carrier gas flowrate (2* - 8 L min^{-1}), the mass of powder in the aerosol generation chamber (2 - 15 g), the number of nozzle scans and the maximum permissible pressure in the vacuum chamber were varied. *Some deposition was possible without the assistance of carrier gas flowrate at all. Here, a pressure gradient was established between the vacuum chamber (5 - 10 mbar) and the aerosol generation tube (1 bar). Opening the isolation valve between the tube and the chamber resulted in a short burst of deposition and this deposition was sustained to some degree by the flow of leakage air (into the AGC from non-vacuum sealed joints) from the AGC into the VC.

The standard deposition conditions outlined in Section 7.3, Results chapter 2, were generally considered the optimum for producing anchor layers, although analysis was hindered by the need to employ cross sectional electron microscopy. The standard conditions are paraphrased below:

Powder was dried for 12+ h at 150 °C and then sieved through 200 µm nylon mesh, to break up any large agglomerates, prior to deposition via the Leeds system. Standard deposition parameters were as follows; ~8 g of powder, deposited at 4 L min^{-1} in 3 successive bursts of deposition. Each deposition burst had a duration of ~12 s and consisted of 3 passes of the nozzle from the origin to x = +40 mm and back to the origin (x = 0). The produced aerosol jet is presumed not to have diverged significantly from the geometry of the nozzle, given that film widths (y-direction, ~10 mm) did not differ significantly from the nozzle-slit width (8 mm). Typically, six 12 x 15 or 12 x 20 mm SUS304 stainless steel substrates were coated over their entire length (x-direction) and ~half their width (y-direction). This allowed for multiple destructive experiments to be performed upon films from the same deposition batch, without the use of a sectioning saw.

8.1.2 characterisation of PAD films from Leeds

A CBN28 powder was synthesised from precursor oxides and carbonates by calcination at 1200 °C for 20 h. The powder was then ball milled for 24 h and attrition milled with 650 µm beads for 1 h, then heat treated at 1000 °C for 4 h and deposited at 4 L min^{-1} in three 12 s scans under standard conditions. An SEM SE micrograph of the powder can be seen in Figure 94(d).

The SEM image and EDX elemental maps in Figure 95 show a ~1 µm thick layer of niobium, oxygen, barium and (most-likely) Ca on a Fe containing SUS304 stainless steel substrate. The film cross-section was produced by fixing the sample in resin (Epothin, Buehler) which contains C, before mechanically abrading with SiC papers and polishing with diamond pastes of sequentially decreasing size (from 9, 6 to 3 µm). Some scratches are evident on the substrate, these are present due to imperfect polishing. In the backscatter electron micrograph, the CBN28 layer is of a lighter contrast when compared with the substrate below.

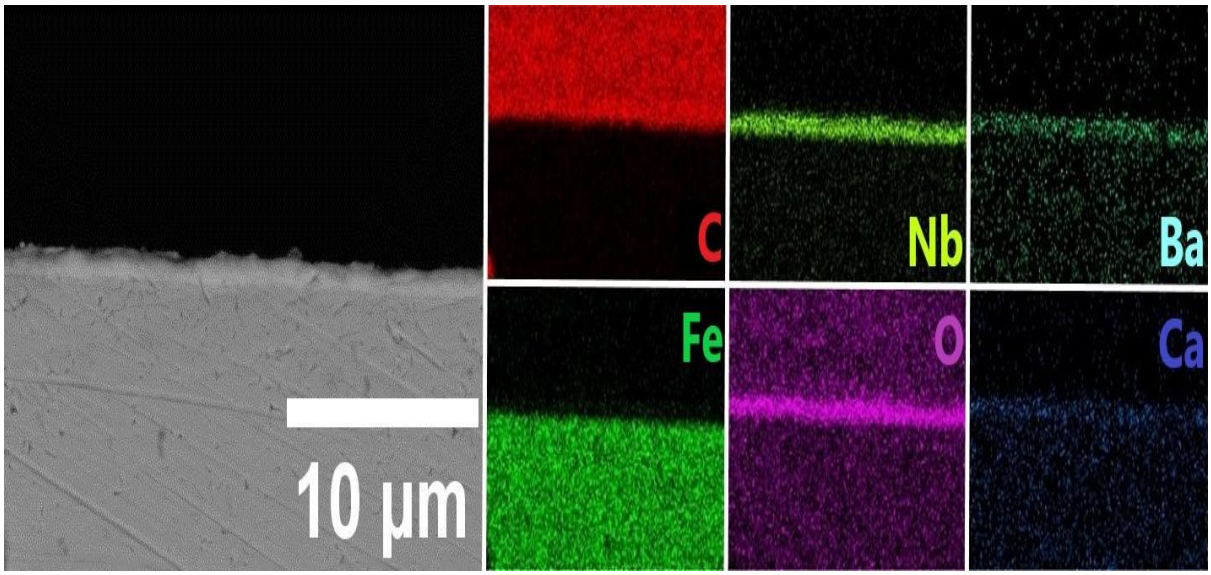

Figure 95. A back scattered electron micrograph of a mechanically cross-sectioned ~1 µm thick CBN28 film, “CBN28_Leeds”, deposited on stainless steel (SUS304). The CBN28 powder was synthesised from precursor oxides and carbonates by calcination at 1000 °C for 20 h. The powder was then ball milled for 24 h and attrition milled with 650 µm beads for 1 h, then heat treated at 1000 °C for 4 h and deposited at 4L min^{-1} in three 12 s scans. The elemental maps confirm the presence of a Nb, O, Ba and (most likely) a Ca containing layer. Scratches in the substrate are a product of mechanical cross-sectioning with imperfect polishing.

All CBN films were electroded with Au, according to the protocol outlined in the Section 3.5 (methodology). Images of freshly electroded films are shown in Appendix 14. The 2 mm diameter electrodes can be seen, on a dark anchor layer and a (white) low-density powder compact in Appendix 13. The electrodes have broken down on the powder compact, either due to poor bonding or disintegration of the compact beneath the electrode. From the CBN28_Leeds film's P-E response, the permittivity-electric field response was obtained, See Figure 96(a) and (b). Measurements were taken by the author and Dr. Yizhe Li at the University of Manchester. The P-E loop in Figure 96(a) has a lossy, but characteristically non-ferroelectric, form. The polarisation at the maximum applied field, of 50 kV cm^{-1} (~ 0.75 µC cm^{-2}) was low, but ~3x higher than the lower-density CBN28 film produced in Erlangen (~ 0.25 µC cm^{-2}, Section 7, Results chapter 2, Figure 92). Due a low polarisation response and relatively high losses, P_{Max} did not coincide with the maximum applied field. The permittivity-electric field response, shown in Figure 92(b), likewise does not show a typically ferroelectric character. Contrary to a characteristically ferroelectric response, permittivity decreases with increasing field strength. Losses significantly increased with field strength, from tan δ = ~0.5 at 20 kV cm^{-1} to tan δ = ~1.3 at 50 kV cm^{-1}. This low resistivity inhibits any meaningful comparisons with less-lossy films. However, it is still clear that the high-density anchor layer, seen in Figure 95, has a low polarisation response. This suggests that, similarly to the SNN and Al_2O_3 anchor layers of Section7, Results chapter 2, high levels of strain are present. This strain likely inhibits the <001> unit cell distortion which is primarily responsible for the polarisation response in TBs [Glass, A. M. 1969].

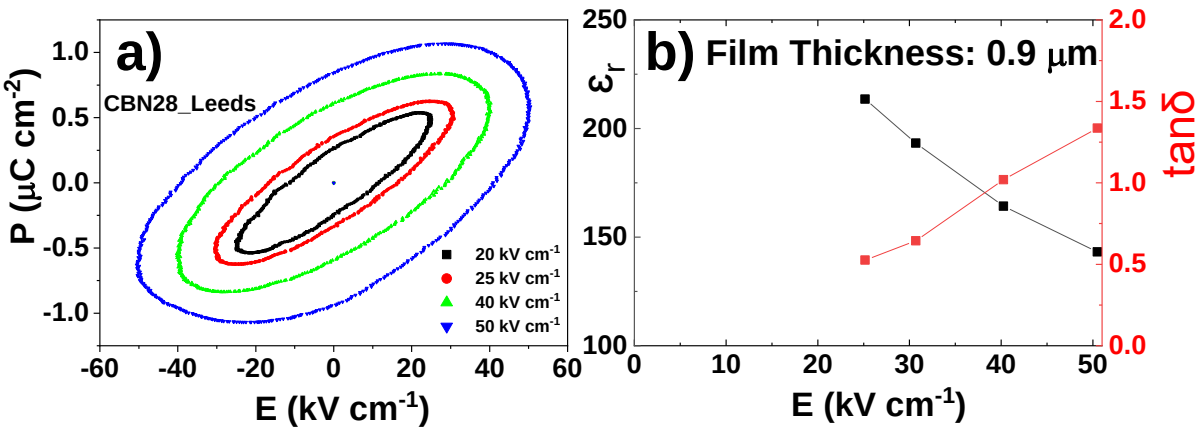

Figure 96. Polarisation-electric field loops for a ~1 µm CBN28 film, "CBN28_Leeds", deposited on stainless steel (SUS304) and imaged in Figure 3 are shown in (a). Permittivity-electric field response is shown in (b). Measurements performed by the author and Dr. Yizhe Li, of the University of Manchester.

8.1.3 Summary of the deposition of CBN28 by the Leeds PAD system

It is concluded that sub-micron anchor-layer films, produced by PAD at Leeds, are typically unsuitable for dielectric analysis due to their poor resistivity. The propensity of PAD to generate particle-substrate impacts with a range of momentums likely results in perforations of the sub-micron layer [Kim, H-K. 2012].

Some practical appreciation of the relationships between powder properties, operational conditions and film defects was acquired in this preliminary investigation. Operating at higher flowrates (> 4 L min^{-1}) tended to produce pin-hole perforations in film anchor layers. For the successful deposition of anchor layers, no practical lower limit of carrier gas flowrate was found. The pressure gradient between the aerosol generation chamber (at 1 bar when without carrier gas flow-through), and the vacuum chamber (initially, < 10 mbar) was sufficient for anchor layer deposition. The build-up of thick (5+ µm) high-density films was not achieved, this is assumed to be due to the limitations of the vacuum pump and a failure to maintain low pressure (< 10 mbar) throughout operation, as identified in Section 7, Results chapter 2.

Powder preparation techniques allowed for the deposition of anchor-layers but could yet be further refined. The fine control of particle size-distribution, agglomeration and operational conditions may, at the least, serve to reduce anchor-layer perforation and improve the resistivity of any films produced by the Leeds system, given that 1.5 µm thick $BaTiO_3$ PAD films have been shown to be non-conductive [Kim, H-K. 2012].

A dense CBN28 anchor layer was shown to have low polarizability (Figure 96), similar to the less dense CBN28 film produced in Erlangen (Figure 92, Section 7). Given that high levels of deformation are common in the anchor-layers, and that ferroelectricity appears repressed, a thermal post-treatment of deposited films may be required to recover electrical properties for functional applications. This treatment may exacerbate conductivity in perforated anchor-layers. As such, thicker AD films (5+ µm), are desired for more robust functional analysis. In pursuit of thicker films, powders were deposited using the Manchester PAD system. This rig could maintain very low vacuum chamber pressures (< 1 mbar) during operation and used a brush generator for improved control of particle aerosolization.

8.2 Deposition in Manchester

A CBN28 powder was synthesised by the 'standard' mixed oxide route in Leeds (by calcination for 20 h at 1200 ^{o}C followed by 24 h ball milling and 1 h of attrition milling with 650 µm beads). This powder then underwent granulation in Manchester, by Dr. Yizhe Li. Granulation was performed using a B-290 spray dryer (Buchi UK Ltd, UK), by a comparable method to that described by Xie, B. *et al* [2024]. In that report, granulation improved the efficacy of Al_2O_3 deposition. The granulated CBN28 powder was deposited on steel substrates by the author and Dr. Yizhe Li using the PAD system at Manchester. Additionally, a non-granulated (multi-)doped-CBN powder was deposited. Its composition corresponds to the bulk ceramic $Ca_{0.1525}Ba_{0.6975}Ag_{0.03}Sr_{0.03}Y_{0.03}Ce_{0.03}Nb_{1.85}Ta_{0.15}O_6$ shown in the Appendices 15, 16 and 17 and referred to as "w = 0.03". The doped-CBN powder was calcined for 12 h at 1200 ^{o}C before ball milling for 24 h (and was not then attrition milled). A bulk ceramic produced from the doped-CBN powder had improved temperature-stability of permittivity, when compared to the bulk ceramic CBN28 (compare Appendix 16 to Section 5, Results chapter 1, Figure 53(a)). It was hoped that processing via PAD would further improve this temperature stability towards very wide temperature ranges (-55 to 300+ ^{o}C).

The PAD system at Manchester was dissimilar to the Leeds system in that it had integrated pressure control, could operate at very low pressures (<< 1 mbar), and used a brush-type aerosol generator. The powder tube in the brush generator was 7mm in diameter. A description of the PAD system at Manchester is given by Xie, B. *et al* [2024]. The granulated CBN powder was deposited onto stainless steel substrates at N_2 carrier gas consumption flowrates of 13 L min^{-1} and 18.8 L min^{-1}. Other operational conditions were fixed at a nozzle-scan speed of 5 mm s^{-1} and feed rate of the loosely compacted tube of powder in the brush generator of 100 mm h^{-1}. The doped-CBN powder was deposited at a flowrate of 13 L min^{-1} and a feed rate of 50 mm h^{-1}. Vacuum chamber pressures were maintained at ~2 mbar for the duration of deposition.

8.2.1 Deposition and physical characterisation of CBN28 granules and doped-CBN powder

Optical micrographs of the CBN28 granule films deposited at 13 L min^{-1} and 18.8 L min^{-1} and the doped-CBN powder film deposited at 13 L min^{-1} are shown in Figures 97, 98 and 99 respectively. Profilometry of the 3 films is shown in Figure 100. Attempts to link the presence of surface defects, identified by OM, to variation in film thickness are made.

Surface secondary electron micrographs and FIB-SEM cross-sectional micrographs for the 13 L min^{-1} CBN28 granule and doped-CBN powder films are presented in Figures 101 and 102. Later, in Section 8.3, Figures 105 and 106, surface and cross-sectional electron micrographs are shown for the 18.8 L min^{-1} CBN28 granule film, after annealing at 400 and 750 °C. Annealing at 400 °C is presumed not to

have caused significant film densification or evolution of particle morphology. These micrographs were obtained by John Harrington on a FIB-SEM.

Optical microscopy and profilometry

Optical microscopy of the CBN28 granule films, deposited at 13 and 18.8 L min^{-1} was performed by stitching a 25 x 25 grid of individual micrographs. These can be seen in Figures 97(a) and 98(a). A similar micrograph for the doped-CBN powder film is shown in Figure 99(a). Both CBN28 granule films were visibly white, matching the deposited powder, whilst the doped-CBN film was cream/light brown, also comparable to the powder.

A defect at the periphery of the 13 L min^{-1} is shown by the white box in Figure 97(a) and observed at higher magnification in 97(b). This defect reveals a layered structure, with at least 4 layers that likely correspond to the 5 passes of the nozzle during deposition. This structuring was not identifiable in the cross-sectional FIB-SEMs (Figure 102), and so the layering is presumed to be a local feature at the edge of the deposited film.

Some pinholes, with darker contrast, can also be seen in the CBN28 granule films deposited at 13 L min^{-1}, these mostly occur in a band (from left to right, coinciding with the pass direction of the nozzle) just above the centre of the film. In Figure 97(c) the centre region, with fewer pinholes, is bounded by the black lines, with pinhole-banded regions either side. Alongside the pinholes are lighter contrasted spots, believed to be loosely compacted powder, possibly the residuals from soft agglomerate impaction. Comparable OM of an Al_2O_3 anchor layer shows light and loosely compacted powder clusters, in Appendix 18. On the Al_2O_3 film the clusters are deposited where the anchor layer has been damaged, suggesting that either the anchor layer was more resistive to deposition than the exposed substrate or that the clusters caused the damage, presumably in a high momentum (i.e. agglomerate) impact.

In the CBN28 granule film deposited at 13 L min^{-1} the (assumed) powder clusters cover a greater fraction of the film surface in the pinhole-band region, when compared to the centre region. Notice the variation in the density of the lighter contrast patches within the yellow box in Figure 97(c). From the coincidence of pinholes and powder clusters it was assumed that:
a) agglomerates caused the pin-holing and clusters;
or b), that the damaged region was more receptive to agglomerate deposition/cluster presence;
or c), that the pressure bow at the centre of the film deflected agglomerates to the defect band whilst the higher jet velocity in the this region (caused by the radial jet-substrate interaction effect [Benchaita, M. 1983]) simultaneously allowed for the impact of larger, damage-causing single particles.

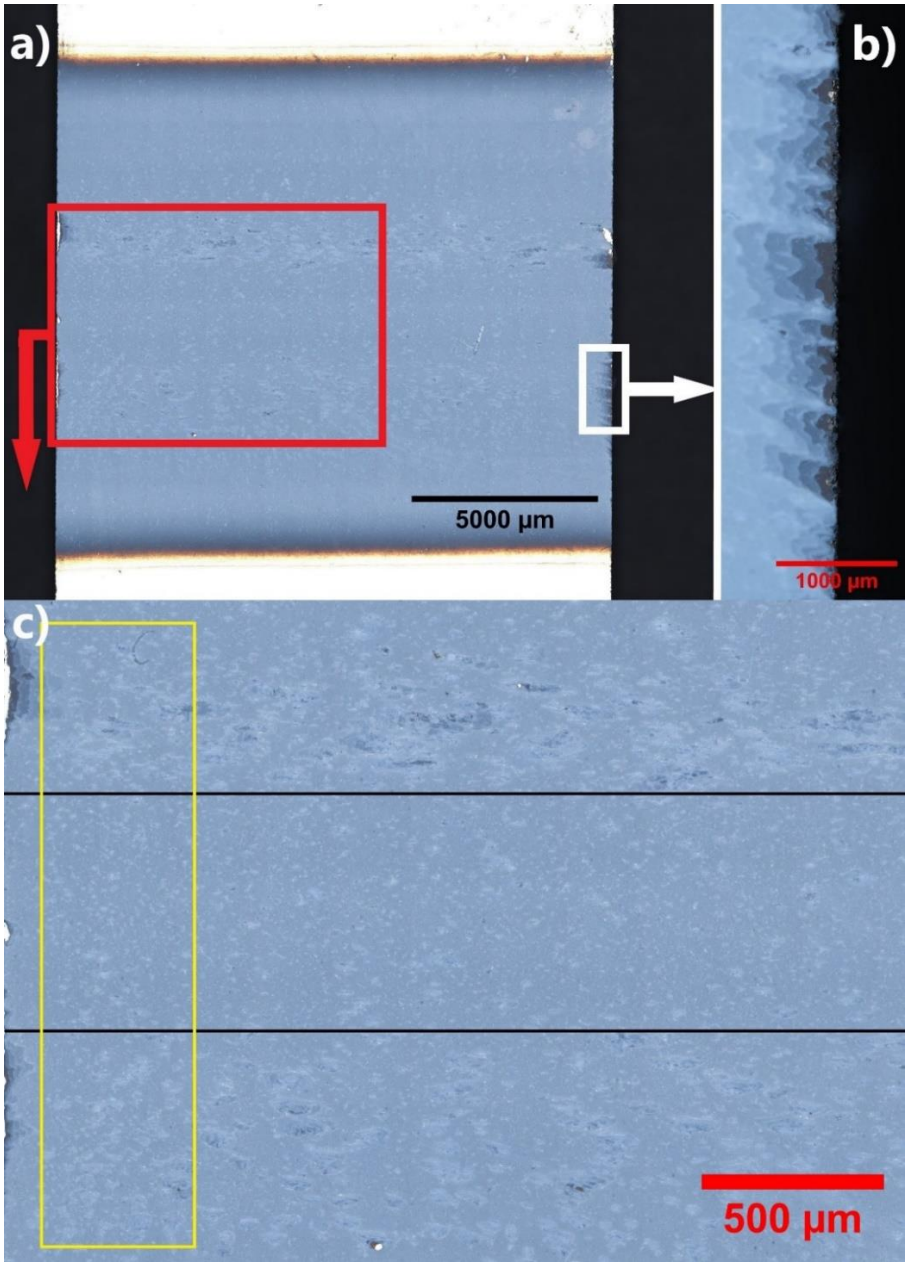

Figure 97. An optical micrograph of a CBN28 granule film deposited at 13 L min^{-1} is shown in (a), this micrograph was produced by stitching together a 25 x 25 grid of micrographs using the optical lenses of a confocal laser scanning microscope. The white box (with arrow) in (a) corresponds to (b). In (b) an edge of film defect reveals a layered structure, at least 4 layers can be seen and these likely correspond to the 5 passes of the nozzle over the film during deposition. The red box (with arrow) in (a) corresponds to area shown in (c). In (c), two types of surface feature can be identified, lighter spots which likely correspond to loosely compacted powder, possibly residuals from agglomerate impacts, and darker spots which are pinholes. A centre region in (c) is identified between the 2 black lines, this region is largely free from pinholes. A comparison of the lighter spots in the yellow box shows that, in the centre region, a lesser fraction of the film's surface is covered by loosely compacted powder/agglomerate residuals.

OM of the CBN28 granule film deposited at 18.8 L min^{-1} revealed that the density of pinholes and (assumed) powder clusters was lower, Figure 98(a). The pinhole-band distribution seen in Figure 97 is likewise observed in Figure 98(b), however powder cluster density was much reduced but appeared to also be highest in the pinhole-band region either side of the centre and particularly above the centre. Individual pinholes were sometimes darker and larger than those present in the 13 L min^{-1}, suggesting higher momentum impacts occurred when depositing at higher carrier gas flowrates. The CBN28 film deposited at 18.8 L min^{-1}, likewise to the 13 L min^{-1} film, had a periphery defect which revealed an apparent layered structuring which was likewise absent from FIB-SEM cross-sectional micrographs in Figure 107.

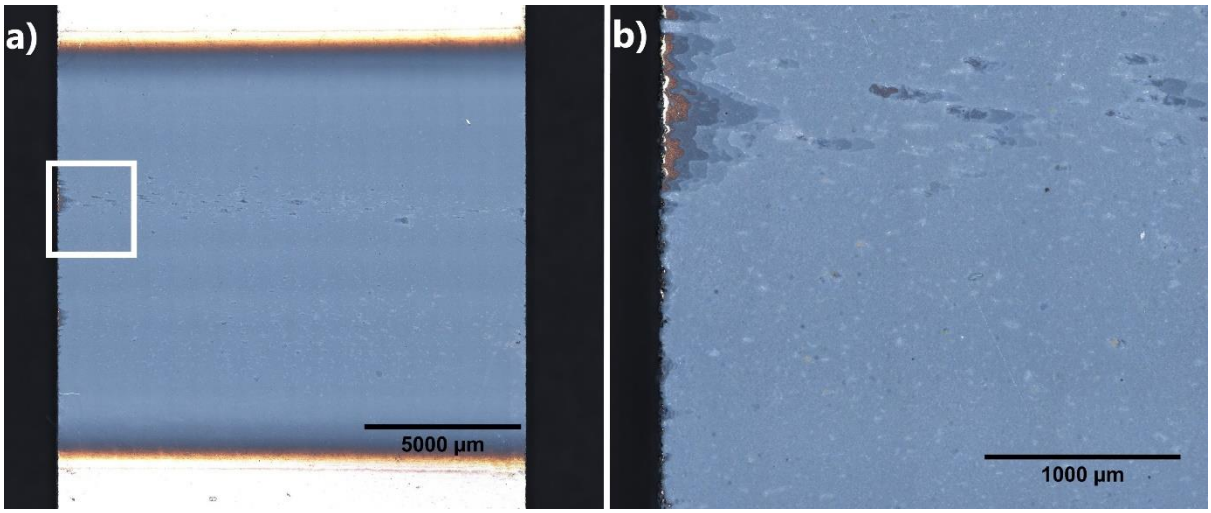

Figure 98. An optical micrograph of a CBN28 granule film deposited at 18.8 L min^{-1} is shown in (a), this micrograph was produced by stitching together a 25 x 25 grid of micrographs using the optical lenses of a confocal laser scanning microscope. The white box in (a) corresponds to the area shown in (b). In (b) a film-defect reveals a layered structure, similar to that observed in Figure 97(a). The pinholes in 6(b) are larger than those in Figure 5(b), they are also banded either side of the centre region of the film and more numerous above the centre region than below. Lighter spots, presumed to be loosely compacted powder, are less common in this film, which was deposited at higher flow rates (18.8 compared to 13 L min^{-1}).

A doped-CBN powder film deposited at 13 L min^{-1} is shown in Figure 99(a), lighter contrasted (assumed) powder clusters are relatively evenly distributed across the film surface and pinholes, if present, are not easily distinguished. The region bounded by the black lines in 99(b) roughly corresponds to the profilometry shown in Figure 100(c), the green box, with a darker contrasted point at its centre, relates to a region approximately 3.5 to 4 mm along the profile in which the film thickness drops to ~10 µm.

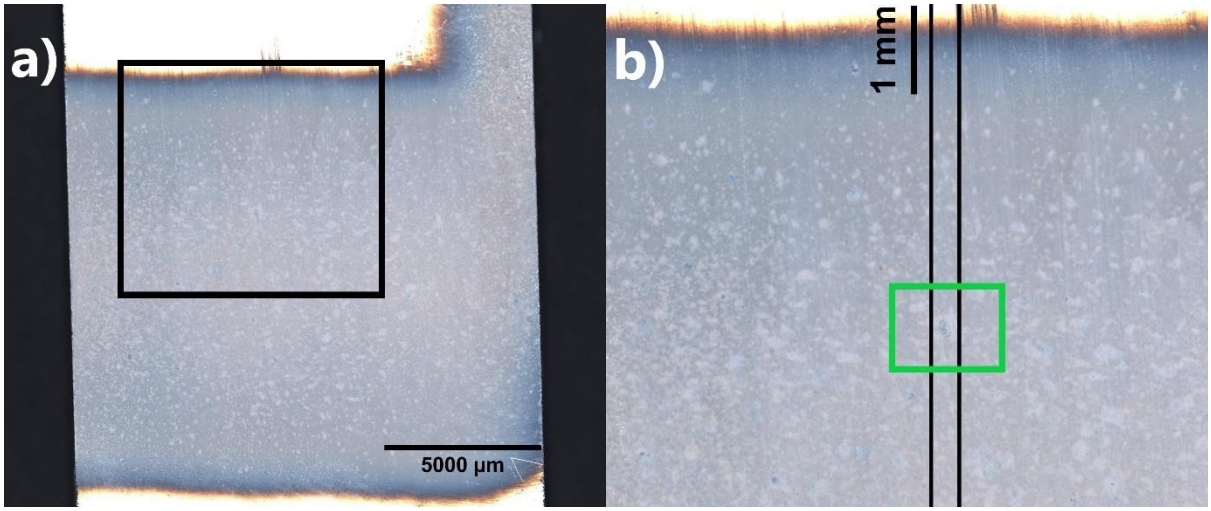

Figure 99. An optical micrograph of a doped-CBN powder film deposited at 13 L min^{-1} is shown in (a), this micrograph was produced by stitching together a 25 x 25 grid of micrographs using the optical lenses of a confocal laser scanning microscope. The black box in (a) corresponds to the area shown in (b). In (b), the area between the black lines relates to the region in which the profilometry data are taken and shown in Figure 100(c). The green box, with a darker contrasted point at its centre, relates to a region approximately 3.5 to 4 mm along the profile in 100(c), in which film thickness decreased to ~10 µm. Pinholes in this film, if present, are not easily distinguished. Lighter contrasted (assumed) powder clusters are relatively evenly distributed across the surface.

The surface profiles of the CBN28 granule films, deposited at 13 and 18.8 L min^{-1}, are shown in Figure 100(a) and (b), and were produced by laser scanning confocal microscopy passing from the exposed substrates at the bottom of the optical micrographs to the top, and vice versa for surface profile of the doped-CBN film, shown in Figure 100(c).

The CBN28 film deposited at 13 L min^{-1} was on average thicker (18 - 20 µm) than the film deposited at 18.8 L min^{-1} (13 - 14 µm). Local thickness variations in 100(a) and (b) are more acute at lengths of 7 - 9.5 mm, corresponding to the upper pinhole-bands seen in Figures 97 and 98. Local thickness variations are also more acute in 100(a) compared to (b), corresponding to the greater density of surface features observed for the CBN28 granule film deposited at 13 L min^{-1} (Figure 97).

From the exposed substrate, at the extreme periphery, film thickness increased over a ~1.5 mm length to the centre plateau of the CBN28 films and over a ~2 mm length to the thicker region in the doped-CBN film. The doped-CBN film was rougher and more variable in thickness, typically ~28 - ~38 µm.

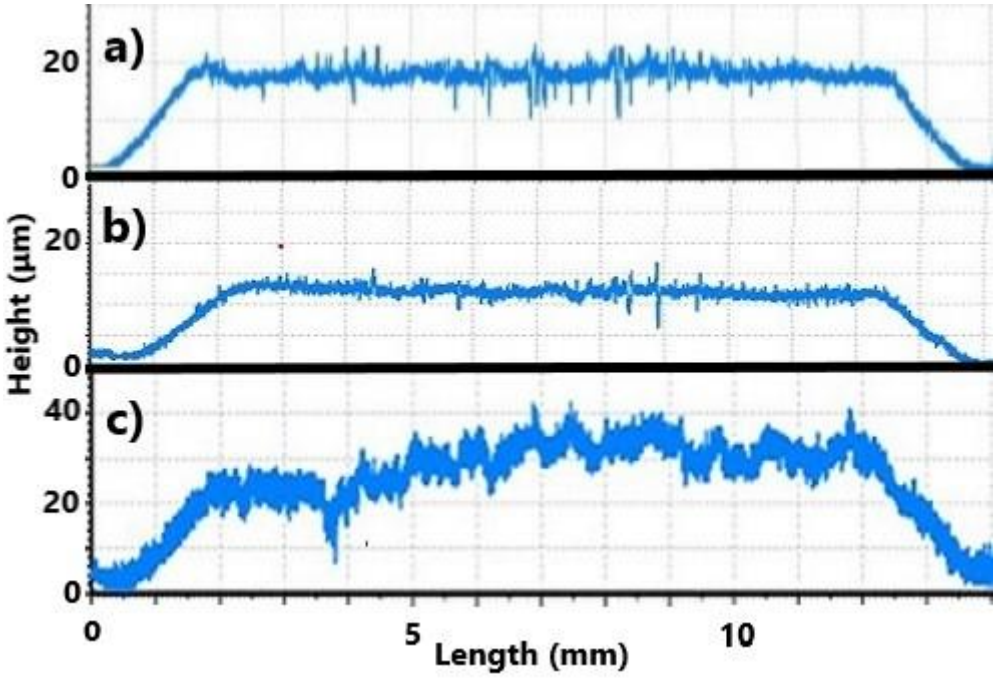

Figure 100. Profilometry scans of CBN28 granule films, deposited at 13 and 18.8 L min^{-1}, are shown in (a) and (b) respectively. Profilometry of the doped-CBN powder film is shown in (c). Data were acquired by a Laser scanning (confocal) microscope. Corresponding optical micrographs are shown in Figure 97(a), 98(a) and 99(a). Profiles in (a) and (b), 14 mm in length, were extracted from the exposed substrate at the bottom of the micrographs (0 mm) to the exposed substrate at the top (14 mm). The profile in (c) was extracted from near the top (0 mm) to near the bottom (14 mm) of the micrograph in 99(a).

Granule and powder film density comparisons

A CBN28 granule film deposited at 13 L min^{-1}, with an apparent crater on its surface, can be observed in the secondary electron micrograph in Figure 101(a). This surface is shown, in Figure 101(b), to be coated with particles that are typically < 0.5 µm in scale. In contrast, the doped-CBN powder film has a cracked surface (Figure 101(c)) and also has larger particles embedded or resting on its surface, see Figure 101(d). This wider range of particle sizes is likely due to the absence of high energy attrition milling of the doped-CBN during powder preparation. Both films appeared largely continuous at lower magnification despite a surface coating of non-deformed particles. These surface electron micrographs are of limited use in assessing the deformation and densification that may be present within the films. A broadly comparable micrograph for a CBN28 granule film deposited at 18.8 L min^{-1} and annealed at 400 °C is shown in Figure 106(a).

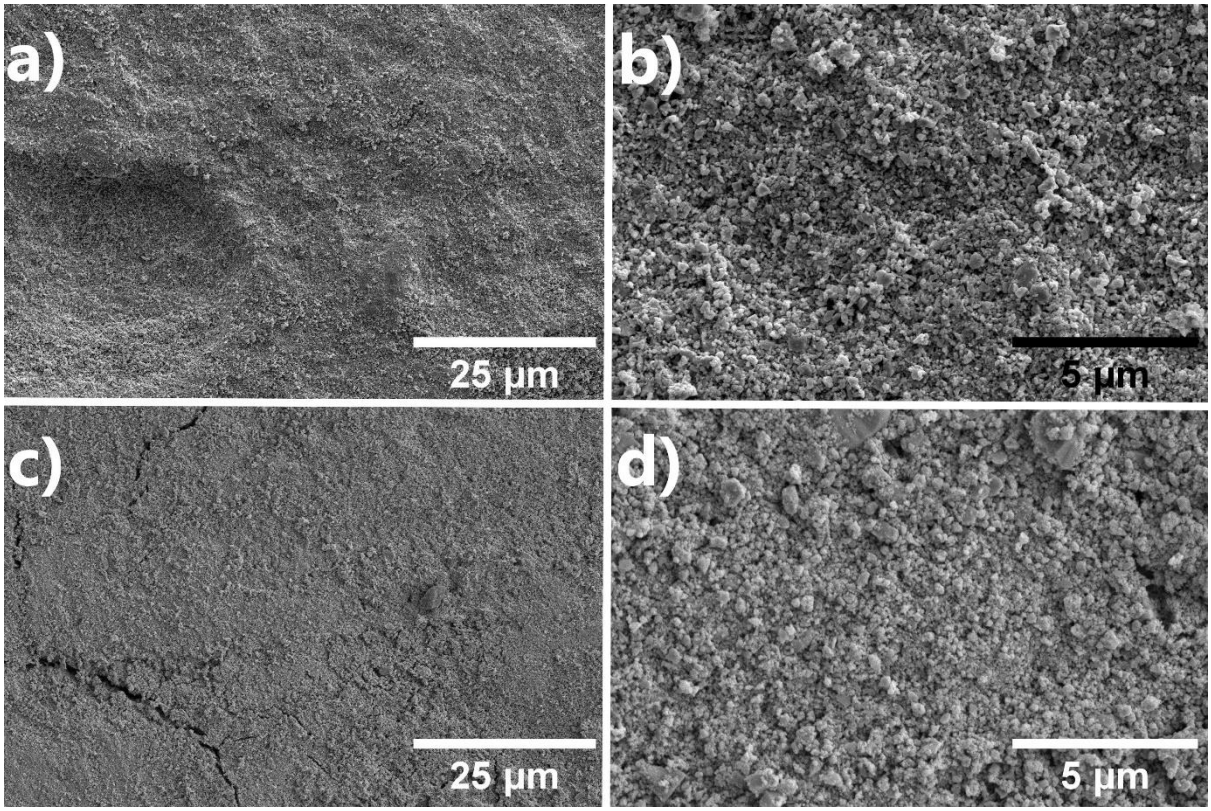

Figure 101. Secondary electron FIB-SEM micrographs of a CBN28 granule film deposited at 13 L min^{-1}, at 5 and 25 kx mag, are shown in (a) and (b). Similar micrographs for the doped-CBN powder film are shown in (c) and (d). Micrographs obtained by John Harrington.

Figure 102 shows cross-sectional FIB-SEM micrographs for a CBN28 granule film deposited at 13 L min^{-1}, in (a), and a doped-CBN powder film, in (b). A curtaining effect from inconsistent FIB milling (vertical white lines) can be seen in both micrographs and is a common occurrence when sectioning low density, porous or open structures with Ga ions [Denisyuk, A. 2017] and [Wollschläger, N. 2017]. Both films show incomplete densification and a retention of grain structure without the significant grain deformation observed in the SNN anchor layer (Section 7, Results chapter 2, Figure 79).

In Figure 102(a), the Pt protective coating, applied before milling, can be seen in white at the top of the micrograph. This section of film is 15 - 17 µm in thickness, differing only slightly from the section of film that underwent profilometry in Figure 99(a) (~18 - 20 µm). A low-density region can be seen near the substrate, a ~3 µm crack emanates from the highest point of this region, into the denser portion of this film. Particles in the anchor layer-region appear smaller, on average, than those in the rest of the film. Cross-sectional FIB-SEM micrographs for the CBN28 granule film deposited at 18.8 L min^{-1}, annealed at 400 and 750 ^{o}C are shown later, in Figure 107. These films also possess incomplete densification. Their thickness is variable (~9 and ~12 µm), and slightly lower than the measured thicknesses in the profilometry shown in Figure 100(b) (13 - 14 µm).

The doped-CBN powder film, in 102(b), was ~33 µm thick, also within the thickness-range shown by profilometry in Figure 100(c). A low-density area near the anchor layer region can be seen bottom right of Figure 102(b). Some larger particles (~1 µm) can be seen in this low-density region, when compared with the rest of the anchor layer. A low-density region at the film surface, or the active deposition layer, is also observed. This region has some of the largest discernible particles, up to ~3 µm in size. The densification of PAD films is not believed to solely occur due to the initial impact of the particles. Rather, the hammering of subsequent particles impacting on the film promotes further particle size reduction, bonding and densification throughout the film [Kim, H-K. 2015]. It is likely that in this surface region only limited or no hammering-induced densification occurred.

To estimate film densities, the percentage area of cavities (dark space) in the cross-sectional micrographs was assessed and subtracted from 100 %. The grayscale/colour saturation of the dark space was thresholded and the percentage of pixels associated with that space was calculated. For the CBN28 Film deposited at 13 L min^{-1} in Figure 102(a), ~10 % of the pixels had grayscale saturations of 60 (out of 255) or less and were classified as dark space. See Appendix 19(a) for an example of manually thresholding, as well as data from an automatic colour-banding software, which gave a darkest colour band percentage of 9.7 %. Corresponding manually obtained dark space threshold percentages of 6 and 7 % were found for the CBN28 film deposited at 18 L min^{-1} and annealed at 400 and 750 °C, with automatically calculated values of 7.6 and 9.2 % showing a similar trend, though values were slightly higher. This indicates that that higher flowrates may have helped densify the CBN28 film. However, the small sample area of the film cross sections does limit how representative the density estimates are. For the doped-CBN the manually and automatically calculated values were 15 and 14.8 %. Overall, the films clearly possessed densities below that of 95 %, which will limit quantitative comparison of the electrical properties of the films to that of bulk ceramics.

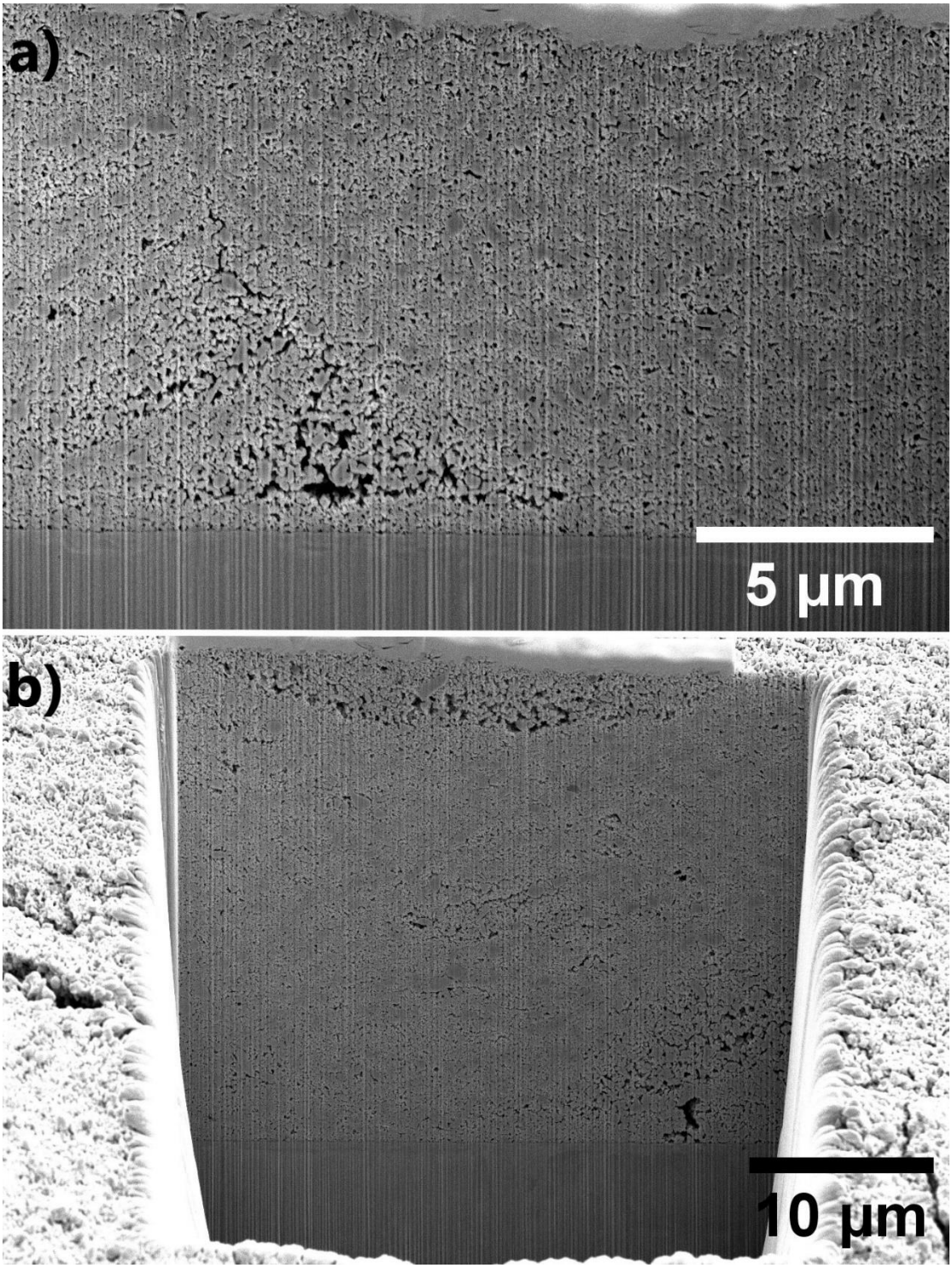

Figure 102. Cross-sectional FIB-SEM micrographs of a Pt-coated CBN28 granule PAD film, shown in (a), deposited at 13 L min^{-1} and a doped-CBN powder PAD film, shown in (b), at magnifications of 15 kx and 8 kx respectively. The Pt-layer (in white) was added at the start of the FIB milling process to prevent charging of the sample and to limit Ga ion damage to the top surface of the film. Regions of lower particle density can be seen in both films. A curtaining affect due to inconsistent Ga ion milling, resulting from film porosity, is apparent, taking the form of vertical lines with lighter contrast. Micrographs obtained by John Harrington.

To summarise, there was a lower density of pinholes and assumed powder clusters on the surface of CBN28 granule films deposited at higher flowrates (18.8 vs 13 L min^{-1}) and this corresponded to fewer local variations in film thickness. Powder granulation produced CBN28 films with reduced thickness variation, when compared to (non-granulated) doped-CBN. The produced films were thick (5+ µm) but of low density. These films should have sufficient resistivity for electrical testing.

8.2.2 Comparison of the electrical properties of the granule films and the doped-CBN film

After electroding at Leeds, as described in the Section 3 (methodology), electrical measurements for the CBN28 granule films were taken by the author and Dr. Yizhe Li at the University of Manchester.

Contact profilometry of the films, directly over the electrodes, was required to give accurate thickness measurements with a precision of < ±1 µm. Film thickness at the electrode were 19 and 16 µm for the granulated CBN28 deposited at 13 and 18.8 L min^{-1} respectively. The doped-CBN film was 33 µm thick at the electrode. Thickness measurements were required to calculate the correct voltage to apply during P-E analysis and, when deriving permittivity, to calculate the change in polarisation with respect to a change of field strength (kV cm^{-1}). Given the level of precision, polarisation-electric field-derived ε_r errors, due to variations in thickness measurement, may be up to ~10 %, given the thicknesses of the films (19 and 16 µm).

The polarisation-electric field response for CBN28 granule films, deposited at 13 and 18.8 L min^{-1}, are shown in Figures 103(a) and (c) respectively, with derived permittivity-electric field responses in (b) and (d) respectively. At 50 kV cm^{-1}, the P_{Max} values for the 13 L min^{-1} film (~0.35 µC cm^{-2}) were comparable to, but lower than, those for the 18.8 L min^{-1} film (0.4 µC cm^{-2}). The P-E loops were not characteristically ferroelectric, though slightly lossy. Greater losses (larger area within the loop) were seen in the 13 L min^{-1} film and, similarly in the permittivity-electric field response, tan δ values were also ~30 - 15 % higher. Relative permittivity values were similar and within the assumed 10 % error, ε_r was around 80 for the 13 L min^{-1} film and 85 for the 18.8 L min^{-1} film.

The electrical properties of the films appear therefore to be comparable, although losses were lower when using the higher (18.8 L min^{-1}) carrier gas flowrate. The CBN28 film deposited at 18.8 L min^{-1} appears to be of higher density when comparing the FIB-SEM cross-sections of the CBN28 granule film deposited at 13 L min^{-1} in Figure 102(a) to the CBN28 granule film deposited at 18.8 L min^{-1} (and annealed at 400 °C for 4 h in Figure 107(a). In the annealed film, the retention of sharp facet edges and the absence of any other clear signs of densification allow for the assumption that further densification of the 18.8 L min^{-1} film did not occur during annealing at 400 °C.

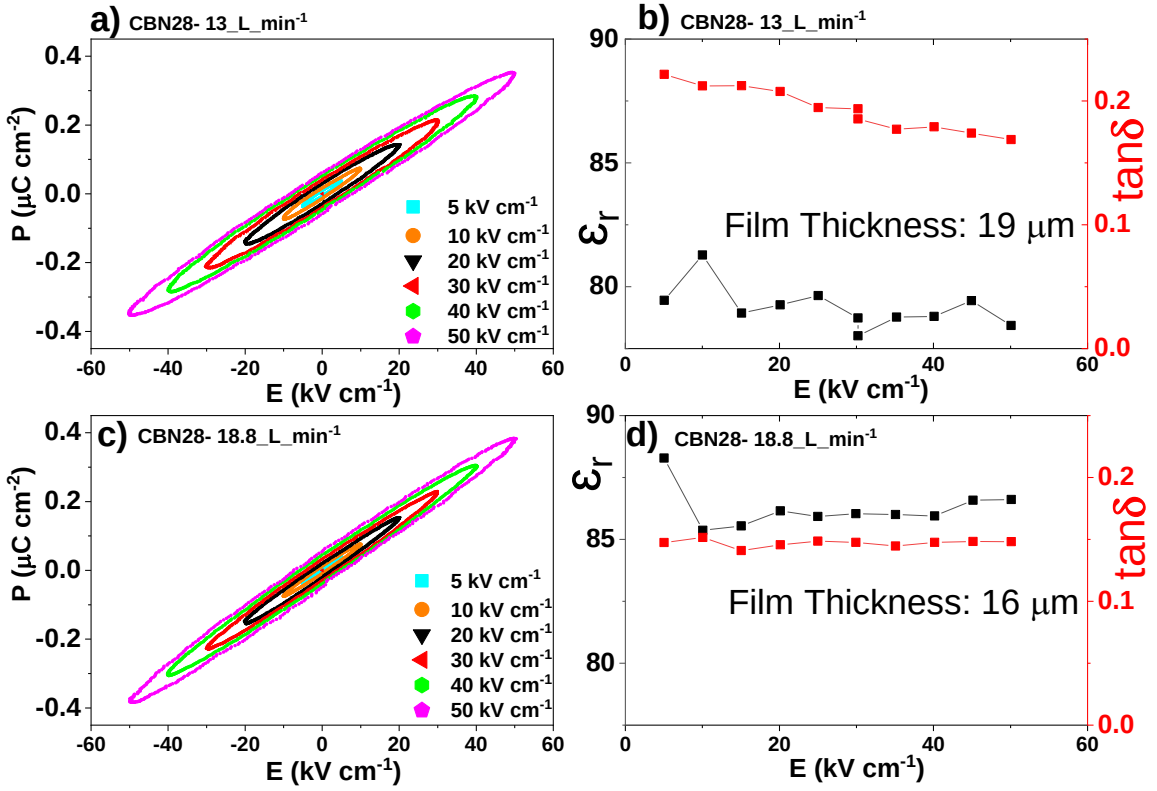

Figure 103. The polarisation-electric field response of CBN28 granule films, deposited at 13 and 18.8 L min^{-1}, are shown in (a) and (c) respectively. Derived permittivity-electric field and tan δ-electric field responses are shown in (b) and (d), respectively. Values are comparable, with the film deposited at 18.8 L min^{-1} showing only slightly ~5 - 10 % increased P_{Max} and permittivity at 50 kV cm^{-1}. A reduction in losses, with increased flowrate, was apparent from the P-E loop and the tan δ values. Measurement of the film's polarisation-electric field response was performed by the author and Dr. Yizhe Li, of the University of Manchester.

The permittivity- and tan δ- temperature responses from the CBN28 granule films, deposited at 13 and 18.8 L min^{-1}, are shown in Figures 104(a) and (b) respectively. There were some dissimilarities in the measurement approach for each film. The 13 L min^{-1} film was measured by Dr. Yizhe Li at the University of Manchester, with heating curve data shown in Figure 104(a). The 18.8 L min^{-1} film was measured by the author at Leeds, and cooling curve data are shown in Figure 104(b), with corresponding heating curve data in the Appendix 20. The Leeds heating curve data was affected by high-frequency measurement errors, possibly due to poor contact with the electrode during measurement. However, it can be said that the permittivity-temperature responses for the films were broadly comparable.

For the 13 L min^{-1} film, measured at 1 kHz, relative permittivity (at 50 ^{o}C) was ~80, see Figure 104(a). This corresponded well with the permittivity-electric field data in Figure 103(b). A spike in permittivity below 50 ^{o}C likely corresponds to the disturbance of water vapour within pores in the film [Caballero, A. C. 1999]. A peak in 1 kHz tan δ values was observed between 50 and 150 ^{o}C, this loss peak may be due to poor contact with the electrode during measurement, given that the loss data is noisy in that temperature range. However, it may also be associated with unstable defects which can be detected dielectrically upon their removal during the initial heating of a PAD film [Khansur, N. H. 2018]. A second 1 kHz loss peak is present above 200 ^{o}C. The reduction in this loss peak above 325 ^{o}C corresponds to an unexplained increase in permittivity, which appears by its frequency dispersion to be related to conductivity. Some frequency dependence of the permittivity coincided with frequency dependence of tan δ, and this limited the temperature stability of the permittivity in the 13 L min^{-1} film.

The permittivity- and tan δ- temperature responses of the 18.8 L min^{-1} film were measured at Leeds, see Figure 104(b). A good contact could not be made with the electrode used for P-E responses in Figure 103(c). Another of the 5 deposited electrodes, comparable in area but differing by ~2 mm in location, was used (see Appendix 14 for examples of the 5 electrodes deposited onto each film). The thickness of the 18.8 L min^{-1} film is believed to be variable, judging by the FIB-SEM cross sections of annealed films from this batch, which vary locally in thickness, from 8 - 9 µm (Figure 107(a)), and differ from the profilometry measurements in Figure 100 (13 - 14 µm). This thickness variability, and possible variations in film density may account for some discrepancy between the permittivity-electric field and permittivity-temperature responses.

For the 18.8 L min^{-1} film, measured at 1 kHz, relative permittivity (at 50 ^{o}C) was ~60, this differed from that of the permittivity-electric field responses (ε_r = ~85 at 10+ kV cm^{-1}). The high frequency (100 kHz) permittivity response of the 18.8 L min^{-1} film was nearly invariant with temperature from 50 to 350 ^{o}C. Lower frequency measurements saw increases in permittivity at higher temperatures which coincided with increased losses, most likely due to ionic conduction. A 100 kHz measurement error can be seen above 200 ^{o}C, causing a recorded elevation in losses, this is assumed to be caused by poor contact with the electrodes.

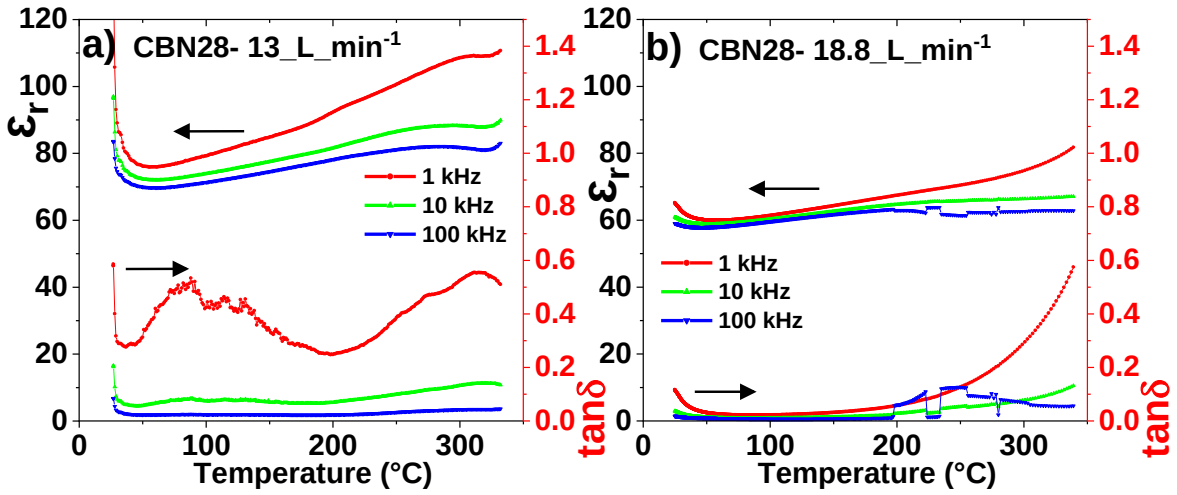

Figure 104. The permittivity- and tan δ- temperature responses of CBN28 granule films, deposited at 13 L min^{-1} and 18.8 L min^{-1}, shown in (a) and (b), respectively. Figure (a) shows heating curve data and was obtained by Dr. Yizhe Li of the University of Manchester. Figure (b) shows cooling curve data and was obtained by the author at Leeds, some elevated losses at 200 - 230 ^{o}C and also 285 ^{o}C are apparent for the 100 kHz data in (b). In (b), the frequency dependence of permittivity and loss is reduced, when compared with (a), suggesting that conductivity in the 18.8 L min^{-1} film, upon cooling, was lower. This relative reduction in losses is still present, though to a lesser extent, in the heating curve data (Appendix 20).

The permittivity- and tan δ- temperature responses of the doped-CBN powder film are shown in Figure 105(a) and are compared with a bulk ceramic produced from the same powder in (c). Corresponding P-E responses are shown in 105(b) and (d), respectively. See Appendices 15, 16 and 17 for X-ray diffraction patterns, permittivity-temperature plots and polarisation-electric field responses for this "high-entropy" doped-CBN bulk ceramic solid solution at various dopant levels. The doped-CBN film in this chapter has the same composition as $Ca_{0.1525}Ba_{0.6975}Ag_{0.03}Sr_{0.03}Y_{0.03}Ce_{0.03}Nb_{1.85}Ta_{0.15}O_6$, referred to as "w = 0.03" in the Appendix.

The permittivity of the doped CBN film, at 50 ^{o}C, was ~1/20th that of the bulk and ~1/3rd that of the CBN28 granule films. Film permittivity was stable with respect to temperature, from 50 to 350 ^{o}C, with some increase in high temperature 1 kHz-permittivity coinciding with increased losses, likely due to ionic conductivity. Below 50 ^{o}C, a spike in permittivity and dielectric loss likely correspond to the disturbance of water vapour in the film's pores [Caballero, A. C. 1999]. The bulk ceramic shows temperature stable permittivity (ε_r = 490 ±15 %) from -68 to 201 ^{o}C. The P-E response of the bulk ceramic, in Figure 105(d), shows a narrow and pinched form, comparable to that of an ergodic relaxor or antiferroelectric [Qi, H. 2023]. Antiferroelectric TBs with pinched P-E loops have been observed elsewhere [Li, K. 2018]. At 40 kV cm^{-1}, the bulk ceramic P_{Max} was ~2.9 µC cm^{-2}. The P-E

response of the film was also narrow in form, lacking any pinching of the loops at low field levels (Figure 105(b)). For the doped-CBN film, values of P_{Max} of ~0.18 µC cm^{-2} were low (at +40 kV cm^{-1}), ~1/18th that of the bulk and 1/3rd that of the CBN28 granule films.

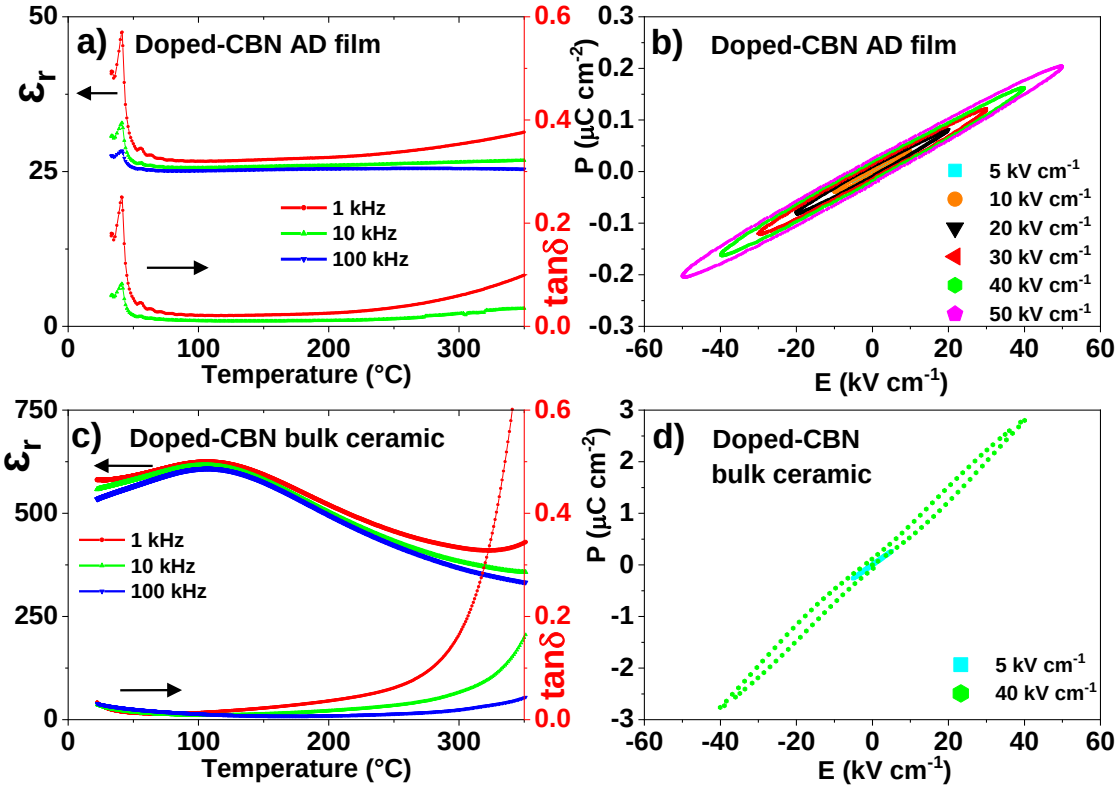

Figure 105. The permittivity- and tan δ- temperature response of a doped-CBN powder film is shown in (a), with polarisation-electric field data shown in (b). The permittivity- and tan δ- temperature response of a bulk ceramic produced from the same powder, is shown in (c) with polarisation-electric field loops in (d). The film shows linear permittivity from 50 to 350 ^{o}C, when measuring at 100 kHz. Some increase in 1 kHz permittivity above 200 ^{o}C coincides with increasing 1 kHz losses. A spike in losses and permittivity below 50 ^{o}C likely corresponds to the disturbance of water vapour in this low-density film. The bulk ceramic had permittivity values, at 50 ^{o}C, ~25x higher than the film, P_{Max} (at +40 kV cm^{-1}) values were also 15 - 20x higher in the bulk. The bulk ceramic showed temperature stable permittivity (ε_r = 490 ±15 %) from -68 to 201 ^{o}C, see Appendix 16. Figure (a) shows heating curve data and was obtained by Dr. Yizhe Li, of the University of Manchester.

To summarise, thick (5+ µm) mechanically stable PAD films were produced from CBN28 spray dried granules and doped-CBN powders using the Manchester deposition systems. The films were not fully densified but were suitable for electrical testing. The low density of CBN in the films (85 - ~90 %), when compared with bulk CBN ceramics (> 95 %), cannot fully explain the low permittivity responses of the films. Frequency dispersion of permittivity and losses, above 250 °C, suggests ionic conductivity at high temperatures in all films. These may be comparable to the losses observed in CBN28 bulk ceramics (Section 5, Results chapter 1, Figure 43). Low permittivity was also observed in a dense CBN28 anchor layer produced in Leeds (Figure 96). As such it is concluded that the polarisation response in these films is inhibited by microstrains, despite the retention of a lot of primary particle structure (Figure 102). Similar suppression of polarisation response and permittivity response has been observed in other PAD films and annealing has partially recovered these properties [Zhou, F. 2022]. Hence, annealing shall be investigated with the aim of producing more functional electroceramics for capacitor and energy storage applications. The low losses, observed in the P-E responses of the films, would be ideal for energy storage applications, if polarizability could be recovered.

8.3 Post deposition thermal treatment of PAD films

Figure 106 displays secondary electron micrographs, taken of the surface on CBN28 granule films deposited at 18.8 L min^{-1} and then annealed for 4 h at 400 ^{o}C, in (a) and (b), and annealed at up to 750 ^{o}C, in (c) and (d). The XRD patterns in Figure 108(a) were produced from the sample as shown in Figure 106(c) and (d), after annealing for 4 h at various temperatures up to 750 °C.

The films had comparable topographies, when viewed at 5 kx magnification, in 106(a) and (c). Higher (25 kx) magnification images show that after annealing at 400 ^{o}C, surface particles remained comparable to non-annealed particles on the as-deposited surface of a CBN28 granule film deposited at 13 L min^{-1} (Figure 106(b) vs Figure 97(b) respectively). After annealing up to 750 ^{o}C, no significant surface particle growth was observed, though there appeared to be some reduction in particle facets, i.e. the surface particles were smoother [Bentzen, M. 2023].

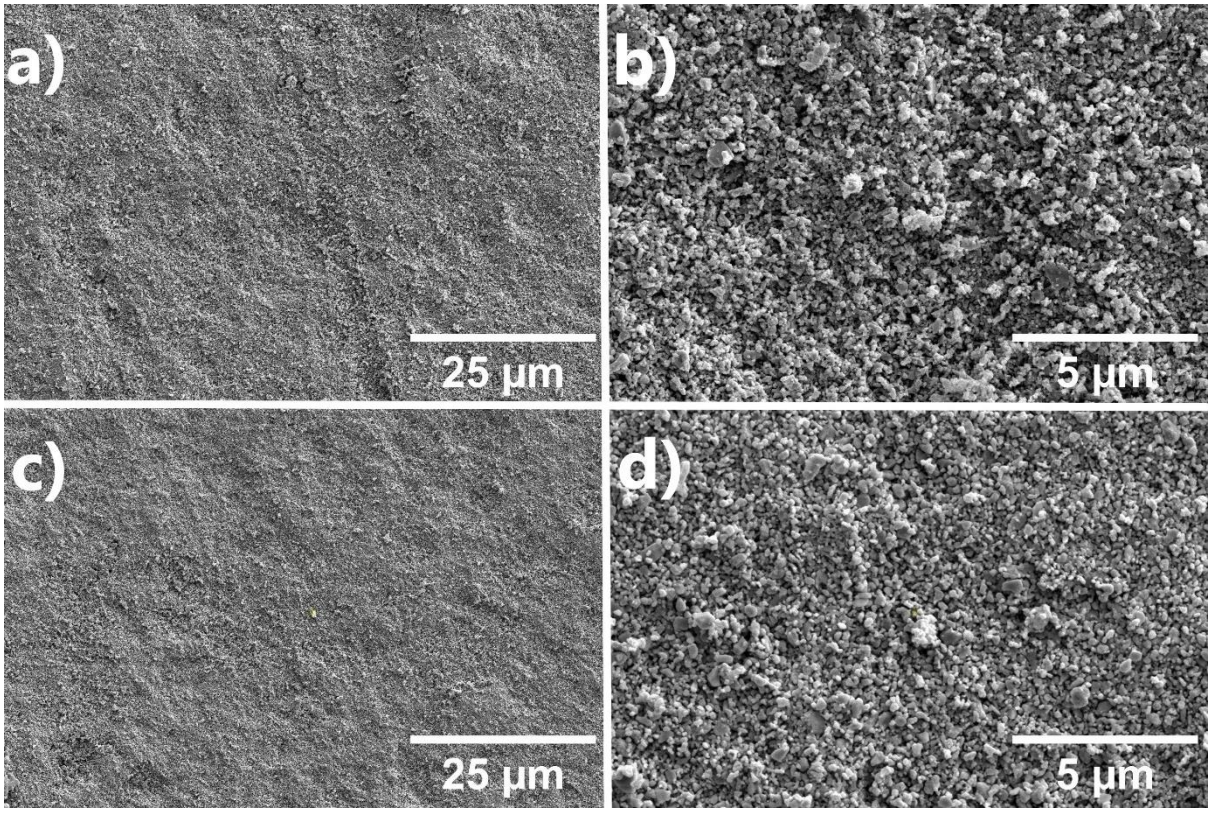

Figure 106. Secondary electron FIB-SEM micrographs of CBN28 granule films deposited at 18.8 L min^{-1} are shown, after annealing for 4 h at 400 ^{o}C, in (a) and (b). A film from the same deposition batch is shown in (c) and (d), after annealing for 4 h each at various temperatures up to 750 ^{o}C. The 25 kx magnification image, (b), shows particles with sharp facets and rough edges, similar to non-annealed CBN28 deposited at 13 L min^{-1} (Figure 97(b)). After annealing at 750 ^{o}C there is some rounding of the particles, but no evidence of grain growth. Micrographs obtained by John Harrington.

Cross-sectional secondary electron micrographs of CBN28 granule films annealed at 400 and 750 °C are shown in Figure 107(a) and (c). The density of the as-deposited 18.8 L min^{-1} films appears higher than the as-deposited CBN28 granule film deposited at 13 L min^{-1} in Figure 98(a). The particles in Figure 107(a) have sharp facets and rough edges, annealing at 400 ^{o}C does not appear to have initiated any significant densification of the film, with no clear signs of necking between the particles. Hence, the improved density of this CBN28 film, over CBN28 deposited at 13 L min^{-1}, is presumed to be due to the higher carrier gas flowrate of 18.8 L min^{-1}. The annealed films, produced in the same deposition-run, show some variation with thicknesses of 8 - 9 µm in Figure 107(a) and of 11 - 12 µm in Figure 107(c). A 3rd film from the same batch was determined to have a thickness of 16 µm by contact profilometry before it was electrically analysed in Figure 103(c) and (d). Further profilometry on this 3rd film, by confocal microscopy in Figure 100(b), showed thickness varying from 14 - 15 µm. Annealing up to 750 ^{o}C appears to have initiated some densification, with necked bonds present between smoother particles. However, these initial stages of densification are not believed to be responsible for the observed variation in film thickness between the as-deposited and the annealed films. Rather, poor control of powder feed rate during the deposition is assumed. A low-density region, in Figure 107(c) near the scale bar, is also presumed to have been produced during deposition, rather than by annealing.

The micrographs in Figures 107(b) and (d) are of the 400 ^{o}C- and up to 750 ^{o}C- annealed films respectively. They were produced in a FIB-SEM by illuminating with the Ga-ion beam and detecting the emitted electrons. The ion beam partially etches the surface producing secondary electrons and backscatter electrons. The resulting images have compositional and (substrate-grain) orientational contrast. A very fine (< 200 nm) substrate-anchor layer region can be seen in Figure 107(b), in which substrate grains are heavily deformed and significantly reduced in size. After increasing the annealing temperature to 750 ^{o}C grain growth of this substrate-anchor layer is apparent, with larger (~1 µm) substrate grains present, see 107(d).

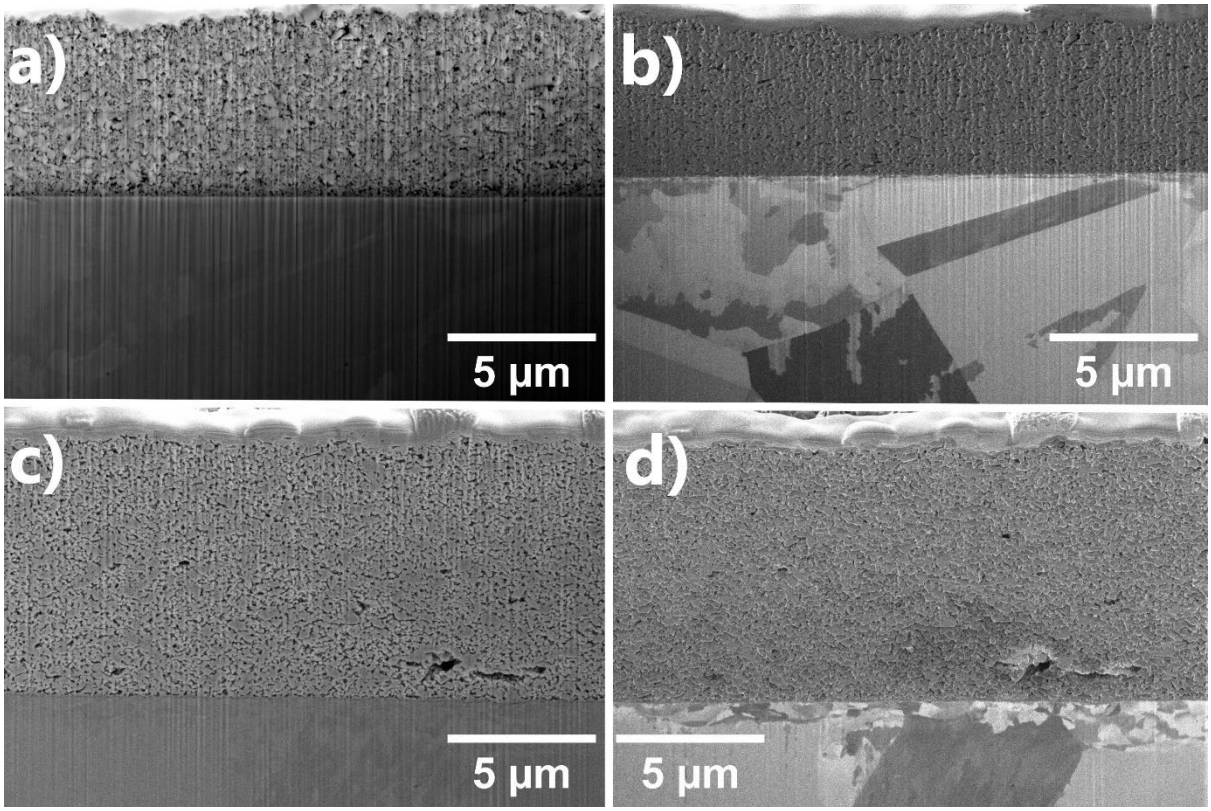

Figure 107. Cross-sectional FIB-SEM SE micrographs of CBN28 films, deposited at 18.8 L min^{-1}, and annealed for 4 h at 400 ^{o}C, in (a). Annealing for 4 h each at various temperatures up to 750 ^{o}C produced the film in (c). The films were produced in the same deposition-run, however their thicknesses vary from 8 - 9 µm in (a) to 11 - 12 µm in (c). Annealing is not believed to have caused this variation. Micrographs of the 400 ^{o}C- and 750 ^{o}C- annealed films were also obtained using SE electrons generated by illumination with the Ga-ion beam, in (b) and (d) respectively. The ion beam etched the surface, producing secondary electrons alongside a backscatter electron component. These micrographs had increased compositional and (substrate-grain) orientation contrast. The secondary electron micrograph of the annealed film in (a) shows incomplete densification, but without the very low-density region seen in the as-deposited 13 L min^{-1} film (Figure 98(a)). In the Ga-ion beam image, (b), a fine (< 200 nm) layer of the substrate shows significant deformation and very fine grains or grains containing defect boundaries. After annealing up to 750 ^{o}C, grain growth in the substrate at the anchor layer is apparent, particularly at the extreme left of image (d). Densification of the CBN28 film due to thermal treatment appears limited, with only some (apparent) rounding and increased necking of the grains in (c), when compared to (a). Micrographs obtained by John Harrington.

8.3.1 XRD analysis of an annealed CBN28 granule film

Figure 108(a) shows XRD patterns of a CBN28 granule film, deposited at 18.8 L min^{-1} and then annealed at 400, 500, 600, 700 and 750 ^{o}C. After annealing at 700 and 750 ^{o}C some tarnishing of the SUS304 stainless steel substrate was observed and annealing experiments were ceased, to prevent oxidation induced delamination of the film prior to permittivity temperature measurements, shown in Figure 110.

Only a minor variation in peak breadth was observed between the as-deposited and annealed films up to 600 ^{o}C film, see Figure 108(b). In powder XRD the broadening of peaks has three main contributions, the instrumental effect (which is assumed constant between the measurements), the crystallite size affect and the microstrain effect. The relative consistency of the peak FWHM suggests only minor variations in crystallite size and microstrain occurred when annealing up to 600 ^{o}C. The measurement for annealing at 500 ^{o}C showed increased peak broadening, which is presumed to have been caused by an instrumental factor, given that the Bruker D8 X-ray diffractometer underwent repairs shortly after the measurement. However, the precise cause of the broadening is unknown. After annealing at 700 and 750 ^{o}C peak FWHM decreased from ~0.26 to 0.24 and 0.18 $^{o}2\theta$. This is presumed to be due to a reduction in microstrain and/or an increase in crystallite size. An attempt to quantify the relative contributions of each of the crystallite-size and microstrain effects, to peak broadening, was made via the production of Williamson-Hall plots. A sample Williamson-Hall plot, for the as-deposited film and after annealing at 700 ^{o}C are shown in Figure 109.

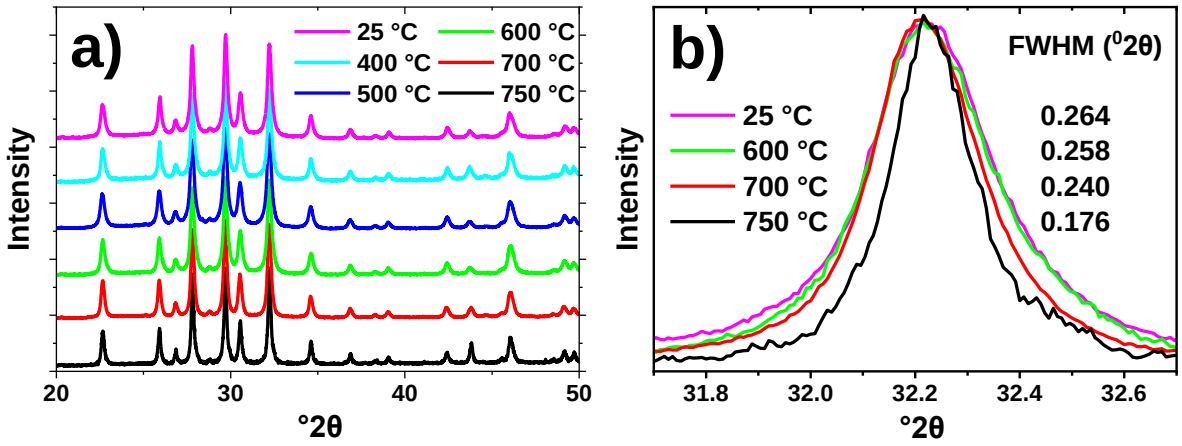

Figure 108. X-ray diffraction patterns of a CBN28 granule film, deposited at 18.8 L min^{-1} and then left at ~25 °C prior to diffraction. All peaks can be ascribed to P4bm structured CBN. Subsequent annealing of the same film for 4 h each at 400, 500, 600, 700 and 750 °C was performed, with XRD performed between each thermal treatment. As shown in (a), no new peaks associated with secondary phases were identified after annealing. Shown in (b), the profile of the peaks did not alter significantly when annealing up to 600 °C. A slight decrease in detected X-ray intensity is observed between the 25 °C and 600 °C around 31.8 - 32.0 °2θ. A further, more distinct, decrease in peak broadness is observed after annealing at 700 °C. This peak is slightly offset when compared with the non-annealed sample, but not significantly skewed. A further reduction in peak breadth was observed after annealing at 750 °C. The noise in the 750 °C-pattern is at least partly present due to the (5x) lower intensity of detected X-rays for this measurement when compared to the 700 °C pattern. Variation in experimental set-up (sample mounting) may be responsible for this.

In the Williamson-Hall plot method the change in peak broadening (B) with increasing °2θ is linearly correlated by plotting Bcosθ on the y-axis against 4sinθ on the x-axis. The gradient of the line then gives microstrain and the y-intercept gives crystallite size [Mote, V. D. 2012]. The trend line required for deduction of the y-intercept was produced by a least squares regression, as shown in Figure 109. The broadening of major peaks between 20 and 50 °2θ was measured for each pattern and a regression optimised line of best fit was produced. If r^2 values were lower than 0.9, data points were removed so as to improve the fit, sometimes resulting in a minimum of 4 data points that were used for the fit, see Figure 109(a). The fitting results are shown in Table 20.

Instrumental broadening was first subtracted prior to construction of the plots, this instrumental broadening was approximated to be 0.085 °2θ by measurement of peak broadening in similarly acquired XRD plots of bulk CBN28 sample of micrometre grain size (as reported in Section 5, Results chapter 1). This fixed contribution to the PAD film broadening (area) was subtracted using FWHM (width) measurements and a formula to relate width to area, (FWHM:measured^2-

FWHM:instrumental$^2)^{0.5}$ [Mote, V. D. 2012]. The bulk CBN28, used as a standard for deducting the instrumental broadening, showed some increase in peak broadening with $^o2\theta$, indicating the presence of microstrain in the sample. The presence of any microstrain, or fine (<200 nm) crystallites, in the bulk may result in an overestimate of the instrumental effect, a downwards translation of the line on the Williams-Hall plot and an overestimate of crystallite sizes in the measured films. However, the set of results from the PAD films should possess some internal consistency.

Up to 700 °C, calculated crystallite sizes varied inconsistently between 105 and 155 nm. This inconsistency could be accounted for by imperfect fitting of the minimum-regression lines. After annealing at 750 °C crystallite size increased to 270 nm. Microstrain estimates decreased consistently with annealing of the as deposited film, from 0.138 to 0.114 %, excluding the value found after annealing at 500 °C (0.184 %).

After annealing at 700 °C, A reduction in peak FWHM from ~0.26 $^o2\theta$ to 0.24 $^o2\theta$ would suggest that some reduction in microstrain and/or increase in crystallite size did occur. After annealing at 750 ^{o}C a more significant decrease in FWHM to ~0.18 $^o2\theta$ coincides with more significant decreases in microstrain and an increase in crystallite size.

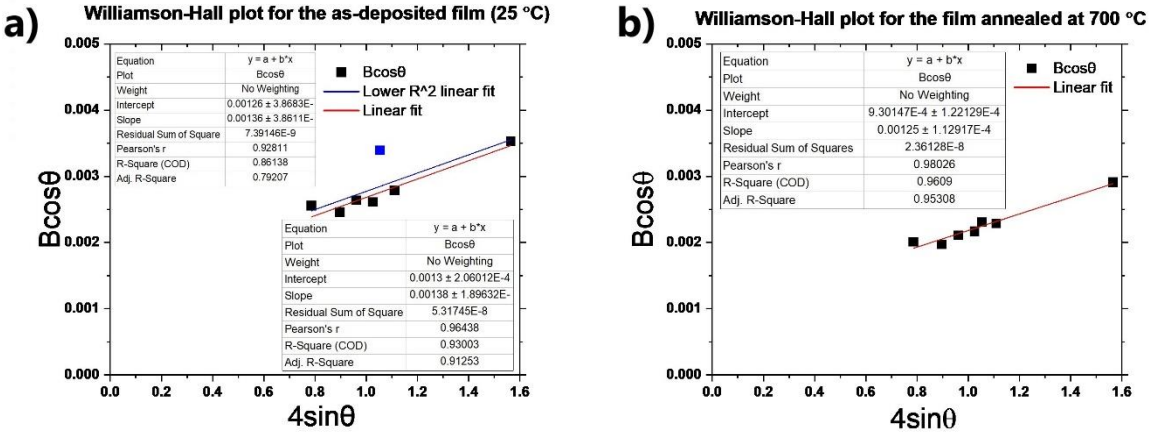

Figure 109. Sample Williamson-Hall plots for a CBN28 film as-deposited at 18.8 L min^{-1}, in (a), and after annealing up to 700 ^{o}C, in (b). In (a), the Willaimson-Hall plot for the as deposited film (25 °C annealed), a datapoint (in blue) had been omitted to improve the linear fit from r^2 = 0.86 to 0.93. The gradient of the plot corresponds to the presence of microstrain XRD peak broadening whilst the extrapolated y-intercept indicates the contribution of average crystallite size to peak broadening. Table 20 contains Williamson-Hall plot derived -microstrain and -crystallite size values for the film after annealing at various temperatures for 4 h.

In Table 20, trends are obscured by the measurements of the film annealed at 500 ^{o}C. The 500 ^{o}C-annealed measurement displayed greater and unexplained peak broadening. Looking at the as-deposited, 400, 600, 700 and 750 ^{o}C-annealed calculations, a trend of decreasing microstrain with annealing, from 0.138 to 0.114 % is observed. This microstrain corresponded to inconsistent evaluations of crystallite size (of 105 - 155 nm), from 25 to 700 ^{o}C, and then an increase in average crystallite size to 270 nm after annealing at 750 ^{o}C. The sensitivity of these calculations to poor data fitting, reduces their validity. However, this suggested reduction in microstrain and increase in crystallite size with annealing is corroborated by the TEM with *in situ* heating observations, in Figures 111 to 113.

Table 20. The average crystallite size (nm) and microstrain (%) of a CBN28 granule film, deposited at 18.8 L min^{-1} and annealed at various temperatures up to 750 ^{o}C. The raw XRD data, used for the annealed at 500 ^{o}C* calculations showed high levels of broadening which are presumed to be due an unknown measuring error, rather than an increase in internal strain up to the value calculated.

Annealing temperature (^{o}C)	regression fit (r^2=)	crystallite size (nm)	microstrain (%)
25	0.93	115	0.138
400	0.96	125	0.136
500*	0.96	150	0.184
600	0.99	105	0.130
700	0.96	155	0.125
750	0.94	270	0.114

After annealing at 750 °C and undergoing XRD the CBN28 granule film, deposited at 18.8 L min^{-1}, was electroded and its permittivity- and tan δ- temperature response was recorded on the dielectric analyser at Leeds. In contrast to the as-deposited film, low temperature ($T < T_m$, where T_m refers to that of the bulk ceramic) tan-δ values were frequency dispersed- increasing with increasing frequency, see Figure 110. A frequency dispersion of low temperature permittivity (decreasing with increasing frequency) also occurred and combined these frequency dispersions are comparable to those of relaxor ferroelectrics [Hou, S. 2022]. Permittivity, measured at 1 kHz and 50 ^{o}C, was also increased from ~60 to ~200 after annealing at 750 ^{o}C. At higher temperatures above 150 ^{o}C, low frequency tan δ values increased, possibly resulting in an increase in low frequency permittivity values at 250 ^{o}C. Beyond 275 ^{o}C errors associated with poor contact with the electrode resulted in noisy data, and may also be responsible for the increase in 10 kHz tan δ values around 250 ^{o}C and the corresponding decrease in higher permittivity values (of 10 kHz and above).

The 50 °C permittivity of the annealed film was lower (~1/2) than that of the bulk. It is not clear to what extent that the lower film-density is responsible for this reduction. The increased temperature stable permittivity relative to the bulk is assumed to occur by microstrain disordering and suppression of the increased dielectric response seen around T_C in normal ferroelectrics. Certainly, there is retention of some microstrain in the film even after annealing at 750 °C (e.g. Table 20).

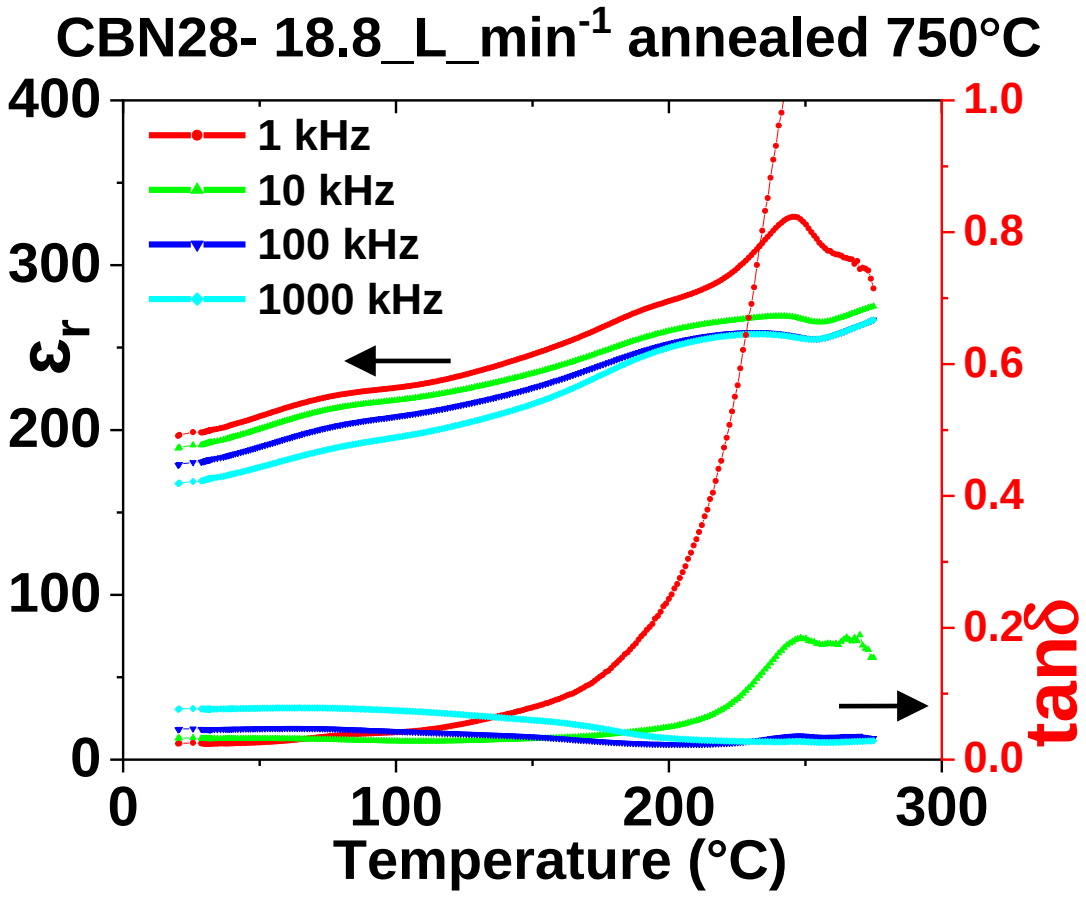

Figure 110. Permittivity- and tan δ- temperature responses for the CBN28 film, deposited at 18.8 L min^{-1}, and annealed for 4 h at various temperatures up to 750 °C. X-ray diffraction patterns for this film, in Figure 108, show reduced peak broadening after annealing at 750 °C. A small decrease in higher frequency (10+ kHz) permittivity values around 250 °C may correspond to poor contact with the electrodes.

To summarise, a CBN28 PAD film was annealed up to 750 °C. Microstrain reduction and crystallite size increase were evidenced by XRD peak broadening-derived Williamson-Hall plots. In comparison to an as-deposited film, in Figure 104(b), the annealed film has ε_r ~3 x higher and shows frequency dispersion but still has lower ε_r and improved temperature stability relative to the original bulk ceramic. This recovery in dielectric properties may indicate an increase in the size of polar units, with annealing, though, presumably to sizes below that present in bulk ceramic CBN28, where frequency dispersion of ε_r is absent or minor.

To further investigate the structural evolution of PAD films during annealing, TEM with *in situ* heating up to 1100 °C was performed on an as-deposited CBN28 PAD film. Micrographs and electron diffraction patterns were obtained.

8.3.2 Annealing of the CBN28 granule film, observed by *in situ* TEM

A TEM micrograph of a thin lamella (prepared by FIB-sectioning) is shown in Figure 111. It was produced from the same CBN28 granule film, deposited at 13 L min^{-1}, that was analysed by FIB-SEM in Figure 102(a). The orientation of the film is flipped such that the substrate is visible at the top of the micrograph (in a < 100 nm strip). During the Ga-ion beam milling that produced the thin lamella the low-density film was damaged. This may be due to the selective milling of the section of the film proximal to the substrate or it may be due to buckling of the unsupported film section due to internal strains. Particle sizes were typically submicrometre but some extended up to 2 µm. Regions, A, B, C, D and E were selected for electron diffraction (ED) and higher magnification imaging.

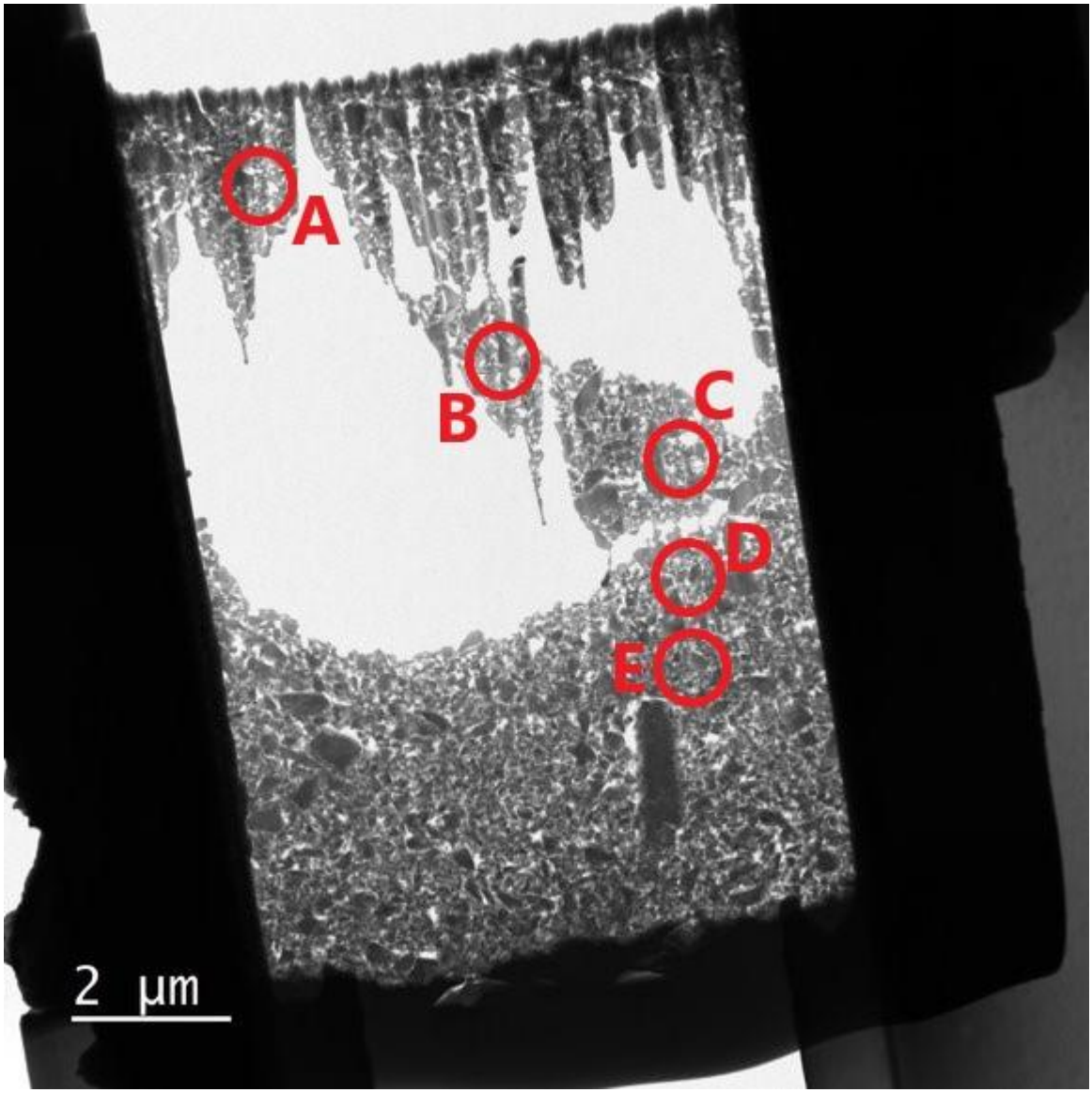

Figure 111. A TEM micrograph of the CBN28 granule film, deposited at 13 L min^{-1}, which was imaged by FIB-SEM in Figure 102(a). The orientation of the film is inversed with reference to Figure 102(a). A small (~0.25 µm) section of the substrate can be seen, in darker contrast, at the top of the film cross-section. Damage to the film occurred during production of the TEM lamella, this damage may have been caused by preferential milling of the deeper section of the film, by the Ga-ion beam. However, this damage may also have been caused by buckling of the film-lamella due to its own internal strain, which is shown in Figure 113 to be higher in the deeper sections of the film. The letters A to E correspond to micrographs and ED patterns in Figures 112, 13 and Appendices 21 and 22. The lamella was produced and mounted onto a dedicated TEM grid with *in situ* heating element by Stuart Micklethwaite. TEM micrographs and diffraction patterns were obtained by Dr. Zabeada Aslam, with the assistance of the author.

The film underwent *in situ* annealing up to 1100 ^{o}C in the vacuum of the TEM. Micrographs and ED patterns of the film at region A were taken prior to annealing, at 1000 ^{o}C and at room temperature after annealing at 1100 ^{o}C, in Figure 112. Corresponding micrographs, taken at 400, 800, 900 and 1100 ^{o}C are shown in the Appendix 21. Prior to annealing, at 25 ^{o}C, the ED pattern shows broad electron diffraction bands which suggest high and disordered strain (microstrains). Also present are diffraction spots which indicate a retention of crystallinity. After heating to 1000 ^{o}C, no significant grain growth was observed. Although, some mass transfer is evidenced by narrowing of some necked bonds, with the breakage of some necks occurring after heating to 1100 ^{o}C, see the bottom-centre of Figure 112 (region A:post 1100 ^{o}C). Despite low grain growth, the breadth of the diffraction bands in the ED patterns decreased indicating relaxation of microstrains.

A larger grain (~250 nm) can be seen in the top left quadrant in the micrographs in Figure 112. This grain has incoherently diffracting regions, suggestive of polycrystallinity. After heating to 1000 and 1100 °C, there is a slight, apparent decrease in polycrystallinity and an increase in crystallite size. See also Appendix 21. Further micrographs were taken at 400, 800, 900 and 1100 °C. These findings correspond well to the XRD data (annealed at 750 ^{o}C), which also suggested a combination of decreased microstrain and increasing crystallite size, with annealing (Table 20). From the data available it is not clear whether initial decreases in microstrain (at and below 600 ^{o}C) occur in the absence of crystallite growth or if crystallite growth is intimately tied to microstrain reduction.

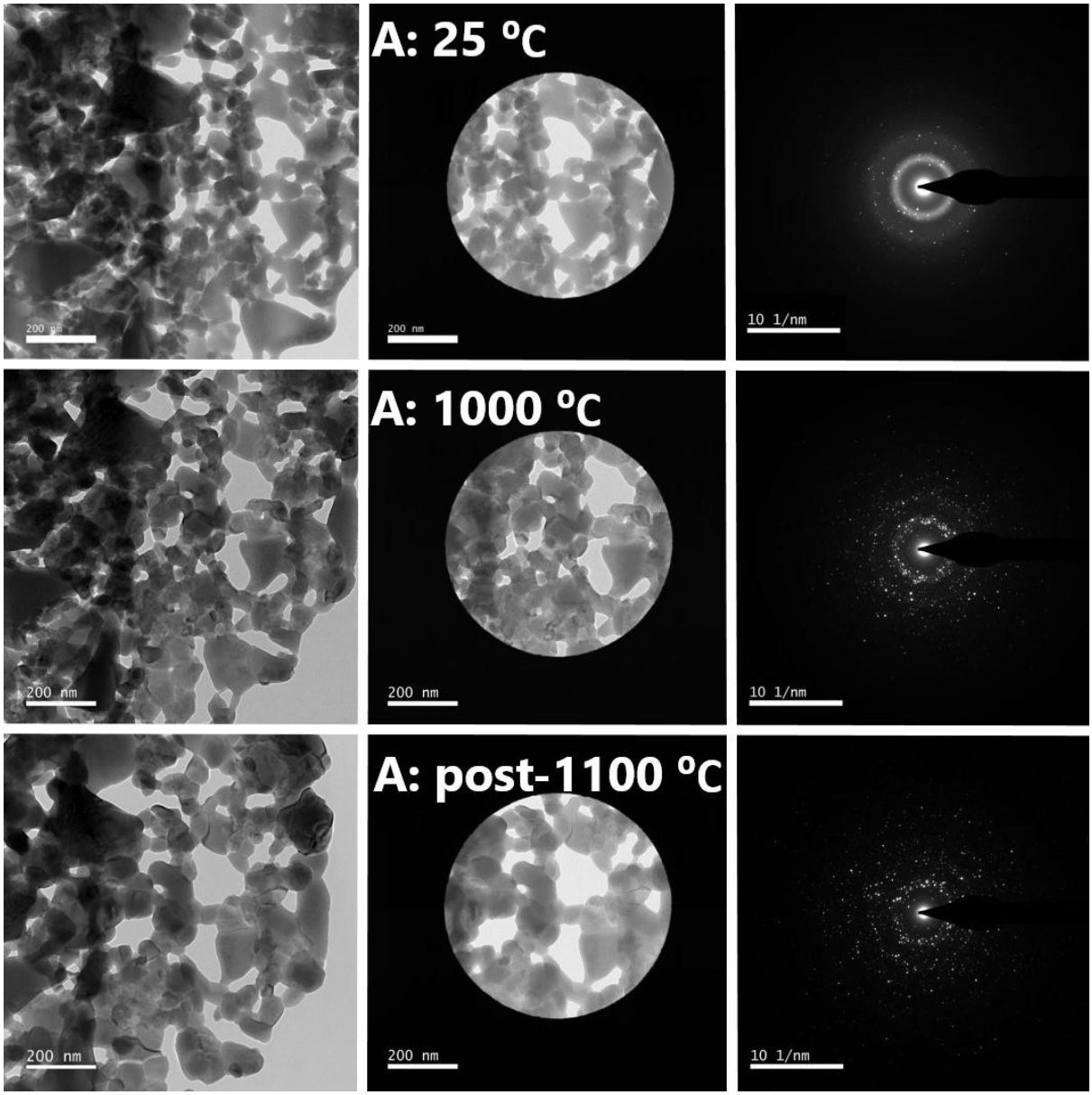

Figure 112. Micrographs and ED patterns correspond to region A in Figure 111. Centrally positioned micrographs show the selected area for the diffraction patterns (to the right). Prior to *in situ* annealing the ED pattern, "A: 25 ^{o}C", shows diffuse diffraction rings or bands indicating some highly strained or amorphous material is present alongside regions of crystalline order (indicated by the diffraction spots). Heating to 1000 ^{o}C reduced the breadth and intensity of the diffraction band and more diffraction spots were visible. These trends continued after heating to 1100 ^{o}C and then returning to room temperature. Heating was near-instantaneous with dwell times between 10 - 20 mins at each temperature. Micrographs were taken after 5 minutes and ED patterns were obtained during the last ~5 minutes of the dwell. Micrographs and diffraction patterns obtained by Dr. Zabeada Aslam, with the assistance of the author.

Electron diffraction patterns for the regions A and E are shown in Figure 113 prior to annealing. The room temperature ED patterns show a greater diffraction band intensity proximal to the substrate (region A), consistent with grains close to the substrate having increased deformation and microstrain. The ED patterns for site's B, C, D and E, prior to annealing and at 1000 °C, are shown in the Appendix 22. They further affirm this microstrain gradient through the film and suggest that it is reduced or removed by annealing. Elsewhere thicker films have been shown to possess greater strain [Kim, H-K. 2015], and here the distribution of that strain is elucidated.

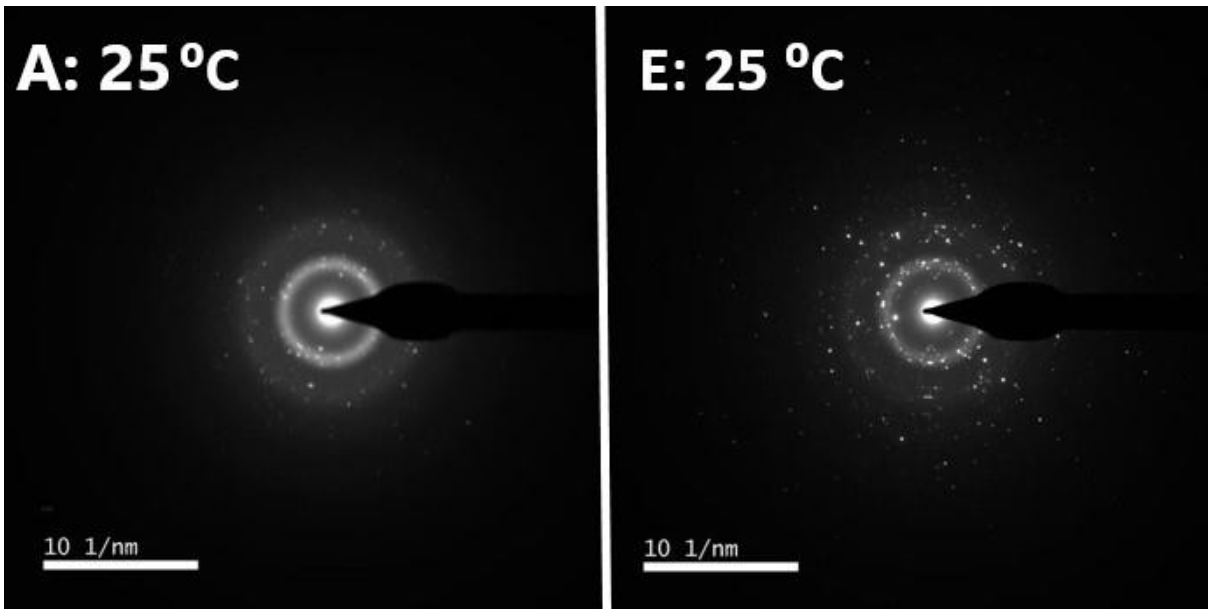

Figure 113. Electron diffraction patterns for regions A and E prior to annealing, showing broader more intense diffraction bands closer to the substrate. The pattern for site A is repeated here from Figure 112. The pattern for region E, along with region's B, C, D and E, can be seen prior to annealing and at 1000 °C in the Appendix 22. Micrographs and diffraction patterns obtained by Dr. Zabeada Aslam, with the assistance of the author.

8.4 Discussion

8.4.1 Powder pre-treatment, pressure dynamics and the formation of anchor layers

Milling and thermal pre-treatment of CBN powders was shown to influence the density of resulting PAD films. Finer, high-energy attrition milled particles, see Figure 94, tended to agglomerate, due to van de Waals forces [Francis, L. F. 2015], in the vibrating bed AGC and produce low-density powder compacts. The dispersion of kinetic energy upon agglomerate impact has been postulated elsewhere as a cause of low-density PAD films in agglomerate rich powders [Nam, S-M. 2004] and [Mihara, K. 2009]. As-calcined, or milled and then thermally pre-treated powders, were judged qualitatively to be less prone to agglomeration in the AGC and tended to produce anchor layers in Leeds. Low energy ball milled powders, whose particle size was greater than that of the high energy attrition milled powders, also produced anchor layers, see Figure 94 (1+ vs 0.5 µm). Assumed agglomerates, of low density, were also shown to be prone to deflection away from the centre region, as inferred from the optical micrograph of the CBN28 granule film, deposited at 13 L min^{-1} (Figure 97(a) and (c)) [Benchaita, M. 1983]. This is likely due to the jet substrate interaction effect deflecting the low-density agglomerates. The importance, therefore, of controlling agglomeration is shown, particularly when operating at higher deposition chamber pressures, i.e. in the system at Leeds, or at conditions which promote the stagnation of the jet above the substrate, i.e., when depositing onto a wide substrate or sample stage which induces a 90^{o} deflection of the jet. It is proposed that the narrowing of the sample stage may reduce jet stagnation and the segregation of agglomerates. Reducing the variation in impact velocities may also be achieved by narrowing of the sample stage, which may prevent the pin-holing defect bands observed in optical micrographs in Figure 97 and 98.

The electrical properties of submicron films produced in Leeds were affected by film conductivity, presumably due to perforation of the film due to higher momentum impacts/pin-holing. A similar affect was seen in 0.2 µm-thick $BaTiO_3$ films [Kim, H-K. 2012]. Modification of the sample stage, or the VC in general, to reduce variations of impact-momentum may allow for resistive submicron films, given that resistive films with 1.5 µm thickness have been demonstrated [Kim, H-K. 2012].

In Leeds, anchor layer formation was achievable at low carrier gas flowrates, nominally at 0 L min^{-1} assisted flow. Here, the initial burst of deposition associated with pressure equalisation between the AGC (1 bar) and the VC (< 20 mbar) caused deposition and some visible deposition persisted across the 40 mm wide deposition zone (i.e. 2 second span). This suggests that the impact forces required for anchor layer formation are well below that of the typical operational flowrates employed in the production of thicker films. The nominal carrier gas flowrates employed at Leeds, 2 to 8 L min^{-1}, may be of reduced comparability to other rigs given that the flow meter employed was calibrated for atmospheric conditions. However, precise comparisons of deposition conditions are generally of low

value between deposition systems due to the bespoke design conditions of each system, i.e. the lack of commercial system as yet. The modelling of jet flow dynamics required is typically absent but would increase the comparability of findings between different deposition systems.

8.4.2 Mechanistic inferences

The mechanisms present during RTIC are obscured or confounded by the fine scales of the particles, the range of particle properties, the jet-substrate interactions and the low (< 1 %) deposition efficiency of the process. Furthermore, the process depends on behaviour not typically associated with bulk ceramics, namely plastic deformation or accumulated slip and “room temperature” bonding. However, some inferences regarding deposition mechanics can be made. This includes the requisite transfer of kinetic energy due to impact into some form of bonding energy, that appears to not occur in the agglomerate impacts noted above.

There is a lower density region, towards the surface of the doped-CBN powder film, in Figure 102(b). The densification of the underlying film is believed to be promoted by the subsequent hammering of further deposition. Hence a surface layer is always in a state of active or incomplete densification [Nam, S-M. 2004], [Lee, D-W. 2011] and [Kim, H-K. 2015]. The increase in strain in material within the film at increasing proximity to the substrate, observed in the ED patterns in Figure 113, suggests that subsequent hammering and film build up increases strain not just at the surface layer of a film. This microstrain gradient may explain the increasing XRD peak broadening with film thickness observed elsewhere [Kim, H-K. 2015]. The strain gradient should be considered when attempting to draw comparisons between dissimilarly thick films, as is often required.

There is limited evidence that the entire film undergoes active densification during film build up- not just the region being directly hammered. The typically finer particle size of the grains in the FIB-SEM cross sections at the anchor layer may be present due to this ongoing increase in strain, particle size reduction and densification (Figure 102). The stainless steel (SUS304) substrate has a lower hardness than CBN28, as such the particle size reduction cannot be explained by the correlation between increasing substrate hardness and particle size reduction [Lee, D-W. 2012]. Furthermore, upon annealing up to 1000 ^{o}C (seen in Figure 112 and Appendix 22), the strain gradient appeared (qualitatively) to be removed or at least severely reduced whilst the film remained well adhered. This implies that higher strain levels at the anchor layer are not essential for the continued adherence of the anchor layer and as such the higher strains and possibly the reduced particle size are the later effects of prolonged hammering. However, it may be that this low efficiency (< 1 %) deposition process is selective and the formation of anchor layers from initially finer particles is promoted. Perhaps this could be due to the greater fraction of a smaller particle that could be

interlocked with the substrate, given the same magnitude of deformation or cratering [Kim, H-K. 2015].

8.4.3 Structural and electrical properties of as-deposited and annealed films

In comparison to the CBN28 bulk ceramic, the PAD CBN 28 film deposited at 18.8 L min^{-1} showed 1 kHz permittivity values that were much reduced (~5x) at 50 ^{o}C, see Figure 104(b). Temperature stability was improved although the films permittivity at 250 ^{o}C (~80) was 30x lower than a typical value for the bulk near T_C (Figure 53(a) in Section 5, Results chapter 1). Polarisation-electric field responses also showed (15x) lower P_{Max} values and less characteristically ferroelectric/lossy forms. This low polarisation response is unsuitable for energy storage or capacitor applications, but polarization may be recovered by annealing [Zhou, F. 2022].

After annealing up to 750 ^{o}C the film showed (~3 x) increased 1 kHz permittivity at 50 ^{o}C (ε_r = ~200), see Figure 110. This permittivity was frequency dispersed, decreasing by ~15 % with increasing frequency from 1 kHz to 100 kHz at low temperatures ($T << T_M$, where T_M refers to the permittivity maxima of the bulk around 250 ^{o}C). Frequency dispersion of low temperature dielectric loss was also observed, increasing with increasing frequency. Together, these frequency dispersions are relaxor-like. It can be said that PAD of CBN28 caused a reduction in ferroelectric character and that subsequent annealing caused a partial recovery of polarisation and the onset of relaxor-like properties.

The microstructural causes of these property transformations are suggested, by XRD and TEM-ED to be due to the modulation of microstrains and crystallite size within the film. Microstrain reduction is evidenced after annealing at 750 ^{o}C in the XRD-derived Williamson-Hall plots, Table 20, and by the TEM micrographs and the 1000 °C ED patterns, in Figure 112. A possible increase in the coherently diffracting region size and an inferred decrease in polycrystallinity of grains is evidenced when comparing the micrographs taken at 25 and 1000 °C in Figure 112. The Williamson-Hall plots also suggest an increase in crystallite size, at least at high temperature (750 °C). The precise temperature dependence and interrelation of microstrain and nano-crystallinity in PAD films requires further investigation, particularly at lower temperatures (< 600 ^{o}C).

8.5 References

Benchaita, M. Griffith, P. Rabinowicz, E. 1983. Erosion of Metallic Plate by Solid Particles Entrained in a Liquid Jet. *J. Eng. Ind*. **105**. 215-222

DOI: https://doi.org/10.1115/1.3185891

Bentzen, M. Maier, J. Eckstein, U. He, J. Henss, A. Khansur, N. Glaum, J. 2023. Enhanced grain growth and dielectric properties in aerosol deposited BaTiO3. *J. Am. Ceram. Soc*. **43**. 4386-4394

DOI: https://doi.org/10.1016/j.jeurceramsoc.2023.03.012

Caballero, A. C. Villegas, M. Fernandez, J. F. 1999. Effect of humidity on the electrical response of porous $BaTiO_3$ ceramics. *J. Mater. Sci. Lett*. **18**. 1297-1299

DOI: https://doi.org/10.1023/A:1006662805186

Denisyuk, A. Hrnčíř, T. Oboňa, J. V. Sharang. Petrenec, M. Michalička, J. 2017. Mitigating Curtaining Artifacts During Ga FIB TEM Lamella Preparation of a 14 nm FinFET Device. *Microsc. Microanal.* **23**. 484-490

DOI: https://doi.org/10.1017/S1431927617000241

Francis, L. F. Sadler, B. J. H. Roberts, C. C. 2015. Materials Processing: A Unified Approach to Processing of Metals, Ceramics and Polymers. *Academic Press*. 58

DOI: https://doi.org/10.1016/C2009-0-64287-2

Glass, A. M. 1969. Investigation of the electrical properties of $Sr_{1-X}Ba_xNb_2O_6$ with special reference to pyroelectric detection. *J. Appl. Phys*. **40**. 4699-4713

DOI: https://doi.org/10.1063/1.1657277

Han, X. Wei, L. Yang, Z. Zhang, T. 2013. Phase formation, dielectric and ferroelectric properties of $Ca_xBa_{1-x}Nb_2O_6$ ceramics. *Ceram. Int.* **29**. 2853-2860

DOI: https://doi.org/10.1016/j.ceramint.2012.11.078

Hou, S. Xu, S. Yang, L. Liu, X. Wei, L. Chao, X. Wu, D. Liang, P. Yang, Z. 2022. High energy storage performance of $Ca_{0.15}(Sr_{0.6}Ba_{0.4})_{0.85}Nb_{2-x}Ta_xO_6$ relaxor ferroelectric ceramics. *Ceram. Int*. **48**. 28382-28390

DOI: https://doi.org/10.1016/j.ceramint.2022.06.148

Khansur, N. H. Eckstein, U. Benker, L. Deisinger, U. Merle, B. Webber, K. G. 2018. Room temperature deposition of functional ceramic films on low-cost metal substrate. *Ceram. Int*. **44**. 16295-16301

DOI: https://doi.org/10.1016/j.ceramint.2018.06.027

Kim H-K, Oh J-M, Kim S, Kim H-J, Lee -W, Nam S-M. 2012. Relation between electrical properties of aerosol-deposited BaTiO3 thin films and their mechanical hardness measured by nano-indentation. *Nano. Res. Lett*. **22**. 264.

DOI: https://doi.org/10.1186/1556-276X-7-264

Kim, H-K. Lee, S-H. Lee, S-G. Lee, Y-H. 2015. Densification mechanism of BaTiO3 films on Cu substrates fabricated by aerosol deposition. *Electron. Mater. Lett*. **11**. 388–397

DOI: https://doi.org/10.1007/s13391-015-4419-0

Kudo, Y. Yasuda, M. Matsusaka, S. 2020. Effect of particle size distribution on flowability of granulated lactose. *Adv. Powder Tech*. **31**. 121-127

DOI: https://doi.org/10.1016/j.apt.2019.10.004

Lee, D-W. Kim, H-J. Kim, Y-H. Jeon, M-S. Nam, S-M. 2012. Substrate hardness dependency on properties of Al2O3 thick films grown by aerosol deposition. *Surf. Coat. Technol*. **209**. 160-168

DOI: https://doi.org/10.1016/j.surfcoat.2012.08.012

Lee, D-W. Kim, H-J. Kim, Y-H. Yon, Y-H. Nam, S-M. 2011. Growth Process of α-Al2O3 Ceramic Films on Metal Substrates Fabricated at Room Temperature by Aerosol Deposition. *J. Am. Ceram. Soc*. **94**. 3131-3138

DOI: https://doi.org/10.1111/j.1551-2916.2011.04493.x

Li, K. Zhu, X. L. Liu, X. Q. Ma, X. Fu M. S. Kroupa, J. Kamba, S. Cheng, X. M. 2018. Electric-field-induced phase transition and pinched P–E hysteresis loops in Pb-free ferroelectrics with a tungsten bronze structure. *NPG Asia Mater*. **10**. 71-81

DOI: https://doi.org/10.1038/s41427-018-0013-x

Mihara, K. Hoshina, T. Takeda, H., Tsurumi, T. 2009. Controlling factors of film-thickness in improved aerosol deposition method. *J. Ceram. Soc. Jpn*. 117. 868-872

DOI: https://doi.org/10.2109/jcersj2.117.868

Mote, V. D. Purushotham, Y. Dole, B. N. 2012. Williamson-Hall analysis in estimation of lattice strain in nanometer-sized ZnO particles. *J. Theor. Appl. Phys*. **6**. 6

DOI: https://doi.org/10.1186/2251-7235-6-6

Nam, S-M. Mori, N. Kakemoto, H. Wada, S. Akedo, J. Tsurumi, T. 2004. Alumina Thick Films as Integral Substrates Using Aerosol Deposition Method. *Jpn. J. Appl. Phys.* **43**. 5414

DOI: https://doi.org/10.1143/JJAP.43.5414

Santomaso, A. Lazzaro, P. Canu, P. 2003. Powder flowability and density ratios: the impact of granules packing. *Chem. Eng. Sci*. 58. 2857-2874

DOI: https://doi.org/10.1016/S0009-2509(03)00137-4

Qi, H. Hu, T. Deng, S. Liu, H. Fu, Z. Chen, J. 2023. Giant dynamic electromechanical response via field driven pseudo-ergodicity in nonergodic relaxors. *Nat. Commun.* **14**. 2414

DOI: https://doi.org/10.1038/s41467-023-38006-6

Wollschläger, N. Palasse, L. Häusler, I. Dirscherl, K. Oswald, F. Narbey, S. Ortel, E. Hodoroaba, V-D. 2017. Characterization of the inner structure of porous TiO2 nanoparticle films in dye sensitive solar cells (DSSC) by focused ion beam (FIB) tomography and transmission Kikuchi diffraction (TKD) in the scanning electron microscope (SEM). *Mater. Charact.* 131. 39-48

DOI: https://doi.org/10.1016/j.matchar.2017.06.030

Xie, B. Li, Y. Pan, J. Hall, D. A. 2024. Process optimisation of alumina coatings by modification of powder characteristics in the aerosol deposition method. *J. Eu. Ceram. Soc*. **44**. 3147-3157

DOI: https://doi.org/10.1016/j.jeurceramsoc.2023.12.085

Zhuo, F. Eckstein, U. R. Khansur, N. H. Dietz, C. Urushihara, D. Asaka, T. Kakimoto, K-I. Webber, K. G. Fang, X. Rödel. J. 2022. Temperature-induced changes of the electrical and mechanical properties of aerosol-deposited BaTiO3 thick films for energy storage applications. *J. Am. Ceram. Soc.* **105**. 4108-4121

DOI: https://doi.org/10.1111/jace.18377

9. Outcomes, future work, and conclusions

In this PhD project the tungsten bronze (TB) structured calcium barium niobate (CBN) was selected for chemical and structural modification, with the ambition of producing next generation high-temperature dielectrics with temperature stable permittivity from -55 to 300+ °C, for power electronics applications. The high T_C (~250 °C) of $Ca_{0.28}Ba_{0.72}Nb_2O_6$ (CBN28) and the structural complexity of the TBs held promise for achieving high and temperature stable permittivity in chemically modified (doped) CBN.

CBN28, and doped CBN, were found to possess elevated dielectric losses above 250 °C, due to ionic conductivity, which may be associated with oxygen vacancies. Modifying CBN28 with Y improved the temperature stability of permittivity whilst Y and Ta co-doping induced strong frequency dependence of permittivity and narrow polarisation-electric field loops, suggesting potential for energy-storage applications.

Particle aerosol deposition (PAD) of CBN28, using a deposition system at Manchester, produced a thick film with high levels of microstrain (0.1 - 0.2 %), suppressed polarisation and permittivity responses, and improved temperature stability of permittivity. Annealing of this film to 750 °C, caused a partial reduction in microstrain and a recovery of permittivity, whilst retaining the improved temperature stability of permittivity. Frequency dependence of permittivity was again observed in this annealed CBN28 film.

9.1 Objectives and outcomes

Objectives 1 and 2:

- Manufacture calcium barium niobate (CBN) powders of controlled composition and physical properties using conventional techniques, such as mixed oxide sintering.
- Understand the role of chemical modification on the microstructure and dielectric properties of the bulk ceramic.

Outcomes:

- CBN28 was shown to have irregular grain growth and exhibited ionic conductivity above 250 °C, most likely due to oxygen vacancies. A site donor doping, with Y, was performed. The Y is assumed to have preferentially substituted on the (Ca) A1 site and induced additional A site vacancies. This doping stabilised grain growth, though grain size distribution remained wide, and did not alleviate losses due to ionic conductivity.

A-site doping of CBN28, with Y, stabilised grain growth, most likely due to substitute-ion pinning of the grain boundaries [Cao, H. 2006]. Control of grain growth is important as it is linked to ferroelectric domain size [Kitel, C. 1946] and increased permittivity, as has been shown in $BaTiO_3$ [Jiang, B. 2019]. Evidence of fine domain-size dependant increases in permittivity in CBN28 are also shown in this thesis by the correlation between low temperature ($T < T_M$) high-frequency (1000 kHz) dielectric losses and permittivity maxima (at T_M), with the increased losses being associated with the hysteresis loss of small and mobile domains [Xu, R. 2014].

The presence of variable low-frequency (1 kHz) high temperature (250+ ^oC) losses, sometimes associated with frequency dependence of the magnitude of 1 kHz permittivity maxima, were highly suggestive of ionic conductivity, most likely due to oxygen vacancies. The presence of oxygen vacancies in Nb containing perovskites and tungsten bronzes, promoted by the reduction of Nb^{5+} to Nb^{4+}, has been noted elsewhere [Ofoegbuna, T. 2019]. A site donor doping, with Y^{3+}, and A- and B-site doping, with Y^{3+} and Ta^{5+}, did not alleviate these losses. Future work, doping CBN with variable valency ions such as $Mn^{(2\ to\ 4+)}$ could allow for a reduction in the density and migration of oxygen vacancies, as has been shown with $BiFeO_3$ [Wu, J. 2011].

- The modification of CBN28 with Y reduced T_M and increased the temperature stability of permittivity whilst P-E hysteresis loops narrowed slightly but remained characteristically ferroelectric. Further doping with a combination of Y and Ta induced significant frequency dependence of permittivity and narrow, though non-linear, P-E loops.

Donor doping of CBN28 has consistently reduced $T_{C/M}$ [Niemer, A. 2012] and [Wei, L. 2014-May]. Doping, by substituting equal levels of Ca and Ba for Y, at higher levels than previously performed, in the formulation $(Ca_{0.28}Ba_{0.72})_{0.94}Y_{0.04}Nb_2O_6$, achieved greater temperature stability of permittivity, although frequency dependence of permittivity was limited at this composition, which was the single-phase limit [Peirson, H. 2023]. A more recent report of doping of CBN28, substituting solely the Ca by a variety of ions of broadly comparable ionic radii, retained a single-phase to higher dopant levels, in the formulation $Ca_{0.16}R_{0.08}Ba_{0.72}Nb_2O_6$, where R = Bi, Pr, Nd, Sm [Cao, L. 2024]. These CBN-based samples possessed significant frequency dependence of permittivity and very narrow P-E loops, with potential for energy storage applications. Despite high dopant levels, the temperature stability of permittivity in these samples was less than in $(Ca_{0.28}Ba_{0.72})_{0.94}Y_{0.04}Nb_2O_6$. The greater temperature stability achieved when substituting Ca and Ba for Y may be due to chemical disordering and vacancy addition occurring across both the A1 and A2 sites. This may have allowed for a broader range of local chemical environments (greater disorder) and a more diffuse permittivity peak around T_M [Trubelja, M. P. 1996]. Doping with Y

and Ta reduced T_M, only slightly improved the temperature stability of permittivity, and induced strong frequency dependence of permittivity in the formulation $(Ca_{0.28}Ba_{0.72})_{0.94}Y_{0.04}Nb_{1.8}Ta_{0.2}O_6$. The similar charge (5+) and ionic radii (0.64 Å) of the Ta and Nb ions may have limited the variations in local chemical environment and so limited permittivity peak broadening around T_M. Frequency dependence of permittivity is associated with the disruption of long-range polar order and doping at high total levels, (Y) 0.04 + (Ta) 0.20 = 0.24, may have aided with this disordering [Li, F. 2018]. Elsewhere in CSBN, the outer shell electron structure of Ta^{5+}, which lacks a lone pair of electrons, has been cited as a possible cause of decreased long-range polar order [Hou, S. 2022]. With the Ta ion being assumed to be less prone to ferroelectric polarisation, i.e. exhibiting weaker polarisation along the *c*-axis, and so disruptive of long polar chains [Hou, S. 2022].

A combination of reduced and frequency dependant T_M with narrow P-E loops holds promise for energy storage application, in CBN with Y and Ta addition. Whilst assumed disordering of both the A1 and A2 sites and also the B sites has occurred, ions more dissimilar to Nb than Ta may be required for temperature stable permittivity over very wide temperature ranges. To achieve stability to higher temperatures, i.e. -55 to 250+ °C, a reduction in the Ca:Ba ratio may be required, as is demonstrated in the formulation $(Ca_{0.22}Ba_{0.78})_{0.94}Y_{0.04}Nb_{1.8}Ta_{0.2}O_6$.

Objectives 3 and 4:

- Commission a particle aerosol deposition (PAD) system in Leeds.
- Understand how aerosol deposition process variables can be controlled to deposit high quality CBN dielectric films.

Outcomes:

- A PAD system was commissioned at Leeds, it produced anchor layer films of up to 3 µm thickness. Deposited CBN28 films possessed high levels of deformation and suppressed polarisation responses. The control of carrier gas flowrate to below 8 L min^{-1} reduced the presence of pinhole defects. Powder processing, with a combination of high energy milling, thermal pretreatment and granulation was conducive to the deposition of thick (5 - 20 µm) films, using the Manchester PAD system.

A systematic study into the effect of varying PAD operating conditions on film thickness and density was not achieved. This was due to the limited control of vacuum chamber pressure during operation and the sole production of films with micrometre-scaled thicknesses at Leeds. These anchor layer films required cross-sectional electron microscopy to fully characterise them. However, operating at

higher flowrates (> 4 L min^{-1}) was linked to the presence of pin-hole defects. This was presumably due to higher momentum impacts which are erosive, according to the theory of room temperature impact consolidation (RTIC) [Akedo, J. 2008].

The high energy milling of PAD input powders reduced particle size and size distribution and appeared to increase the propensity for powder agglomeration in the aerosol generation chamber, under the influence of a vibrating bed. Thermal pretreatment at 1000 °C, ~350 °C below the sinter temperature for CBN28, induced some aggregation in high energy milled powders. When deposited using the Manchester PAD system, which is equipped with a brush aerosol generator, high energy milled and granulated powders produced thick films (5 - 20 μm). These films were not satisfactorily densified (ρ < 95 %), but ongoing work has subsequently produced higher density films (99+ %) of CBN28 at Manchester. These films would be suitable for the planned reproduction of the electrical characterisation and annealing experiments that are reported in this thesis (Section 8), as well as for further study.

Objectives 5 and 6:

- Investigate structure-property relations in the PAD films.
- Manufacture films exhibiting stable relative permittivity (ε_r > 500 ±15 %) from -55 to 300 ^{o}C.

Outcomes:

- The presence of high levels of microstrain and/or reduced crystallite size, in as-deposited PAD films, was identified by XRD peak broadening analysis. Williamson-Hall fitting suggested that annealing above 700 °C significantly reduced microstrain and regrew crystallites. In comparison to the bulk, PAD films exhibited supressed permittivity that was relatively temperature stable. An annealed PAD film showed a partial recovery of permittivity and the induction of frequency dependence of permittivity, with the retention of some temperature stability.

The presence of (micro)strain in PAD films has been noted elsewhere, with microstrain levels increasing with film thickness [Kim, H-K. 2015]. In this thesis, the distribution of that microstrain was elucidated by electron diffraction, with microstrain being higher when closer to the substrate. A combination of high strain (> 0.11 %) and fine crystallite size (< 200 nm) was indicated by XRD peak broadening analysis. Elsewhere, as deposited PAD films have shown XRD peak broadening due to microstrain and/or crystallite size reduction alongside supressed polarisation response and permittivity [Khansur, N. H. 2018] and [Zhou, F. 2022]. Annealing a

PAD CBN28 film above 700 °C reduced microstrain and regrew crystallites, as judged by a reduction in XRD peak broadening and electron diffraction polycrystalline band intensity. In HAADF STEM micrographs of an annealed CBN28 film, apparent increases in the length-scales of coherently diffracting regions also corroborated with an increase in crystallite size by XRD. These structural changes coincided with a partial recovery of room temperature permittivity (ε_r = ~200) and a retention of some improved temperature stability of permittivity (in comparison to the bulk). This improved temperature stability and the induction of frequency dependence of permittivity suggested that some microstrain disordering of local environments and disruption to the length-scales of polar units was retained in the CBN28 PAD film after annealing at 750 °C.

The low density (ρ < 95 %) CBN28 film did not achieve the desired metric of ε_r = 500 ±15 % from -55 to 300 °C, its permittivity stability was ε_r = ~225 ±15 % from ~20 to ~240 °C. Further experiments on fully dense (99+ %) films with a variety of annealing conditions may help raise the median ε_r value of CBN28 PAD films towards 500. Doped-CBN films hold promise for achieving temperature stability down to -55 °C, although experimentation is required to confirm this. To expand the temperature range of stable permittivity, i.e. from -55 to 300+ °C, the annealing of doped-CBN films will be required. The composite deposition of CBN and similarly structured SBN, could also be trialled. Partial thermal synthesis during annealing, or (mechanical) milling/deposition induced intimate mixing, may produce a CSBN film with a range of local Ca:Sr(:Ba) ratios, which may also extend the range of temperature stable permittivity in a PAD film.

9.2 Future work

The results of this PhD project have prompted a desire for further enquiry into CBN and PAD. The following experimentation would serve to expand on the existing work.

9.2.1 Mitigation of ionic conductivity in CBN28 by Mn modification

The doping of CBN28 with a variable valency ion, such as $Mn^{(2\ to\ 4+)}$, may reduce the observed high-temperature losses. A nominal composition of $Ca_{0.26}Mn_{0.02}Ba_{0.72}Nb_2O_6$ could be trialled. Here the direct A1 site substitution of Ca^{2+} for $Mn^{(2+)}$ is likely appropriate in terms of ionic radii and charge, with radii, at CN8, being 1.12 and 0.96 Å, respectively. Oxidation of the transition metal Mn could then mitigate oxygen vacancy formation that may exist due to Nb^{5+} reduction to Nb^{4+}. Wu, J. *et al* [2011] successfully supressed oxygen vacancy presence in $BiFeO_3$ by Mn modification ($BiFe_{0.95}Mn_{0.05}O_3$).

Permittivity- and tan δ- temperature measurements from room temperature to 400 °C would be sufficient to assess the effect of Mn inclusion on high-temperature losses. The analysis of Impendence spectroscopy is more time intensive, but following positive tan δ- temperature results, it would give a better appreciation of losses in terms of the real and imaginary parts of impedance.

The variable valency and ionic radii of the Mn ion may (at higher valency's) promote Mn inclusion on the B sites or the (typically vacant) C site. Investigation of the octahedral cage distortion present in $Ca_{0.26}Mn_{0.02}Ba_{0.72}Nb_2O_6$ by Raman spectroscopy, or average site occupancy by XRD, could assess this hypothesis. However, the low concentration levels of Mn may obscure bond and average site investigations. If ionic conductivity is only partially supressed, then higher Mn concentrations could be trialled, such as $Ca_{0.24}Mn_{0.04}Ba_{0.72}Nb_2O_6$.

9.2.2 Improved temperature stability of permittivity by dissimilar-B site modification of CBN28

In this thesis the modification of CBN28 with Y and Ta did not significantly improve the temperature stability of permittivity over the solely Y doped samples. It is suggested that the comparability of the Ta ion to the Nb ion, in terms of charge and ionic radii, may not be conducive to chemical disordering of the TB sites and improved temperature stability of permittivity.

Aliovalent B site doping, for example with Ti^{4+}, is hypothesised to produce a more disordered local chemical environment. To ensure charge balancing, an equal concentration of Y^{3+} could be substituted for Ca and Ba in the formulation $(Ca_{0.28}Ba_{0.72})_{1-w}Y_wNb_{2-w}Ti_wO_6$, w = 0.08. Recent work has produced single phase samples with A site doping at this level (w = 0.08) [Cao, L. 2024].

The presence of vacancies on the A sites is believed to promote chemical disorder and improve temperature stability of permittivity, whilst also reducing $T_{C/M.}$ In comparison to the Y doped CBN28 in this thesis, the proposed Y and Ti doped CBN would have a lower vacancy concentration. Hence,

to increase vacancy concentration, doping with a higher valency ion such as Ce^{4+} may be preferable, in the formulation $(Ca_{0.28}Ba_{0.72})_{1-3w/2}Ce_wNb_{2-w}Ti_wO_6$, w = 0.08.

For these samples phase and microstructural analysis by XRD, SEM and SEM-EDX would be required prior to permittivity- and tan δ- temperature analysis. In the work of Cao, L. *et al* [2024], strong frequency dependence of permittivity was induced when doping at high levels (w = 0.08). If it was likewise observed in these samples then they may be more appropriately employed as (temperature stable) energy storage devices. Further substitution of Nb for Ta (i.e., at r = 0.12 in the formulation $(Ca_{0.28}Ba_{0.72})_{1-3w/2}Ce_wNb_{2-w-r}Ti_wTa_rO_6$, w = 0.08) could then be employed to reduce T_M to below the desired operational temperature, which would reduce the operational losses associated with submicron domains at $T < T_M$ in relaxor materials. For temperature-stable high-temperature applications, modification of the Ca:Ba ratio in Y or Ce and Ti doped CBN could increase T_M (by reducing Ca content i.e. in the formulation $(Ca_{0.22}Ba_{0.78})_{1-3w/2}Ce_wNb_{2-w}Ti_wO_6$, w = 0.08), if required.

9.2.3 Evolution of microstrain, crystallite size, ferroelectric recovery and relaxor onset in high density, annealed CBN28 and doped CBN PAD films

In this thesis the suppression of polarisation response and permittivity in a low-density (< ~95 %) CBN28 PAD film was shown and related to the presence of microstrain and fine crystallite size. Annealing of the film up to 750 °C partially recovered permittivity, which was frequency dependent with accompanying relaxor-like dielectric losses. An as-deposited doped-CBN film was also characterised and shown to have greater levels of permittivity suppression, in comparison to the bulk material. The characterisation protocol for the annealed film was broadly successful in relating dielectric and structural properties but could be refined to give a better appreciation of the evolution of these properties, particularly at low temperatures (< 600 °C).

Low-density (< 95 %) bulk ferroelectric samples can have reduced ε_r and sometimes increased permittivity-temperature stability. Hence, a repetition of the dielectric measurements on fully dense (99+ %) PAD films would give a more apt comparison of the dielectric properties to high-density bulk ceramics. On going work has achieved fully dense (99+ %) PAD CBN28 films using the Manchester deposition system, in part by increasing the efficacy of granulation in calcined and high-energy planetary-milled CBN28 powders (personal communications with Dr. Yizhe Li, of the University of Manchester).

Annealing of the doped-CBN PAD film, as-presented in this thesis or reproduced with higher density, would further assess the ability of annealing to recover permittivity. Permittivity- and tan δ- temperature analysis after annealing at a variety of temperatures (or with *in situ* annealing/dwelling) would give insight into the evolution of dielectric properties and could be paired with XRD peak

broadening analysis at annealing-temperatures intervals of 50 or 100 °C. For greater comparability, hot-stage XRD, following the same temperature profile as the dielectrically analysed sample, could be performed. Here, scanning over a narrow range of °2θ values (i.e. 28 to 33 °2θ, to capture the CBN (410) peak) for 1 h, may be appropriate so as to give a sufficiently low XRD-step size and high exposure time. TEM, with *in situ* heating, of a fully dense sample may reveal different mass transfer properties in comparison to the low density (and damaged) lamella presented in this thesis. Electron diffraction patterns at lower temperatures (< 600 °C) would further elucidate microstrain and possibly crystallite size evolution.

9.2.4 Modified CBN and CBN-SBN/CSBN annealed PAD films

In this thesis a doped-CBN PAD film showed increased permittivity suppression and temperature stability (in terms of absolute ε_r), when comparing it and CBN28 to their respective bulk ceramics. The use of mixed/composite powders was not assessed but could also result in improved temperature stability of permittivity in comparison to the CBN28 PAD film. The electrical defect properties of mixed-phase films may be complex to study and potentially disadvantageous given that dielectric breakdown tends to occur at the weakest point (and so dielectric breakdown strength is sometimes increased in single-phase compositions which may lack compositional interfaces). As such, powder mixtures of binary solid solutions that can form into a tertiary solid solution such as CBN and SBN may be preferential.

The isostructural compositions CBN28 and SBN61 ($Sr_{0.61}Ba_{0.39}Nb_2O_6$) could be co-deposited. The permittivity peaks associated with the respective $T_{C/M}$ values of ~250 and ~80 °C for CBN28 and SBN61, would, with sufficient microstrain induced permittivity-broadening, extend the range of temperature stable permittivity. Other CBN and SBN compositions (Ca:Ba and Sr:Ba ratios) could be trialled to tailor temperature stability of permittivity (ε_r ±15 %) and stability temperature range. Co-milling of CBN and SBN, during the synthesis of granulated powders with a submicron primary particle size, may facilitate some mechanochemical synthesis of CSBN. Partial CSBN synthesis, during milling, deposition, thermal pretreatment, or PAD film annealing may promote micron-scaled variations in Ca:Sr:Ba ratio within a parent TB phase, which, if stable at operational temperatures, could improve temperature stability of permittivity.

Initial structural and dielectric characterisation of a PAD film produced from a co-granulated powder composite (50:50 ratio of CBN28 and SBN61, calcined separately and high-energy milled and granulated as a mixture), would allow comparison to CBN28 and doped CBN PAD films whilst also serving as a control experiment for the refinement of CBN-SBN co-deposition.

The propensity for mechanical alloying or mechanochemical CSBN synthesis, due to extended high-energy milling could be assessed by comparing dielectric properties of milled and deposited powders. The influence of thermal pretreatments and annealing on CBN28:SBN61 PAD films' dielectric properties could also be explored.

The initial permittivity-temperature profile of the CBN28:SBN61 co-deposited PAD film would inform subsequent compositional variations. To improve the temperature range of stable permittivity, lower Ca-content CBN (higher T_C) and higher Sr content SBN (lower T_M) could be co-deposited, i.e. in a 50:50 ratio of the formulations CBN20 and SBN70. To tailor the permittivity stability in terms of % variation of permittivity (i.e. to ±15 %), the relative proportion of CBN:SBN could be modified, presumably by increasing the CBN content (i.e. to a 60:40 ratio), given that the ε_r-maxima of the SBN61 bulk ceramic is higher (and presuming that microstrain induced permittivity suppression would be comparable for both).

9.3 Conclusions

Next generation high-temperature dielectrics require high and temperature stable permittivity over very wide temperature ranges (ε_r > 500 ±15 % from -55 to 300+ °C). Low dielectric losses are also desirable (tan δ < 0.02).

Elevated dielectric losses (sometimes with tan δ > 0.2) due to ionic conductivity were observed in CBN28 and chemically modified CBN at higher temperatures (> 250 °C), though these losses, if associated with oxygen vacancies, may be addressable by Mn doping.

Chemical modification of CBN, with Y in the formulation $(Ca_{0.28}Ba_{0.72})_{1-3w/2}Y_wNb_2O_6$ [$0 \leq w \leq 0.20$] and Y and Ta in the formulation $(Ca_{0.28}Ba_{0.72})_{1-3w/2}Y_wNb_{1.8}Ta_{0.2}O_6$ [w = 0.02 and 0.04], did not achieve temperature stable permittivity to the desired metrics. Although, relatively high and temperature stable permittivity was achieved in the single-phase compositions $(Ca_{0.28}Ba_{0.72})_{0.94}Y_{0.04}Nb_2O_6$ (ε_r = 1143 ±15 % from 71 to 210 ^oC) and $(Ca_{0.22}Ba_{0.78})_{0.94}Y_{0.04}Nb_{1.8}Ta_{0.2}O_6$, ε_r = 972 ±15 % from -9 to 166 ^oC. Further chemical modifications of the complex TB structure hold potential for further improvement of permittivity-temperature stability, although the retention of high permittivity (median-ε_r > 500) over wide temperature ranges may be challenging. This is evidenced by the "doped-CBN" used for PAD film production $(Ca_{0.28-4.25w}Ba_{0.72-0.75w}Ag_wSr_wY_wCe_wNb_{2-5w}Ta_{5w}O_6$ [w = 0.03], bulk ceramic (median) ε_r = 490 ±15 % from -68 to 201 ^oC).

Though not fully explored in this thesis, potential energy storage applications of A- and B- site doped CBN are evidenced by the narrow P-E loops of Y and Ta doped CBN (P_r at 40 kV cm^{-1} = ~0.5 µC cm^{-2}), here the reduction in T_M associated with Ta addition may reduce operational losses, if T_M is lower than operation temperature.

Initial dielectric analysis of an annealed CBN28 PAD film showed improved temperature stability but low median-ε_r values (ε_r = ~225 ±15 % from ~20 to ~240 °C). Further experimentation is required, but CBN-based PAD films hold good potential for achieving temperature stable permittivity across very wide temperature ranges (-55 to 300+ °C). However, the suppression of permittivity, which was retained in the annealed CBN28 sample, may necessitate the use of higher-ε_r base materials.

Overall, TB structured CBN-based dielectrics, with sufficient chemical- and/or processing induced structural- modification, hold good potential for temperature-stable permittivity over very wide temperature ranges. The retention of sufficiently high median-ε_r over these ranges may be challenging, particularly when processing with PAD. CBN-based PAD films may be better suited to energy storage applications, where a high polarisation response is still required but intermediate polarisation responses could be mitigated by (potential) high dielectric breakdown strengths.

9.4 References

Akedo, J. 2008. Room Temperature Impact Consolidation (RTIC) of Fine Ceramic Powder by Aerosol Deposition Method and Applications to Microdevices. *J. Therm. Spray Technol.* **17**. 181-198

DOI: https://doi.org/10.1007/s11666-008-9163-7

Cao, H. Min, J. Y. Wu, S. D. Xian, A. P. Shang, S. K. 2006. Pinning of grain boundaries by second phase particles in equal-channel angularly pressed Cu–Fe–P alloy. *Mater. Sci. Eng. A*. **431**. 86-91

DOI: https://doi.org/10.1016/j.msea.2006.05.081

Cao, L. Wang, Y. Yuan, Y. Zhu, J. Barzegar-Bafrooei, H. Mao, M. Liu, B. Li, H. Wang, D. Lu, Z. Wang, G. Song, K. 2024. Low temperature relaxor, polarization dynamics and energy storage properties of $Ca_{0.28}Ba_{0.72}Nb_2O_6$ tungsten bronze ceramics. *J. Chem. Eng*. **479**. 147664

DOI: https://doi.org/10.1016/j.cej.2023.147664

Hou, S. Xu, S. Yang, L. Liu, X. Wei, L. Chao, X. Wu, Di. Liang, P. Yang, Z. 2022. High energy storage performance of $Ca_{0.15}(Sr_{0.6}Ba_{0.4})_{0.85}Nb_{2-x}Ta_xO_6$ relaxor ferroelectric ceramics. *Ceram. Int*. **48**. 28382-28390

DOI: https://doi.org/10.1016/j.ceramint.2022.06.148

Jiang, B. Locozzia, J. Zhao, L. Zhang, H. Harn, Y-W. Chena, Y. Lin, Z. 2019. Barium titanate at the nanoscale: controlled synthesis and dielectric and ferroelectric properties. *Chem. Soc. Rev*. **48**. 1194-1228

DOI: **https://doi.org/10.1039/C8CS00583D**

Khansur, N. H. Eckstein, U. Benker, L. Deisinger, U. Merle, B. Webber, K. G. 2018. Room temperature deposition of functional ceramic films on low-cost metal substrate. *Ceram. Int*. **44**. 16295-16301

DOI: https://doi.org/10.1016/j.ceramint.2018.06.027

Kim, H-K. Lee, S-H. Lee, S-G. Lee, Y-H. 2015. Densification mechanism of BaTiO3 films on Cu substrates fabricated by aerosol deposition. *Electron. Mater. Lett*. **11**. 388–397
DOI: https://doi.org/10.1007/s13391-015-4419-0
Kittel, C. 1946. Theory of the structure of ferromagnetic domains in films and small particles. *Phys. Rev*. **70**. 965-971

DOI: https://doi.org/10.1103/PhysRev.70.965

Li, F. Zhang, S. Damjanovic, D. Chen, L-Q. Shrout, T. R. 2018. Local Structural Heterogeneity and Electromechanical Responses of Ferroelectrics: Learning from Relaxor Ferroelectrics. *Adv. Funct. Mater*. **28**. 1801504

DOI: **https://doi.org/10.1002/adfm.201801504**

Niemer, A. Pankrath, R. Betzler, K. Burianek, M. Muehlberg, M. 2012. Dielectric Properties and the Phase Transition of Pure and Cerium Doped Calcium-Barium-Niobate. *World J. Condens. Matter Phys*. **2**. 80-84

DOI: https://doi.org/10.4236/wjcmp.2012.22014

Ofoegbuna, T. Darapaneni, P. Sahu, S. Plaisance, C. Dorman, J A. 2019. Stabilizing the B-site oxidation state in ABO_3 perovskite nanoparticles. *Nanoscale*. **30**. 14303-14312

DOI: https://doi.org/10.1039/C9NR04155A

Peirson, H. Pan, J. Li, Y. Hooper, T. E. Hall, D. A. Brown, A. P. Drummond-Brydson, R. M. Milne, S. J. 2023. Structure and dielectric properties of yttrium-doped $Ca_{0.28}Ba_{0.72}Nb_2O_6$ ceramics. *J. Alloys Compd*. **950**. 169891

DOI: https://doi.org/10.1016/j.jallcom.2023.169891

Trubelja, M. P. Ryba, E. Smith, D. K. 1996. A study of positional disorder in strontium barium niobate. *J. Mater. Sci*. **31**. 1435-1443

DOI: https://doi.org/10.1007/BF00357850

Wei, L. Yang, Z. Chao, X. Jiao, H. 2014-May. Structure and electrical properties of $Ca_{0.28}Ba_{0.72}Nb_2O_6$ ceramics with addition of rare earth oxides (CeO_2, La_2O_3). *Ceram. Int*. **40**. 5447-5453

DOI: http://dx.doi.org/10.1016/j.ceramint.2013.10.130

Wu, J. Wang, J. Xiao, D. Zhu, J. 2011. Migration Kinetics of Oxygen Vacancies in Mn-Modified $BiFeO_3$ Thin Films. *Appl. Mater. Interfaces.* **7**. 2504-2511

DOI: https://doi.org/10.1021/am2003747

Xu, R. Karthik, J. Damodaran, A R. Martin, L W. 2014. Stationary domain wall contribution to enhanced ferroelectric susceptibility. *Nat. Commun.* **5**. 3120

DOI: https://doi.org/10.1038/ncomms4120

Zhuo, F. Eckstein, U. R. Khansur, N. H. Dietz, C. Urushihara, D. Asaka, T. Kakimoto, K-I. Webber, K. G. Fang, X. Rödel. J. 2022. Temperature-induced changes of the electrical and mechanical properties of aerosol-deposited BaTiO3 thick films for energy storage applications. *J. Am. Ceram. Soc.* 105. 4108-4121

DOI: https://doi.org/10.1111/jace.18377

10. Appendix

10.1 Appendices relating to Section 5: Results chapter 1

Appendix 1, corresponding to data in Figures 44 and 45.

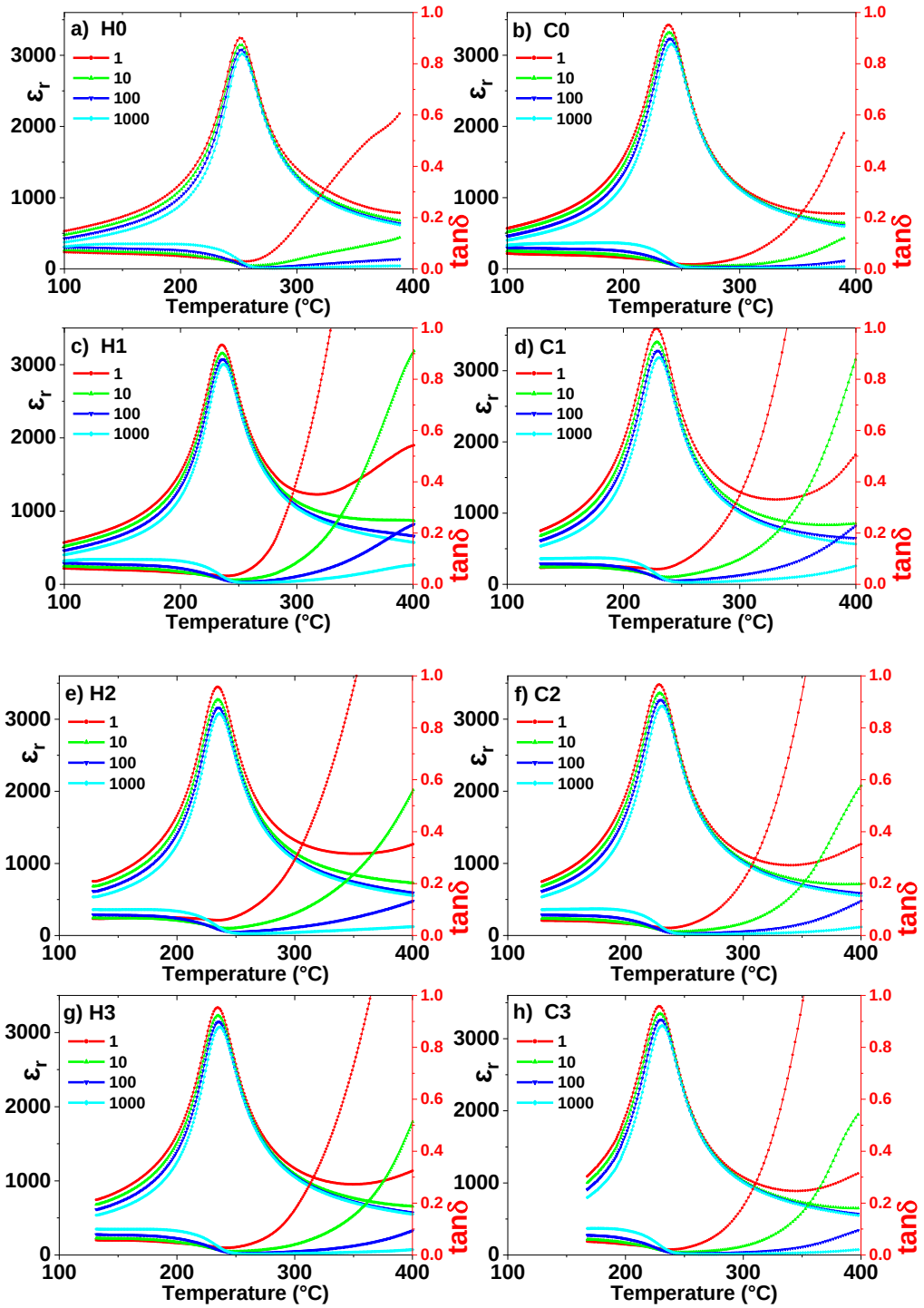

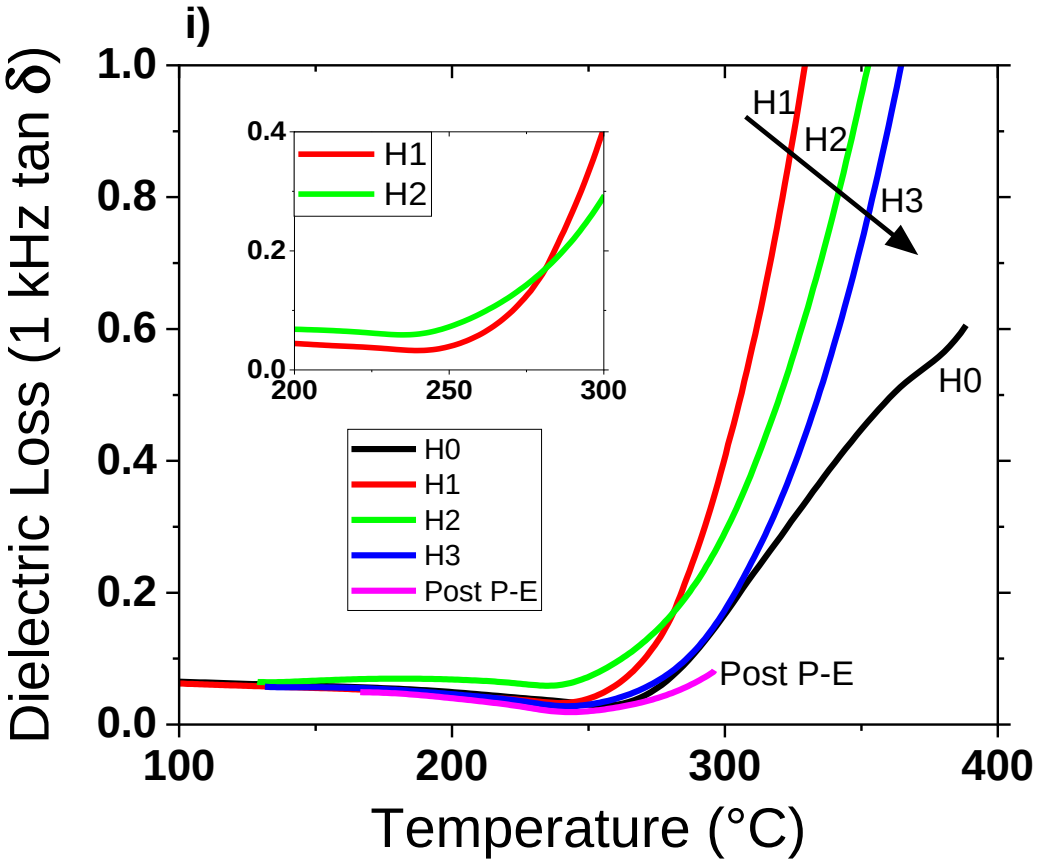

Appendix 1. Relative permittivity- and tan δ- temperature responses for $Ca_{0.28}Ba_{0.72}Nb_2O_6$ calcined for 12 h at 1200 ^oC and sintered at 1350 ^oC for 4 h, upon; (a) heating and (b) cooling. This sample was left untouched for 15 months before dielectric measurements were performed under cyclical heating and cooling, referred to in the text as experiment "CE1". Heating curve data is displayed in (c), (e) and (g). Cooling curve data is displayed in, (d), (f) and (h). Measurement codes, e.g. "H1", refer to heating (H) or cooling (C) and cycle number (1, 2 or 3). The variation in 1 kHz tan δ values for the heating cycles is shown in (i) (and also Figure 44).

Appendix 2, where H1, H2, C1 and C2 correspond to the 1000 kHz data in Figure 45(d) and “4 h calcined CBN28 (R1.3)” corresponds to CBN28 from the Y doped CBN28 experiments, Figure 53(a):

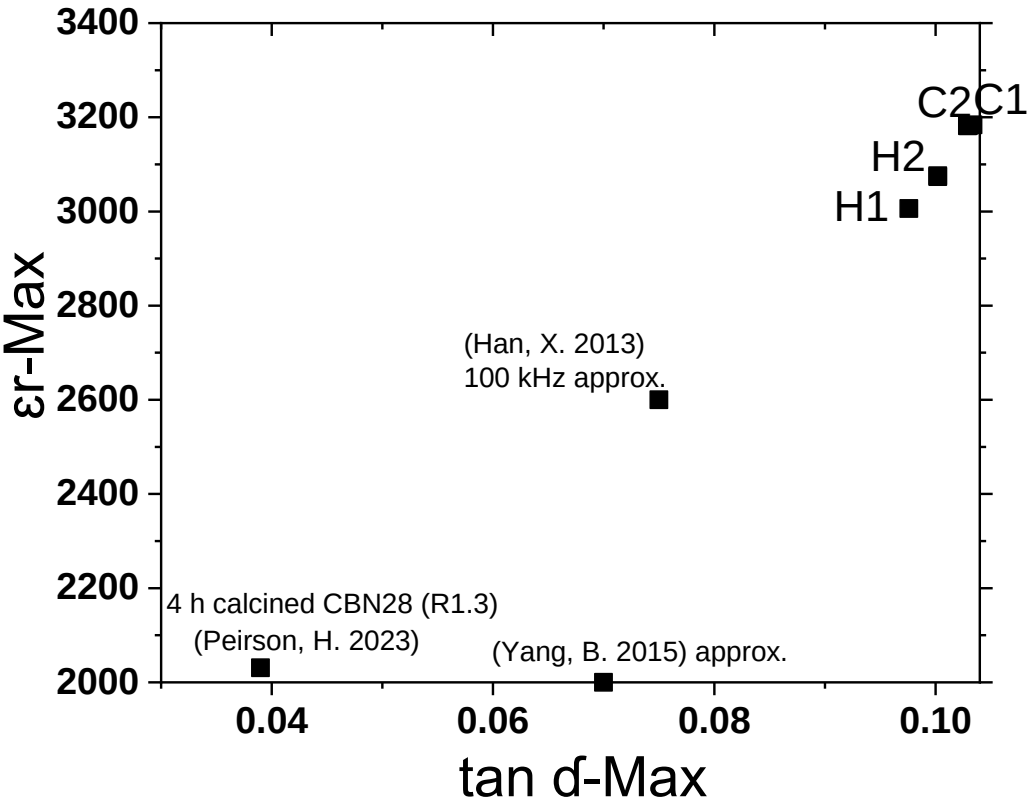

Appendix 2. The correlation between 1000 kHz tan δ-Max and ε_r-Max values in the CBN28 dielectric data (H1, H2, C1 and C2) taken from Experiment “CE1”. Comparisons with other published CBN28 data show an extension of the correlation to different CBN28 samples. The work of Yang *et al.* shows a slight elevation of 1000 kHz permittivity above 1 kHz values at T_C, this may indicate the presence of an additional high frequency loss mechanism. This could be the cause of the observed deviation from the trend.

Appendix 3, corresponding to data in Figures 44 and 45:

Appendix 3. Select dielectric data from a single pellet of $Ca_{0.28}Ba_{0.72}Nb_2O_6$, calcined for 12 h at 1200 ^oC and sintered at 1350 ^oC for 4 h, including data from thermal cycling experiments. Measurement codes correspond to those in Figures 44 and 45. The code "CE2" is not mentioned in the text, it refers to a second set of thermal cycling, from which the "Post-PE" data in Figure 44 is taken.

Measurement code	ε_r-Max at 1000 kHz	tan δ-Max at 1000 kHz (±0.001)	T_C (^oC)	ε_r-Max at 1 kHz	1 kHz tan δ at 300 ^oC (±0.001)
H0	3021	0.097	253	3242	0.172
C0	3155	0.102	241	3424	0.045
H1 (CE1)	3006	0.098	237	3269	0.396
H2 (CE1)	3076	0.100	235	3448	0.293
H3 (CE1)	3074	0.100	237	3336	0.179
C1 (CE1)	3184	0.103	230	3593	0.345
C2 (CE1)	3182	0.103	231	3480	0.209
C3 (CE1)	3182	0.103	231	3449	0.194
H1* (CE2)	3026	-	235	3235	0.075
H2 (CE2)	3060	~0.101**	235	3280	0.080
H3* (CE2)	3059	~0.102**	237	3276	0.082
C1 (CE2)	3164	0.103	230	3411	0.082***
C2 (CE2)	3165	0.103	231	3412	0.083***
C3 (CE2)	3166	0.103	231	3412	0.084***

* See Appendix: 1, furnace repeatedly overshot desired temperature and then dwelled. This likely limited the accuracy of measurements such as T_C.

** tan δ-Max not observed in the measured temperature range (no inflection point on plot). Included values were measured at 160 ^oC and 166 ^oC, for H2 (CE2) and H3 (CE2).

*** data recorded at 295 ^oC.

Appendix 4, the variable permittivity temperature responses of Y doped CBN28 when solely substituting Y for Ca. These correspond to the XRD data in Figure 47:

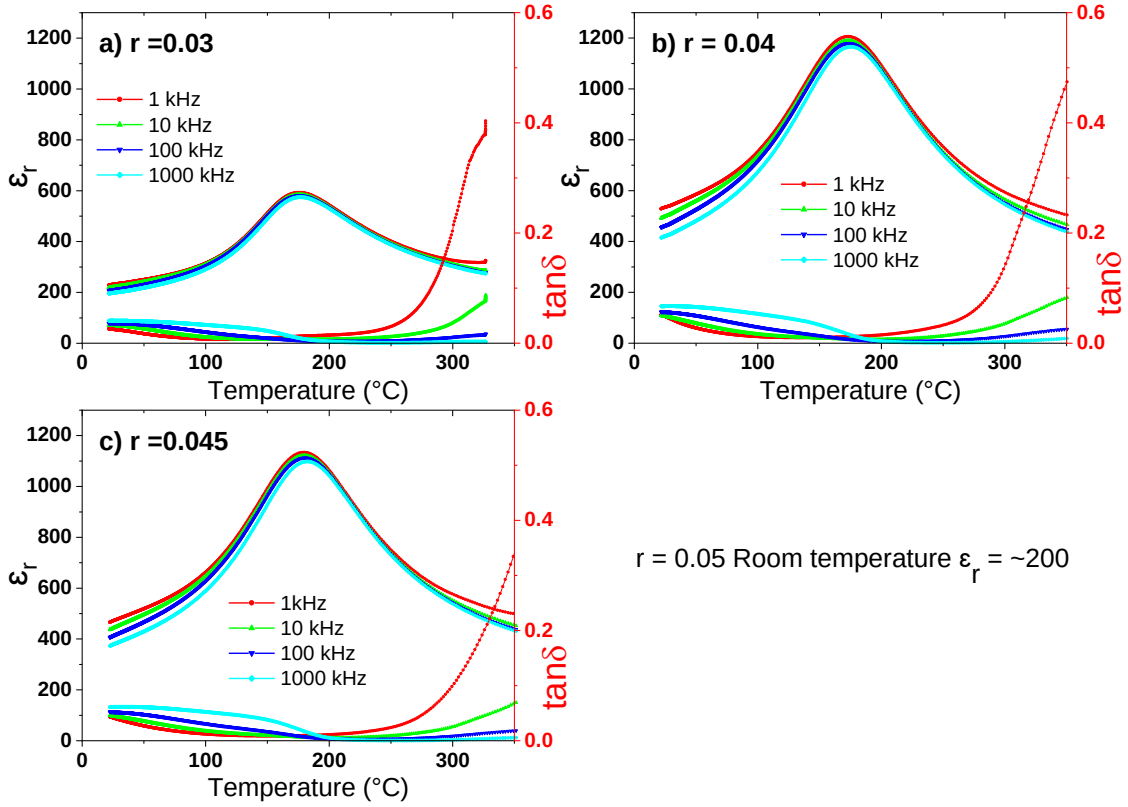

Appendix 4. Relative permittivity-and tan δ- temperature responses for $Y_rCa_{0.28-3r/2}Ba_{0.72}Nb_2O_6$ ($0.03 \leq r \leq 0.05$) ceramics, measured at 1 to 1000 kHz. a) r = 0.03, b) r = 0.04, c = r =0.045. Only room temperature data was acquired for r = 0.05.

10.2 Appendices relating to Section 7: Results chapter 2

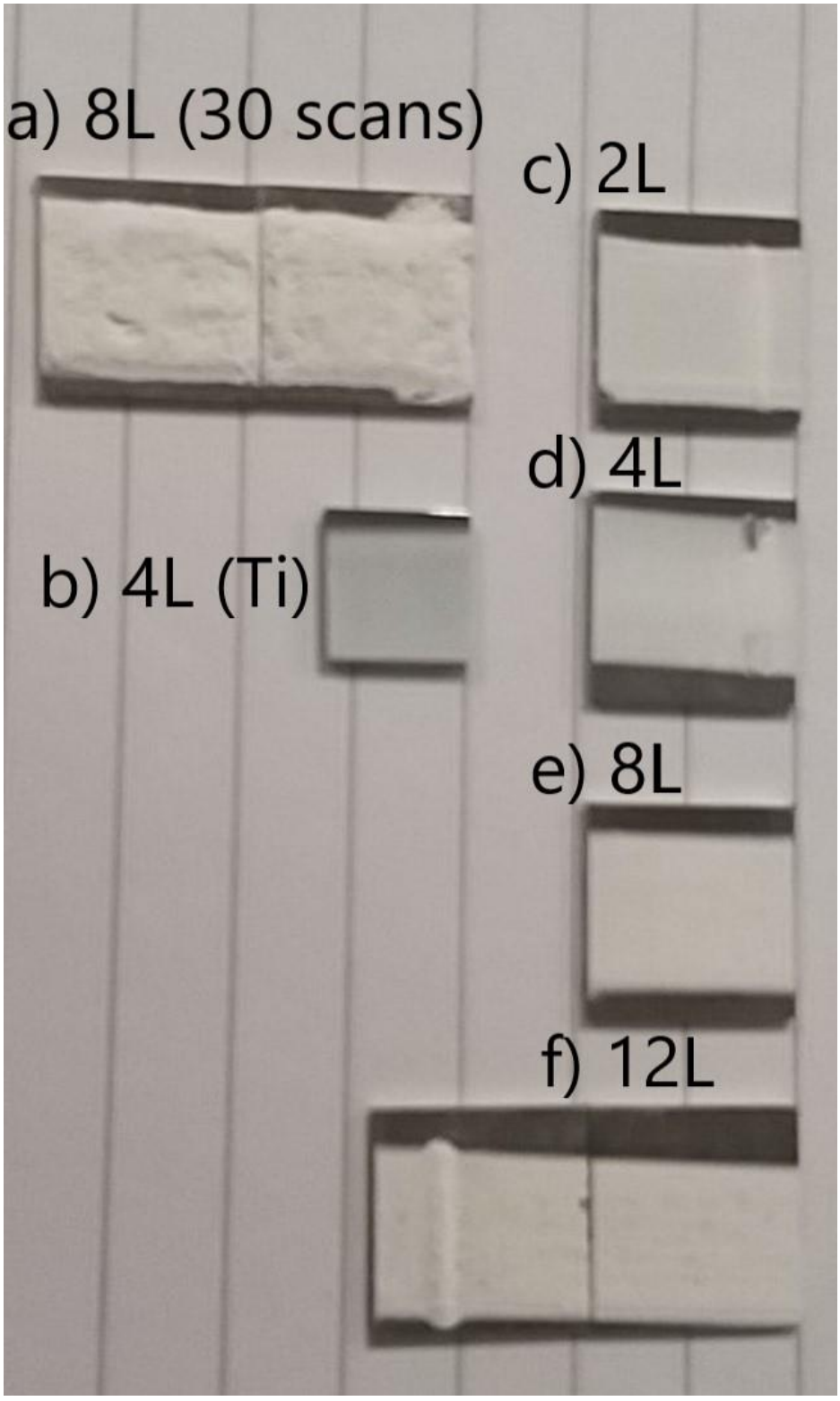

Appendix 5. A photograph of CBN films produced by PAD in Erlangen. Stainless steel substrate dimensions are ~12 x 12 mm. Ti-alloy substrate dimensions are ~8 x 8 mm. Films deposited on SUS304 stainless steel for 10 scans, at the indicated N_2 carrier gas flowrates of 2-12 L min^{-1}, except for (a) which was deposited for 30 scans and (b) which was deposited on Ti-4V-6Al Ti-alloy.

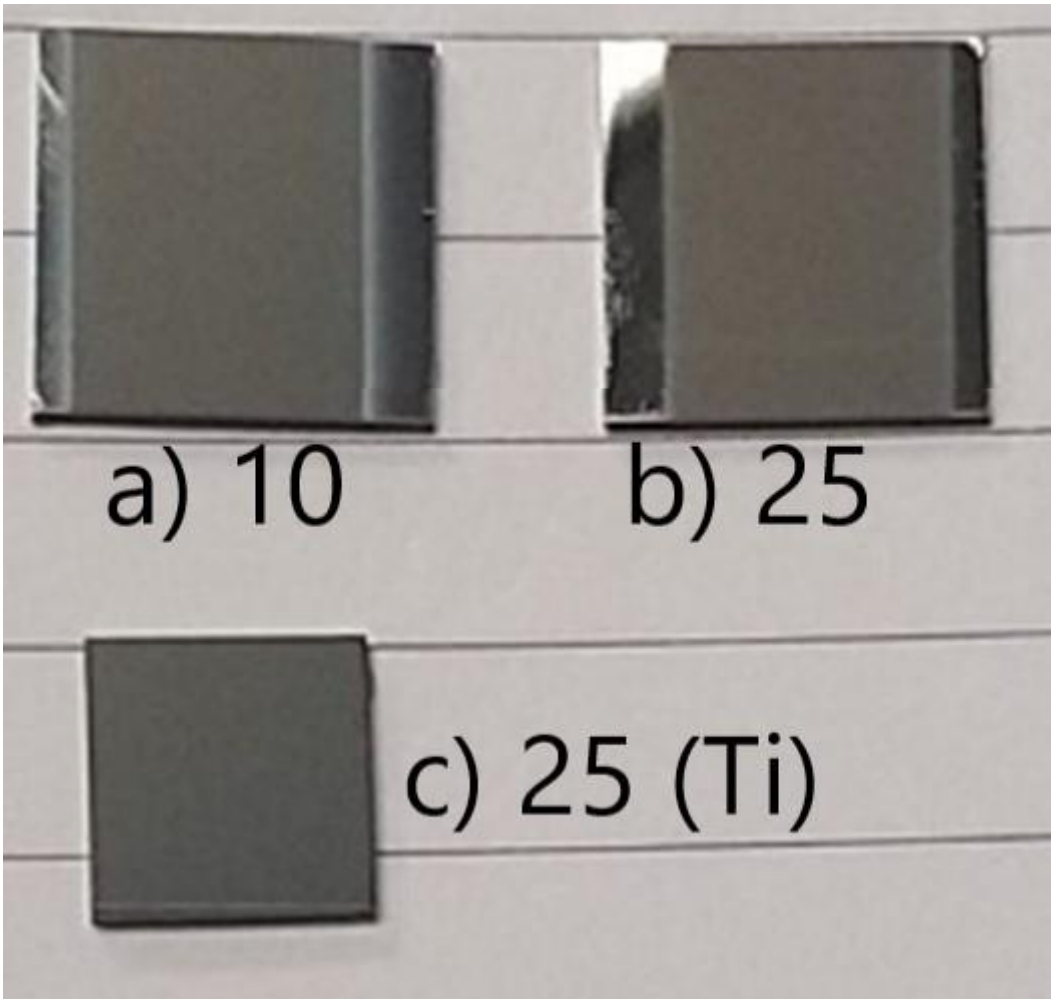

Appendix 6. A photograph of SNN films produced by PAD in Erlangen. Stainless steel substrate dimensions are ~12x12 mm. Ti-alloy substrate dimensions are ~8x8 mm. Films deposited on SUS304 stainless steel for the indicated number of scans at N_2 carrier gas flowrates of 4 L min^{-1}, except for (c) which was deposited on Ti-4V-6Al Ti-alloy.

Appendix 7. Optical micrographs of SNN films deposited on stainless steel and Ti-alloy substrates at 4 L min^{-1}.

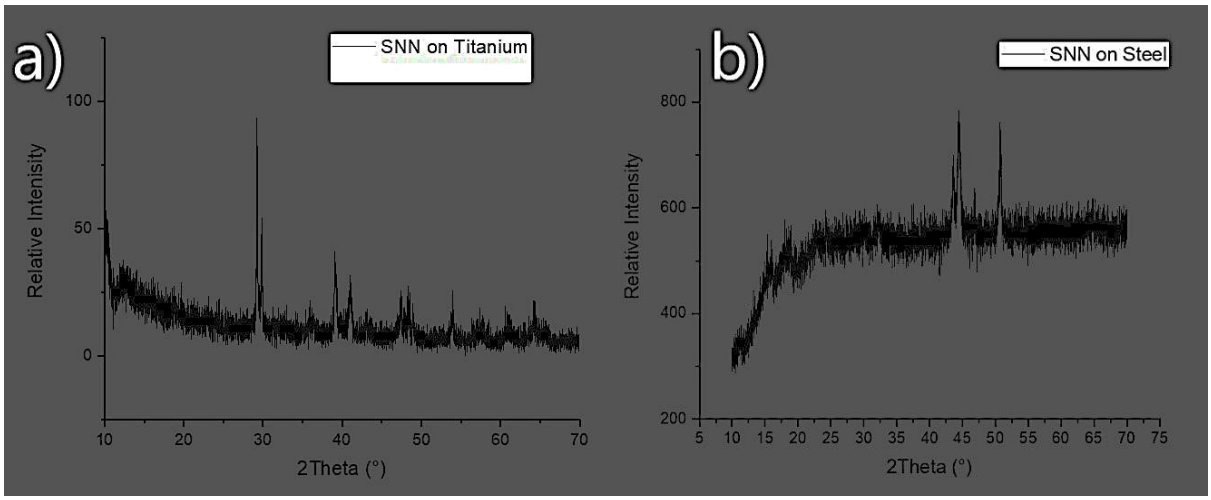

Appendix 8. XRD patterns for SNN deposited onto Ti-alloy and Stainless steel. Both patterns are inconclusive, showing no clear TB structure, likely due to the films submicron thickness.

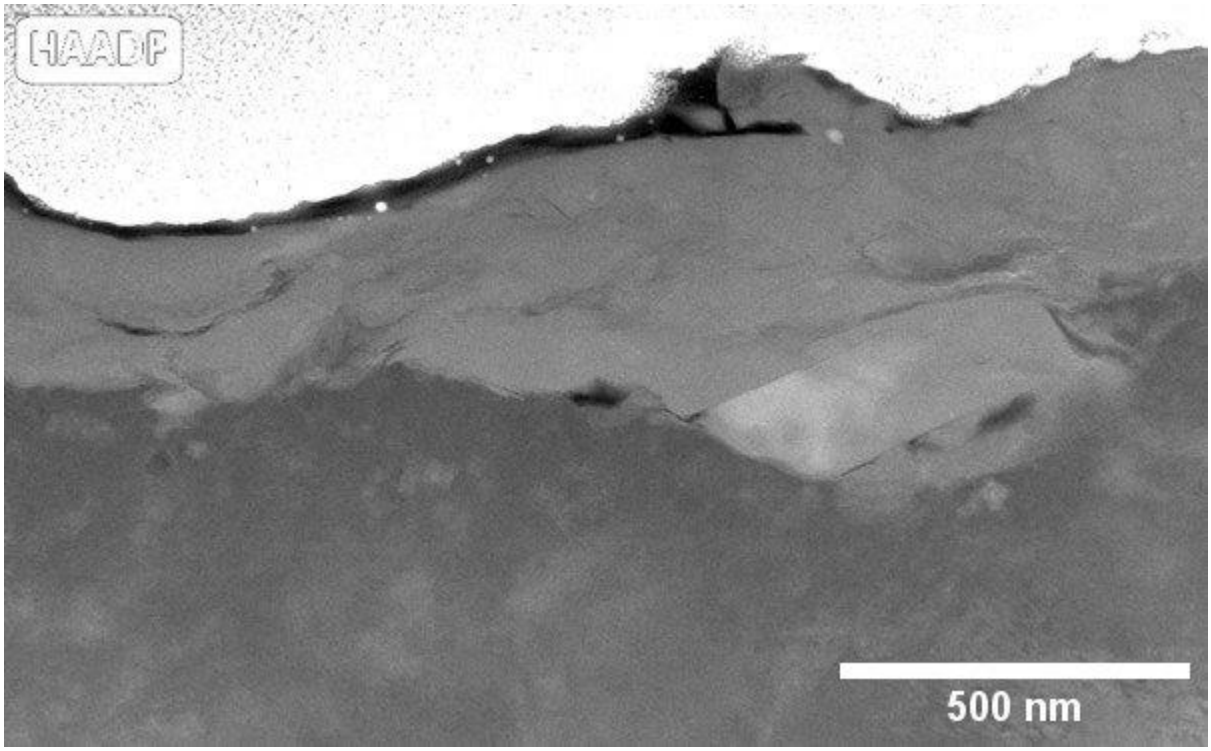

Appendix 9. A HAADF micrograph of a SNN PAD film, corresponding to Figure 7(a) and showing signs of flow-like deformation (top left of film).

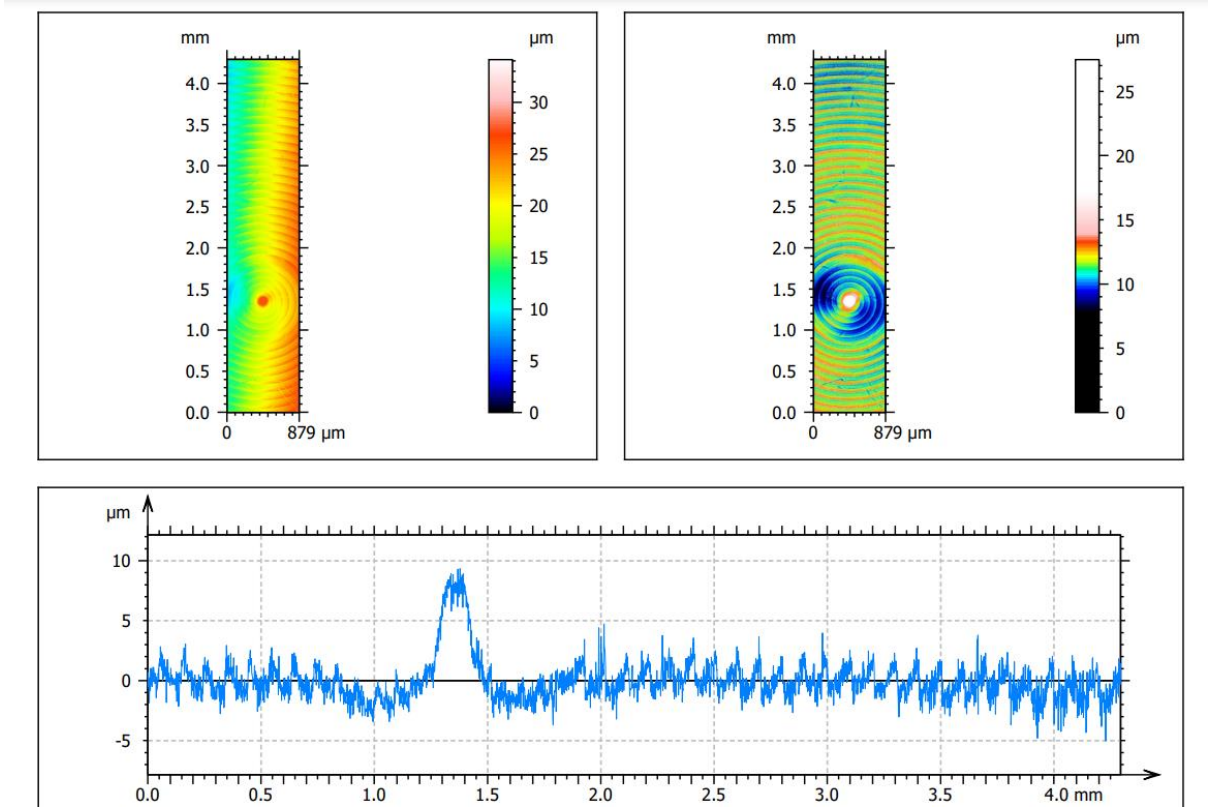

Appendix 10. Profilometry from the initial deposition of Al_2O_3 onto a textured aluminium SEM stub. The thickness of the layer was not determined but is presumed to be submicron.

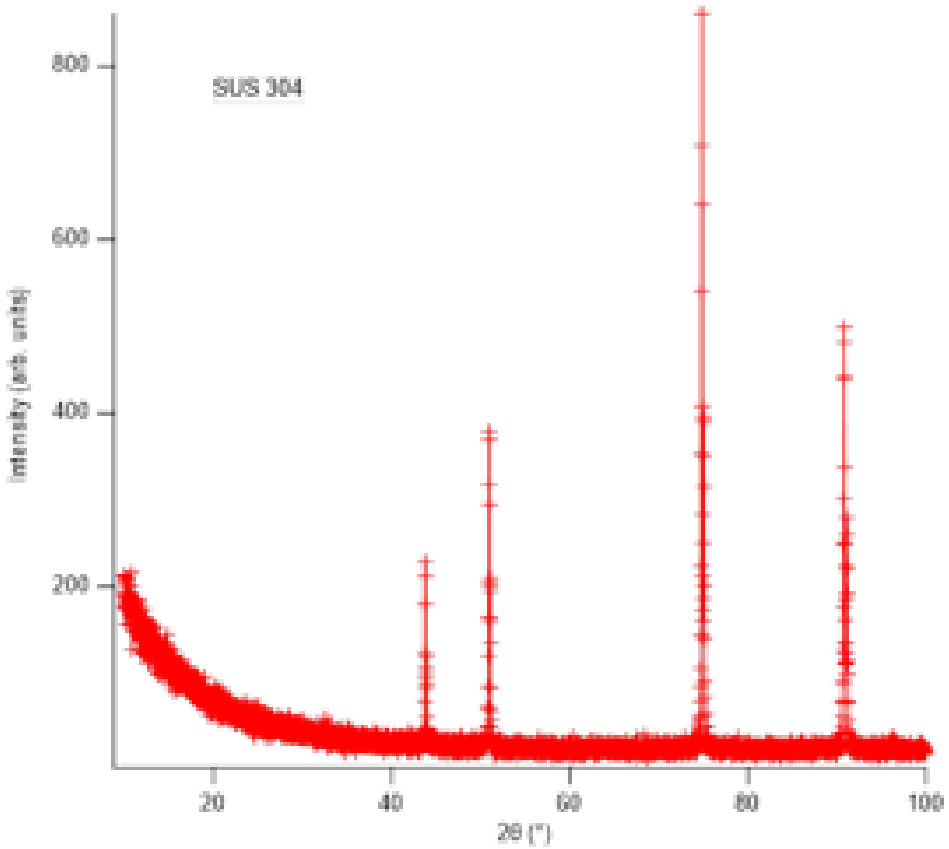

Appendix 11. An XRD pattern of a stainless steel SUS304 substrate, courtesy of Dr. Neamul Khansur, of the University of Erlangen-Nuremburg.

10.3 Appendices relating to Section 8: Results chapter 3

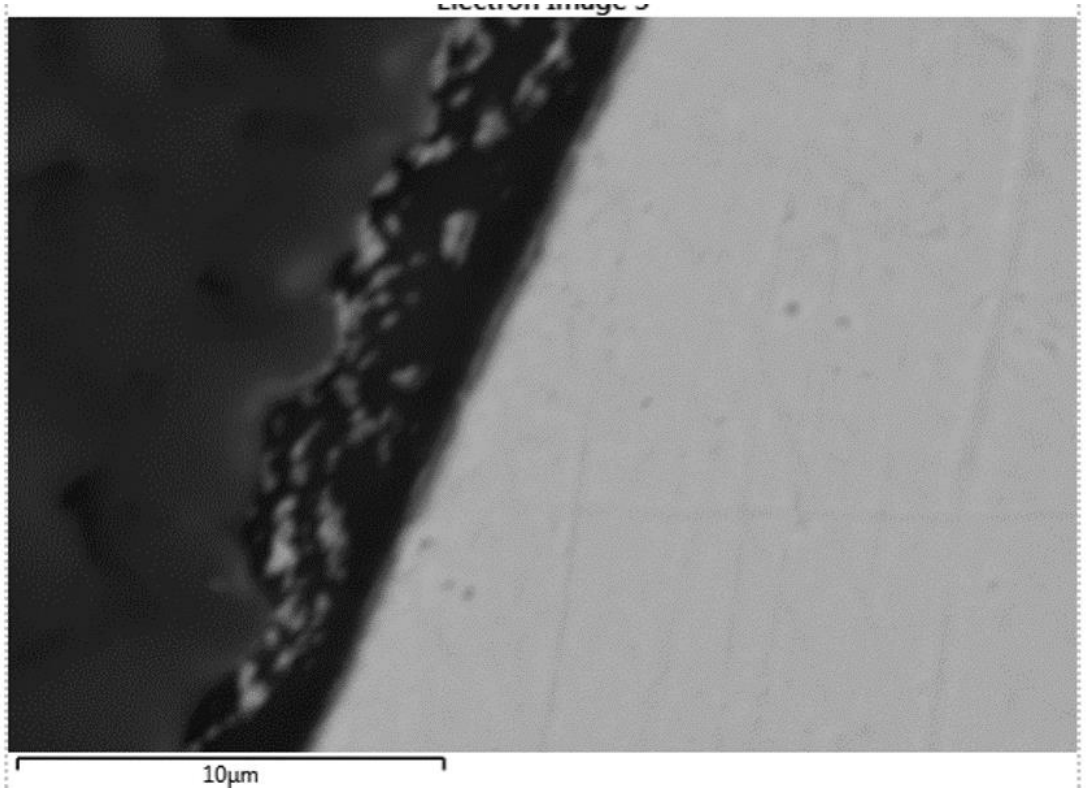

Appendix 12. A ~0.7 µm yttrium-doped CBN film, of slightly lighter contrast than the SUS304 substrate (right). The resin (darker contrast, on the left), used for mounting, has pulled away from the surface and damaged the film.

Appendix 13. The pattern of 2 mm diameter Au electrodes employed for the electrically analysed films, shown on a dark anchor-layer (~1 µm) and a thick (~250 µm) powder compact. Partial disintegration of the powder compact and breakdown of the electrode has occurred in the powder compact. The films resulted from powders that were produced by either thermally pre-treating or spray drying the attrition milled powder shown in Figure 94(c), respectively.

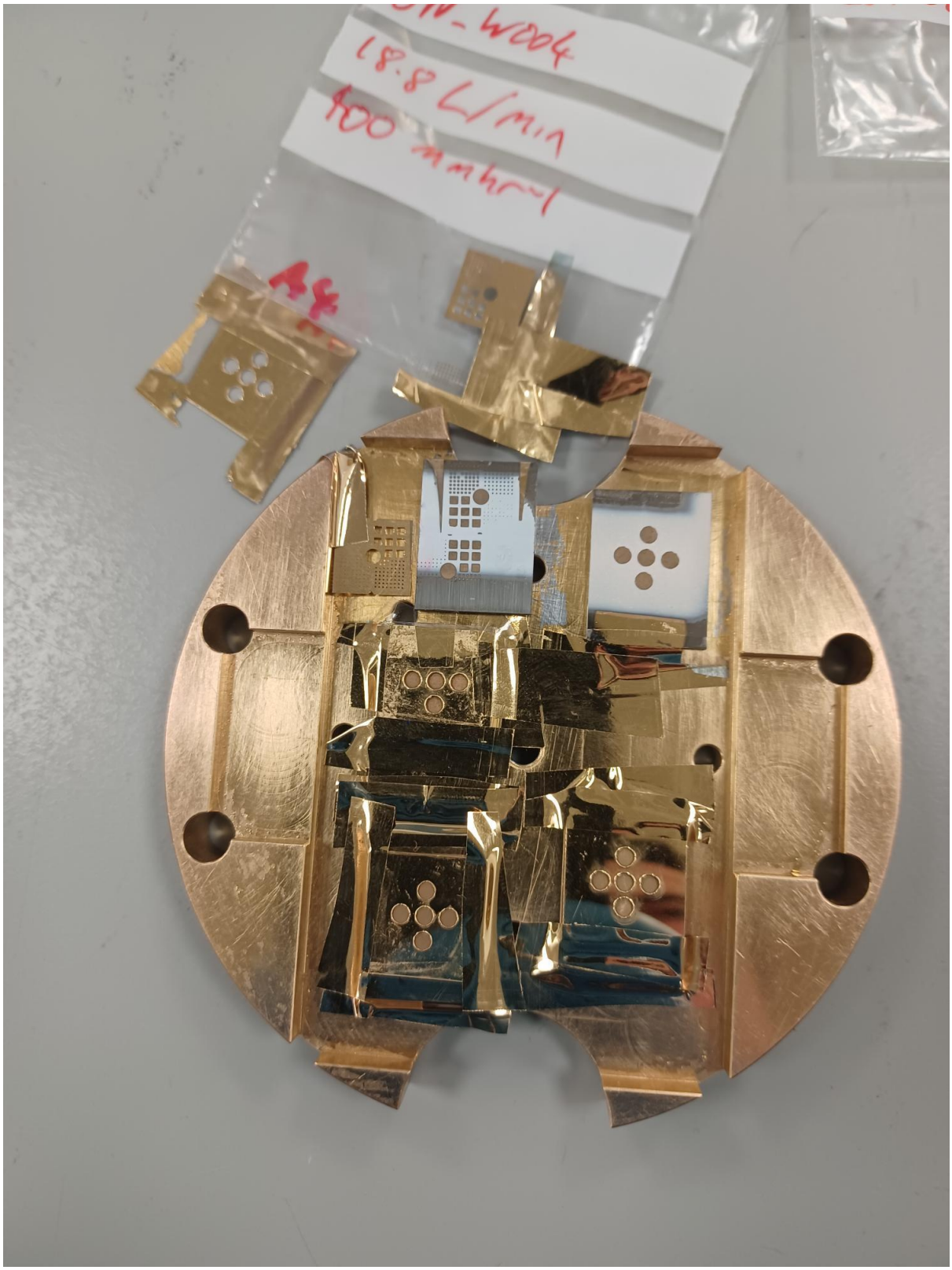

Appendix 14. The sputtering of Au electrodes onto the PAD films using electrode masks. Top right, the 5 electrodes applied to the films that were electrically characterised. Top left, other electroding patterns.

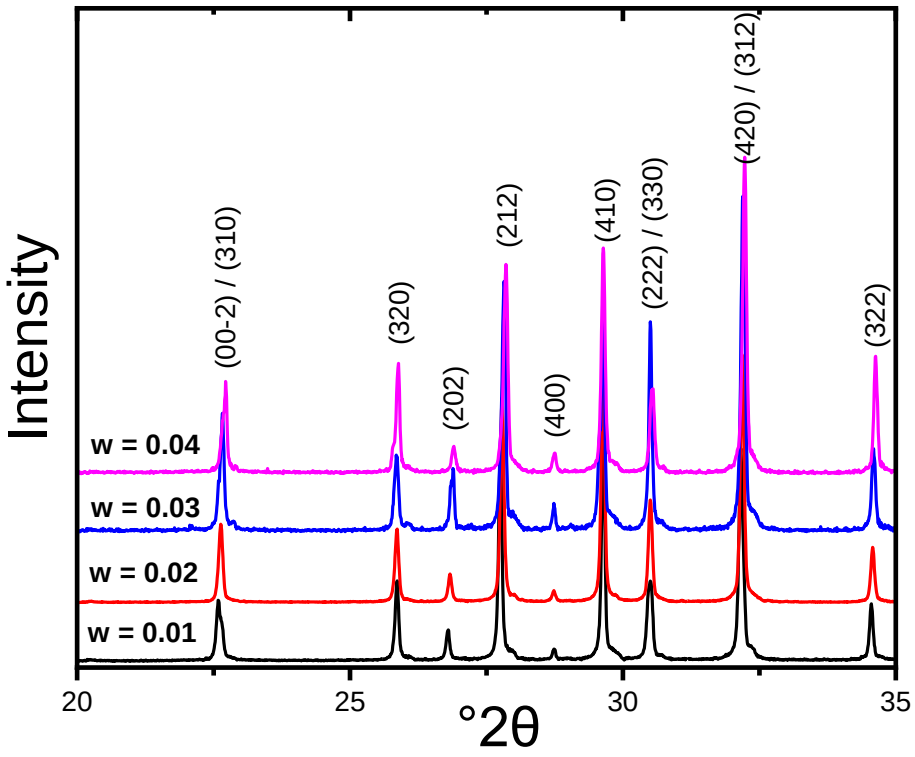

Appendix 15. X-ray diffraction patterns of "doped-CBN" $Ca_{0.28-4.25w}Ba_{0.72-0.75w}Ag_wSr_wY_wCe_wNb_{2-5w}Ta_{5w}O_6$ [$0.01 \leq w \leq 0.04$] crushed sintered pellets, indexed according to P4bm (ICCD 05-001-0283). Samples were calcined for 12 h at 1200 ^oC prior to sintering for 4 h at 1300 °C. Shoulders at °2θ values just above the primary peaks are particularly apparent in w = 0.03, they may be caused by imperfect stripping of $K_{\alpha 2}$ radiation. Secondary phases were assumed to be present, given the high level of dopants, however clear secondary phase peaks were not detected. Numerous, low wt.% (< 5 wt.%) secondary phases would be difficult to detect by XRD. The doped-CBN referred to in Section 8, Results chapter 3 has the composition w = 0.03 ($Ca_{0.1525}Ba_{0.6975}Ag_{0.03}Sr_{0.03}Y_{0.03}Ce_{0.03}Nb_{1.85}Ta_{0.15}O_6$).

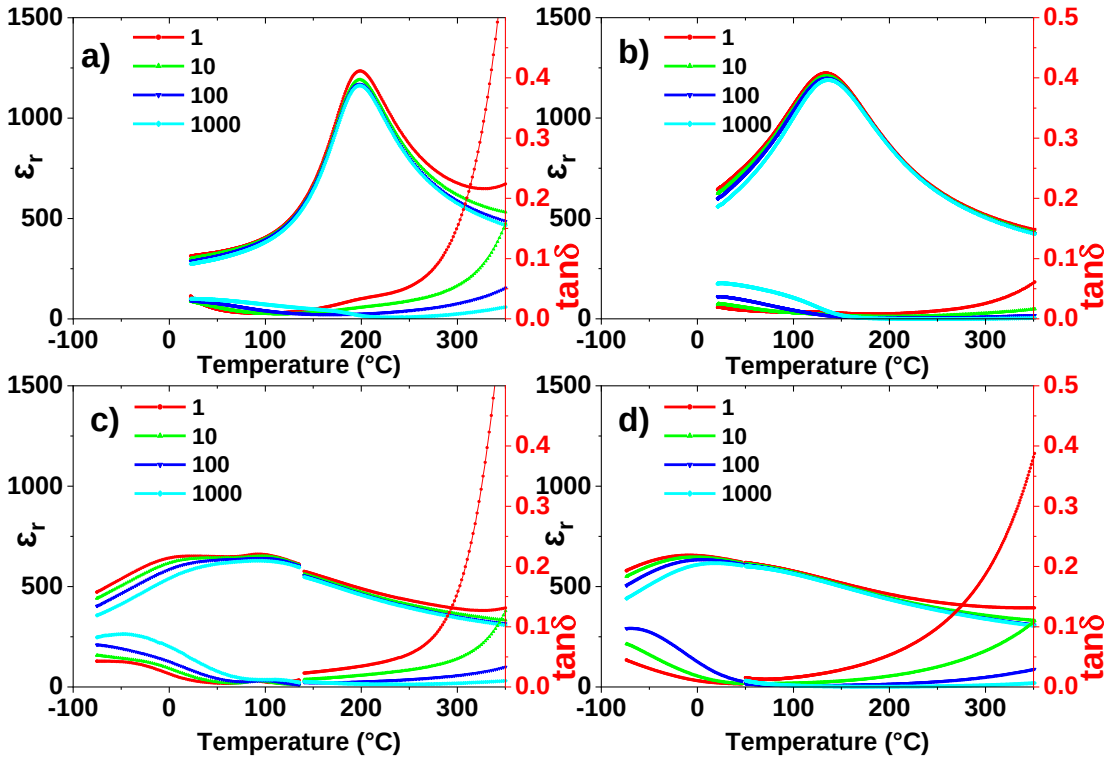

Appendix 16. Relative permittivity- and tan δ- temperature responses for $Ca_{0.28-4.25w}Ba_{0.72-0.75w}Ag_wSr_wY_wCe_wNb_{2-5w}Ta_{5w}O_6$ [0.01 ≤ w ≤ 0.04] ceramics; (a) w = 0.01, (b) w = 0.02, (**c) w = 0.03,** (d) w = 0.04, measured at 1 to 1000 kHz. Repression of low frequency permittivity values in sample w = 0.03 around 50 ^oC may be associated with water vapour in the environmental chamber, as the repression is not seen when measuring permittivity in the tube furnace. The doped-CBN referred to in Section 8, Results chapter 3 has the composition w = 0.03 ($Ca_{0.1525}Ba_{0.6975}Ag_{0.03}Sr_{0.03}Y_{0.03}Ce_{0.03}Nb_{1.85}Ta_{0.15}O_6$).

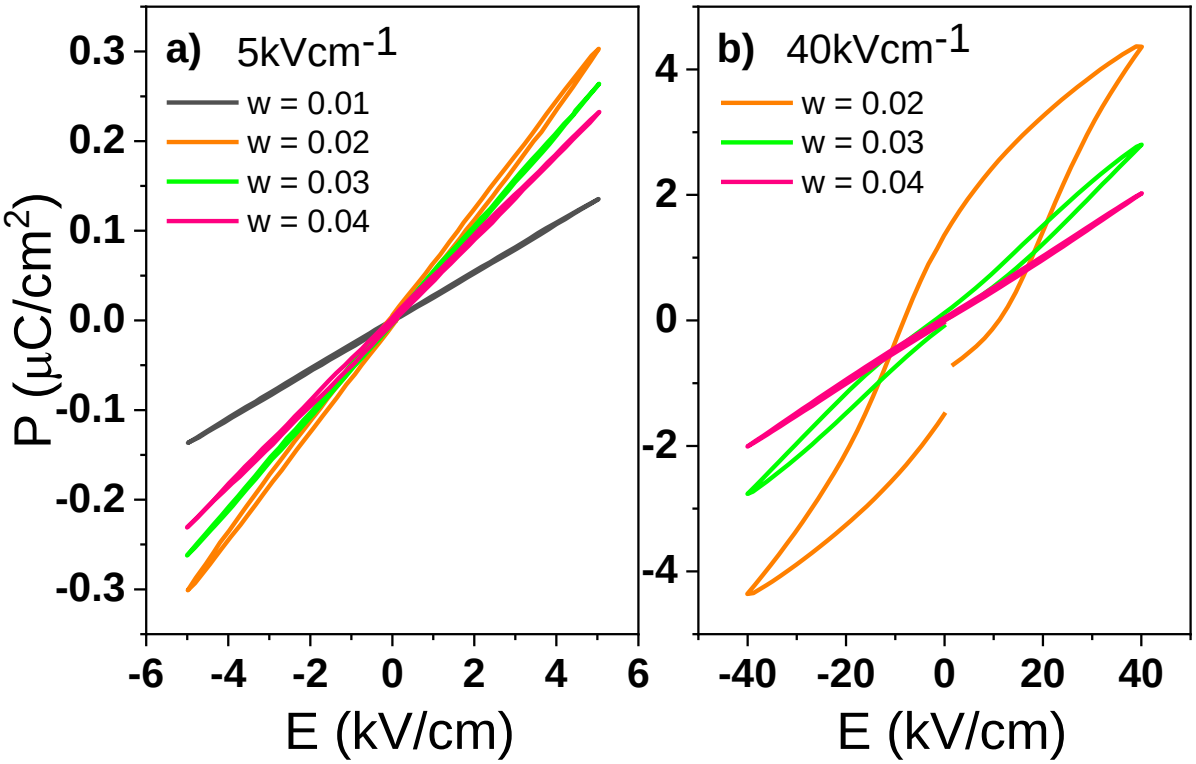

Appendix 17. Comparison of P-E loops for $Ca_{0.28-4.25w}Ba_{0.72-0.75w}Ag_wSr_wY_wCe_wNb_{2-5w}Ta_{5w}O_6$ [0.01 ≤ w ≤ 0.04] ceramics at; (a) 5 kV cm^{-1} and (b) 40 kV cm^{-1}. The response of w = 0.01 is out of trend with the higher dopant levels samples, w = 0.01 underwent dielectric breakdown at an applied field of ~15 kV cm^{-1}. The characteristically ferroelectric response of w = 0.02, measured at 40 kV cm^{-1}, gave way to a pinched and narrow response for w = 0.03 and a linear response for w = 0.04. The doped-CBN referred to in Section 8, Results chapter 3 has the composition w = 0.03 ($Ca_{0.1525}Ba_{0.6975}Ag_{0.03}Sr_{0.03}Y_{0.03}Ce_{0.03}Nb_{1.85}Ta_{0.15}O_6$).

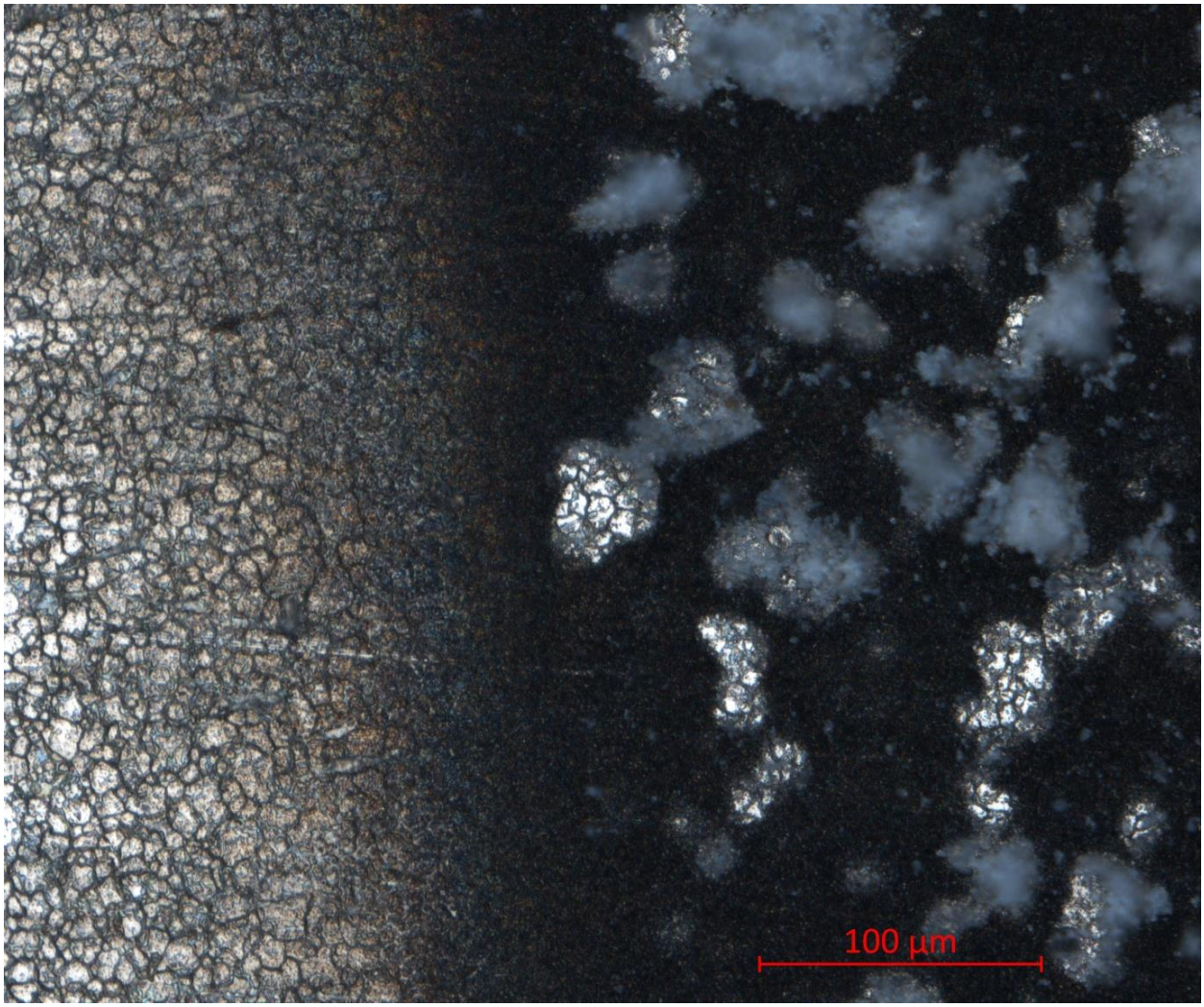

Appendix 18. Optical microscopy of an Al_2O_3 film deposited on an unpolished SUS304 stainless steel substrate (left). Lighter contrasted low density powder compacts or agglomerates can be seen on the dark Al_2O_3 anchor layer. The agglomerates tend to be positioned over damaged sections of the film (exposed substrate), suggesting that the agglomerates are the cause of the damage, or else the anchor layer is resistive to adhesion.

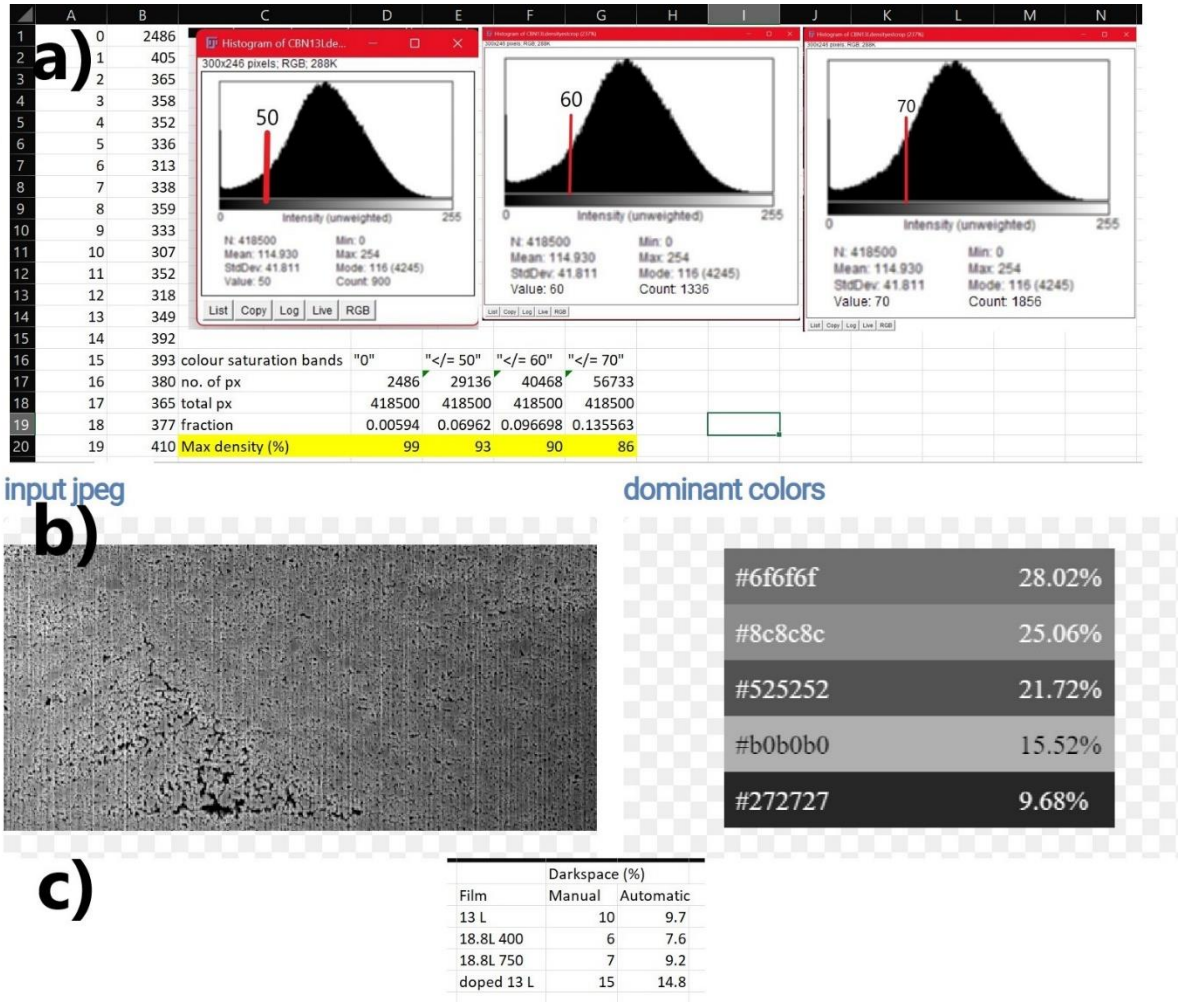

Appendix 19. Dark space/pseudo-density calculations for a CBN28 film deposited at 13 L min^{-1}, in (a). The calculated dark space was ~10 %, although errors due to imperfect colour bounding (i.e. if the dark space was bound was inaccurate) may be several percentage points, as indicated by the "</= 50" and "</= 70" bands. In (b), an automatic tool gave a darkest colour band percentage of 9.7 %. This software was accessed from https://onlinejpgtools.com/find-dominant-jpg-colors. In (c), the manually and automatically calculated dark space percentages for the CBN28 films deposited at 13 L min^{-1}, 18 L min^{-1} and annealed at 400 °C, 18 L min^{-1} and annealed at 750 °C, and the doped CBN film deposited at 13 L min^{-1} are shown.

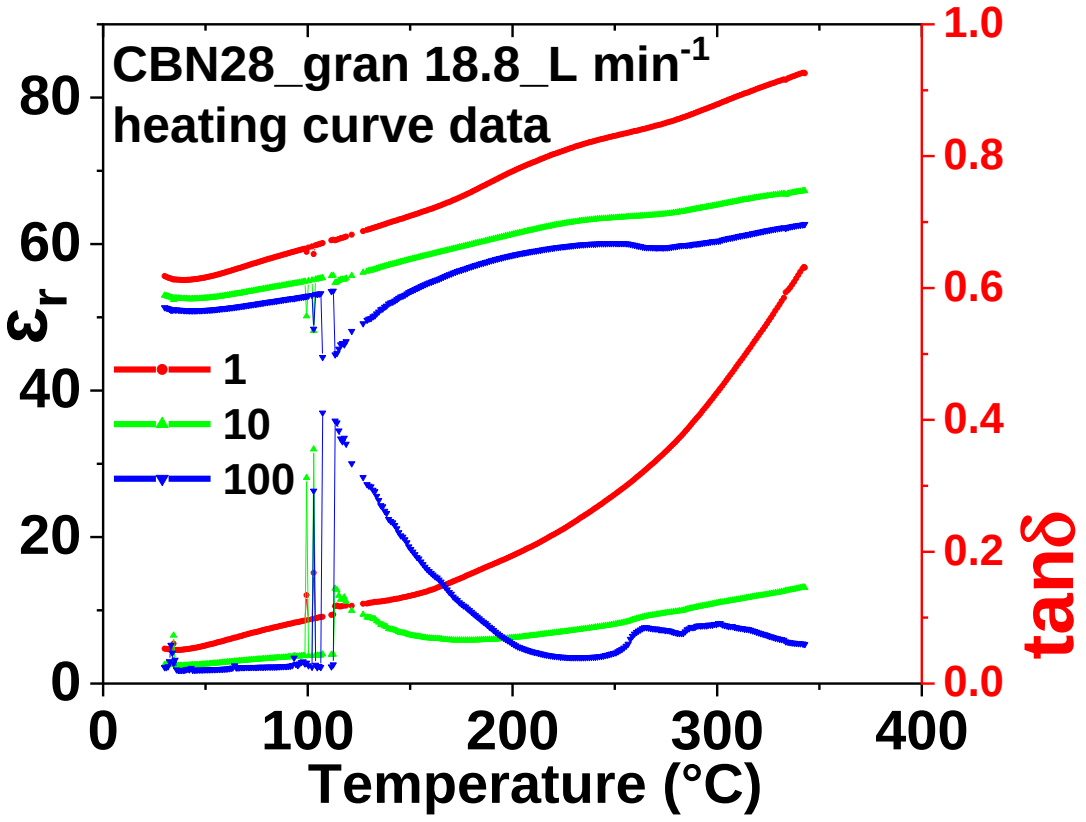

Appendix 20. Heating curve data associated with the cooling curve data in Figure 104(b) for the permittivity- and tan δ- temperature response of a CBN28 film, deposited at 18.8 L min^{-1}.

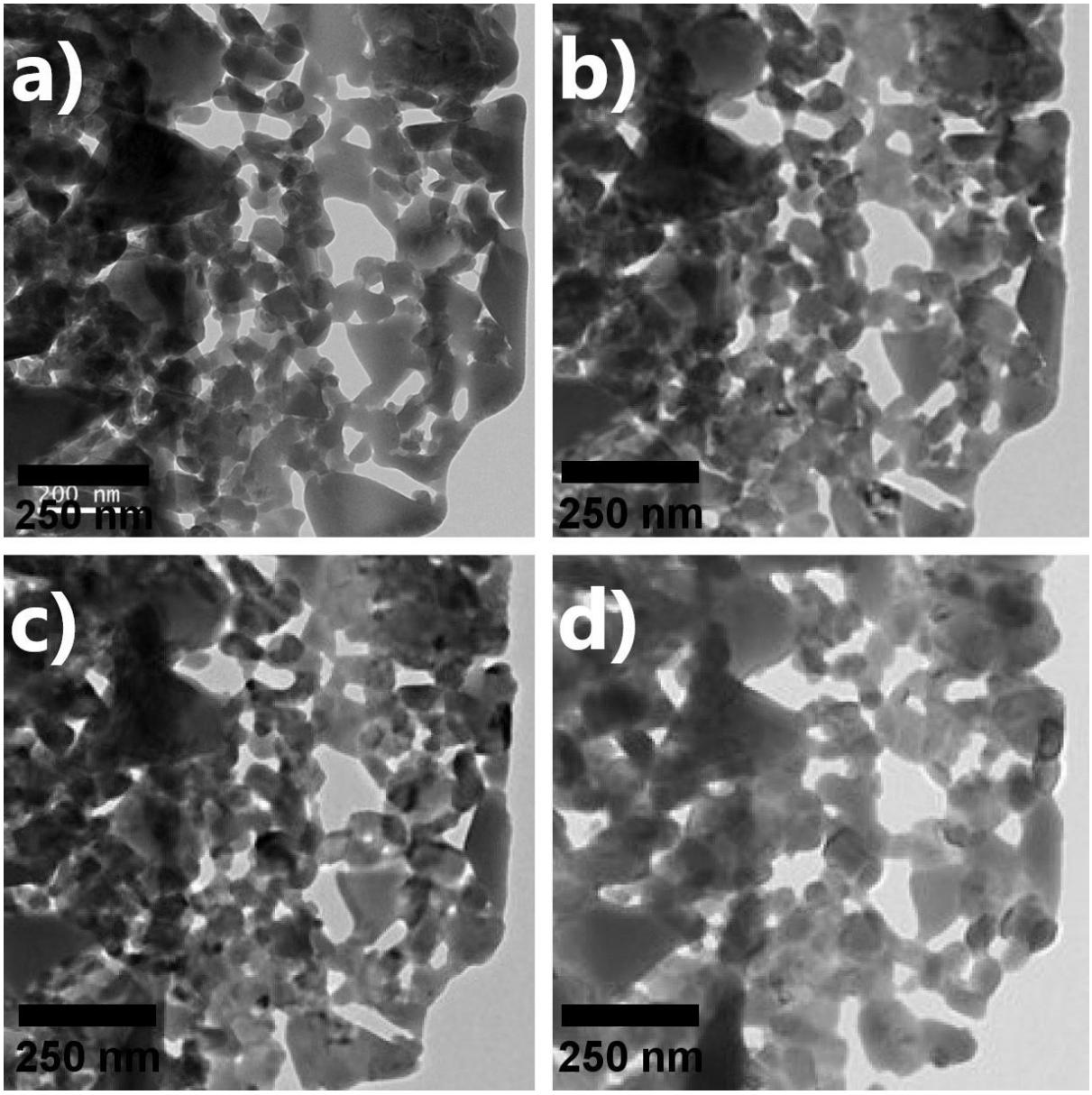

Appendix 21. Micrographs correspond to region A in Figure 111, obtained at 400, 800, 900 1100 ^{o}C, and shown in (a) - (d) respectively. These show no change in particle size but a change in contrast within particles suggest an increase in crystallite size and/or a decrease in microstrain with temperature. Micrographs and diffraction patterns obtained by Dr. Zabeada Aslam, with the assistance of the author.

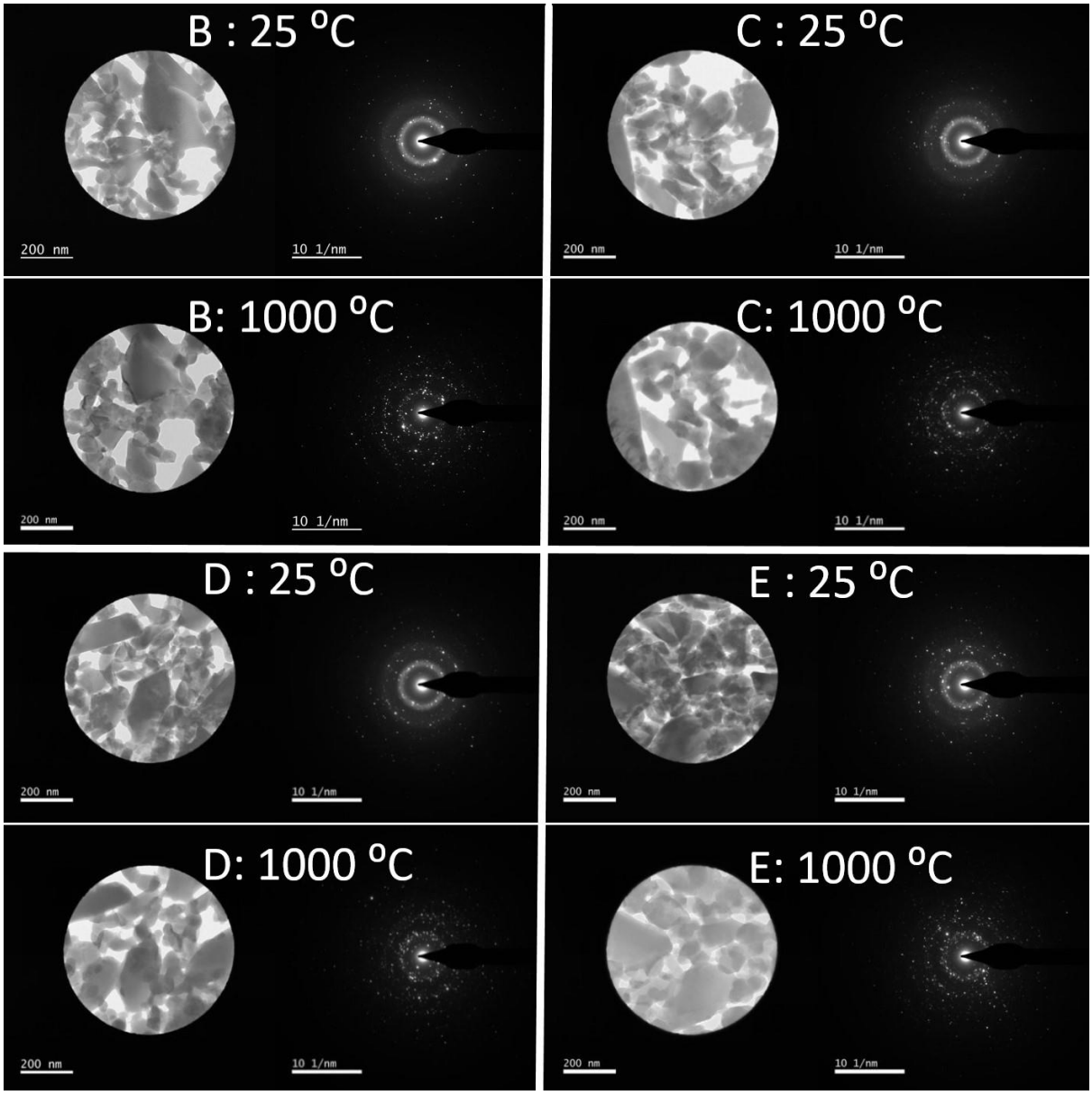

Appendix 22. Micrographs of the region's B, C, D and E were taken at 25 °C and 1000 °C, the sites correspond to red rings in Figure 111. Selected area electron diffraction patterns for these sites are shown to the right of each micrograph. This figure serves as context for the comparison of 25 °C diffraction rings in Figure 113. Diffraction band intensity, and assumed strain, prior to annealing, at 25 °C, generally increased with increasing depth into the film from region E to region D and region C. Region B may have a less intense diffraction band than region C, indicating a greater presence or retention of crystalline order. Micrographs and diffraction patterns obtained by Dr. Zabeada Aslam, with the assistance of the author.